M.Sc. John Burbank

Reactive Boundary Layers in Metallic Rolling Contacts

BAM-Dissertationsreihe · Band 143
Berlin 2016

Die vorliegende Arbeit entstand an der Bundesanstalt für Materialforschung und -prüfung (BAM).

Impressum

Reactive Boundary Layers
in Metallic Rolling Contacts

2016

Herausgeber:
Bundesanstalt für Materialforschung und -prüfung (BAM)
Unter den Eichen 87
12205 Berlin
Telefon: +49 30 8104-0
Telefax: +49 30 8104-72222
E-Mail: info@bam.de
Internet: www.bam.de

Layout: BAM-Referat Z.8

ISSN 1613-4249
ISBN 978-3-9817502-5-6

Reactive Boundary Layers in Metallic Rolling Contacts

vorgelegt von

John Burbank
(Master of Science)
geb. am 11. Februar 1986 in Winnipeg, Kanada

von der Fakultät III – Prozesswissenschaften
der Technischen Universität Berlin
zur Erlangung des akademischen Grades

Doktor der Ingenieurwissenschaften
- Dr.-Ing. -

Genehmigte Dissertation

Promotionsausschuss:

Vorsitzender: Prof. Dr. Aleksander Gurlo
1. Gutachter: Prof. Dr. rer. nat. W. Reimers
2. Gutachter: Dr.-Ing. M. Woydt

Tag der wissenschaftlichen Aussprache: 20.11.2015

Berlin 2016
D83

„Die existierenden wissenschaftlichen Begriffe passen jeweils nur zu einem sehr begrenzten Teil der Wirklichkeit, und der andere Teil, der noch nicht verstanden ist, bleibt unendlich.“

Werner Heisenberg

Dedicated to my father, prof b.

Acknowledgments

This thesis is the result of three years research at the BAM (Federal Institute for Materials Research and Testing in Berlin, Germany) in the division Macrotribology and Wear Protection (BAM 6.3). The completion of this work would not have been possible without the generous funding provided by the German Research Foundation (DFG) in cooperation with the BAM (DFG WO 521/9-1).

First and foremost, I would like to express my most sincere gratitude to my supervisor Dr.-Ing. Mathias Woydt. Dr. Woydt gave me a great opportunity to begin my professional development in the field of tribology. Even though he has been busy coordinating many different research programmes and directing the research in our division, all of which requires him to undertake regular intercontinental travel, he still found time to guide me in my research, utilizing his years of experience to provide a wealth of helpful insights, and helping to ensure the achievement of a level of research quality that I would not have been able to reach without him. Additionally, I thank Dr. Woydt for his participation in the doctoral examination committee.

I thank Prof. Dr. rer. nat. Walter Reimers, head of the division Metallic Materials of the Technical University Berlin (TU Berlin), for his role as a member of the doctoral examination committee, as well as for his undertaking of residual stress and residual austenite measurements of the alloys in my study.

I also wish to thank Prof. Dr. Aleksander Gurlo, head of the division Ceramic Materials of the TU Berlin, for his role as chairman of the doctoral examination committee.

Many thanks go to my predecessor Dr.-Ing. Christian Scholz, now of KYB Corporation (Tokyo, Japan). Christian provided strong guidance and direction from day 1, and taught me a plethora of measurement techniques he himself had used during his own doctoral research at the BAM. Even after moving nearly 9,000 km, he still managed to find time between his busy workdays and taking care of his family to discuss my research and provide guidance.

I would like to thank the staff of division 6.3, both former and present, for providing such a positive work environment. Notably I thank Dipl.-Ing. Norbert Kelling for investing much of his time in maintaining the twin disk test rigs used in this study, and Sigrid Binkowski for the many hours of metallographic analysis of my samples.

In addition to my colleagues in division 6.3, I would like to thank several other colleagues of mine at the BAM for their assistance with material analyses performed for this study including, but not limited to: Sigrid Benemann (SEM-EDX analysis), Astrid Zunkel (spark emission spectroscopy), Gabriele Oder (electron microprobe analysis), Dr.-Ing. Ping Xu (residual austenite and residual stress analysis by XRD), Romeo Saliwan Neumann (EBSD analysis), Prof. Dr. rer. nat. Heinz Sturm (Raman spectroscopy) and Dr. Thomas Gross (XPS analysis).

A very special thank you goes out to my mother Helen, father Garin and brother Paul. Mom, you always managed to keep me in good spirits with an immature joke (or five). You were always there for me, in both good times in bad. Dad, I would not be where I am today without you as my role model. I have come to know true academic exceptionalism through your example. Paul, your quick wit and mastery of both the written and spoken word are awe inspiring. I am proud to call you my brother.

And last, but certainly not least, I would like to thank my wife Helen for her love and support during this, at times, rather trying endeavour, and my daughter Louisa, for giving up some of her play time with dad to let him finish his work.

Abstract

In order to meet the goal of reducing CO_2 emissions, automotive industry places significant importance on downsizing components to achieve greater efficiency through lower weight and reduced friction. As friction reductions are associated with energy efficiency and wear protection with resource conservation, ever greater attention has been given to adamantine carbon-based coatings and high-alloyed steels. Such applications are, however, associated with high production costs and energy expenditures, as well as many technical difficulties. Therefore a key issue in meeting the goals of friction reduction, wear protection and development of comprehensive lightweight strategies is whether or not the functional profiles of state-of-the art alloys can be enhanced by affordable solutions.

The running-in phase of mechanical systems is inevitable and, from a tribological standpoint, critical for the lifetime of such systems, though receives little attention and is poorly understood. The growth of micro-cracks accelerates premature material failure and wear during this phase of heightened friction. With this in mind, the ultimate goal of this current work is to transfer the running-in phase into the final step of the mechanical finishing process through the targeted pre-conditioning of novel, high toughness steel bearings without thermo-chemical treatments and compare these to conventional, case-hardened steels. Two mechanisms were investigated:

a. Cold work hardening and
b. Chemical tribofilm formation.

Steels that showed a tendency toward work hardening and tribofilm formation in previous testing were chosen for this investigation. Thorough characterization of the chosen steels was carried out before any pre-conditioning techniques were applied. The widely used 20MnCr5, seen as a reference gear steel, underwent case-hardening and subsequent deep freezing treatments in an attempt to yield discrete sample groups with respect to residual austenite. This allowed for a more thorough investigation into the effects of residual austenite on the properties of this material. The high-performance alternative steels, 36NiCrMoV1-5-7 (hot working steel) and 45SiCrMo6 (spring steel), were heat treated as recommended by their respective manufacturers, and were not case-hardened. The selection of materials with and materials without case-hardening allows for an investigation into whether or not case-hardening is even necessary to deliver acceptable friction behaviour and wear performance. Elemental analyses were conducted by multiple methods to ensure accurate results. Residual austenite contents of the steels and the depth profiles of residual stresses were determined by X-Ray diffraction (XRD), for 20MnCr5 ranging from approximately 6 – 14 vol.%, and under 2 vol.% for the alternative alloys. Hardness profiles were taken from the testing surfaces into the material core. The carburization of 20MnCr5 led to higher hardness and the greater concentration of carbon in the carburization zone more representative of a hardened SAE E52100, or 100Cr6/102Cr6, than of a non-case-hardened 20MnCr5. Residual stresses from machining and case-hardening were measured directly at the sample surface. The high-performance steels fulfilled manufacturer expectations in terms of elemental content, with hardness values between 50 – 55 HRC and strongly martensitic microstructure character. With characterization of the chosen materials complete, the materials could then be subjected to pre-conditioning.

The first pre-conditioning method involved targeted generation of cold work hardening as induced boundary layers to protect the contact zone against wear. Work hardening was identified both by variations in residual stress profiles, i.e. the introduction of beneficial compressive residual stresses, and hardness increases in the contact zone, providing enhanced wear resistance. Parameters for work hardening were further optimized to reduce damage to the surface substrates of the treated materials. The second pre-conditioning method involved the targeted generation of chemically reactive tribolayers (tribofilms) on twin disk testing rigs. The lubrication strategies were based on:

a. $CaCO_3$, which is predominant in engine oils, and
b. MoDTC, which is commonly used in engine and gear oils.

The films generated in pre-conditioning were analyzed by SEM-EDX with Element-Mapping, Raman spectroscopy, and XPS to elucidate their molecular composition and concentration on the sample surfaces. The combination of these methods of analysis gave a clear indication that 10^4 cycles were sufficient to generate stable and lasting tribofilms. CaO and $CaCO_3$ were the main components of the tribofilm from the first lubricant package, while MoS_2, MoO_2 and MoO_3 were the main components from the second lubricant package.

Finally, slip-rolling endurance testing (T = +120 °C, 10^7 cycles, approximately 19 days in a factory fill engine oil) was carried out on all materials. It was shown that both pre-conditioning methods could achieve significant reductions in friction and wear during testing at up to and including P_{0Mean} =1.94 GPa (P_{0Max} = 2.91 GPa, F_N = 2,000 N). Ultimately, this research showed that:

1. non-case-hardened high-performance steels offer competitive wear performance and better friction behaviour than the case-hardened 20MnCr5.
2. pre-conditioning led to COF reductions to under 7/10 and wear coefficient reductions to an astonishing 1/10 of the original values for the untreated steels under mixed/boundary lubrication.
3. the observed improvements to friction behaviour and wear performance are indicative of a technically simple, cost- and energy-efficient pre-conditioning strategy that may prove an appropriate substitute for existing thermochemical treatments for steel alloys.

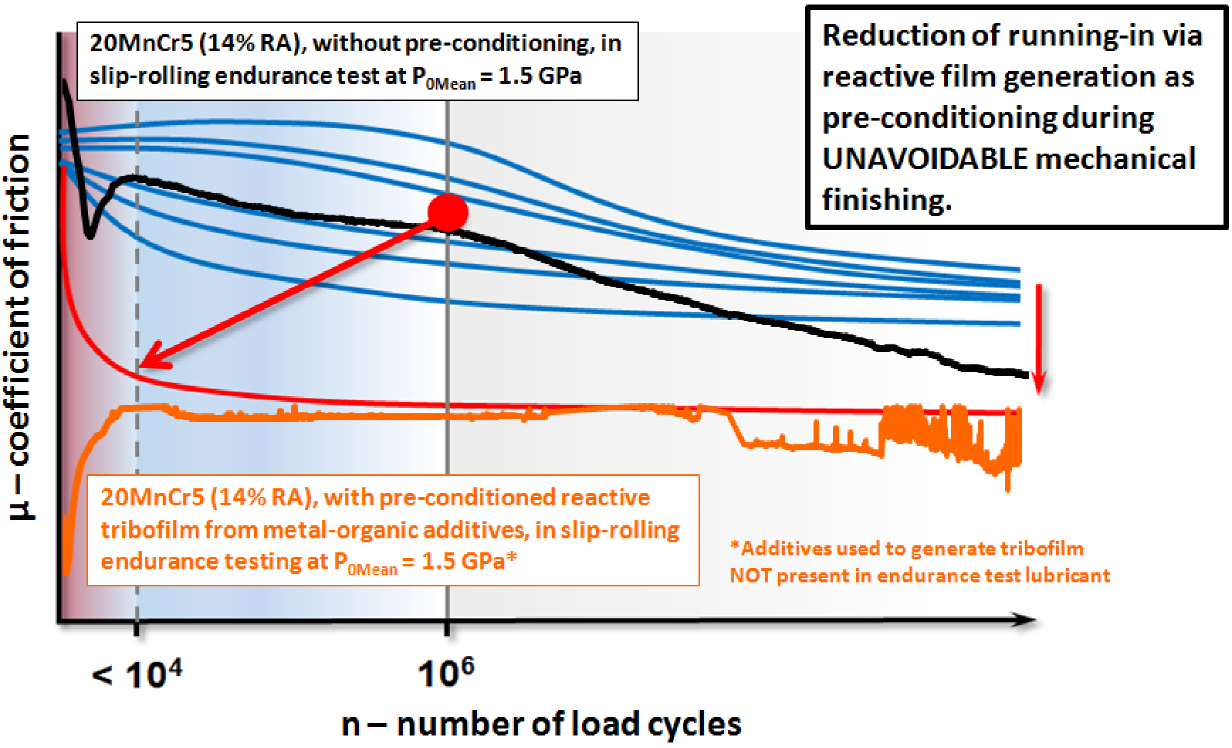

Ultimate goal of accelerated running-in with one “best of” example from actual slip-rolling endurance testing at P_{0Mean} *= 1.5 GPa (*P_{0Max} *= 2.25 GPa,* F_N *= 930 N) and T = +120 °C in BMW FF SAE 0W-30 VP1, ACEA A3/B4, with dynamic viscosity at +120 °C = 5.33 mPa·s.*

Zusammenfassung

Die Automobilindustrie legt im Hinblick auf das Ziel der CO_2-Emissionsreduktionen viel Wert auf die Erhöhung des Wirkungsgrades von mechanischen Komponenten durch Leichtbau. Eine Reduzierung der Reibung wirkt sich direkt auf die Energieeffizienz aus, währenddessen eine Verschleißminderung zu Materialeinsparungen führt. Aus diesen Gründen genießen diamantartige, kohlenstoffbasierte Beschichtungen und hochlegierten Stähle derzeit große Aufmerksamkeit. Deren Herstellung ist allerdings sowohl mit einem hohen Energie- und Kostenaufwand verbunden, als auch technisch sehr anspruchsvoll. Zur Erreichung der Ziele der Reibungsminderung, des Verschleißschutzes und der Entwicklung umfassender Leichtbaustrategien ist es daher von großer Bedeutung, ob sich das Leistungsprofil neuartiger Legierungen durch kostengünstigere Lösungen verbessern lässt.

Obwohl der mechanische Einlauf aus tribologischer Sicht entscheidend für die Lebensdauer mechanischer Systeme ist, genießt er wenig Aufmerksamkeit und ist bis heute nur begrenzt verstanden. So kann die Ausbreitung von Mikrorissen während dieser Phase der erhöhten Reibung zum vorzeitigen Materialversagen führen. In diesem Sinne war es das oberste Ziel dieser Forschungsarbeit, den Einlauf in die mechanische Endbearbeitung vorzuverlegen. Neuartige Stähle wurden dabei ohne kostenintensive, thermochemische Behandlungen gezielt vorkonditioniert und ihre so verbesserten Eigenschaften mit denen von gängigen Einsatzstählen verglichen. Zu den untersuchten Vorkonditionierungsmechanismen gehören die Erzeugung von:

a. Kaltverfestigungen und
b. chemischen Tribofilmen.

Stähle, die in Vorversuchen eine Zuneigung zur Kaltverfestigung und Tribofilmentstehung, wurden für diese Forschungsarbeit ausgewählt. Die ausgewählten Stähle wurden vor jeglicher Vorkonditionierung einer gründlichen, metallurgischen Charakterisierung unterzogen. Der Referenzgetriebestahl 20MnCr5 wurde einsatzgehärtet und in getrennten Gruppen bei verschiedenen Temperaturen tiefgekühlt, um Proben in verschiedenen Nuancen des Restaustenitgehaltes zu erhalten. Damit ließ sich der Einfluss des Restaustenits auf die Materialeigenschaften genauer untersuchen. Die Hochleistungsstähle, 36NiCrMoV1-5-7 (Warmarbeitsstahl) und 45SiCrMo6 (Federstahl), wurden nach den Vorschriften der jeweiligen Hersteller wärmebehandelt, und wurden nicht einsatzgehärtet. Die Auswahl an Stählen, mit und ohne Einsatzhärtung, lässt eine Untersuchung darüber zu, ob eine Einsatzhärtung überhaupt notwendig ist, um gutes Reibungs- und Verschleißverhalten zu erzielen. Elementanalysen wurden mittels mehrerer Methoden zur Gewährleistung der bestmöglichen Genauigkeit der Ergebnisse durchgeführt. Die Restaustenitgehalte der Stähle und Eigenspannungstiefenprofile wurden an einem Röntgendiffraktometer ermittelt. Die Restaustenitgehalte des 20MnCr5 lagen zwischen 6 – 14 Vol.-% und die Restaustenitgehalte der Alternativstähle lagen unter 2 Vol.-%. Härtetiefenprofile wurden auch ermittelt. Die Aufkohlung des 20MnCr5 führte zu einer Steigerung der Härte und der Kohlenstoffkonzentration im Randbereich, sodass dieser Bereich des Stahls eher einem gehärteten SAE 52100, oder 100Cr6/102Cr6, als einem nicht einsatzgehärtetem 20MnCr5 entsprach. Eigenspannungen, die durch die mechanische Endbearbeitung entstanden, wurden direkt unter der Oberfläche detektiert. Die Hochleistungsstähle erfüllten mit Härtewerten zwischen 50 – 55 HRC und ihrem ausgeprägt martensitischen Charakter die Herstellervorgaben. Nach dem Abschluss der metallurgischen Charakterisierung wurden die Stähle vorkonditioniert.

Zur ersten Vorkonditionierungsmethode gehörte die Erzeugung gezielter Kaltverfestigungen an Zweischeibenprüfständen in der Form von induzierten Grenzschichten, die die

Randschicht gegen Verschleiß schützen. Die Wirksamkeit dieser Vorkonditionierung wurde anhand der Zunahme der vorteilhaften Druckeigenspannungen und der Steigerung der Oberflächenhärte nachgewiesen. Beide Eigenschaften verleihen den Stählen eine erhöhte Verschleißbeständigkeit. In einem weiteren Schritt wurden die Vorkonditionierungsparameter zur Erzeugung von Kaltverfestigung optimiert, um die evtl. Deformierung der Substratoberflächen abzumildern.

In einer alternativen, zweiten Vorkonditionierung wurden zwei verschiedene Schmierstoffkonzepte implementiert, um an den Zweischeibenprüfständen chemisch reaktive Triboschichten (Tribofilme) zu generieren. Die Schmierstoffkonzepte basierten auf:

a. $CaCO_3$, was überwiegend in Motorenölen eingesetzt wird und
b. MoDTC, was häufig in Motoren- und Getriebeölen eingesetzt wird.

Die durch die Vorkonditionierung erzeugten Tribofilme wurden mittels REM-EDX mit Element-Mapping, Raman-Spektroskopie und XPS analysiert, um ihre molekulare Zusammensetzung und Oberflächenkonzentration zu ermitteln. Der Tribofilm aus dem ersten Schmiermittel bestand hauptsächlich aus CaO und $CaCO_3$ und der Tribofilm aus dem zweiten Schmiermittel bestand hauptsächlich aus MoS_2, MoO_2 und MoO_3. Aus diesen Analysen wurde ersichtlich, dass 10^4 Laufzyklen zur Generierung stabiler und beständiger Tribofilme vollkommen ausreichend sind.

Anschließend wurden alle Stähle in Dauerwälzversuchen (T = +120 °C, 10^7 Zyklen, etwa 19 Tage in einem Erstbefüllungsmotorenöl) in ihrem Reibungs- und Verschleißverhalten untersucht. Es wurde gezeigt, dass durch vorkonditionierte Kaltverfestigungen oder durch vorkonditionierte Tribofilme die Reibung und der Verschleiß in Wälzkontakten bei Dauerwälzen bis P_{0Mean} =1,94 GPa (P_{0Max} = 2,91 GPa, F_N = 2.000 N) signifikant erniedrigt werden können.Im Endeffekt wurde in dieser Arbeit gezeigt, dass:

1. nicht einsatzgehärtete Hochleistungsstähle konkurrenzfähig zu dem einsatzgehärteten 20MnCr5 sind.
2. die Vorkonditionierungen zu einer Senkung des Reibungskoeffizienten bis auf 7/10 und zu einer Senkung des Verschleißkoeffizienten bis auf 1/10 der Koeffizienten der nicht vorkonditionierten Stähle unter Misch-/Grenzreibungsbedingungen führten.
3. die Verbesserungen des Reibungs- und Verschleißverhaltens auf eine technisch einfache, energie- und kosteneffiziente Vorkonditionierungsstrategie weisen, die noch bestehende thermochemische Behandlungen ersetzen könnte.

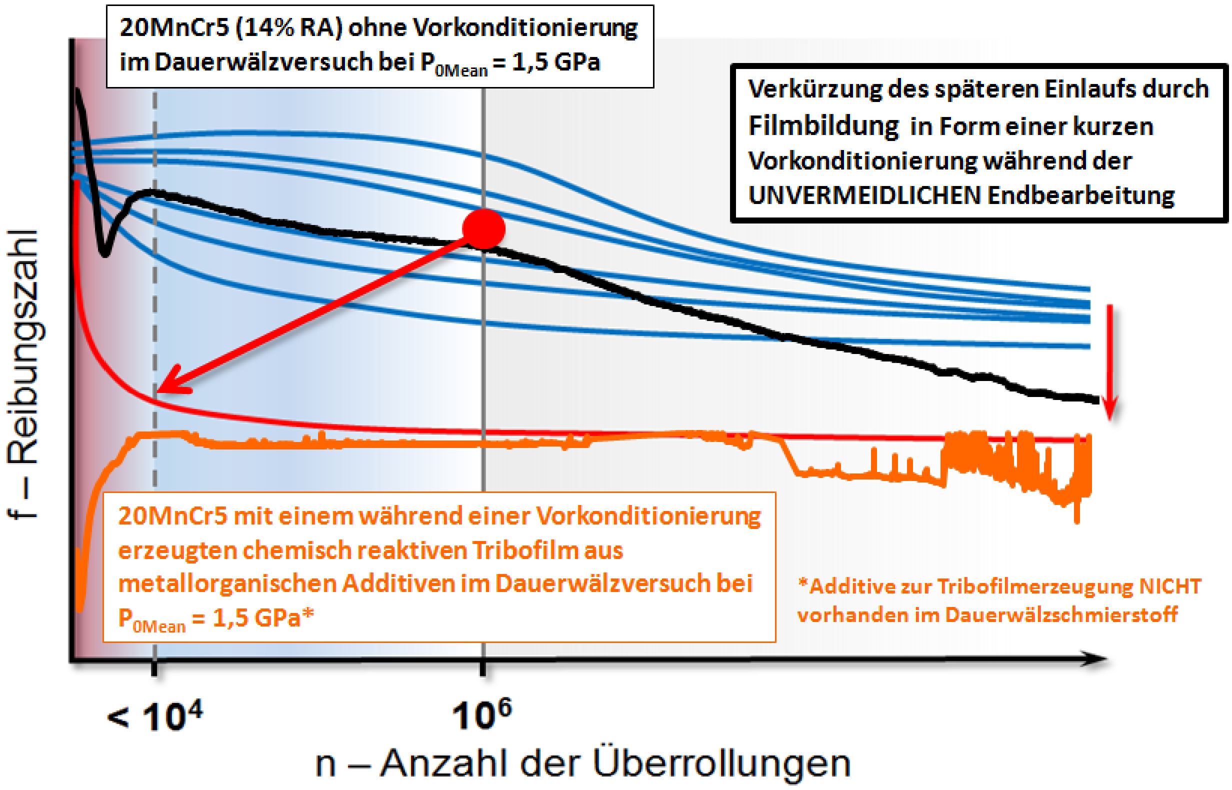

Bildliche Darstellung des beschleunigten Einlaufs mit einem “best of” Beispiel aus den realen Dauerwälzversuchen bei P_{0Mean} *= 1,5 GPa (*P_{0Max} *= 2,25 GPa,* F_N *= 930 N) und T = +120 °C in BMW FF SAE 0W-30 VP1, ACEA A3/B4, dynamische Viskosität bei +120 °C = 5,33 mPa·s.*

List of Publications

1. J. Burbank, M. Woydt, Comparison of slip-rolling behaviour between 20MnCr5 gear steel, 36NiCrMoV1-5-7 hot working tool steel and 45SiCrMo6 spring steel, WEAR 328-329 (2015) 28–38.

2. J. Burbank, M. Woydt, Friction and wear reductions under slip-rolling contact through chemically reactive tribofilm generation during pre-conditioning of steel alloys, WEAR 338-339 (2015) 133-143.

3. J. Burbank, M. Woydt, Optimization of pre-conditioned cold work hardening of steel alloys for friction and wear reductions under slip-rolling contact, WEAR, in press.

4. J. Burbank, M. Woydt, Friction and wear reductions in slip-rolling steel contacts through pre-conditioned chemical tribofilms from bismuth compounds, WEAR, submission under review.

Table of Contents

Nomenclature

Symbols

α_p	[GPa^{-1}]	Pressure-velocity coefficient
η	[-]	Asymmetry corrective factor for calculation of Hertzian contact pressures
$\eta_{(T)}$	[mPa·s]	Dynamic viscosity
λ	[-]	Tallian parameter
μ	[-]	Coefficient of friction
ν	[-]	Poisson’s ratio
ξ	[-]	Asymmetry corrective factor for calculation of Hertzian contact pressures
ρ	[g/cm^3]	Density
σ_u	[MPa]	Ultimate nominal stress
a	[m]	Semi-major axis
b	[m]	Semi-minor axis
E	[GPa]	Young’s modulus
Eht	[mm]	Case depth
F_N	[N]	Normal force
F_R	[N]	Frictional force
HTHS	[mPa·s]	High-temperature high-shear
k	[-]	Elliptical form parameter
K_{IC}	[MPa·m$^{1/2}$]	Fracture toughness
KV	[J]	Charpy toughness
k_v	[mm^3/Nm]	Wear coefficient
n	[-]	Work hardening exponent
P_{0Max}	[GPa]	Initial maximum Hertzian contact pressure
P_{0Mean}	[GPa]	Initial average Hertzian contact pressure
r	[mm]	Radius
R	[mm]	Radius of curvature
R_a	[µm]	Arithmetic mean roughness
R_m	[MPa]	Tensile strength
R_{WC}	[mm]	Radius of curvature of tungsten carbide roller
R_z	[µm]	Average maximum height
s	[%]	Slip
T	[°C]	Temperature
V	[m/s]	Velocity

Abbreviations

ACEA	Association des Constructeurs Européens d’Automobiles
AISI	American Iron and Steel Institute
AW	Anti wear
Bi-ddbsa	Bismuth dodecylbenzenesulfonate
BiDTC	Bismuth dialkyl-dithiocarbamate
CAB	Calcium-argon treatment
CAS	Chemical Abstracts Service
COF	Coefficient of friction
CWH	Cold work hardening
DEA	Dark etching area
DIN	Deutsches Institut für Normung
DLC	Diamond-like carbon
EBSD	Electron backscattering diffraction

EDX	Energy-dispersive X-ray spectroscopy
EHD	Elastohydrodynamic
EN	Europäische Norm
EP	Extreme pressure
FM	Friction modifier
FWHM	Full width at half maximum
FZG	Forschungsstelle für Zahnräder und Getriebebau
HESP	High-energy shot peening
HRC	Rockwell hardness C
HV	Vickers hardness
ISO	International Organization for Standardization
JIS	Japanese Industrial Standards
LPB	Low Plasticity Burnishing
LVDT	Linear Variable Differential Transformer
MoDTC	Molybdenum dialkyl-dithiocarbamate
OEM	Original equipment manufacturer
RA	Residual austenite
RIE	Reactive ion etching
SAE	Society of Automotive Engineers
SEM	Scanning electron microscopy
SFB	Sonderforschungsbereich
TTT	Time-temperature-transformation
VAR	Vacuum Arc Remelting
VIM	Vacuum Induction Melting
WB	White band
WDX	Wavelength Dispersive X-ray Spectroscopy
WEA	White etching area
XPS	X-ray photoelectron spectroscopy
ZDDP	Zinc dialkyl-dithiophosphate

1 Introduction

Currently, global reduction of emissions is a central focal point for automotive original equipment manufacturers (OEMs). This is both a consequence of strict governmental legal directives, particularly in the European Union [1] and, more recently, the United States [2], but also to improve profit margins through the reduction of inefficiencies. It was reported by Leonhard that certain Japanese and European manufacturers have been able to reduce CO_2 emission to curb weight ratios of many of their vehicles to their respective legally required levels well before 2015 [3]. These efforts will need to be intensified to meet the even more stringent requirements for the coming years, such as the EU gCO_2/km target of 95 by 2021 and the US/Canadian gCO_2/km target of 93 by 2025 (see Figure 1.1).

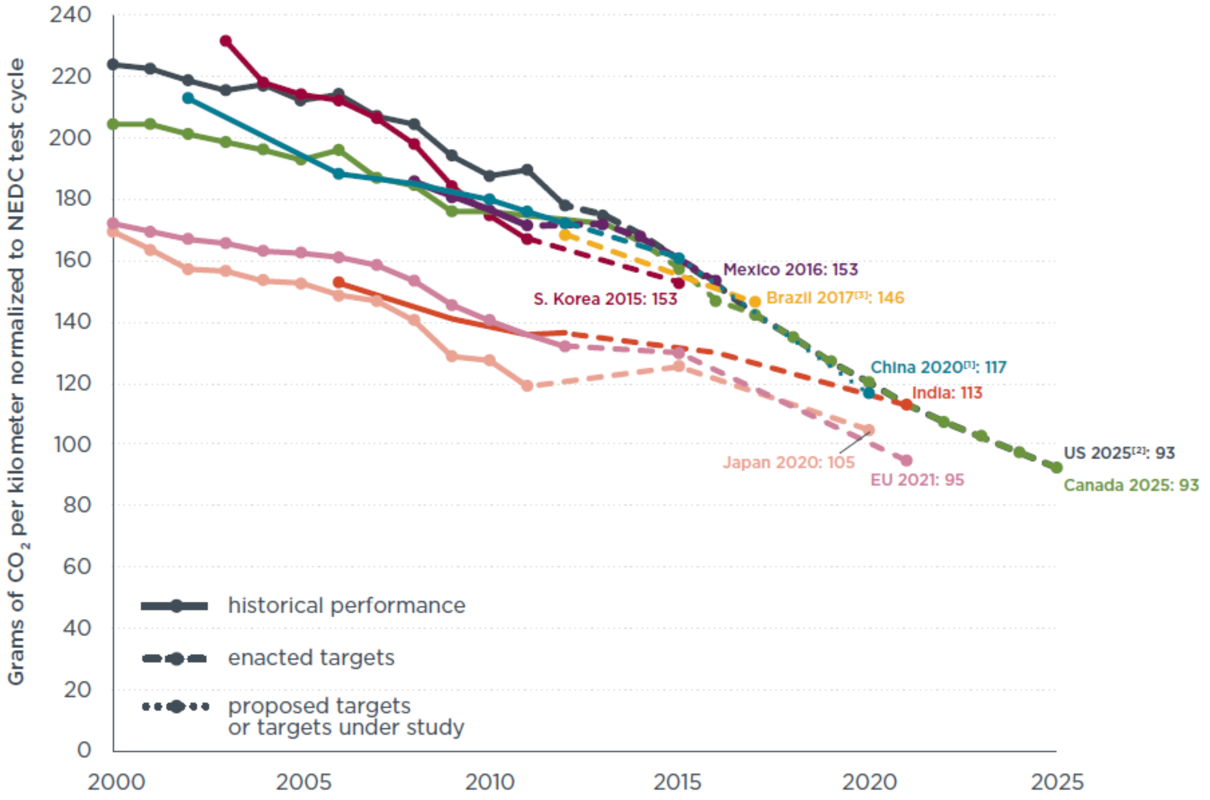

[1] China's target reflects gasoline vehicles only. The target may be higher after new energy vehicles are considered.
[2] US standards GHG standards set by EPA, which is slightly different from fuel economy standards due to low-GWP refrigerant credits.
[3] Gasoline in Brazil contains 22% of ethanol (E22), all data in the chart have been converted to gasoline (E00) equivalent
[4] Supporting data can be found at: http://www.theicct.org/info-tools/global-passenger-vehicle-standards.

Figure 1.1:LITERATURE: Comparison of global passenger vehicle emissions standards normalized to NEDC gCO_2/km [4].

Component downsizing in the powertrain is seen as a critically important approach in the efforts to both improve power efficiency in and reduce CO_2 emissions from automobiles. Weight reductions also represent an important contribution to material efficiency. Component downsizing involves either achieving comparable torques with components of lighter weight or achieving higher torques with components of comparable weight. Both cases result in increases in Hertzian contact stresses and loads to the root of gear teeth. This means that new strategies that do not lead to a deterioration in frictional profile, wear and fatigue life must be implemented, preferably on an affordable and globally available basis. One such strategy involves the application of thin film coatings such as diamond like carbon (DLC). It was demonstrated by Scholz et al. that DLC coatings can be applied to novel steels to achieve significant reductions in friction and wear [5]. Today, these coatings are widely used in automobile engines. Unfortunately, the application of DLC and related thin film coatings can be quite expensive, energy intensive and technically complex. Furthermore, the temperatures at which these coating processes are carried out, often between 300 – 400 °C, require metallurgies that have a high enough annealing temperature so as to avoid any excessive material softening. Scholz et al. also demonstrated that alternative and uncoated steels can significantly reduce the friction under mixed/boundary lubrication [6]. Unfortunately, some of those steels are highly alloyed and require demanding heat treatment cycles. Furthermore, alloys and alloying elements displaying volatile stock exchange prices and subjected to embargo regulations have a limited future in a globalized production concept.

Another important and partially related consideration in reduction of emissions is the practice of “running-in.” Today’s automobile customer is often advised to avoid “stop-and-start” driving and hard acceleration during the first 1000 kilometres of owning a new vehicle. This remains an uncontrolled running-in, varying from customer to customer. The reason for this is that new cars need to be “run in” properly, because piston rings and contacting cylinder surfaces have microscale roughness that yields greater friction and wear during initial operation until the normal operational working roughness is reached. The mechanically contacting surfaces are grinded and smoothed down as a result of the heightened friction. Furthermore, an increase in surface hardness and residual stresses, which have a significant influence on material lifespan, can often be observed. The necessary friction-driven work during the running-in period results in a significant expenditure of energy, which is related to one of the most pressing concerns of automobile manufacturers: lowering CO_2 emissions by the reduction of friction related inefficiencies. Many automobile OEMs, particularly those involved in the production of luxury automobiles, take it upon themselves to run in components before they reach their final customer, negating the need for the customer to run in the engine themselves. Furthermore, the running in of components can be achieved far more efficiently in a controlled production facility setting than by every-day commuters on the road.

With the considerations of downsizing and running-in in mind, this work focuses on the development of pre-conditioning methods that aim to transfer the running-in process into the last steps of machining and finishing of the tribological surfaces in a controlled manner. To this end, a two-fold strategy has been pursued, involving the generation of:

a. work hardening as induced boundary layers and
b. tribo-chemical protective layers, or simply, tribofilms.

Work hardening and tribofilm formation are recognized as among the most effective mechanisms in reducing friction and wear in slip-rolling contacts, and are thoroughly represented in the literature. The novelty of this work is in the generation of such boundary layers through pre-conditioning, rather than regular operation. For work hardening, this means the introduction of beneficial compressive residual stresses and increase hardness that are maintained throughout slip-rolling endurance testing, i.e. normal operation. For chemical tribofilms, this means only using targeted tribofilm-generating additives during pre-conditioning, and, ideally, maintaining the generated tribofilms for as long as possible during endurance testing. Additionally, all pre-conditioning is carried out on the same twin-disk rigs that are used for endurance testing, further exemplifying the simplicity of the pre-conditioning process developed in this research.

In order to evaluate the effectiveness of the developed pre-conditioning strategies, appropriate materials need to be evaluated for comparison. Case-hardened 20MnCr5 (1.7147, AISI 5120) is a well known gear steel that has found industrial applicability for many decades. As a result of such widespread application, much standardization work has been done on the material, and it is, therefore, seen as an appropriate choice as a reference steel in this work.

The core fracture toughness of 20MnCr5 is known to be approximately K_{IC} = 80 MPa·$m^{1/2}$, while K_{IC} = 22 MPa·$m^{1/2}$ at the case-hardened surface. It is important to note that while case-hardening is not necessarily a technically complex process, it is certainly an energy- and time-intensive process, which is often associated with high costs and distortion of component geometry. Moreover, the effectiveness of downsizing components to improve energy efficiency is reduced by the significant energy expenditure through case-hardening. Therefore it is worthwhile to find alternative steels that do not require carburization for good wear performance. Surface hardness is still seen in DIN EN ISO 2639 and ISO 6336-5 as a key property for gears [7,8]. The increase in strength and alloys with higher fracture toughnesses may enhance the slip-rolling resistance under increased contact stresses that result from downsizing [9].

In this regard, the hot working tool steel 9966 Super C from Buderus (36NiCrMoV1-5-7) and silicon alloyed spring steel V300 from Aubert & Duval (45SiCrMo6, 1.8062) were selected for comparison to the reference gear steel. In spite of the fact that neither of these alternative alloys are case-hardened, the intention is to show that they can show friction behaviour and wear performance equal to, or better, than the case-hardened reference steel. 36NiCrMoV1-5-7 has an enhanced molybdenum content for high temperature strength, fracture toughness K_{IC} of 121 MPa·$m^{1/2}$ and high nickel content that reduces tempering brittleness. This martensitic steel has a very low residual austenite content of 1.6 ± 0.3 vol.%. 45SiCrMo6 is enriched with extra silicon to help encourage work hardening behaviour through strain hardening and has a high annealing temperature. It too has a very low amount of residual austenite at 1.9 ± 0.3 vol.% and a high fracture toughness K_{IC} of 80 MPa·$m^{1/2}$ [6].

All materials were characterized before any pre-conditioning was applied. This involved determination of elemental and residual austenite content, and the state of residual stresses and hardness variations in the material. Work hardened materials were evaluated by changes to their hardness and residual stress profiles, while chemical tribofilms were detected by multiple surface analysis techniques, including SEM-EDX, Raman Spectroscopy and XPS. The slip-rolling endurance testing used to evaluate the chosen materials, as well as the effectiveness of the pre-conditioning methods applied to them, has been carried out up to loads of F_N =5,000 N, which yields contact pressures of over P_{0Max} = 4,200 MPa for the chosen spherical vs. cylindrical contact geometry. For comparison, a load stage 12 in the FZG test rig is achieved at P_{0Max} of 1,875 MPa, and is the most intense and relevant testing procedure currently given for gear components. Lubrication was provided by the synthetic factory fill engine oil BMW SAE 0W-30 “VP1” (ACEA A3/B4, $\nu_{120°C}$= 5.33 mPas, sulphated ash of 1.20 wt.-%.), selected for its temperature resistance, which was crucial as all endurance tests were run at +120 °C, typical conditions for automobile engines. Friction and wear coefficients were determined for both untreated and pre-conditioned materials to allow for performance comparisons, along with additional surface and microstructural analysis.

2 State of the Art

2.1 Review of Relevant Steels

The standardization of gear materials has sought to elucidate the most important mechanical properties that determine the performance of gear components. ISO 6336-5, for example, describes allowable quantities of permissible material stress, but mentions only hardness and strength as the essential selection criteria for gear steels in specific application severities [8]. The standard does caution that specific influences on permissible stresses such as surface durability, lubrication effects, surface roughness and gear geometry need to be considered on a case by case basis when selecting appropriate gear steel, but fails to address some extremely critical mechanical properties in detail. Fracture toughness is of particular importance, because this property determines the ability of a material to hinder the spread of cracks, which can cause pitting failures. In the standard ISO 683-11 on wrought case-hardening steels, only the notched bar impact strength is specified, rather than the fracture toughness [10]. Nonmetallic inclusions in steels can also influence the development of sub-surface cracks, so material cleanliness is a related concern.

The aforementioned permissible material stresses have been quantified by ISO 6336-5, and are determined in accordance with three different material classes: ML (low quality), MQ (medium quality) and ME (high quality), whereby the appropriate choice of class depends on the type of production and quality control exercised. The requirements of case-hardened wrought steels (forged or rolled steels) are of relevance to this work. The material classes can be differentiated by several quality requirements. Grain size is not specified for ML, but fine grain (predominantly 5 or lower) is specified for MQ and ME. A minimum surface hardness of 600 HV or 55 HRC is given for ML, while 660 HV to 800 HV or 58 HRC to 64 HRC are given for MQ and ME. ME requires less than 10% bainite in the surface structure, while MQ merely recommends this and ML has no specification. In similar fashion to bainite, limits to residual austenite of 25% are given, though this requires some additional scrutiny, as modern heat treatments are easily able to achieve much lower residual austenite contents than this. It is specified in DIN ISO 3990-5 that an upper limit of 20% residual austenite for the ME grade is permissible, though this is still insufficient [11]. Carbides are also addressed: semi-continuous networks are permissible for ML, discontinuous carbides are permissible for MQ and only dispersed carbides are permissible for ME.

ISO 14635 provides manufacturing details for FZG type A test gears of the gear steel 16MnCr5 [12]. The specified heat treatment states that the test gears are carburized and case-hardened to a case depth of 0.6 mm to 0.9 mm (at a hardness of 550 HV10). The target surface hardness after tempering is 60 HRC to 62 HRC, and the core strength in tooth root centre is 1,000 N/mm² to 1,250 N/mm² (in accordance with ISO 4964). However, there is no mention of yield or ultimate strength, strain hardening coefficients or residual stresses. Awareness of the potential for strain hardening, for example, could be utilized in the strengthening of the tooth root, improving component lifetime. A residual austenite content of 20% is given, but it is unclear whether this should be at the surface or in the material core. Furthermore, no statements on martensite or bainite are given.

Material selection must always be based on the requirements for a specific application. As will be discussed, steels used in gear applications and steels used in bearing applications are typically expected to meet different requirements. The tooth root strength of a gear and the overall surface hardness are of important consideration when choosing an appropriate gear steel, but gear components are typically not required to endure the same extreme contact pressures as bearing components. For example, FZG load stage 12 testing at a contact pressure of

P_{0Max} = 1,825 MPa is considered most extreme for gears, while rolling bearings are typically manufactured to withstand contact pressures of over P_{0Max} = 4,500 MPa.

2.1.1 Bearing and Gear Steels

Though the concept of the bearing may date back to the ancient Romans, or possibly even the Babylonians, bearings would not become a pivotal force mechanical engineering until much later in history. The first modern, recorded patent of a ball bearing design was awarded to Philip Vaughan, a British inventor and ironmaster, in 1794 [13]. With the introduction of the modern bearing design, modern machinery was able to operate significantly more efficiently, a factor that helped to propel the industrial revolution. New and improved bearing designs would be recorded over the following century and a half though work done by Stribeck that identified the metallurgy of 100Cr6 (AISI 52100) proved to be most significant, particularly in the context of 20th century inventions such as railcars, motorcars and aeroplanes [14,15]. The carburizing grades AISI 4320 (15NiVCr1Mo15) and AISI 9310 (10NiCrMo13-5) were also used for such applications.

Rapid advances began in the mid 1950's with the advent of the aircraft gas turbine engine. This would require materials capable of withstanding higher speeds, higher temperatures and higher loads (without premature critical material failure) than previously seen before. In this context, Wilcock and Booser reported in 1957 that AISI 52100 is not useful for applications above 350 °F (177 °C), and that the tool steels AISI M-1 and AISI M-10, which retain their hardness up to 1000 °F (538 °C), are available for such applications [16]. The exploration of such tool steels as bearing materials, led to the development of similar alloys involving greater contents of molybdenum, chromium and tungsten, most notably M-50 for aircraft engines, as reported by Zaretzky [17]. M-50 would become the steel of choice for such high temperature applications, whereas AISI 52100, with a Rockwell C hardness of at least 60, is still useful for low-temperature applications, i.e. under 150 °C. Processes such as Vacuum Induction Melting (VIM) and Vacuum Arc Remelting (VAR) or electro-slag remelting (ESR) were developed as material quality became increasingly important through improved cleanliness. These processes are implemented with the intention of removing non-metallic inclusions, which have been shown to negatively impact fatigue life and are far more prominent in steels that are melted and casted under regular atmospheric environments. More specifically, non-metallic inclusions directly reduce fatigue life by their capability to initiate microcrack development under repeated contact stressing. While processes such as those mentioned above help to remove non-metallic inclusions, improving material quality and, ultimately, fatigue life, the absence of any material defects that drive crack formation is beyond the control of the steel producer, particularly the material is exposed to increasingly extreme conditions. Implicitly, fracture toughness, the material property that defines the stress required to initiate rapid fracture in the presence of a local defect, requires significant attention when designing fatigue resistant components. With the inadequate fracture toughness of through-hardened steels becoming apparent, typically represented by values of $K_{IC} \leq 24\ \mathrm{MPa \cdot m^{1/2}}$ [18], carburizing steel grades would become necessary for applications requiring greater toughness [19].

The production goal for carburized, specifically case-hardened steels, is to generate a hard surface layer, equivalent to that of a through-hardened steel, with a tough material core that has a corresponding high ductility and high fracture toughness. Steels with reduced carbon content are suitable for case-hardening, because the fracture toughness of a material is inversely proportional to its carbon content and hardness. Improved surface hardness is achieved by case-hardening, which involves diffusing carbon into the surface layer prior to heat treatment. This is critical, as carbon content is a contributing factor in material hardness. Extra wear resistance is provided by the hardened surface, while the propagation of microcracks is hindered by the toughened core. Furthermore, fracture toughness can be improved by the addition of nickel, with minimal effect on hardness. This additional nickel has also been shown to induce austenitic phase transformations in low-carbon, high chromium steels above 875 °C. This led to the metallurgical design of AISI M-50 NiL (Ni for nickel and L for low carbon) by Bamberger in 1983 [20]. This steel is also known for its fine carbide structure, which contributes to its improved fatigue life in comparison to AISI M-50 [21]. Like AISI M-50, AISI M-50 NiL is used in high temperature applications, particularly in aerospace technology. Low temperature applications can be met with AISI 9310 or AISI 8620 (20NiCrMo2-2). It is noteworthy that carburized gear steels have proven useful for bearing applications in addition to traditionally case-hardened gear components [22].

Rolling-loaded gear steels have typically followed the concept of offering a hardened contact surface, achieved through case-hardening, and a tough core. The current demand for downsized gear components means that both the tooth flank (pitting, adhesive wear) and the tooth base (fatigue strength of the contact area) experience greater stresses from external contact. As greater loads are applied to lighter materials, the tooth base experiences increasingly intense bending loads, and the necessity of improved materials for rolling contacts becomes ever clearer.

AISI 9310 and AISI 8620 have been cited in the literature as appropriate for most aerospace applications [17]. M-50 NiL has been studied more recently for more advanced applications under extreme conditions, eg. high temperatures [23]. Choosing an appropriate material for a desired application is done in accordance with the required load carrying capacity, operating speeds, lubrication composition and temperature. In other words, less costly materials can be utilized if they meet the desired operating specifications. Nitriding and case-hardening of gear components is undertaken to improve pitting fatigue life and wear resistance. Nitrided gear components can, advantageously, be used directly after nitriding without any additional finishing, as material distortion during the nitriding process is minimal. The same cannot be said for case-hardened gear components, which require additional grinding after hardening due to geometric distortion. Case-hardening is, however, more useful than nitriding when greater case depths are required. Other surface treatment techniques, such as shot peening, have been addressed thoroughly in the literature [24,25]. This will be discussed in greater detail in section 2.6.

Automobile applications are of the most prevalent for many types of gear steels. To this effect, Kanisawa et al. reported the development of a promising new gear steel based on the steel JIS SCM 420 (1.7218, 20CrMo) [26]. They determined through roller pitting fatigue tests that the fatigue life of gears made of this new steel could be more than doubled. The silicon content of the steel was reduced to discourage the formation of grain-boundary oxidized layers, while molybdenum and vanadium (the latter of which also contributes to grain refinement) were added to compensate for lost hardenability. Furthermore, this steel also provides a slight contrast to typical nickel-chromium-molybdenum low alloy steels such as AISI 4320 and AISI 8620, described by Abudaia, as a result of the consistently higher chromium content and increased molybdenum content [27]. Cost factors and good hardenability of AISI 8620, in spite of lack of nickel content compared to, say EN 36 (1.5752, 14NiCr14), make it applicable as a material for small gears, and consequently, one of the more useful steels in automobile gear manufacturing. In this context, the case-carburizing gear steels 16MnCr5 (1.7131) and 20MnCr5 (1.7135) are also currently of great importance [28]. Therefore further literature investigation and review is worthwhile.

2.1.2 Constitution of 16MnCr5 and 20MnCr5 in the Literature

Inhomogenieties in elemental material composition can result from thermal or transformation stresses, phase transformations or strains during phase transformations. Evidence of these phenomena was found in a study on forged disks with a centre hole made of 20MnCr5 [29]. The investigated material was annealed to a ferrite-pearlite structure. The samples were analyzed metallographically and by wavelength dispersive X-ray mappings (WDX). Mappings of cross-sections of the disks were made to characterize asymmetry in the circumferential direction. Results for C, Cr and Mn are provided in Figure 2.1.

The second and third rows of the figure show further processing of WDX results: in the middle row, the moving average (average radius 2 mm) and in the bottom row, the corresponding standard deviation. A decrease in concentration of all three elements in the inner area of the sample is observed, though this is particularly observable for carbon. As alloying elements can have a significant influence on phase transformations, the speed and intensity of such phase transformations may vary between the inner and outer domains, similar to the variation in element concentrations between the domains.

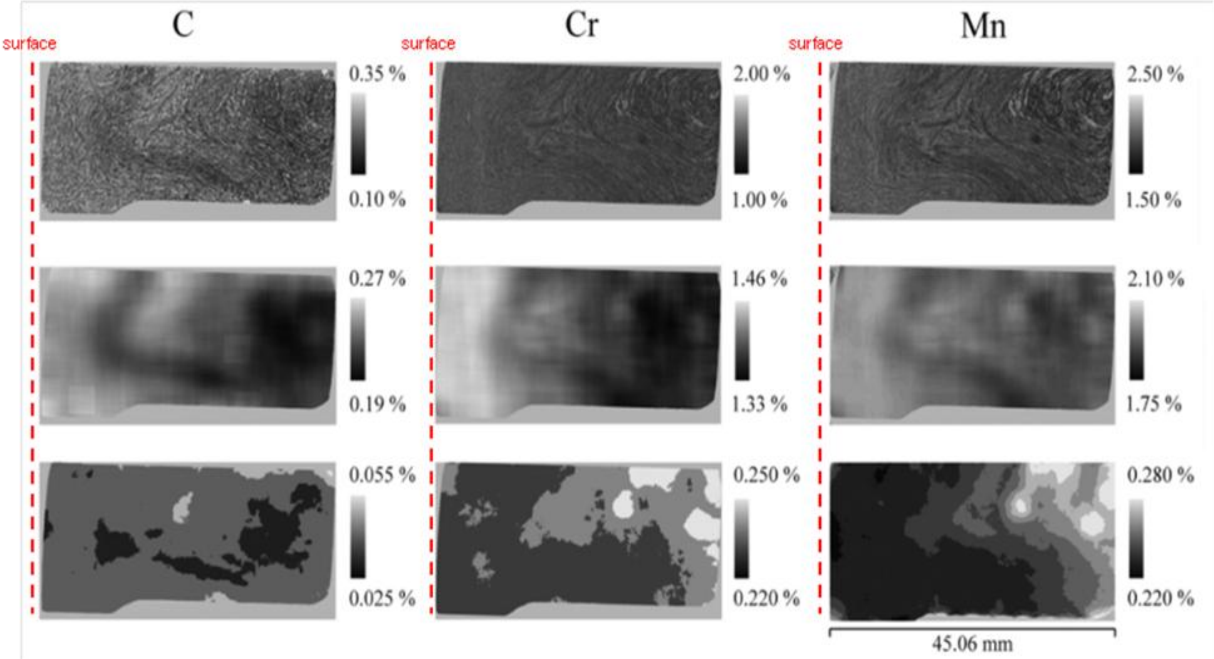

Figure 2.1: LITERATURE: Distribution of the alloying elements C, Cr and Mn at φ = 0 °. Top line: measured concentration from WDX mapping; middle line: moving average of an area with a radius of 2 mm; bottom line: standard deviation of the moving average [29].

In this regard, work by Cheng et al. on the tempering of iron-carbon martensite showed how the different phase transformations occurring during the tempering and ageing processes led to macroscopic volume changes, and consequently, geometric distortions [30]. It had already been established from previous literature data that, the difference in specific volume between austenite and martensite (both 1.1 wt.% carbon) is approximately 4% [31,32]. A volume increase of approximately 0.16 percent was observed in the prepared iron specimens over a heating interval from deep freezing at -180 °C up to room temperature, which is the result of the transformation of approximately 4% of available residual austenite to martensite. This increase in volume due to the transformation of austenite to martensite conforms with results that are already well established in the literature [33,34].

The changes in volume and geometry that accompany martensitic transformations have also been described by Läpple [35]. Using a dilatometer to monitor deviations in length of a steel component (1.3 wt.% carbon) during tempering up to 500 °C, he was able to assign volume increases and contractions discreet temperature ranges. From 100 °C to 200 °C, a volume contraction results from the transformation of tetragonal to cubic martensite. From 200 °C to approximately 300 °C, a volume increase is observed due to the transformation of residual austenite into cubic martensite or lower bainite. From approximately 300 °C to 400 °C, cubic martensite begins to shed carbon, eventually yielding a ferritic composition. This third step is once again associated with a volume contraction, as carbon-free ferrite has a lower lattice constant of $\alpha = 0.2867$ nm compared to that of cubic martensite at $c_M = 0.291$ nm. Above 400 °C, the steel consists of ferrite with embedded cementite, which become increasingly coarse with temperature (coagulation) and eventually become microscopically visible. At this point, the dilatometer curve is no longer influenced by the coagulation process, and a linear relationship between length change and temperature is observed. These processes, in relation to material residual stresses, will be discussed further in section 4.2.

A study by S.C. Wang et al. investigated the microstructure of 20MnCr5 steel tempered at different conditions by EBSD and crystallographic techniques [36]. Normalized 20MnCr5 steel was austenized at 920 °C for 2 h, followed by holding at 860 °C for 30 min and water quenching to obtain martensitic structures. The quenched steel was tempered at 180 °C for 2 h, then cut into samples with the size of 10 mm x 10 mm x 5 mm. The sample, tempered under these conditions, was denoted as A. The IQ and IPF colour maps of the resulting structures from a chosen sample area are given in Figure 2.2.

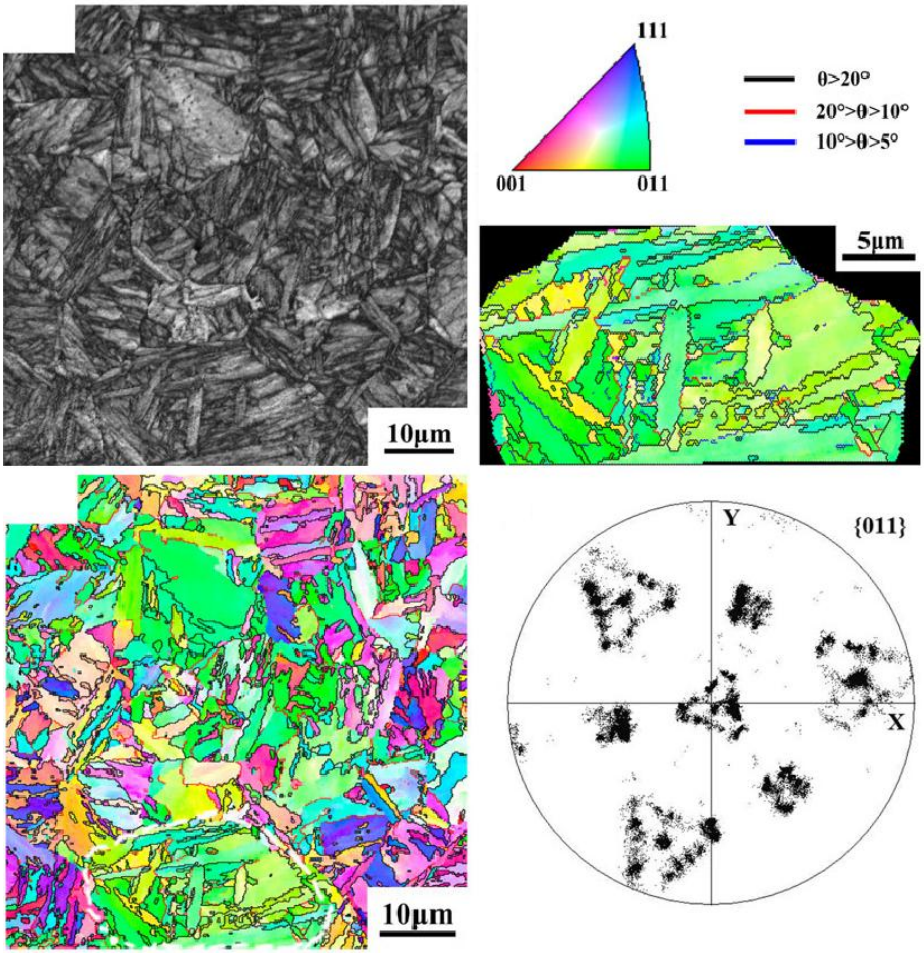

Figure 2.2: LITERATURE: IQ map (top left), IPF colour map (bottom left), an area of prior austenite grain (top right, area found at bottom of IPF colour map) and {011}$_\alpha$ PF of the area in the IPF map [36].

The IQ map from EBSD can clearly reveal the steel's typical lathe martensite structure and depict the prior austenite grain boundaries. The poles on $\{011\}_\alpha$ pole figures distributed continuously on four triangular and three square like areas. While martensitic structures are clearly observed and correspond to the transformed austenite, the IPF colour maps are also suspiciously free of any seriously deformed or distorted structures, such as those encountered in EBSD analyses in similar studies. Therefore it is quite likely that the images presented were thoroughly edited before appearing in this publication. In such a case, careful considerations need to be made to ensure that the results remain as accurate as possible, while still offering worthwhile analytical conclusions to be drawn.

Work done in SFB 570, Project C1, at the University of Bremen explored many aspects of the causes of geometric distortion in metallic components [37]. It is posited that not only heat treatment procedures, but rather every step in the production process can be responsible for geometric distortion. Elastic moduli were determined for 20MnCr5 prior to heat treatment over a range of temperatures from room temperature up to 700 °C. A strong temperature dependence was observed, with an increased dependence on the elongation rate at temperatures above 500 °C. The reasoning behind this is the possible appearance of creep phenomena that result in additional elongation [37].

A heat treatment that would allow for significant martensitic conversion was carried out. This first involved the samples being heated to 940 °C and held for 30 minutes. The samples were then cooled to 840 °C and held for an additional 20 minutes. Finally, the samples were quenched in an oil bath held to 60 °C. The carburization of the samples with 0.40 mass-% and 0.50 mass-% was performed under low pressure. Further details as to how carburization was carried out have already been described in detail [37]. As a result of the high carbon content of these samples, martensitic hardening via high pressure gas quenching was able to be carried out after being held for 20 minutes at 840 °C. Elastic moduli were again determined for 20MnCr5, as well as for the carburized 40MnCr5 and 50MnCr5 samples. These were measured in a temperature range from room temperature up to 400 °C. In this case, there was no clear dependence of the elastic modulus on the temperature observed. The values provided in Table 2.1.were extracted from full distributions available in the referenced report [37].

Table 2.1: LITERATURE: E-moduli for 20MnCr5 and carburized versions measured at a constant elongation rate of $V = 4{\times}10^{-3}\ s^{-1}$ *[37].*

	Elastic Modulus (GPa)			
Temperature	20MnCr5 (before heat treatment)	20MnCr5 (after heat treatment)	40MnCr5	50MnCr5
25	203	221	200	200
100	213	182	194	194
200	217	208	193	193
300	222	177	188	177
400	219	183	-	-
500	174	-	-	-
600	157	-	-	-
700	121	-	-	-

A review of the work done in SFB 570 by Hunkel focuses on the determination of segregations and their influence on phase transformations and plasticity, with attempts at modelling these processes [38]. The initial production of the 20MnCr5 studied is described in detail. Characterization of the material revealed that martensite appeared in areas of higher manganese and chromium content. Pearlite also showed this behaviour in ferrite-pearlite microstructures. Therefore it was determined that the distribution of chemical composition can affect phase transformation kinetics, and it has been shown that distortions of the disks studied are due to segregations [39]. This review addresses anisotropic transformation strain, modifications of phase transformations due to micro-segregations and transformation plasticity. Generation of directed inner stresses during phase transformations was found to be the root cause of anisotropic transformation strain. Microstructural transformation of ferrite/pearlite to banded ferrite/austenite leads to a tensile stress within the austenite and a compressive stress within the ferrite, resulting in anisotropic strain. This is similar to the classic transformation plasticity effect, where an applied external stress results in inner transformation plasticity [40]. The dependency of the position of transformation strain in steel bars with a diameter of 90 mm was also studied. Three dilatometer specimens were used to determine a “difference in strain” value, which provides information on the radius dependency of the transformation strain for heating and quenching [41]. As seen in Figure 2.3, this value is significantly dependent on the radius.

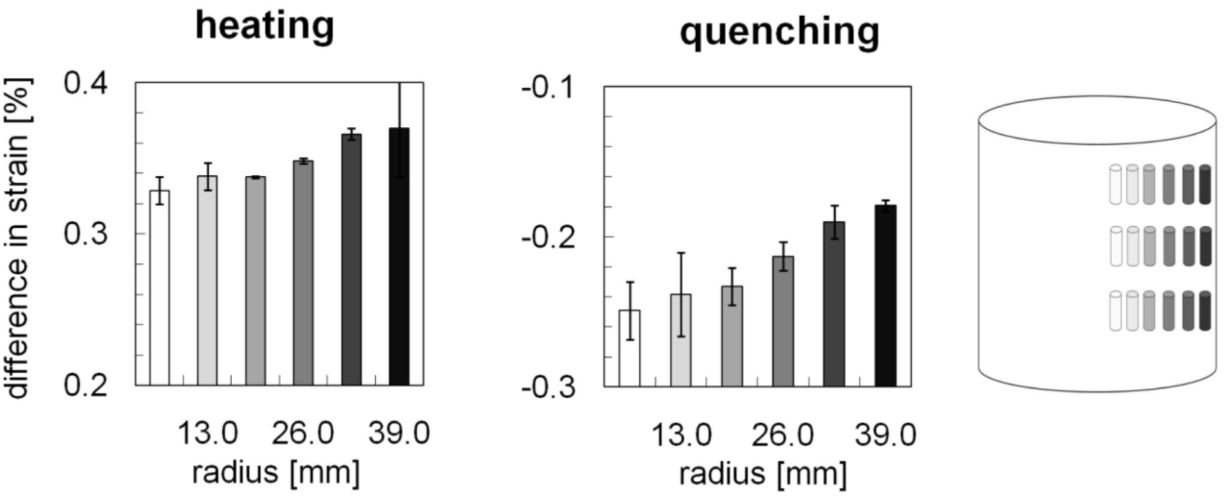

Figure 2.3: LITERATURE: Position dependence of anisotropic strain within a bar of diameter = 90 mm [38].

Transformation plasticity occurring specifically during heating, not quenching, was addressed by this review. Ferrite/pearlite transformations to austenite during heating led to additional creep in the material [42]. Longitudinal anisotropic strain was observed at a heating rate of 5.0 °C/s. For smaller heating rates (longer heating durations) the effects of creep become more and more dominant. It also appears that anisotropic strain is temperature dependent. It was demonstrated that higher heating rates, leading to higher transformation temperatures, caused greater anisotropic strain. It is hypothesized that this is a result of creep phenomena in both the initial state (ferrite/pearlite) and the final state (austenite), which would have an additive effect on the amount of strain. A sign change of the anisotropic strain is also observed during phase transformations, since, at lower temperatures, creep within ferrite/pearlite dominates, while at higher temperatures, creep within austenite dominates. These results are presented in Figure 2.4. It must be noted that the curves representing anisotropic strain vs. temperature at the given heating rate represent three different, constant stress levels, i.e. -10 MPa, 0 MPa and 10 MPa.

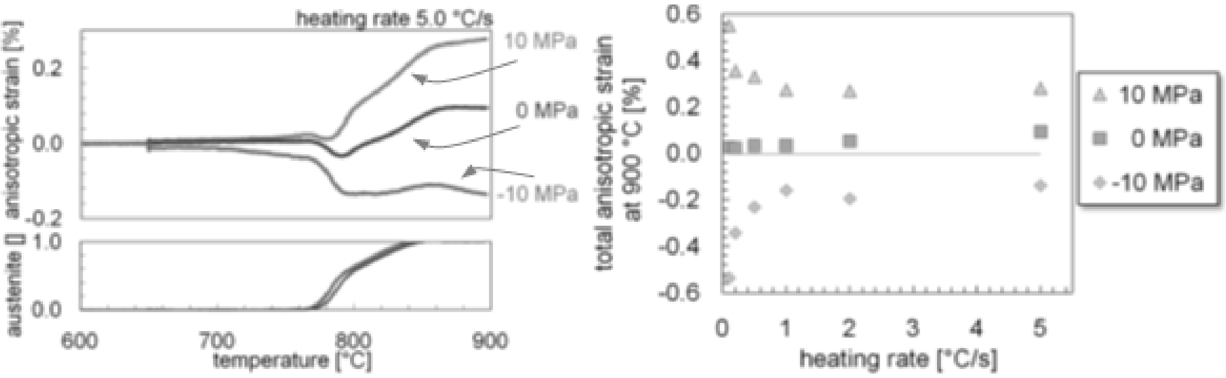

Figure 2.4: LITERATURE: Longitudinal anisotropic strain and austenite content for a constant heating rate of 5.0 °C/s and different stresses (left) and total anisotropic strain at 900 °C for different heating rates and stresses (right) [42].

Control of residual austenite is also of critical importance. A study conducted by Surberg et al. gives some promising insights into control of phase transitions, namely conversion of residual austenite to martensite, during heat treatment of 16MnCr5 and related steels [43]. Guide bolts with an approximate length of 16 cm and composed of 16MnCr5 (1.7131) were carburized at an oven temperature of 930 °C to 0.8 wt.-% carbon, hardened at 850 °C and quenched in an oil bath at 70°C. Samples were then subjected to different intensities of deep freezing treatment for different lengths of time to see what effect this had on residual austenite and geometric stability.

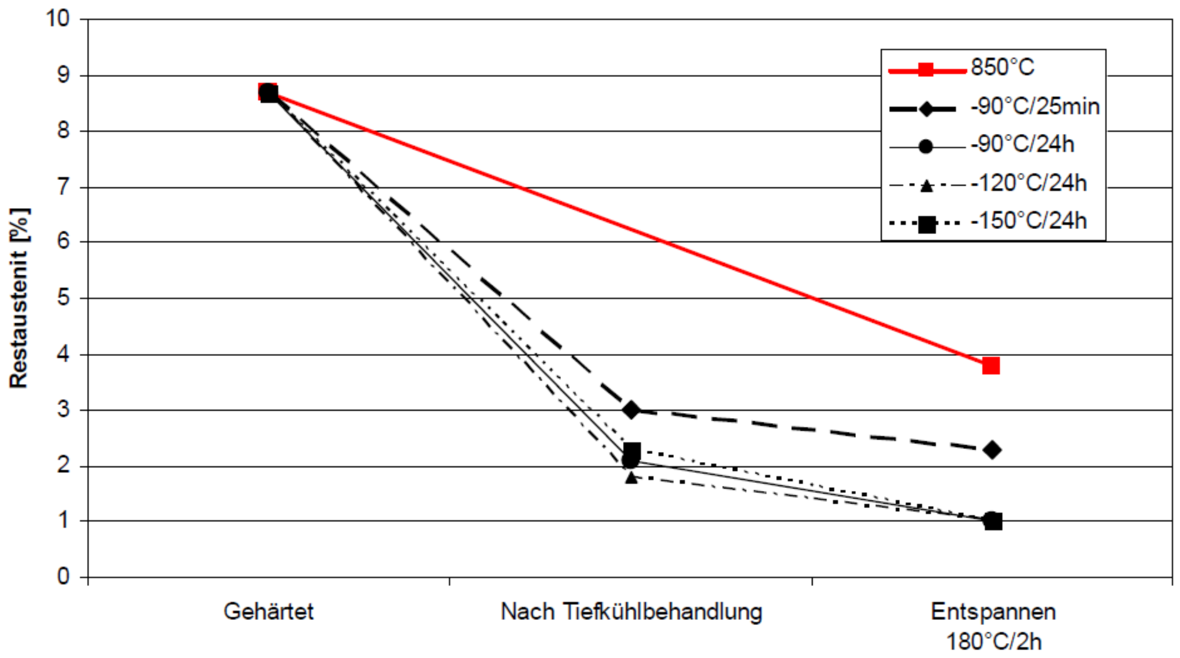

Figure 2.5: LITERATURE: The effect of deep freezing treatment of 16MnCr5 on residual austenite [43].

It can be observed that a significant reduction in residual austenite, i.e. less than 3 % is achieved with a 25 minute deep freezing treatment at -90 °C. Further reduction to approximately 1 % is achieved by lowering the treatment temperature to -120 °C and extending the treatment time to 24 hours, with stress relieving at 180 °C for two hours to follow. Decreasing the treatment temperature further to -150 °C did not lead to a further reduction of residual austenite. This has important implications for the preparation and heat treatment of 20MnCr5. A longer and more intense deep freezing treatment, i.e. at very low temperatures, combined with extended stress relieving time, could be effective in further reducing residual austenite. To yield higher residual austenite contents, an extended tempering duration at an elevated temperature could help to yield higher residual austenite content [44]. This would allow for greater control of distribution of residual austenite contents among discrete sample groups. Important results concerning dimensional stability were also gathered and are presented below.

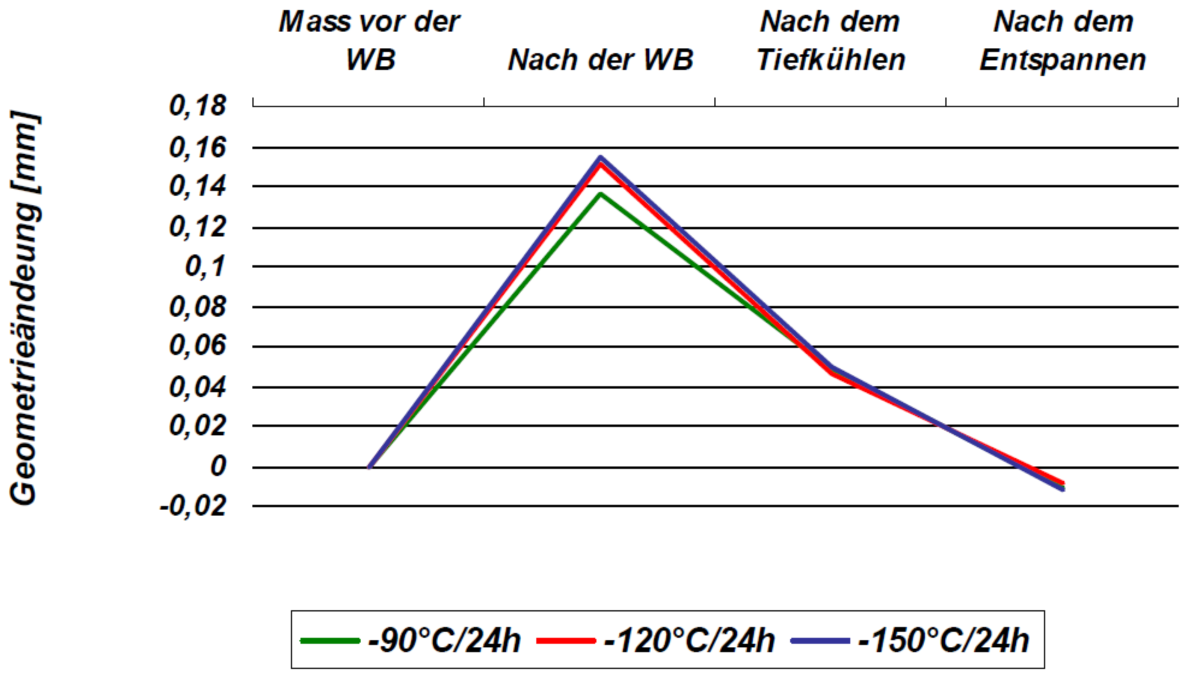

Figure 2.6: LITERATURE: The effect of deep freezing temperature in 24 hour deep freezing treatment on change in sample geometry in terms of bolt length [43].

Deep freezing treatments were carried out at -90 °C, -120 °C and -150 °C for 24 hours, as well as at -90 °C for 25 minutes and for 24 hours. Ultimately it was shown that neither lowering the deep freezing temperature below -90 °C, nor increasing the treatment time to even well beyond 25 minutes, yielded a significant improvement in retention of the original sample geometry.

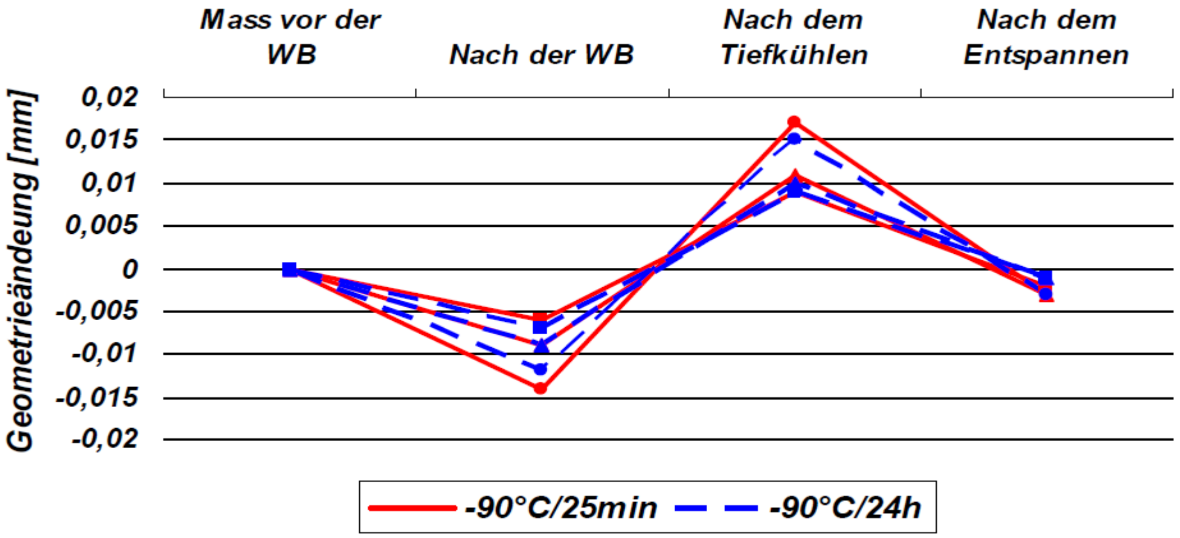

Figure 2.7: LITERATURE: The effect of treatment time during deep freezing treatment on change in sample geometry in terms of bolt length [43].

However the most effective retention of the original sample geometry was obtained by increasing the time of deep freezing treatment. Since it was shown that changes in sample geometry extremely close to zero could be obtained under basic deep freezing conditions, it is unlikely that deep freezing under more extreme conditions, namely lower temperature and increased time, would be worthwhile in yielding zero change in sample geometry.

Other studies have been done on more effective control of residual austenite by deep freezing treatments on 20MnCr5 with the goal of improving the overall wear resistance of the material [45]. In one case, a set of 3 different carburizing treatments along with 4 different cold treatments, seen in Table 2.2, were tested in terms of the residual austenite content and the subsequent effects this had on the sliding wear of the materials. Wear testing was carried out on a pin-on-disk machine (F_N= 100 N, v = 0.4 m/s, P_{0Max} = 412 MPa, T = +25 °C, oil Castrol SLX 0W-30).

Table 2.2: LITERATURE: Residual austenite content in percent for heat treated 20MnCr5 [45].

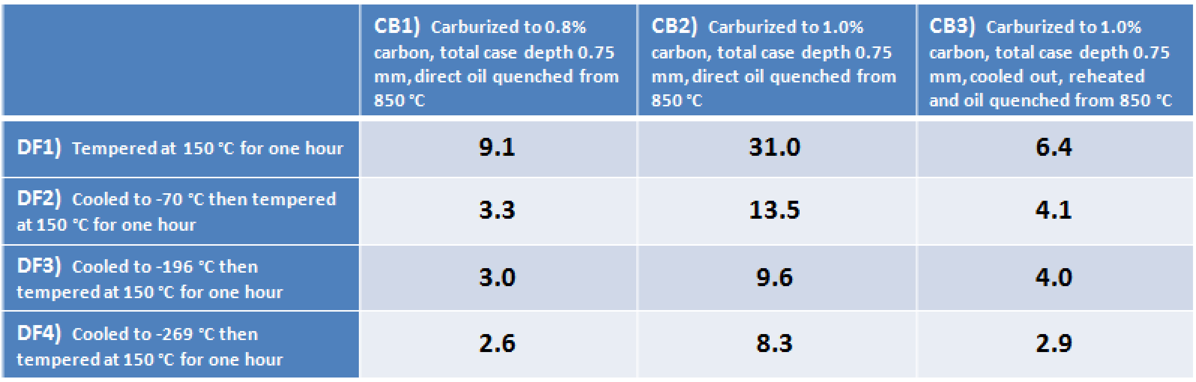

	CB1) Carburized to 0.8% carbon, total case depth 0.75 mm, direct oil quenched from 850 °C	**CB2)** Carburized to 1.0% carbon, total case depth 0.75 mm, direct oil quenched from 850 °C	**CB3)** Carburized to 1.0% carbon, total case depth 0.75 mm, cooled out, reheated and oil quenched from 850 °C
DF1) Tempered at 150 °C for one hour	**9.1**	**31.0**	**6.4**
DF2) Cooled to -70 °C then tempered at 150 °C for one hour	**3.3**	**13.5**	**4.1**
DF3) Cooled to -196 °C then tempered at 150 °C for one hour	**3.0**	**9.6**	**4.0**
DF4) Cooled to -269 °C then tempered at 150 °C for one hour	**2.6**	**8.3**	**2.9**

In contrast to the previously described study by Surberg et al., a significant reduction in residual austenite is observed with a strong decrease in deep freezing temperature. It is also seen that how case-hardening is carried out can have a noticeable effect on residual austenite content, as carburization treatment 2 yielded significantly higher levels of residual austenite in the case of all deep freezing treatments. Normally such heat treatments focus on merely reducing residual austenite content. Controlling residual austenite contents, i.e. limiting them to discrete quantities, is an important aspect of studying the effects residual austenite has on material properties.

The hardness gradients for all cold treatments after carburizing treatment 1 are provided in Figure 2.8 [45]. It can be seen that all the cold treatments resulted in a small increase in hardness near the surface due to the conversion of residual austenite to martensite. The total case depth was 0.65 mm and the effective case depth, at a hardness of 550 HV, was 0.45 mm. The hardness gradients for CB2 and CB3 samples were very similar with the same total and effective case depths [45].

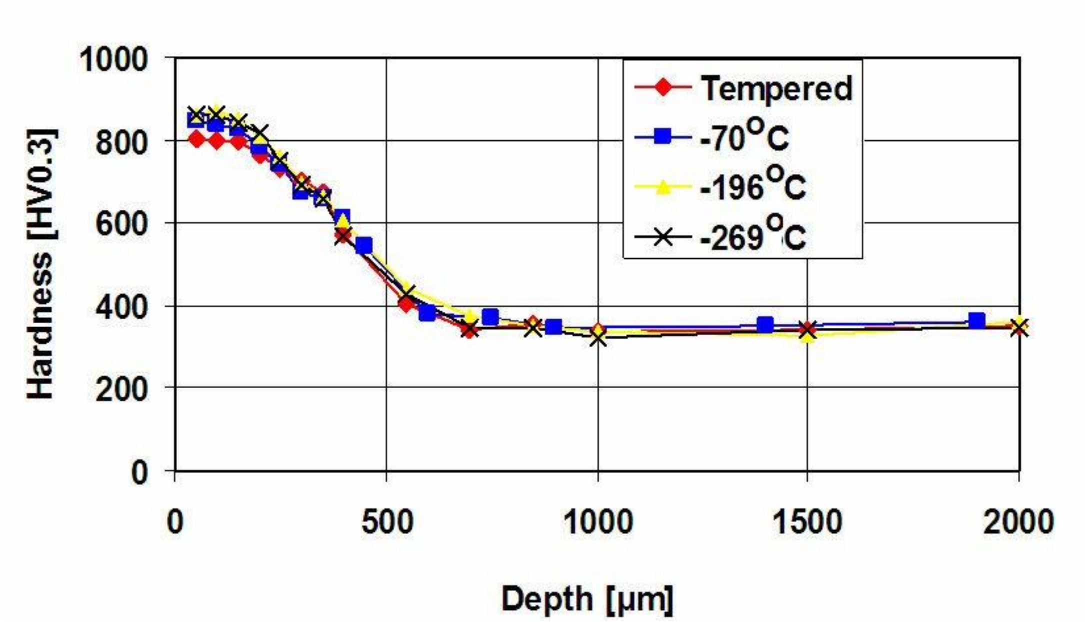

Figure 2.8: LITERATURE: The case profiles for 20MnCr5 after carburizing treatment 1 and varied cold treatments [45].

Observed changes in microstructure are also quite revealing as to the effects of carburizing in deep freezing treatments. The microstructures resulting from CB2, before and after deep freezing treatments, are given [45]. A reduction in residual austenite with the appearance of martensitic structures can clearly be seen.

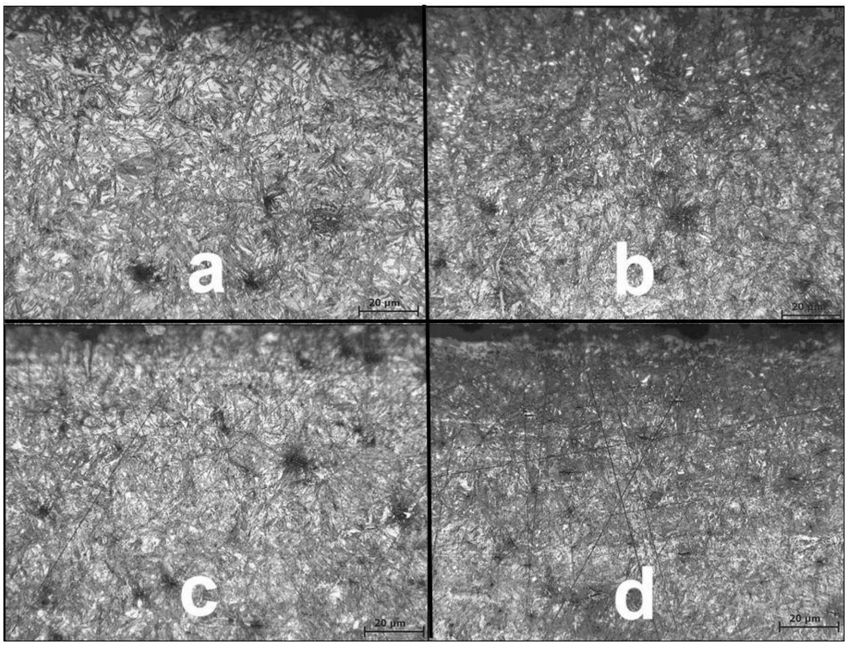

Figure 2.9: LITERATURE: Resulting microstructures after carburization treatment 2 and deep freezing treatments a) temper only, b) -70 °C, c) -196 °C and d) -269 °C [45].

Wear testing was carried out on a pin on disk machine. A 10 kg load was applied to the flat pin. The disk used was made from a cold-working tool steel, which had been hardened and tempered to 58 HRC. The applied sliding speed was 0.4 m/s and the oil temperature was 25 °C. The lubricant used was Castrol SLX 0W-30, multigrade synthetic motor oil. Wear volumes were calculated from an average in three tests per sample.

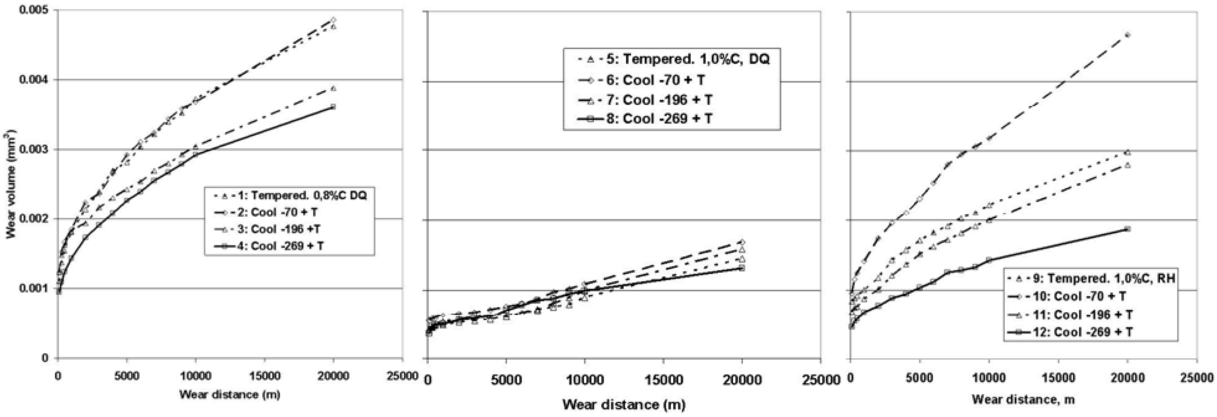

Figure 2.10: LITERATURE: Comparison of wear volumes after carburization treatments 1), 2) and 3), followed by deep freezing treatments a), b), c) and d) [45].

In this case, long term wear rates were established after approximately 5,000 m of sliding, which is, ultimately, more important for the evaluation of wear than the general positioning of the wear curves [45]. These long term wear rates were calculated and evaluated based on the wear volume between 5,000 – 20,000 m of sliding. The results have been re-calculated to report them more succinctly, and to allow for possible comparison with wear results presented further on in this thesis. It should be noted, however, that this would involve comparing wear rates from pin on disk testing at much lower contact pressure to wear rates from slip-rolling contacts at much higher contact pressures.

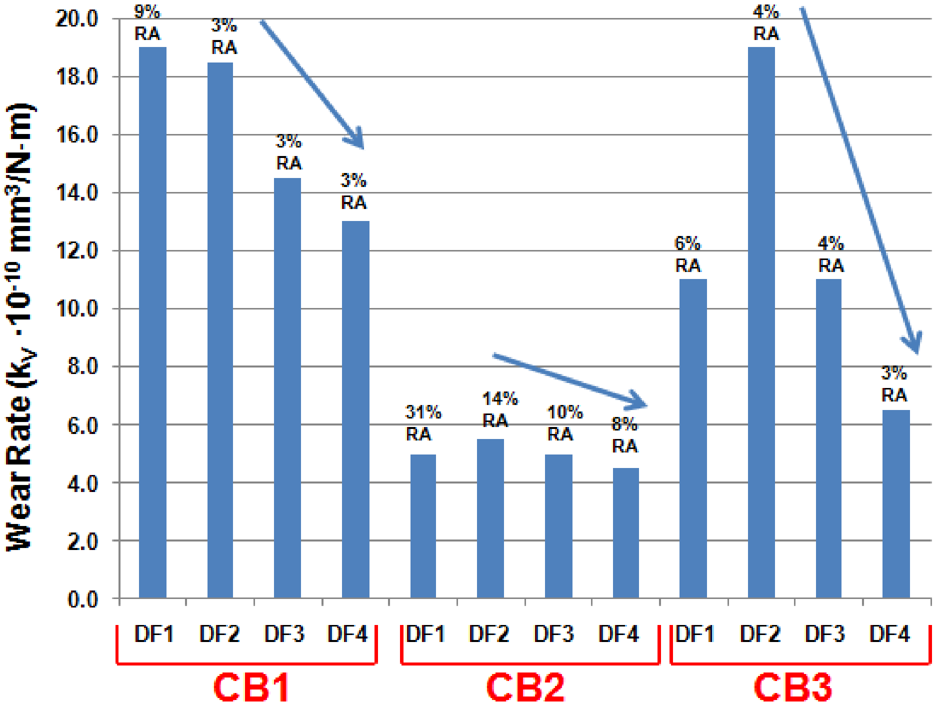

Figure 2.11: LITERATURE: Mean wear rates after 20,000 m of sliding at F_N = 100 N, P_{0Mean} = 275 MPa, P_{0Max} = 412 MPa, in Castrol SLX 0W-30, v = 0.4 m·s^{-1}, T = 25 °C given in 10^{-10} mm^3/N·m [45].

In the case of all three carburization treatments, a very general trend of wear rate reduction with decreased deep freezing temperature can be observed, though this trend is more subtle for CB2. This is observed because samples from CB2 showed significantly higher residual austenite contents, which is normally responsible for reduced wear performance. Further assessment of the case of CB2 is difficult, and more so in the case of CB3, where a surprisingly high wear rate was observed when combined with DF2. The study cannot find a logical explanation for this result, and takes it to be anomalous. A significant improvement in wear rate is observed in all cases where DF4 is applied. This may be accounted for by the precipitation of nanosized carbides [46]. The results indicate that a very intense, low temperature deep freezing treatment is necessary in the case of low carbon steels to have a significant effect on the reduction of wear rates. The implication for this thesis is that lower deep freezing temperatures would need to be pursued in order to yield 20MnCr5 with a residual austenite content lower than 5 %, and furthermore, to improve wear rates.

Comparing carburizing treatments shows that, in this case at least, the carburization process has a much greater influence on the reduction of wear rates than variation of deep freezing treatments. Simply by raising the carbon content of the steel from 0.8 % to 1.0 % essentially led to a 50 % reduction in wear rate, seen in the comparison of CB1 to CB2. However there are further parameters to consider beyond lubricated wear. Materials with higher residual austenite content in the surface layers have, in some cases, proven to offer greater fatigue resistance [47]. Nevertheless, greater contact fatigue resistance can also be yielded by reduction of residual austenite through effective deep freezing treatments [48]. Should residual austenite be present in the surface layers of samples that are to be ground, care must be taken to avoid grinding burns and cracking [49] due to the transformation of austenite to martensite, as well as due to the amorphization [50]. This is especially important because little work hardening can be expected from 20MnCr5, exemplified by its relatively small work hardening exponent, given in Figure 2.12, as a distribution with temperature.

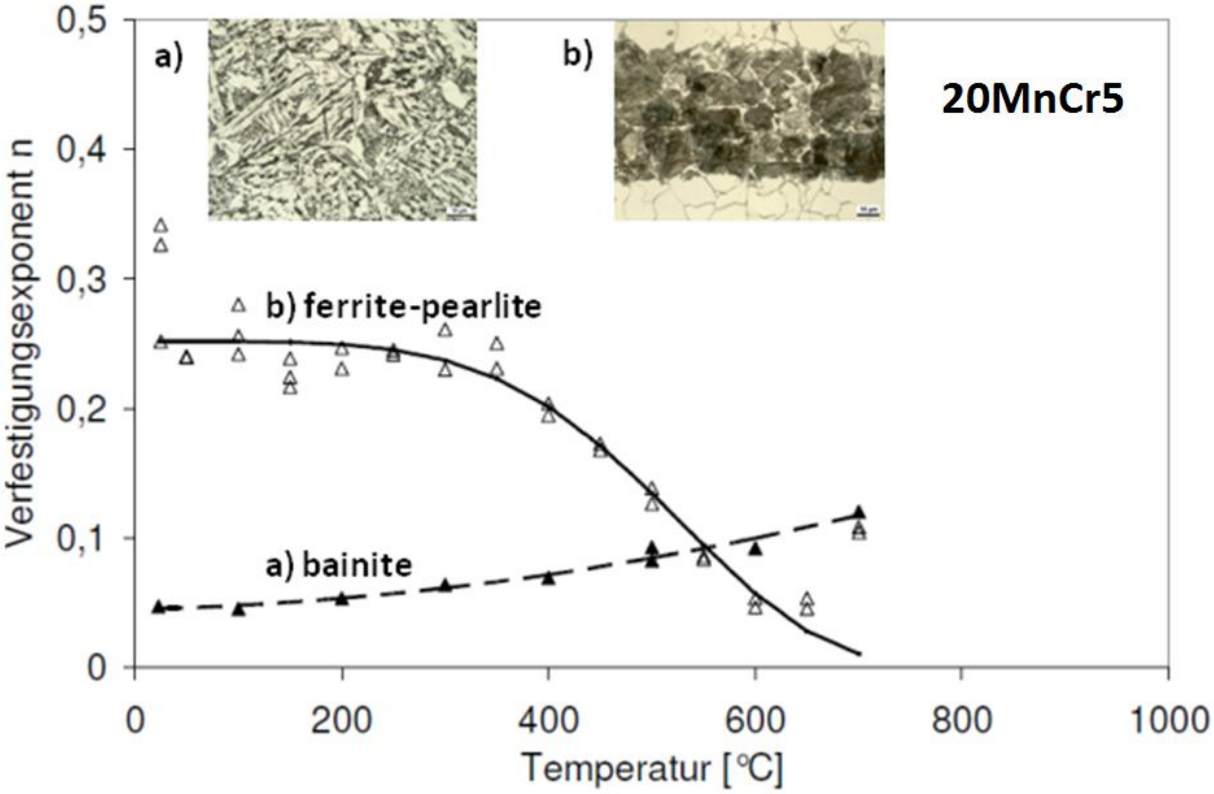

Figure 2.12: LITERATURE: Work hardening exponent, n, dependence on temperature and elongation rates, 10^{-5} s^{-1} for ferrite-pearlite-structure, and $4x10^{-3}$ s^{-1} for bainite [37].

Determination of the work hardening exponent was done based on the Ramsberg-Osgood-Model [51], and was investigated in terms of its dependence on elongation rate, described in detail in SFB 570 [37]. The 20MnCr5 investigated was comprised almost entirely of bainite in its manufactured state, and was tested at the higher elongation rate $V_2 = 4x10^{-3}$ s^{-1}. A slight increase in the work hardening exponent is observed with increase in temperature. After heat treatment, and consequently setting of the ferrite-pearlite-structure, a lower elongation rate $V_1 = 1x10^{-5}$ s^{-1} was chosen due to the lower warming speed of the steel. An initially higher work hardening exponent was observed, which then tapers off after approximately 400 °C. Though the utilization of work hardening processes can be beneficial for a material, where increased hardness can yield greater wear resistance, these processes contribute to significant microstructural transformations. Such transformations can be observed directly by studying the microstructural composition before and after contact stresses, as well as indirectly by analyzing changes to the residual stress profiles of the material.

2.2 Material Stresses and Rolling Contact Fatigue

2.2.1 Residual Stresses

Residual stresses develop reactively in materials to which an external stress has been applied. This may occur as a result of manufacturing processes like grinding and polishing, surface hardness modification procedures such as shot peening, etc., as well as a result of regular component operation. It has been observed in the literature that residual material stresses are able to influence the load carrying capacity of that material [52,53,54] Furthermore, it was observed by Zwirlein and Schlicht that compressive residual stresses can be generated by cyclic stresses when a sufficiently high load is applied [55] This methodology is a fundamental cornerstone of modern material surface treatment techniques, which are discussed in section 2.6. Certain heat treatment approaches, such as case-hardening, are implemented to yield such beneficial residual stresses in addition to increased surface hardness (see section 3.1.1). Whether thermal or mechanical methods are applied to generate residual stresses, the transformation of austenite to martensite is of particular focus, because a measureable volume increase results from this phase transformation, resulting in compressive residual stress as a reaction to the increase in volume.

It was reported by Böhmer that component lifetime can be optimally improved through control of the magnitude of introduced compressive residual stresses [56] It was within this context that he evaluated the evolution of rolling contact induced residual stresses, which are displayed graphically in Figure 2.13. Development of a compressive residual stress maximum of approximately -150 MPa can already be observed at approximately 270 µm from the raceway surface after an applied contact pressure of P_0 = 2410 MPa. As the applied contact pressure is increased up to P_0 = 3060 MPa, the residual stress maximum shifts to approximately -600 MPa. Furthermore, this new maximum is observed at approximately 400 µm from the raceway surface, indicating that increased loads can drive microstructural transformations of available austenite to martensite deeper into the material core. In light of this literature observation it becomes evident that a controlled running-in prior to tribological operation (and assuming no previous material damage) will create a stable metallurgical structure in the subsurface regions that is equal to the one formed during regular tribological operation.

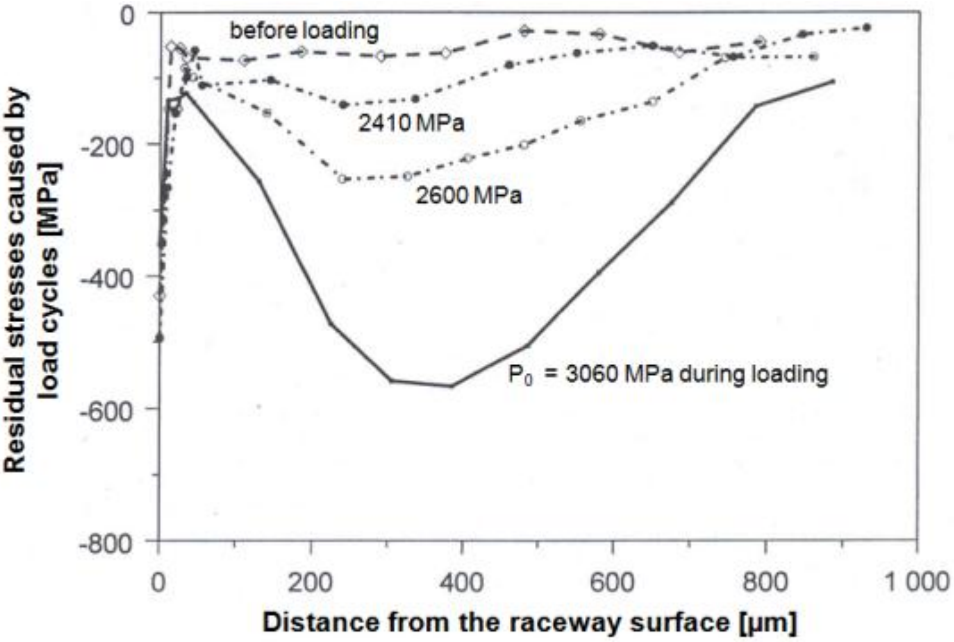

Figure 2.13: LITERATURE: Evolution of residual stresses resulting from cyclic rolling contact with respect to increasing contact pressure [56].

Slip rates are also stated to have significant influence on the residual stress profile of a loaded material. These trends are shown graphically in Figure 2.14, though the magnitudes of the applied slip rates are not specifically provided. It is indicated that implementation of strong slip and low to moderate loads will result in minimal variation of the material residual stress profile compared to the heat-treated state. As previously indicated, increased contact pressures will lead to an increase in compressive residual stresses, and the development of a clear residual stress maximum. At both high contact pressures and strong slip conditions, the depth of the compressive residual stress maximum below the contact surface appears to decrease, though the magnitude of the maximum remains relatively constant.

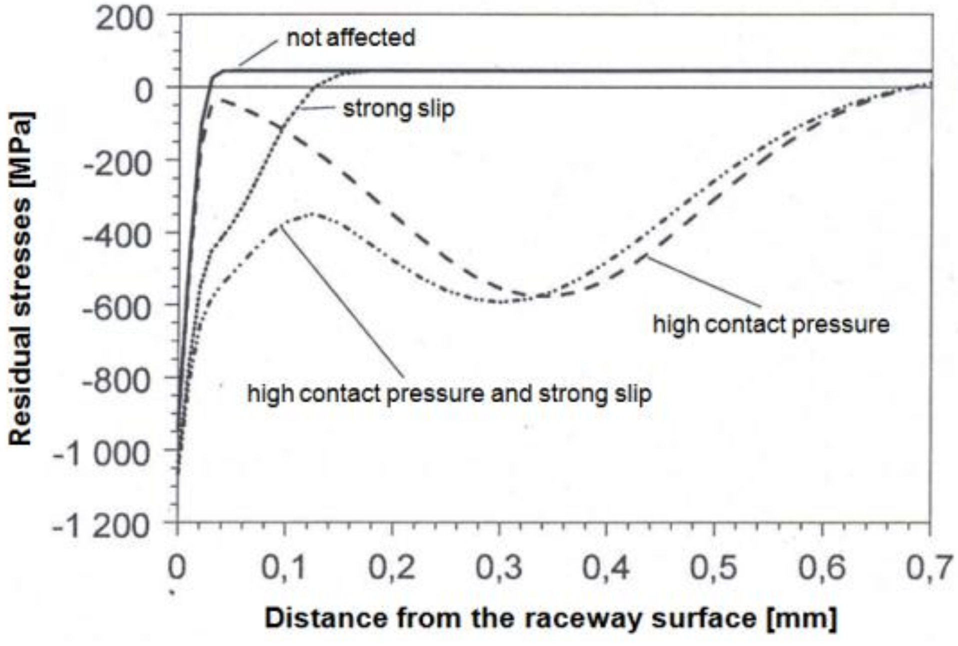

Figure 2.14: LITERATURE: Evolution of residual stresses resulting from cyclic rolling contact with respect to variation in slip [56].

With residual stresses originating from induced structural transformations, it is unsurprising that other mechanical properties are influenced by variations in contact pressure, as well as cycling time. Hardness and strength increases are often the result of increased contact pressure and/or cycling time, though this is discussed in greater detail in section 4.2.2. Regardless of directional changes in hardness, residual stresses have been shown to vary both tangentially and normally. Most importantly, tangential residual stresses are suggested to be a propagating force of the growth of microcracks [57].

2.2.2 Dark Etching and White Etching Areas

The development of microcracks is related to the phenomenon of dark etching (DEAs) and white etching areas (WEAs). The theory of the formation of such areas is still widely discussed, even though it was first presented in detail in the literature over four decades ago [58]. Swahn, and particularly Zwirlein and Schlicht in a later study, illuminated the proximate cause of DEAs as slip motions in underlying lattice formations [55,59]. To better illustrate the phenomenon, they provided images of axial and parallel sections of a deep-grove ball bearing inner ring, where dark sections extended to the contact surface in all but two small areas. They attributed these omitted areas to pure rolling contact, and stated that backward sliding resulted in the middle contact while forward sliding occurred in the outside contacts, both resulting in additional material stress that leads to the formation of DEAs [60]. Adjusting the etching method yielded white bands (WB) in what were previously the darkened areas. These WBs showed different arrangements and angular patterns in accordance with the operating time and pressure of the tested component. This, along with drops in hardness and residual stress profiles with increased operating time, proved to being indicative of martensitic decay, further exemplified by literature research that found WBs to be composed of ferrite particles, surrounded by carbon-rich, carbide-like zones and residual martensite [53,59]. The development of WEAs and DEAs may contribute to rolling contact fatigue.

2.2.3 Rolling Contact Fatigue

Rolling contact fatigue is divided into two main mechanisms:

a. Crack initiation and/or
b. Crack propagation.

In a “brittle” material, cracks propagate so fast that a formal mechanism for crack initiation cannot reasonably be described. In a “tough” material, on the other hand, cracks begin and propagate far more slowly or, as the case may be, do not propagate at all. Ideal slip-rolling materials do not generate cracks or, if initiated, do not allow cracks to propagate. With this in mind, a material must be chosen in proportion to the slip-rolling load to which the material is exposed, i.e. materials with lower toughness may be acceptable for low slip-rolling loads. The relation between loading and fatigue lifetime is expressed by the Lundberg-Palmgren relation [61].

When a load is applied to a material, dislocations and voids can result within the contacting bodies. When such dislocations become sufficiently numerous, microcracks can begin to form. The presence of any subsurface defects in the material may exacerbate cracking when material deformation occurs. Should microcracks continue to grow in a material, eventually, the fracture toughness value will be reached, which will then result in what is known as micropitting, and can cause critical material failure. These steps, leading to rolling contact fatigue, have been described in the literature by Nélias et al [62].A multitude of factors contribute to rolling contact fatigue, including contact geometry, kinematics, load, lubrication properties, temperature, cyclic deformation and surface topography. These influential factors are treated both directly and indirectly in the following sections.

2.3 Rolling Friction

Slip-rolling occurs when two contacting bodies roll against each other at unequal speeds. The velocity vectors of these bodies do not balance to zero at the point of contact and the percentage of occurring slip in this case can be defined by [63]:

$$s = \frac{\vec{V}_1 - \vec{V}_2}{\vec{V}_1} \cdot 100\% \qquad \text{Equation 1}$$

This expression is widely used and is described thoroughly in the literature. The main specimen, i.e. the sample, is represented by vector 1, while the counterbody is represented by vector 2. Both vectors must have a positive magnitude in order to fulfill the basic definition of rolling, though ultimately, the slip ratio depends on the velocity of the counterbody. One can demonstrate from the given equation that if the speed of the counterbody is lower than that of the sample, the slip ratio will be positive. Furthermore, this means the resulting frictional force on the sample will be against the direction of rolling. The opposite applies when the speed of the counterbody is higher than that of the sample. However the amount of slip is so high with the frictional force in the same direction as the rolling motion that the fundamentals of rolling motion are not met and this scenario is therefore neglected.

The presence of friction means that both bodies will undergo some level of deformation, depending on their individual elastic properties. The deformation of the contacting surfaces will lead to the formation of a bead in front of the contact, opposite to the direction of motion. The counterbody can be seen to create a kind of “plowing” effect when under a sufficiently high contact pressure, which leads to even further deformation and slip with respect to the relative motion of the contact bodies. The resulting frictional force is derived from Coulomb’s Law and described by the equation:

$$F_R = \mu \cdot F_N \qquad \text{Equation 2}$$

The velocity of the contact bodies, the presence of lubrication and adhesion between the contact surfaces can also influence slip-rolling friction. Both hard and soft coatings can be developed to help reduce the amount of friction and deformation the contacting bodies experience. Hard coatings offer a lower susceptibility towards fatigue, while soft coatings offer greater adaptability towards the applied load, reducing the Hertzian contact pressure by spreading the contact over a greater surface area.

2.4 Hertzian Contacts

In 1881, the physicist Heinrich Hertz published the first paper to analytically describe the reasons for the deformation of two elastic bodies with curved geometry in a static state [64]. This would become the field of contact mechanics. Contact mechanics involves studying the deformation of solid objects that have one or more points of contact. The contacting bodies considered by Hertz, however, are now referred to specifically as Hertzian contacts.

A defined contact is created between two bodies by adding curvature to one or both of the bodies. This allows for transfer of applied load between the contact bodies when they are put in relative motion. This load is only distributed over a small, local surface. This distribution over such a small surface area means the resulting stresses are considerably higher, than were the load transferred over a larger area. The contact geometry can be linear, circular or elliptical depending on the geometry of the bodies. Specific geometric parameters, namely the radii a and b of defined ellipses, of the contact and the contact pressures can be determined by applying the equations developed by Hertz [63]:

$$a = \xi \cdot \sqrt[3]{\frac{3 \cdot F_N}{\sum k} \frac{\left(1-\nu^2\right)}{E}} \qquad \textit{Equation 3}$$

$$b = \eta \cdot \sqrt[3]{\frac{3 \cdot F_N}{\sum k} \frac{\left(1-\nu^2\right)}{E}} \qquad \textit{Equation 4}$$

where

$$\frac{\left(1-\nu^2\right)}{E} = \frac{1}{2} \cdot \left(\frac{\left(1-\nu_1^2\right)}{E_1} + \frac{\left(1-\nu_2^2\right)}{E_2} \right) \qquad \textit{Equation 5}$$

with E_1, E_2, Young's modulus,1 and 2 referring to the two contacting bodies
ν_1, ν_2, Poisson's ratio, 1 and 2 referring to the two contacting bodies
ξ, η, the corrective factors describing the deviation from ball-on-ball geometry
k, the contact parameters and F_N the normal force

These equations allow for the calculation of the semi major axis, a, and the semi minor axes, b, forming an elliptical contact surface. The maximum Hertzian contact pressure is then calculated by:

$$\mathrm{P}_{\max} = \frac{1}{\xi \cdot \eta} \cdot \sqrt[3]{\frac{3 \cdot F_N \cdot}{8\pi^3 \left(\sum k\right)^2} \frac{\cdot \left(1-\nu^2\right)^2}{E^2}} \qquad \textit{Equation 6}$$

With the values of the semi major and semi minor axes, the average Hertzian contact pressure is calculated as well:

$$\mathrm{P}_{\mathrm{mean}} = \frac{2}{3} \cdot \mathrm{P}_{\max} = \frac{F_N}{\pi \cdot a \cdot b} \qquad \textit{Equation 7}$$

In work by Shigley et al., the maximum shear stress, $\tau_{\max}$, and principle stresses, σ_x, σ_y and σ_z, as a function of maximum pressure, $\mathrm{P}_{\max}$, beneath the surface contact point in a static case of two contacting spheres (Figure below, to the left) and two cylinders (Figure below, to the right right) were evaluated [65].

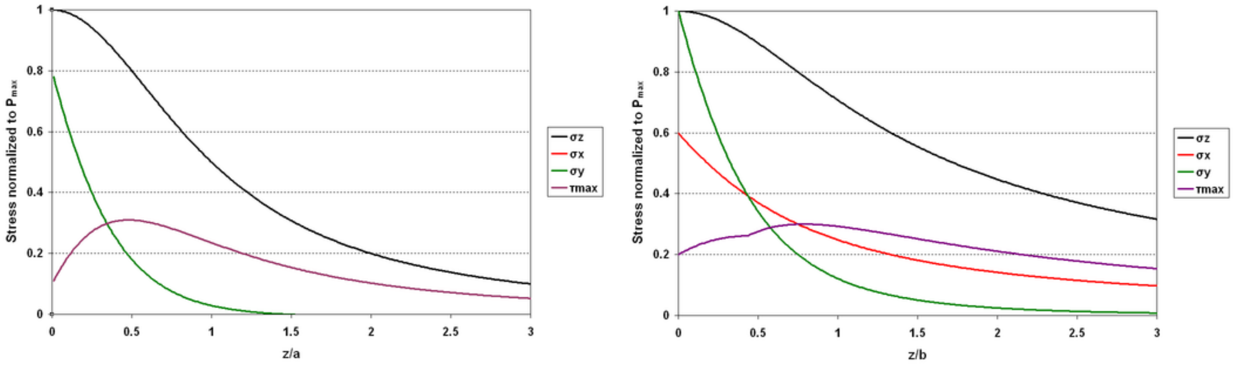

Figure 2.15: LITERATURE: Magnitude of stress components below the surface as function of maximum pressure for contacting spheres (left) and cylinders (right) with $\nu = 0.3$ in static case [65].

Furthermore, the depth and maximum shear and contact stresses are also given for different elliptical parameters, k, in Table 2.3 below. The maximum shear stress occurs at a point beneath the surface on the z-axis.

Table 2.3: LITERATURE: Depth, maximum shear and contact stresses for different elliptical parameters k [65].

k = b/a	0	0.2	0.4	0.6	0.8	1.0
z/b	0.785	0.745	0.665	0.590	0.530	0.480
τ_{Max}/P_{Max}	0.300	0.322	0.325	0.323	0.317	0.310

2.5 Lubrication

Lubrication involves the introduction of a substance between two or more surfaces in close proximity and moving relative to each other, and is employed to reduce friction and wear by separating both surfaces through a film. Lubricants have additional important tasks, described in the literature, including [66]:

- transmission of forces due to hydrodynamic thin films, which reversibly solidify in the contact
- physical or chemical induction of reaction films
- dispersing and deterging of fluid or solid contaminations
- removing of chips and cooling effects when used as cooling lubricant in metalworking
- corrosion protection
- evacuation of heat

Proper lubrication helps to provide reliable operation of equipment, reduces the rate of wear, and helps to prevent excessive stresses or seizures of operating components. A lubricant may be a solid, a solid/liquid dispersion, a pure liquid, a liquid-liquid dispersion or a gas, though the focus of this work will be on liquids. Lubricants may be enhanced with the addition of carefully selected additives to the base oils. Specific additive strategies for the formation of chemically reactive protective films are discussed in the next section. With the increasing importance of the downsizing of components, lubricant packages are becoming ever more complex, whereby the interactions between individual additives need to be carefully considered.

One must also consider the specific application for which the lubricant is intended in designing appropriate and balanced lubricant additive packages. In a technical study by Wink on predicting the scuffing risk to spur and helical gears in commercial vehicle transmissions, five different lubricant formulations (three synthetic and two mineral-based) were tested for their ability to mitigate the scuffing of gears in FZG testing [67]. In total, 50 gear sets were evaluated. The synthetic lubricants yielded both the lowest and highest FZG load stage failures, while the mineral oil-based lubricants showed consistent load stage failures. This is further evidence that, regarding synthetics and mineral oils, one is not necessarily exclusively better than the other, though the current trend appears to be heading toward more use of synthetics due to their applicability over a greater range of temperatures. Both have advantages and disadvantages depending on the application. For example, synthetics can be customized to provide more flexible viscosity performance and temperature extremes, both high and low, but can be susceptible to decomposition effects in certain chemical environments [68].

A most important consideration for the application of a lubricant is the film thickness, which depends on viscosity, pressure in relation to viscosity, geometry and speed. The film thickness, in accordance with the separate domains of the friction regimes in the Stribeck curve, determines the type of lubrication, or the lubrication regime. A graphical description is provided in Figure 2.16. The domains of the Stribeck curve describe the evolution of the coefficient of friction vs. the ratio of lubricant film thickness to component surface roughness, known as the Tallian parameter, λ. The lubrication regimes described are:

I) Boundary lubrication, valid for $\lambda < 1$ – two surfaces are mostly in contact with each other even though a fluid is present.
II) Mixed/boundary lubrication, valid for $1 < \lambda < 3$ – two surfaces are partially separated and partially in contact with each other.
III) Hydrodynamic lubrication valid for $\lambda > 3$ – two surfaces are completely separated by a fluid film and the flow of the film is not influenced by the roughness.

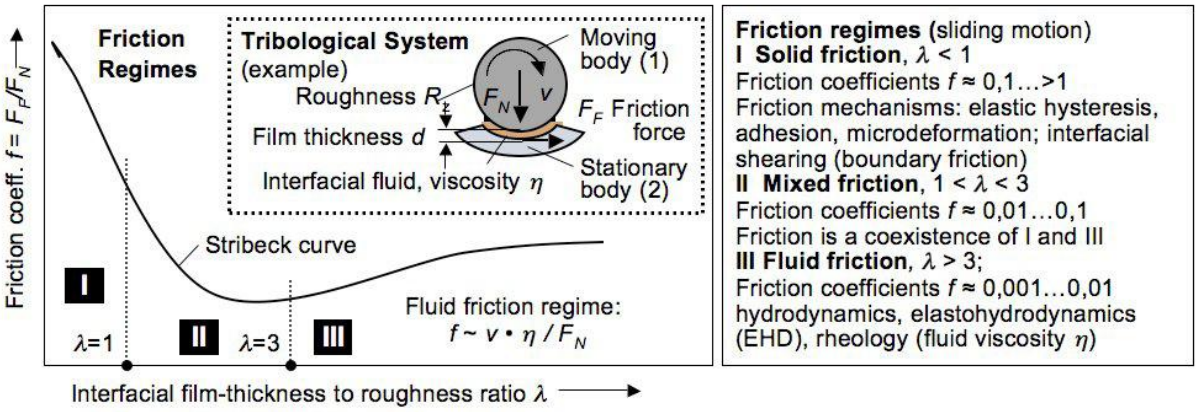

Friction regimes (sliding motion)
I Solid friction, $\lambda < 1$
Friction coefficients $f \approx 0{,}1 \ldots >1$
Friction mechanisms: elastic hysteresis, adhesion, microdeformation; interfacial shearing (boundary friction)
II Mixed friction, $1 < \lambda < 3$
Friction coefficients $f \approx 0{,}01 \ldots 0{,}1$
Friction is a coexistence of I and III
III Fluid friction, $\lambda > 3$;
Friction coefficients $f \approx 0{,}001 \ldots 0{,}01$
hydrodynamics, elastohydrodynamics (EHD), rheology (fluid viscosity η)

Figure 2.16: LITERATURE: Characterization of friction regimes according to the Stribeck curve [69].

Additionally, the surface topography, i.e. orientation of surface roughness, may affect the lubricant film thickness. It is possible under certain conditions, however, to encounter a fourth lubrication regime known has elastohydrodynamic lubrication (EHD). In EHD, contacting surfaces are not actually in contact, but rather are separated by a thin fluid film. In this case, the surface topography becomes irrelevant, as the contact surfaces are completely separated from each other. Knowledge of lubrication conditions is critical when mechanically finishing metal surfaces, including processes to induce work hardening beneath the metal surface.

2.6 Work Hardening

Work hardening occurs as a result of plastic deformation, which is particularly prevalent in ductile materials, and triggers phase transformations. Reversible elastic deformation is observed in a material up to its elastic limit, or yield point. Beyond this point, irreversible plastic deformation occurs as a result of the breaking of inter-atomic bonds. This is especially relevant for metals with significant austenitic composition. As is the case with targeted heat treatment and rapid quenching, martensitic phase transitions can be yielded by mechanical means as well. If sufficient stress (and at rapid enough intervals) is applied to such an austenite-containing metal, the resulting volume increase from the transformation of austenite to martensite will generate compressive residual stresses in sub-surface regions, i.e. below the contacted (stressed) surface. Evidence of work hardening in materials is typically observed through changes to residual stress profiles, discussed previously in section 2.2.1, as well as hardness profiles where an increase in material hardness is observed. The plastic deformation of a material leads to the movement of dislocations that are already present, and the creation of new ones. The greater overall prevalence of dislocations in the material with increasing plastic deformation results in greater resistance of such dislocations to further motion, which essentially means that less and less material is able to migrate under stress, giving the material greater strength [70]. In materials with low austenite content, such work hardening may also be generated through grain-boundary strengthening. Grain boundaries impede the movement of dislocations, so by reducing grain size, and thereby increasing grain-boundary presence, dislocations become less mobile when later introduced to external stresses.

The deformation of metals by a spherical indenter, resulting in work hardening, has been described by Tabor [71]. It was stated that an increase in yield stress will occur where material is displaced around the indentation, but that the elastic limit is not constant at all points around the indentation because of variations in deformation strain. This has already been touched upon in the discussion of Hertzian contact theory in section 2.4. Ultimately, he was able to derive an expression to relate the ultimate nominal stress, σ_u, to the Vicker's hardness, H, and the strain hardening coefficient, n, in the expression:

$$\sigma_u = \left(\frac{H}{2.9}\right)(1-n)\left(\frac{12.5n}{1-n}\right)^n \qquad \text{Equation 8}$$

later simplified by Cahoon [72] to:

$$\sigma_u = \left(\frac{H}{2.9}\right)\left(\frac{n}{0.217}\right)^n \qquad \text{Equation 9}$$

It becomes clear from the simplified expression that an increase in the strain hardening coefficient leads to an increase in the ultimate tensile strength per hardness. This was verified by comparison of calculated values to those from the original expression from Tabor. Only at larger strain hardening coefficient values does deviation between the two expressions become apparent. Most importantly, strong agreement with previous experimental values (also from earlier work by O'neill [73]) was observed.

Work hardening processes in steel alloys have undergone extensive study and are well represented in the literature. For example, Hirano et al. demonstrated in 1966 that the most effective material combinations for the reduction gears of marine turbines were those that showed the greatest work hardening tendencies [74]. Modern applications of such rolling elements have been developed by Nissan Motor Co., Ltd. (Yokohama, Japan) [75]. Furthermore, Lambda Technologies (Cincinnati, Ohio, U.S.A.), also developed a related technique known as Low Plasticity Burnishing (LPB), which was first applied to metal improvement in 1996 [76]. LPB is able to produce compression ranges from a few thousandths of a centimetre (comparable to shot peening) to over 1 cm in the case of nuclear weld applications. Such methodology has been applied for some time to the improvement of wear performance of P/M manufactured steels. A more recent investigation by Jandeska et al. into the effects surface densification on the rolling contact fatigue of a P/M alloy exemplifies this well [77].

The generation of work hardening in a material will essentially mean that this material undergoes some form of deformation. In certain applications this deformation may be undesirable. In such cases, it may be worthwhile to consider other methods for improving material performance, such as through the generation of chemically reactive tribofilms on surface substrates.

2.7 Tribofilms

Tribologically induced protective films, or simply tribofilms, are currently a very prominent area of research. Tribofilms may be generated either during operation or through preconditioning, and can have a significant influence on the friction behaviour and wear performance in tribological systems. Understanding of the metallurgical and chemical processes involved is rapidly increasing with improvements to analytical techniques. There are many different types of films, as well as ways to generate them, which can make describing these processes difficult, if there is not a consistent naming system. Tribofilms may be classified into four specific types [78]:

1. Tribofilms generated from the wear of the major constituents of sliding surfaces;
2. Tribofilms generated from the preferential wear of soft or lubricious constituents of a multi-phase or composite material;
3. Tribofilms with different chemical composition from parent worn and/or crystalline structure as a result of sliding contact;
4. Tribofilms generated as a result of tribo-chemical reactions between the wear products (i.e. wear debris and worn surfaces) and the environmental species.

At the same time, other influential physical processes may be occurring. This should, however, be distinguished from the chemical processes involved in tribofilm formation. This is namely because any physically formed protective layers are not nearly as stable as those resulting from the formation of chemical bonds. Adsorption of gaseous and liquid films on a solid surface, inducement via sliding of plastic deformation layers without changes in underlying crystalline structure and/or chemical composition and solid particles entrapped in a sliding interface without forming a continuous film, whether they are wear debris or from the environment, are all examples of such physical processes [78].

Much work has been done with the additive zinc dialkyl-dithiophosphate (ZDDP) since it is the main anti-wear agent used in many engine, gear and hydraulic oils [79,80]. The historical development of ZDDP to become a central anti-wear component in engine oils has been described in the literature [81]. ZDDP is able to chemically react with steel surfaces to produce a protective tribofilm coating [82]. Phosphorous that passes through the engine combustion chamber, however, interferes with the operation of the exhaust system, so the goal of work with ZDDP is to reduce the amount of phosphorous present in engine oils, while still maintaining good friction and wear performance. While these studies have shown some favourable results in terms of improvement of friction behaviour and wear performance, they are predicated on generating, or rather, replenishing the tribofilm throughout testing, as opposed to generating a stable, production-ready tribofilm through pre-conditioning.

A new model of the interactions of additives with metallic surfaces was introduced by Schulz and Holweger in 2009 [66]. Furthermore, the behaviour of specific additives and their interactions with specific metallic surfaces were discussed in detail at the annual GfT-Meeting in 2011 in Göttingen, Germany [83]. Three possible reaction pathways were postulated (see Figure 2.17, Figure 2.18, Figure 2.19).

These mechanisms are applicable to iron, as well as other metals and alloys. Since mechanisms 1 and 3 involve different groups of molecules, they are not in competition with each other in the way mechanisms 1 and 2 are. This could lead to synergistic effects [84]. Furthermore, mechanisms 1 and 3 have a strong foundation in the literature, particularly concerning the activity of sulfur [85]. With all this in mind, calcium carbonate is often used as a component of lubricant additives. Lubricant formulations containing calcium carbonate were chosen for this current study.

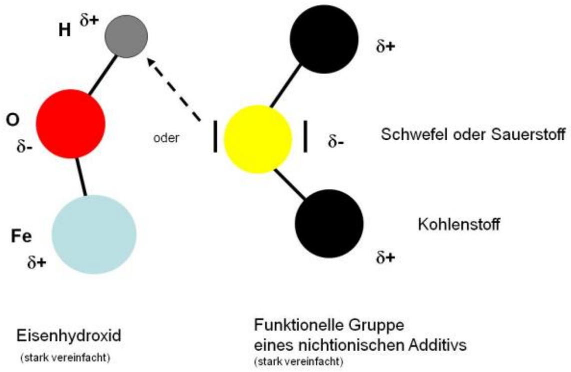

Figure 2.17: LITERATURE: Mechanism 1: Formation of hydrogren bridges with hydroxide [66].

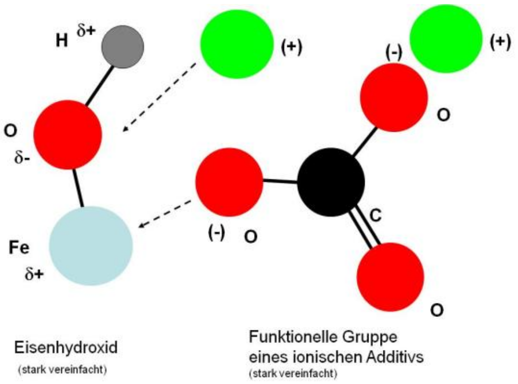

Figure 2.18: LITERATURE: Mechanism 2: Attack from ions on the atoms carrying hydroxide [66].

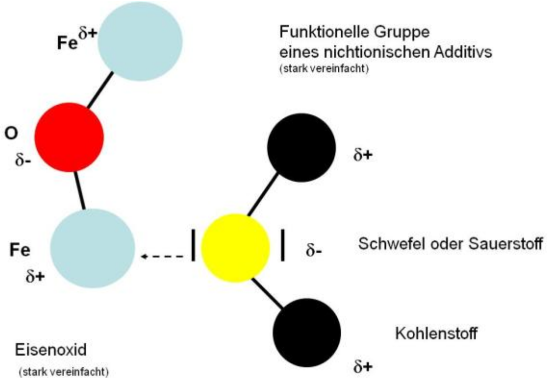

Figure 2.19: LITERATURE: Mechanism 3: Adsorption of oxidic groups on the metal elements [66].

In-situ analysis via spectroscopic measurement of tribochemical reactions under boundary lubrication is extremely difficult. While post-experimental analyses of tribologically impacted surfaces can help to determine the composition of reaction products, i.e. tribofilms, as well as the reaction mechanisms that take place, this may not give further insight into the reaction kinetics involved. Touching on this subject, Endou et al. conducted a theoretical study on the reactivity of diphenyl disulfide (DPDS, [CAS: 882-33-7]) with an Fe(001) surface using a novel quantum chemical molecular dynamics approach [86]. They were able to observe the formation of strong Fe – S bonds, with binding energies in the range between -190 – -240 $KJ \cdot mol^{-1}$. These bonds were evaluated in the context of no further chemical reaction, i.e. DPDS remained "complete" and was not subjected to any further decomposition. Therefore some light bonding interaction between the phenyl rings and iron surface could also be observed. More specifically, the C 2p atomic orbitals of the phenyl groups overlapped with the Fe 3d atomic orbitals of the iron surface, with the resulting orientation yielding π^* molecular orbitals. In this case, a binding energy of -66.9 $KJ \cdot mol^{-1}$ was determined, which is quite weak in comparison to the Fe – S energies previously determined. Nevertheless, this suggests the important role of the interaction of the C 2p and Fe 3d atomic orbitals in determining the absorption state of the diphenyl disulfide molecule on Fe surfaces as well as the formation of Fe – S bonds.

This molecular modelling gives the theoretical underpinning for practical results obtained in other studies. For example, a study conducted by Płaza and Grusińsky et al. on the homogeneous and heterogeneous decomposition of DPDS showed that different compounds can form as a result in the different bond energies of the C – S and S – S bonds [87]. In combination with work from Anand et al. it was shown that DPDS can exhibit positive load carrying properties, though these are dependent on the formation of films through iron organic compounds and the reaction of iron with byproducts from the reaction of thio compounds and hydrocarbon solvent with oxygen [88]. It is expected that oxidation of the byproducts from the decomposition of DPDS can subsequently react with iron to form reactive tribofilms that increase load-carrying capacity of the surface substrate. Furthermore, it has been verified that surface concentration ratios of sulfur to oxygen are extremely important [89,90,91,92].

Similar molecular descriptions have focused on molybdenum dialkyl-dithiocarbamate (MoDTC) as well, such as by Onodera et al. as MoDTC is a critically important friction modifier (FM) in the automobile industry [93]. Using a hybrid quantum chemical/classical molecular dynamics method, they studied the tribochemical reaction dynamics of MoDTC. They investigated the dynamic behavior of MoDTC molecule on the rubbing Fe(001) surface and showed the elongation of Mo – O bonds, forming the Mo_2S_4 and thiocarbamic acid molecules during a friction simulation. The electronic states of the MoDTC molecule and Fe(001) surface were computed to unveil the detailed mechanism of this bond elongation, and the catalytic effects of Fe(001) surface to the molecule was found. Extreme friction was also found to influence the complete Mo – O bond dissociation.

Extensive research has been carried out on the effects of sulfur-containing extreme pressure (EP) and anti-wear (AW) additives in industrial gear oil formulations. Such chemically reactive additives are known to decompose under high load and/or high temperature conditions to form protective, chemisorbed layers on metallic surfaces [94,95]. Attempts by Sarin et al. to introduce additional components in the form of organomolybdenum friction modifiers have been investigated [96]. Since friction modifiers are also surface active substances, they may interact either synergistically or antagonistically with EP/AW additives already present. It has been shown that the activity of organomolybdenum complexes in multi-component systems can been influenced by the presence of S donor compounds, such as sulphides and disulphides [97,98]. This study, however, goes further in that it systematically determines the influence of organomolybdenum compounds on the EP properties of organosulfur EP additives. It builds on work by the same group that reported the effect of four organosulfur EP additives (of varying chemical composition) in a mineral base oil on the friction-reducing properties of organomolybdenum compounds, using an oscillating friction and wear test apparatus, under point contact conditions [99] Ultimately it was shown that the additive-additive interactions are highly chemoselective, as well as dependent upon the composition of the interacting FM-EP pair.

The chemical model of the decomposition of (MoDTC), has been described in the literature and is provided in Figure 2.20 [100]. Friction reduction mechanisms and wear prevention by Mo-based friction modifiers involve both chemical reactions between organomolybdenum compounds and the rubbing contact of metal surfaces [101,102] Similarly, EP performance is enhanced by organosulfur compounds through the formation of a chemisorbed load-carrying surface layer between rubbing metal surfaces [103]. Therefore competition for access to the metal surface contact arises when both Mo-based friction modifiers and organosulfur EP-additives are present in the same lubricant mixture, which may lead to a reduction in performance of friction-reducing AW or EP additive, i.e. antagonism.

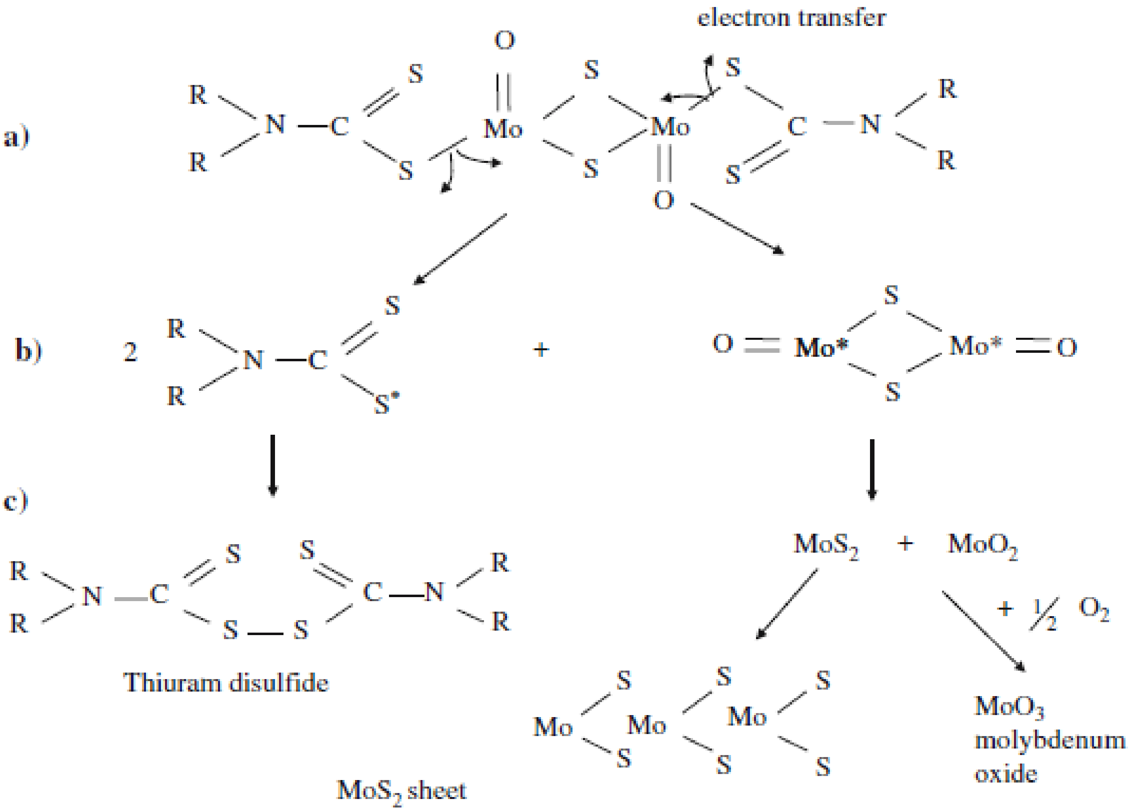

Figure 2.20: LITERATURE: Molybdenum dialkyl-dithiocarbamate (MoDTC) decomposition chemical model [100].

Due to the negative eco-toxicological properties of MoDTC and similar molybdenum containing additives, alternative formulations, such as with bismuth substitutes, in the case of bismuth dialkyl-dithiocarbamate (BiDTC), are sought. This is indeed a reasonable pursuit, as bismuth-based alternative additives have been shown to be quite effective replacements in similar contexts, eg. in the substitution of lead naphthenate with bismuth naphthenate as an EP additive [104]. In conjunction with appropriate metallurgies for enhanced wear protection, eg. through work hardening, such tribofilm-forming additives can further contribute to improved wear resistance of downsized components and help to reduce friction-related energy losses.

3 Experimental Parameters

3.1 Characterization of Materials

3.1.1 Heat Treatment Regimes

The 20MnCr5 samples were subjected to case-hardening at 925 °C for 14 hours in an atmosphere of nitrogen, methanol and propane. This was followed by deep freezing treatments at -180 °C, -40 °C and -18 °C for 1 hour each to generate residual austenite contents of 5%, 10% and 15%, respectively. Samples that were to reach 20% residual austenite did not undergo deep freezing treatment. Tempering was then carried out at 180 °C for 2 hours. It is noted that all samples were heated in the same batch. The main difference in the overall heat treatment was in the way they were subjected to deep freezing treatments. The temperature profiles during heat treatment of these samples are provided in Figure 3.1.

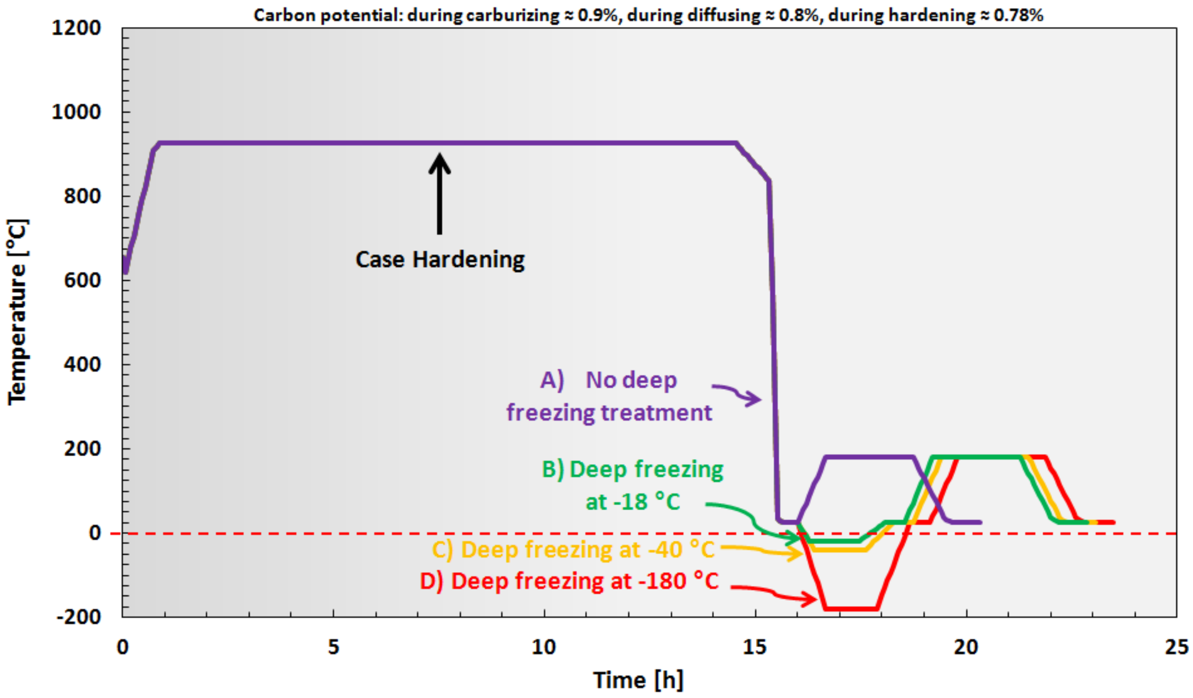

Figure 3.1: Temperature profiles of 20MnCr5 samples during heat treatment.

The chosen heat treatment regime for 20MnCr5, and particularly the extremely rapid quenching performed, was chosen to generate significant conversion of austenite to martensite. The optical images of the surface and core regions of heat treated 20MnCr5 in Figure 3.2 show clear martensitic microstructures. Plate martensite is dominant, particularly in the case-hardened surface layers where carbon concentrations are highest (see Table 4.1). This is not uncommon in iron alloys of carbon concentration above approximately 0.8 wt.-%. Such plate martensite forms and grows in various angular constellations (as opposed to lath martensite), and allows for residual austenite to remain ensconced between the plates. The austenitic grain boundaries are, initially, responsible for hindering plate growth. As new martensitic plates begin to form, they themselves add to the hindrance of new plate growth, resulting in the growth of progressively smaller plates. As will be discussed later, the types of martensitic microstructures formed are indeed important as they can have significant influence on the mechanical properties of the alloys [105,106].

Figure 3.2: Light microscope images of the surface layer and core of heat treated 20MnCr5.

A comparison of the given temperature profiles to the continuous TTT curve for 20MnCr5 in Figure 3.3 shows that significant martensite would have been yielded at a return to room temperature.

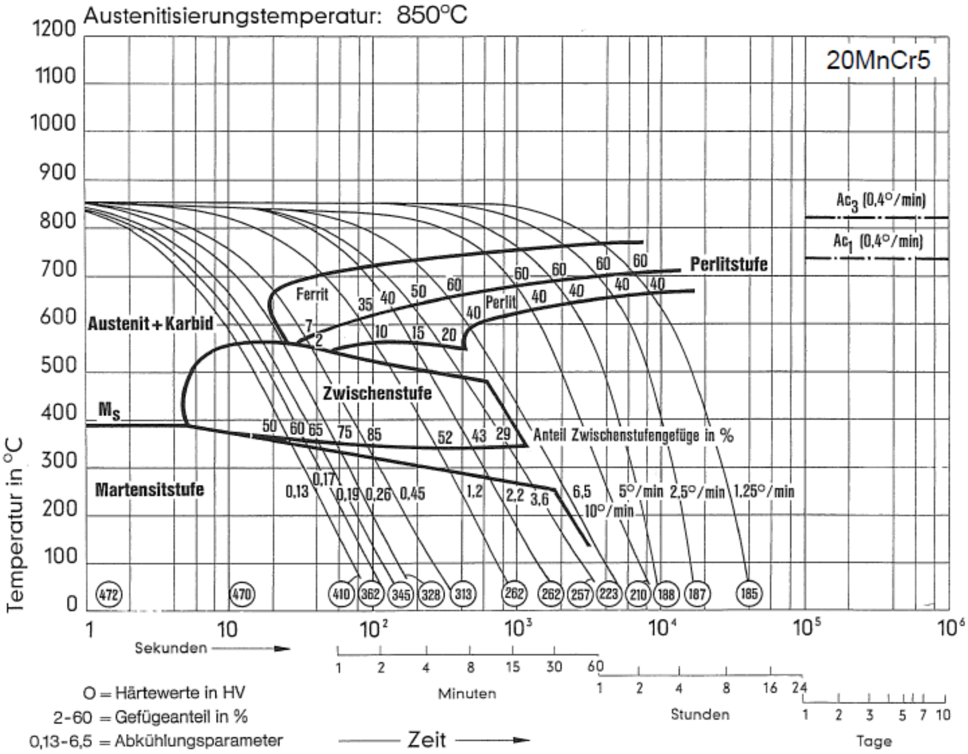

Figure 3.3: LITERATURE: Continuous TTT curve for 20MnCr5 (provided by Saarstahl AG) [107].

The case depth achieved is also of critical importance, as this has a significant influence on the wear resistance the component. Figure 3.4 compares the case depth to the normal module, as defined by DIN 780, and gives the target area for these values to avoid pitting. The case depth for the heat treated 20MnCr5 in this work was approximately 2 mm (see Figure 4.3).

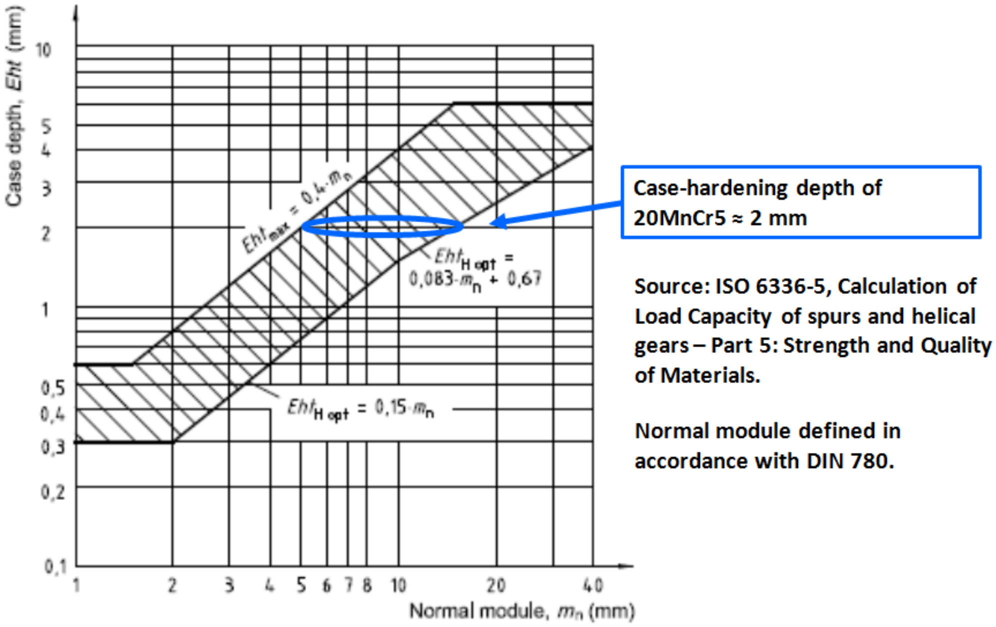

Case-hardening depth of 20MnCr5 ≈ 2 mm

Source: ISO 6336-5, Calculation of Load Capacity of spurs and helical gears – Part 5: Strength and Quality of Materials.

Normal module defined in accordance with DIN 780.

Figure 3.4: LITERATURE: Recommended values of optimum case depth $Eht_{H\ opt}$ regarding surface load capacity and maximum case depth Eht_{max} regarding bending and surface load capacity [8].

Both 36NiCrMoV1-5-7 and 45SiCrMo6 were heat treated as per the recommendations of their respective manufacturers. For 36NiCrMoV1-5-7, heat treatment involved hardening at

880 °C for 8 hours, followed by repeated annealing at 560 °C. In the case of 45SiCrMo6, hardening was carried out at 900 °C for 5 hours, followed by annealing at 410 °C. Neither 36NiCrMoV1-5-7 nor 45SiCrMo6 was case-hardened. The temperature profiles are given in Figure 20.

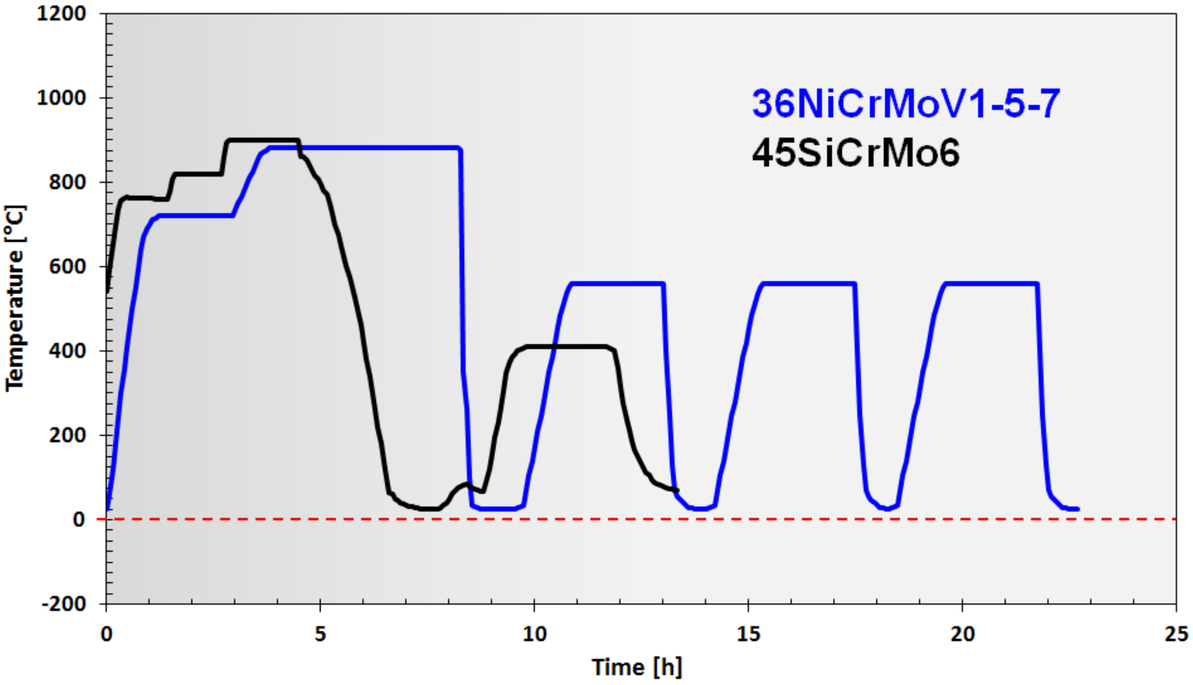

Figure 3.5: Temperature profiles during heat treatment of 36NiCrMoV1-5-7 and 45SiCrMo6.

Optical images of the core regions of the alternative alloys, after heat treatment are provided in Figure 3.6. In contrast to the carburized 20MnCr5, the martensitic microstructures observed in the alternative alloys appear more like lath martensite, rather than plate martensite. This is reasonably expected for low carbon steels, i.e. with carbon concentrations < 0.4 wt.-% (see Table 4.2), and is particularly visible in 36NiCrMoV1-5-7. The same applies to 45SiCrMo6 as well, though due to the presence of α-Fe grains the microstructures and average grain size is less uniform [113].

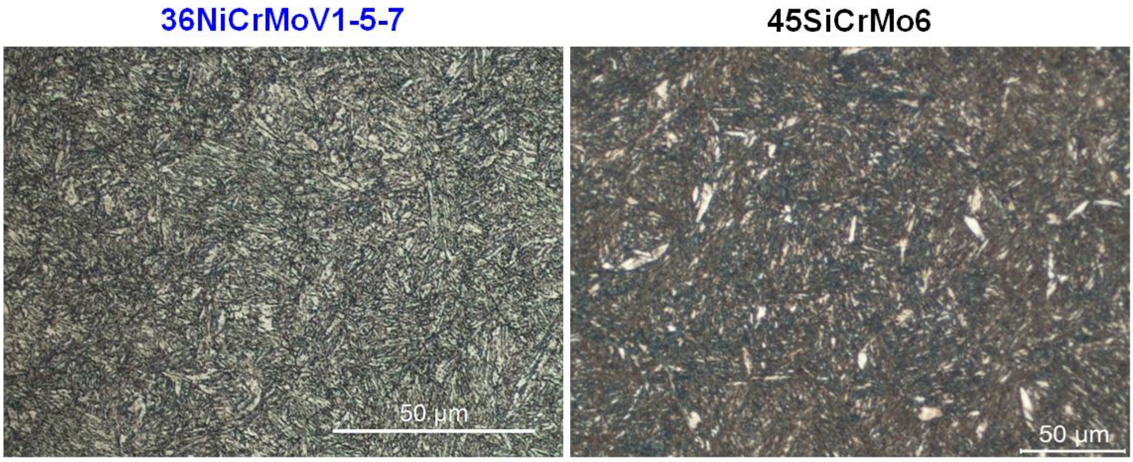

Figure 3.6: Light microscope images of the core of heat treated 36NiCrMoV1-5-7 and 45SiCrMo6.

All testing was performed on twin disk testing rigs, which are described later in section 3.2. Therefore disks of a specified geometry (in this case, cylindrical samples and spherical counterbodies) were machined, then heat treated, for twin disk testing. The heat treated and machined disks were then mechanically finished: the cylindrical samples were grinded and polished, while the spherical counterbodies were simply grinded. The roughness values, R_a and R_z, that resulted from mechanical finishing are given in Table 3.1. In essence, a comparison of operational performance is sought between the case-hardened reference steel and the non-case-hardened alternative steels, and furthermore, how this operational performance is impacted by the generation of work hardening and chemically reactive tribofilms through targeted pre-conditioning.

Table 3.1: Roughness values, R_a and R_z, of mechanically finished cylindrical samples and spherical counterbodies.

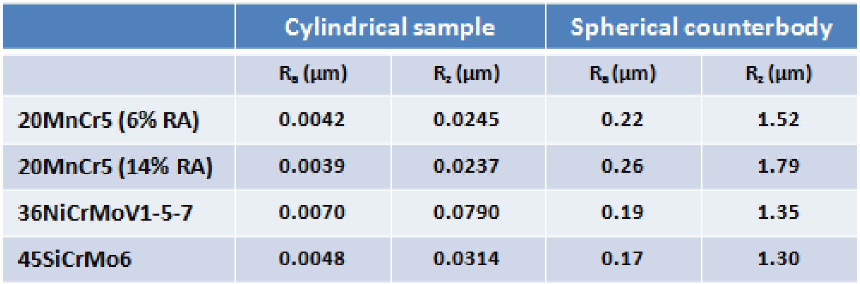

	Cylindrical sample		Spherical counterbody	
	R_a (µm)	R_z (µm)	R_a (µm)	R_z (µm)
20MnCr5 (6% RA)	0.0042	0.0245	0.22	1.52
20MnCr5 (14% RA)	0.0039	0.0237	0.26	1.79
36NiCrMoV1-5-7	0.0070	0.0790	0.19	1.35
45SiCrMo6	0.0048	0.0314	0.17	1.30

3.1.2 Elemental Analysis

In Table 3.2, reference elemental concentrations for 20MnCr5 before heat treatment are provided by the standard DIN EN 10084, the steel mill and an independent spectral analysis by the ISF at the RWTH in Aachen, Germany [108]. Elemental analyses of the carburized zones were carried out by several analytical techniques on the 20MnCr5 samples after heat treatment. Multiple analytical methods were implemented to enhance the accuracy of the overall results and to allow for a comparison between the methods.

Table 3.2: Elemental composition of 20MnCr5 before heat treatment.

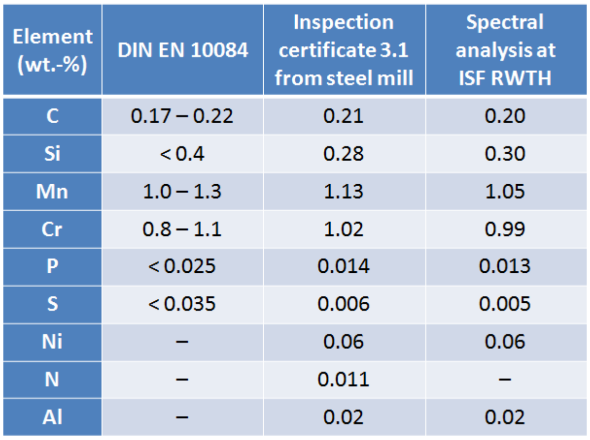

Element (wt.-%)	DIN EN 10084	Inspection certificate 3.1 from steel mill	Spectral analysis at ISF RWTH
C	0.17 – 0.22	0.21	0.20
Si	< 0.4	0.28	0.30
Mn	1.0 – 1.3	1.13	1.05
Cr	0.8 – 1.1	1.02	0.99
P	< 0.025	0.014	0.013
S	< 0.035	0.006	0.005
Ni	–	0.06	0.06
N	–	0.011	–
Al	–	0.02	0.02

Scanning electron microscopy coupled with energy-dispersive X-ray spectroscopy (SEM-EDX) was the first method employed. A Zeiss Supra 40 scanning electron microscope with electron beam generation by way of a thermal emission cathode (Schottky-emitter, ZrO/W-cathode) was used. An in-lens secondary electron detector, SE2 secondary electron detector and QBSD backscattering detector are built into the microscope. Samples in the electron microscope were analyzed under vacuum. Stimulation of the atoms near the sample surface was done with an acceleration voltage of 10 kV. A maximum resolution of 1.5 nm can be achieved at this acceleration voltage. The microscope was coupled to a Thermo NSS 3.1 energy-dispersive X-ray spectrometer with a Bruker X-Flash 5010 3403, Quantax 400 detector. Spark emission spectroscopy was also carried out on the 20MnCr5 samples using a Spectrolab analyzer from Spectro Analytical Instruments. Finally, the 20MnCr5 samples were subjected to electron microprobe analysis. A JEOL Superprobe JXA-8900RL, WD/ED Combined Microanalyzer was implemented. Elemental analysis of 36NiCrMoV1-5-7 and 45SiCrMo6 was conducted by atomic emission spectroscopy (AES), the results of which are found in Table 4.2.

3.1.3 Analysis of Residual Austenite and Residual Stresses

Analyses of residual austenite in 20MnCr5, 45SiCrMo6 and 36NiCrMoV1-5-7 by X-ray diffraction (XRD) were carried out at the BAM. Measurements were taken on an Xstress X3000 G3 X-ray diffractometer in increments of 0.04° in the (2θ) angular range of 60° - 160°. A collimator of diameter 3 mm was employed. Measurements were taken using Cr-K_α radiation in accordance with ASTM E975 [109]. To confirm the accuracy of the results, separate analyses were also done at the TU Berlin. Diffractograms were generated by measurements in increments of 0.05° in the (2θ) angular range of 44° - 130°. All measurements were taking using Co-K_α rays and a round collimator of diameter 3.3 mm. Additionally, a Soller collimator with a divergence angle of 0.7° was used in combination with a LiF-analyzer crystal. The measurement time was set to 40 s. Determination of the proportions of the individual phases was made using Rietveld analysis [110,111]. In an attempt to confirm the XRD findings, microstructural analysis by electron backscattering diffraction (EBSD) was performed. A Leo/Zeiss Gemini 1530 VP scanning electron microscope, complete with InLens-, SE-, VPSE-, 4QBSD-, EDX-, FSD-, EBSD-detectors, was implemented up a maximum acceleration voltage of 30kV. The sample compartment pressure was kept between 1 – 100 Pa. The field emission source was able to yield a resolution of approximately 1 nm for operations at 15 kV, though pixels of approximately 42 nm were generated in the resulting images.

Residual stress analyses were performed at the BAM. As previously mentioned, Cr-K_α radiation was used, operating at 30 kV and 6.7 mA. The 211-ferrite peak was chosen, with a $2\theta_0$ of 156°. In accordance with the $\sin^2\psi$ method, tilt angles, ψ, were evaluated between 0° and ±45° in steps of 6°. Additional analyses at the TU Berlin were performed in increments of 0.05° in the (2θ) angular range of 96.5° - 102°. The round collimator diameter was 1 mm, and measurement time was 30 s. The tilt angles +/-63.435°, +/- 50.787°, +/-39.232°, +/ -26.565 and 0° were evaluated.

3.1.4 Hardness Profiling

All hardness testing was completed using a Duramin 10 semi-automatic hardness tester from Struers, with an Ahotec sample stage upgrade. A diamond indenter in pyramid form with 136° angles was used. A HV 0.2 test load was implemented for all samples. Testing was carried out to a minimum depth of 5 mm for all samples to ensure that any variations in hardness in the carburization zone of 20MnCr5 would be detected.

3.1.5 SEM-EDX Element Mapping

Multiple methods were used to characterize freshly-generated tribofilms. The first method employed was scanning electron microscopy coupled with energy-dispersive X-ray spectroscopy (SEM-EDX). A Zeiss Supra 40 scanning electron microscope with electron beam generation by way of a thermal emission cathode (Schottky-emitter, ZrO/W-cathode) was used for the analysis. An in-lens secondary electron detector, SE2 secondary electron detector and QBSD backscattering detector are built into the microscope. Samples in the electron microscope were analyzed under vacuum. Stimulation of the atoms near the sample surface was done with an acceleration voltage of 10 kV, whereby a maximum resolution of 1.5 nm can be achieved at this acceleration voltage. The microscope was coupled to a Thermo NSS 3.1 energy-dispersive X-ray spectrometer with a Bruker X-Flash 5010 3403, Quantax 400 detector.

3.1.6 Raman Spectroscopy

The second characterization method chosen was Raman spectroscopy. A WITec alpha300 R confocal Raman imaging system was used. The system was equipped with a Peltier-Cooled CCD low light microscope camera from Andor, a P-527 scanning table of dimensions 200 µm x 200 µm x 10 µm from PI and a 20x objective aperture, fibre core diameter = 100 µm from Zeiss. A sample scanning area of 160 µm x 160 µm was chosen to obtain as accurate an overall picture of the tribofilms as possible. Scans of both inside and outside the wear track were taken to ensure any peaks assigned to the tribofilms were the result of tribological contact.

3.1.7 XPS

Finally, X-ray photoelectron spectroscopy (XPS) was carried out with an AXIS Ultra DLD electron spectrometer from Kratos Analytical, UK. XPS spectra were recorded using monochromated Al Kα excitation at pass energy of 80 eV for survey spectra and 20 eV for the core level spectra. The source-to-analyzer angle was 60°. The binding energy scale of the instrument was calibrated following a Kratos Analytical procedure, which uses ISO 15472 binding energy data [112]. Spectra were taken by setting the instrument to the hybrid mode and the slot mode providing approximately a 0.7 x 0.3 mm^2 analysis area.

3.2 Tribological Testing Setups

3.2.1 Amsler Test Rig

Twin disk testing machines provide an optimal basis for experimentation in combination with a specified surface roughness for operation in a mixed boundary lubrication regime [113]. Slip-rolling testing has been carried out on three tribometers, two of type Amsler (A135) and one of more modern type Optimol 2Disc. They enable development of a tribological profile composed of evolution of friction, wear and slip-rolling resistance (fatigue, should it occur) in a single test. Comparable results have been obtained from both setups, but it is important to note that each operates with a different load and speed range.

The sample configuration of the Amsler setup is provided in Figure 3.7. In the Amsler setup, the spherical counterbody disk and the cylindrical sample disk roll against each other. An electric motor and coupling shafts allow for a fixed sample rotation speed of 390 rpm and a fixed counterbody rotation speed of 354 rpm. This allows for a continuous slip of 10%. A normal force is applied via a screw, bolted to a spring, which is capable of delivering up to 2,000 N of force, i.e. an initial average Hertzian contact pressure of P_{0Mean} = 1.94 GPa for the chosen sample configuration. The compression of the spring can also be reduced to allow for testing at lower contact pressures, e.g. 930 N is commonly applied. These values are not merely random assignments, but rather are oriented according to ISO 14635-1, whereby the load stage 12 in the FZG test rig is accurately represented by an average contact pressure P_{0Mean} of 1,250 MPa (or P_{0Max} of 1,875 MPa), and is the most intense and relevant testing procedure currently given for gear components [12]. The initial contact stress of P_{0Max} of 2.25 GPa, the lowest load applied in this study, is located above the FZG load stage of 14. The oil bath sits below the sample at +120 °C, but is in contact with the sample to ensure the lubricant is pulled into contact with both disks, allowing for mixed boundary lubrication [113].

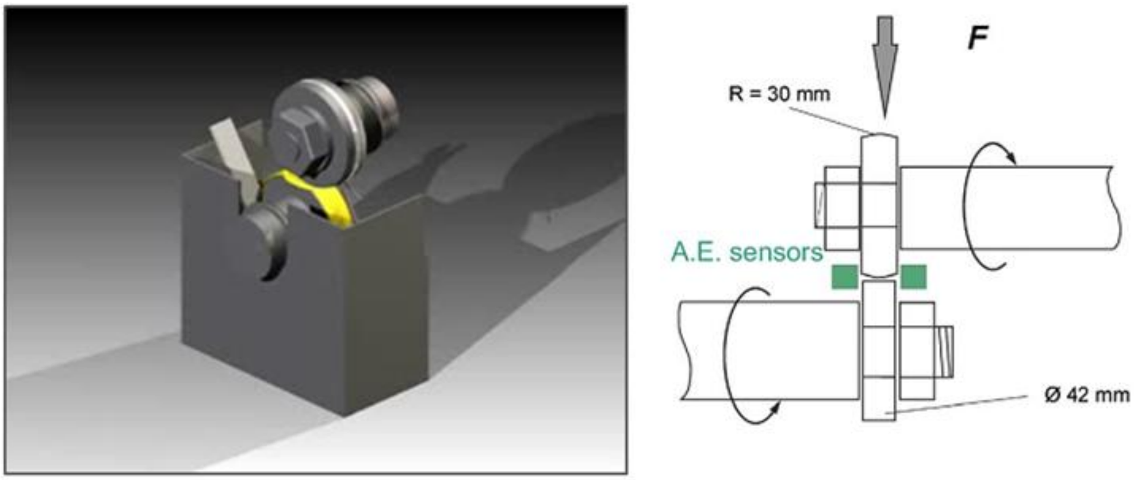

Figure 3.7: Sample arrangement of the Amsler tribometer.

3.2.2 Optimol 2Disc Test Rig

The sample configuration of the Optimol setup is provided in Figure 3.8. The sample and counterbody disks sit level with each other. Two electric motors drive rotation of the disks independently of each other. This allows the amount of slip to be freely adjusted. Lubrication is driven by a gear pump that is fed from an oil bath below the disks, and pumps lubricant from above the disks into the contact point of the disks. This allows for greater control of temperature and circular flow of lubricant. The Optimol 2Disc tribometer is designed for extreme applications, and can produce normal forces up to 5000 N, i.e. an average Hertzian contact pressure up to P_{0Mean} of 2.62 GPa. This is accomplished by way of a computer controlled motor that compresses a spring, fixed between the motor and axel of the cylindrical disk [113].

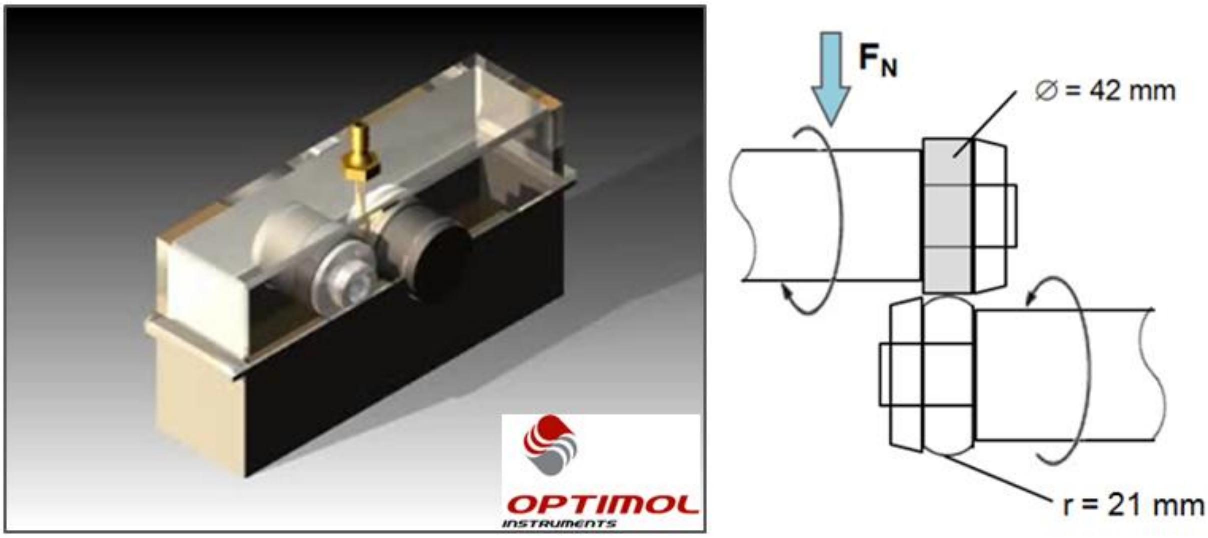

Figure 3.8: Sample arrangement of the Optimol 2Disc tribometer.

With the ability of the 2Disc test rig to reach normal forces of 5,000 N, and therefore average initial Hertzian contact pressures of 2.62 GPa given the chosen ball on cylinder sample geometries, it becomes clear that extreme conditions well above the most intense FZG test rig load stages applied for gearing applications can be represented. An overview of the testing levels applied using the twin disk test rigs is provided in Table 3.3. The expected total deformation of the samples at the respective testing levels is also given.

Table 3.3: Hertzian contact pressures for the tested sample geometries.

Normal force, F_N [N]	930	2,000	4,400	5,000
Average initial Hertzian contact pressure, P_{0Mean} [GPa]	1.5	1.94	2.5	2.62
Maximum initial Hertzian contact pressure, P_{0Max} [GPa]	2.25	2.91	3.75	3.92
Total deformation/ flatening [µm]	13.4	21.2	37.8	41.2

3.2.3 Lubricant Properties

All slip-rolling endurance tests were carried out under lubrication with the synthetic factory fill engine oil BMW SAE 0W-30 “VP1” (ACEA A3/B4, $\nu_{120°C}$= 5.33 mPas, sulphated ash of 1.20 wt.-%.). This oil was selected for its temperature resistance, which was crucial as all endurance tests were run at +120 °C, typical conditions for automobile engines. Table 3.4 provides an overview of the properties of this lubricant. At an operating temperature of +120 °C and load values between 0 and 5000 N, the resulting film thickness, with respect to the roughness of the disk surfaces, results in a Tallian parameter < 1, indicating boundary lubrication at the beginning of testing. The minimum lubricant film thickness, h_{min}, of VP1 at +120 °C and normal force F_N = 2,000 N is 0.0252 µm, while the roughness values of, for example, 20MnCr5 (6% RA) are $R_{a(cyl)}$ = 0.0042 µm and $R_{a(sph)}$ = 0.22. This yields a Tallian parameter of 0.112, which is clearly less than 1. All other roughness parameters, available in Table 3.1, yield Tallian parameters similar to this. Further information on the properties of this lubricant is available [5].

Table 3.4: Viscosimetric properties of the synthetic factory fill engine oil BMW FF SAE 0W-30 VP1.

	BMW FF SAE 0W-30 VP1
Viscosity Index	168
Pour Point [°C]	-57
$\eta_{100°C}$ [mPa·s]	8.04
$\eta_{150°C}$ [mPa·s]	3.34
$\nu_{40°C}$ [mm²/s]	57
$\nu_{100°C}$ [mm²/s]	10.2
$\nu_{150°C}$ [mm²/s]	4.42
HTHS [mPa·s]	2.98
$\alpha_{p80°C}$ [GPa^{-1}]	14.17
$\alpha_{p150°C}$ [GPa^{-1}]	11.9

3.3 Targeted Pre-Conditioning of Testing Materials

3.3.1 Generation of Cold Work Hardening

Cold work hardening was generated in the cylindrical samples using an Optimol 2Disc tribometer. Table 3.5 provides further details as to the conditions under which pre-conditioning was carried out. Thorough metallurgical characterization of all steels subjected to slip-rolling endurance testing, with and without pre-conditioning, has been carried previously [114]. Pre-conditioning via work hardening was completed using only the synthetic factory fill engine oil BMW FF SAE 0W-30 “VP1.” Slip was reduced to as close to as close to 0% as possible to help intensify the work hardening processes. Due to the axial arrangement for the Optimol 2Disc tribometer, some slip was required to ensure the front spindle did not “climb” out of place. This phenomenon is a result of the construction of the testing rig. The front spindle is able to pivot vertically, the motion of which is used to measure friction during testing. Allowing for some minor slip ensured that the front contact was pulled in a downward motion. Essentially all other testing conditions were kept equivalent to those for slip-rolling endurance testing. The most significant factor is the use of polished tungsten carbide rollers and high loads. These hard metal rollers, with hardness and elastic modulus several times greater than the treated alloys, are able to generate beneficial compressive residual stresses that later counteract shearing stresses during endurance testing.

Table 3.5: Experimental parameters for cold work hardening generation using an Optimol 2Disc tribometer.

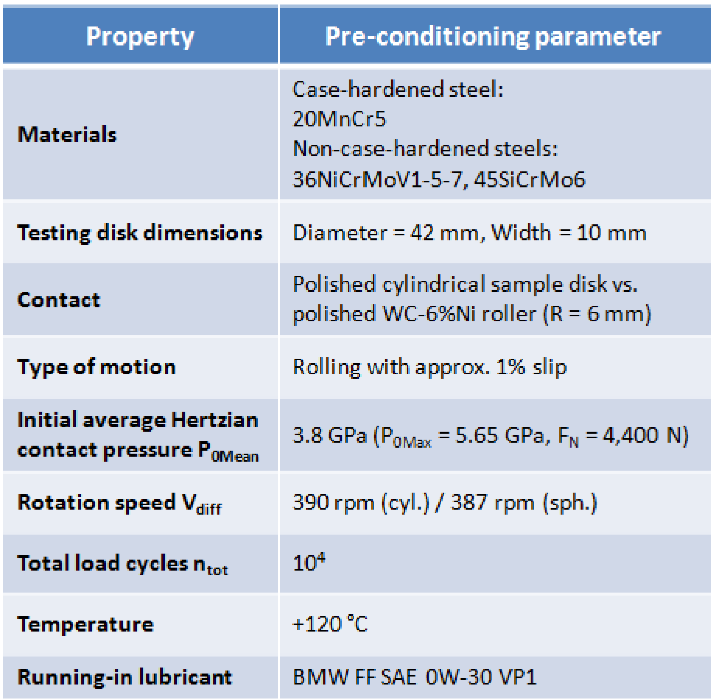

Property	Pre-conditioning parameter
Materials	Case-hardened steel: 20MnCr5 Non-case-hardened steels: 36NiCrMoV1-5-7, 45SiCrMo6
Testing disk dimensions	Diameter = 42 mm, Width = 10 mm
Contact	Polished cylindrical sample disk vs. polished WC-6%Ni roller (R = 6 mm)
Type of motion	Rolling with approx. 1% slip
Initial average Hertzian contact pressure P_{0Mean}	3.8 GPa (P_{0Max} = 5.65 GPa, F_N = 4,400 N)
Rotation speed V_{diff}	390 rpm (cyl.) / 387 rpm (sph.)
Total load cycles n_{tot}	10^4
Temperature	+120 °C
Running-in lubricant	BMW FF SAE 0W-30 VP1

3.3.2 Generation of Chemically Reactive Tribofilms

The reactive tribofilms were generated only on the cylindrical sample surface using both the Optimol 2Disc and Amsler type tribometers. Table 3.6 provides further details as to the conditions under which pre-conditioning was carried out. Additional steels, not initially intended for this study, were also tested for tribofilm pre-conditioning to observe any differences in surface substrate reactivity. Two specific lubricant packages were applied to generate chemically reactive tribofilms on the steel surfaces: Wisura LS514, which is a customized fine cutting fluid from Wisura GmbH (Bremen, Germany) with an enhanced concentration of $CaCO_3$ as the active ingredient, and VPX* + Molyvan 822 [CAS: 71342-89-7], which is from Vanderbilt Chemicals, LLC (Norwalk, CT, USA) and comprised principally of molybdenum dialkyldithiocarbamate (MoDTC). These model lubricants and the corresponding tribofilms generated from them are, henceforth, referred to as LS514 and M822, respectively. The applied additive concentrations, in the case of M822, of 10 wt.-% are quite high for an EP/AW-additive or friction modifier, but intended to ensure the rapid formation of the tribofilms within the selected pre-conditioning time. Tribofilms were generated on the sample surfaces, not on the counterbody surfaces.

*Table 3.6: Experimental parameters for tribofilm generation using twin disk tribometers; *VPX denotes BMW FF SAE 0W-30 VP1 with reduced additive content, but including anti-oxidation and anti-corrosion components.*

Property	Pre-conditioning parameter
Materials	Case-hardened steel: 20MnCr5 Non-case-hardened steels: 36NiCrMoV1-5-7, 45SiCrMo6
Testing disk dimensions	Diameter = 42 mm, Width = 10 mm
Contact	Polished cylindrical sample disk vs. grinded spherical counterbody (R = 21 mm)
Type of motion	Rolling with 10% slip
Initial average Hertzian contact pressure P_{0Mean}	1.94 GPa (F_N = 2,000 N)
Rotation speed V_{diff}	390 rpm (cyl.) / 354 rpm (sph.)
Total load cycles n_{tot}	10^4
Temperature	+120 °C
Running-in lubricants	Wisura LS514 (LS514) VPX* + 10% Molyvan 822 (M822)

VPX is based on the same base oil as VP1, but is free of detergents, dispersants and EP/AW-additive in order to exclude unknown side effects from other additives. Partially as a result of the reduced additive content, it is less viscous than the standard VP1, with kinematic viscosities of 25 mm^2/s and 7 mm^2/s at 40 °C and 100 °C, respectively. Colloidal $CaCO_3$ is sterically stabilized by calcium sulphonates and present in lubricants as nanosized particles, which are squeezed out of the formulation in the highly concentrated slip-rolling contact in order to be smeared onto the surfaces forming a physical film. By contrast, MoDTC is diluted in the base oil. MoDTC forms a thin reaction layer on to surface. The same applies to DBDS and Irgalube 349 (see Figure 4.14).

The process of transferring running-in into the mechanical finishing phase must also be economically viable if it is to find further industrial application. The process as a whole is time-, and therefore, cost-sensitive. The inner and outer races of bearings provide the best available surfaces for such applications. Other parameters chosen are standard for the slip-rolling resistance testing that follows.

3.4 Slip-Rolling Endurance Testing

The relevant parameters for slip-rolling endurance testing have been summarized in Table 3.7. Testing was carried up to 10^7 load cycles, or approximately 19 days. Samples were deemed to have failed the test if damaged surface areas of 1 mm^2 or greater were observed before reaching 10^7 load cycles. Samples that reached 10^7 load cycles without surface failure were subjected to profilometry. Four profiles on each sample were taken perpendicular to the sliding direction spaced at an angle of 90°. Averaging these four profiles allows for deduction of the planimetric wear surface, W_q, which in turn permits the calculation of the volumetric wear rate k_v. The coefficient of friction (COF) was monitored throughout testing with a coupling shaft/pendulum and linear variable differential transformer (LVDT) mechanism in the case of the Amsler tribometers, and an in-situ, software-controlled frictional force detector in the case of the Optimol 2Disc tribometer.

Table 3.7: Experimental parameters for slip-rolling endurance testing.

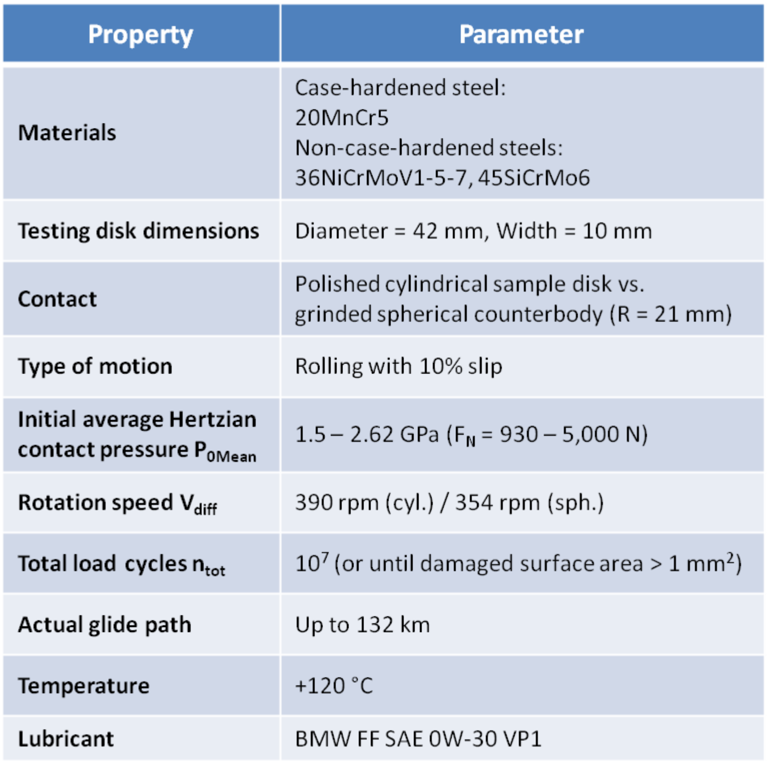

Property	Parameter
Materials	Case-hardened steel: 20MnCr5 Non-case-hardened steels: 36NiCrMoV1-5-7, 45SiCrMo6
Testing disk dimensions	Diameter = 42 mm, Width = 10 mm
Contact	Polished cylindrical sample disk vs. grinded spherical counterbody (R = 21 mm)
Type of motion	Rolling with 10% slip
Initial average Hertzian contact pressure P_{0Mean}	1.5 – 2.62 GPa (F_N = 930 – 5,000 N)
Rotation speed V_{diff}	390 rpm (cyl.) / 354 rpm (sph.)
Total load cycles n_{tot}	10^7 (or until damaged surface area > 1 mm^2)
Actual glide path	Up to 132 km
Temperature	+120 °C
Lubricant	BMW FF SAE 0W-30 VP1

4 Results and Discussion

4.1 Characterization of Materials

4.1.1 Elemental Analysis

The results of all elemental analyses of 20MnCr5 are summarized in Table 4.1. While most elemental concentrations obtained from SEM-EDX analysis showed good consistency with the values obtained before heat treatment, extremely high concentrations of carbon were detected, even with the consideration that the samples were carburized. This is partially a result of some carbon already being present in the SEM-column, which often leads to an artificial increase of carbon values. In an attempt to work around this effect, spark emission spectroscopy was also carried out on the samples. These values, irrespective of carbon, whose values were considerably lower, showed consistency with the values from SEM-EDX. Spark emission spectroscopy cannot focus on as fine an area as SEM-EDX, say, to evaluate purely the boundary area. This means concentrations from deeper in the sample volume have a greater impact on overall results. For further comparison, samples were subjected to electron microprobe analysis. Elemental concentrations were measured at discreet distances from the sample volume to the sample surface. The focus of this analysis was to obtain a more dependable carbon concentration. ISO 6336-5 states an acceptable range in carbon content after carburization of 0.70 to 1.0 wt.-%, up to a maximum of <1.5 wt.-% [7]. All analyses confirmed an increase in carbon content after case-hardening. The present 20MnCr5 samples lie within the prescribed values, but the analytical methods differ in the results.

Table 4.1: Elemental concentrations of 20MnCr5 in wt.-% after case hardening and heat treatment determined by SEM-EDX, spark emission spectroscopy and electron microprobe analysis.

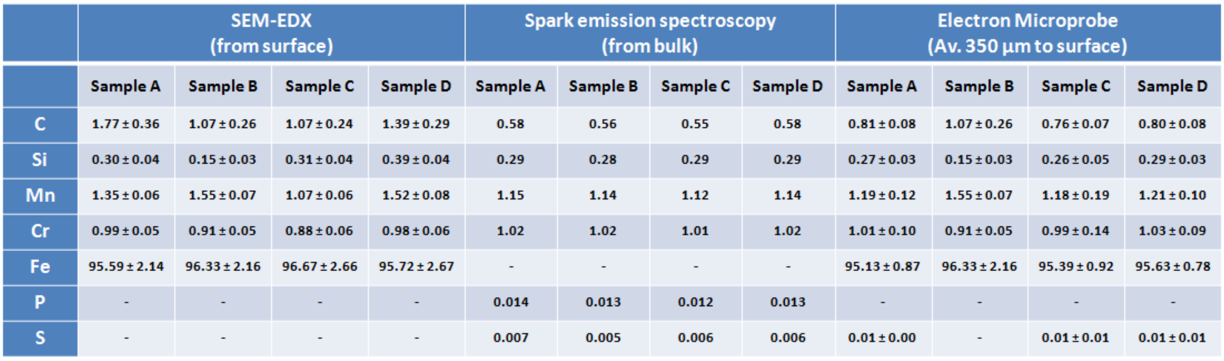

	SEM-EDX (from surface)				Spark emission spectroscopy (from bulk)				Electron Microprobe (Av. 350 µm to surface)			
	Sample A	Sample B	Sample C	Sample D	Sample A	Sample B	Sample C	Sample D	Sample A	Sample B	Sample C	Sample D
C	1.77 ± 0.36	1.07 ± 0.26	1.07 ± 0.24	1.39 ± 0.29	0.58	0.56	0.55	0.58	0.81 ± 0.08	1.07 ± 0.26	0.76 ± 0.07	0.80 ± 0.08
Si	0.30 ± 0.04	0.15 ± 0.03	0.31 ± 0.04	0.39 ± 0.04	0.29	0.28	0.29	0.29	0.27 ± 0.03	0.15 ± 0.03	0.26 ± 0.05	0.29 ± 0.03
Mn	1.35 ± 0.06	1.55 ± 0.07	1.07 ± 0.06	1.52 ± 0.08	1.15	1.14	1.12	1.14	1.19 ± 0.12	1.55 ± 0.07	1.18 ± 0.19	1.21 ± 0.10
Cr	0.99 ± 0.05	0.91 ± 0.05	0.88 ± 0.06	0.98 ± 0.06	1.02	1.02	1.01	1.02	1.01 ± 0.10	0.91 ± 0.05	0.99 ± 0.14	1.03 ± 0.09
Fe	95.59 ± 2.14	96.33 ± 2.16	96.67 ± 2.66	95.72 ± 2.67	-	-	-	-	95.13 ± 0.87	96.33 ± 2.16	95.39 ± 0.92	95.63 ± 0.78
P	-	-	-	-	0.014	0.013	0.012	0.013	-	-	-	-
S	-	-	-	-	0.007	0.005	0.006	0.006	0.01 ± 0.00	-	0.01 ± 0.01	0.01 ± 0.01

In Table 4.2, elemental concentrations of 36NiCrMoV1-5-7 and 45SiCrMo6 are provided. The heat resistant steel 36NiCrMoV1-5-7 has nearly 1 wt.-% less manganese and 0.4 – 0.7 wt.-% greater chromium content compared to 20MnCr5, as well as 0.80 wt.-% molybdenum, which proves to be highly advantageous in terms of its high temperature strength. A carburization was not carried out because recent slip-rolling tests have shown that a carburization for wear resistance in not consequently needed [115]. Other significant advantages of include its critical cooling speed, i.e. the speed at which the first martensitic structures appear, which is reduced, leading to improved hardenability. Furthermore, the tempering brittleness is also reduced due to its high nickel content, which is very important for heat resistant steels. Fine grain formation is also stimulated, which helps to yield a much more homogenous overall structure. Additionally, yield points and strength both show significant increases [116]. The high-temperature strength is a significant advantage of this steel, as it is able to be tempered at over 450 °C.

The steel 45SiCrMo6 is alloyed with an increased silicon content of 1.5 wt.-% Si and is used as a spring steel. This steel has shown strong performance in terms of a low coefficient of friction under mixed/boundary lubrication [113]. It has been proven to be slip-rolling resistant up to 10 million load cycles at P_{0Max} = 3.8 GPa. In spite of such impressive wear resistance, this steel, like 36NiCrMoV1-5-7, is not case-hardened. 45SiCrMo6 was chosen for further investigation based on these results, and because it shows work hardening tendencies [113]. During heat treatment, the silicon must be kept in solution in order to preserve solid solution strengthening and to avoid precipitation of brittle silicides. This spring steel, has a high annealing temperature of 410 °C, allowing it to be subjected to high temperature coating processes. Ultimate tensile strength, 0.2 % yield strength, elongation (5d) and impact strength KCU have been obtained at the higher tempering temperature [117].

Table 4.2: Elemental concentrations of 36NiCrMoV1-5-7 and 45SiCrMo6 in wt.-%.

		C	Si	Mn	P	S	Cr	Mo	Ni	V
36NiCrMoV1-5-7	**Standard Specifications**	0.33	0.25	0.20	0.003	0.002	1.50	0.80	3.00	0.30
	Supplier Specifications	0.33	0.25	0.20	0.003	0.002	1.50	0.80	3.00	0.30
	AES	0.40	0.25	0.25	0.005	0.002	1.65	0.79	3.49	–
45SiCrMo6	**Standard Specifications**	0.42 – 0.50	1.30 – 1.70	0.50 – 0.80	< 0.025	< 0.025	0.50 – 0.80	0.20 – 0.30	–	–
	Supplier Specifications	0.461	1.35	0.65	< 0.009	< 0.0015	0.62	0.22	0.03	0.11
	AES	0.48	1.48	0.65	< 0.001	< 0.001	0.62	0.23	0.03	–

4.1.2 Residual Austenite

The stated goal of the targeted heat treatment for 20MnCr5 was to obtain distinct sample groupings on the basis of residual austenite content. For the sample groupings previously denoted A through D, residual austenite content values of 6.3 ± 0.9 vol.-%, 7.6 ± 2.1 vol.-%, 12.1 ± 1.3 vol.-%, and 14.2 ± 2.2 vol.-%, respectively, were determined by XRD analysis at the TU Berlin. These results were confirmed through independent analysis at the BAM. While variations in deep freezing treatment have been shown to have a significant effect on residual austenite content, complete control of microstructural transformations via deep freezing was not achieved. The upper and lower limits of the sample groups, in terms of residual austenite, are clearly distinct, but sample groups B and C show some statistical overlap with A and D, respectively.

For the case-hardened 20MnCr5, a particular focus was put on microstructural composition directly below the surface. With this in mind, EBSD was deemed an appropriate method to confirm the findings from XRD analysis. EBSD was employed to give both visual images and quantitative distributions of structural entities in the material. Images from the EBSD analysis of a 20MnCr5 sample from group D can be found in Figure 4.1. The size of the pixels, however, is only 42 nm and is thus limited to the upper surface regions. EBSD can also assign crystallographic phases to each pixel, e.g. ferrite, austenite or cementite. The results obtained were more difficult to interpret than those from X-ray diffraction. A large proportion of the distributions (assigned as black dots) did not give readable signals and could not be correctly indexed, which resulted in the structures found in these regions being unable to be correctly characterized. It is noted that EBSD offers a much higher resolution than X-ray diffraction but is far more localized, i.e. it operates on the order of nanometres. This means that the focus of these measurements was directly at and absolutely on the sample surface. In some cases, the mechanical finishing carried out after heat treatment, namely grinding and polishing, can trigger the phase transformations of the austenite present at the treated surface. In this particular case, it is suspected that the residual austenite present after heat treatment was so metastable, that it was able to undergo phase transformations quite easily during the mechanical processing. Similar results are already available in the literature [118]. As a result, characterization by EBSD of this material is seen as extremely difficult in terms of austenite.

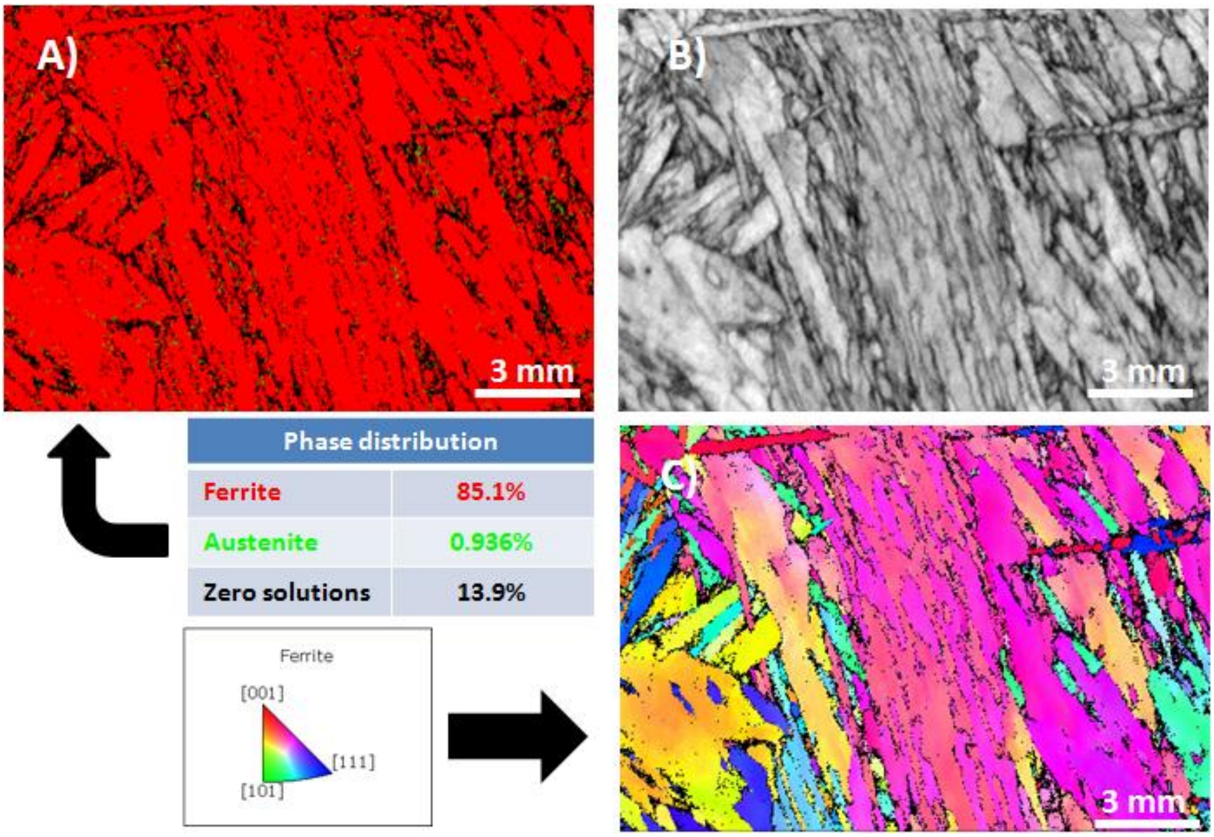

Phase distribution	
Ferrite	85.1%
Austenite	0.936%
Zero solutions	13.9%

Figure 4.1: EBSD analysis of 20MnCr5 (14.2 ± 2.2 % residual austenite by XRD) on the tribological surface comprised of A) Phase Map, B) Pattern Quality and C) IPFZ Map.

Further attempts to improve sample preparation were made with the intention of obtaining more favourable results. Mechanically processed samples were electrolytically polished in order to yield a more homogeneous sample surface for analysis. The logic here was to eliminate any possible shadow effects from uneven surface structures that may have occured during the intitial EBSD analysis. In spite of this, a significant improvement in results was not seen. Therefore the results of EBSD would match those from XRD if one assumes the transformation of the austenite to martensite (cubic body centered) can be assigned to the “black dots.” As sample preparation can have a significant influence over the outcome of measurements by EBSD, which is highly sensitive to residues from polishing, it must be very carefully considered. This includes the mechanical processing of the materials after heat treatment. Other methods for sample preparation, such as reactive ion etching (RIE), as well as those implemented in a study by Wang et al., deserve consideration [119].

Both 36NiCrMoV1-5-7 and 45SiCrMo6 are described by their respective manufacturers as martensitic steels, and were heat treated to yield extremely low residual austenite contents. Both samples indeed showed very little residual austenite. XRD measurements at the TU Berlin found residual austenite contents of 1.6 ± 0.3 vol.-% for 36NiCrMoV1-5-7 and 1.9 ± 0.3 vol.-% for 45SiCrMo6. Attempted confirmation by XRD analysis at the BAM was able to confirm that 36NiCrMoV1-5-7 and 45SiCrMo6 have less than 2.5 vol.-% residual austenite. More precise results could not be obtained, as this was below the detection limit for the diffractometer used.

Results from EBSD analysis of 36NiCrMoV1-5-7 and 45SiCrMo6 after slip-rolling testing at P_{0Mean} = 2.5 GPa are available in Figure 4.2. Measurements were taken from 7 mm below the wear track, which means the measured area showed essentially no direct exposure to load stresses than areas directly at the sample surface and can, consequently, be compared more reasonably to results for 20MnCr5 in the heat-treated state.

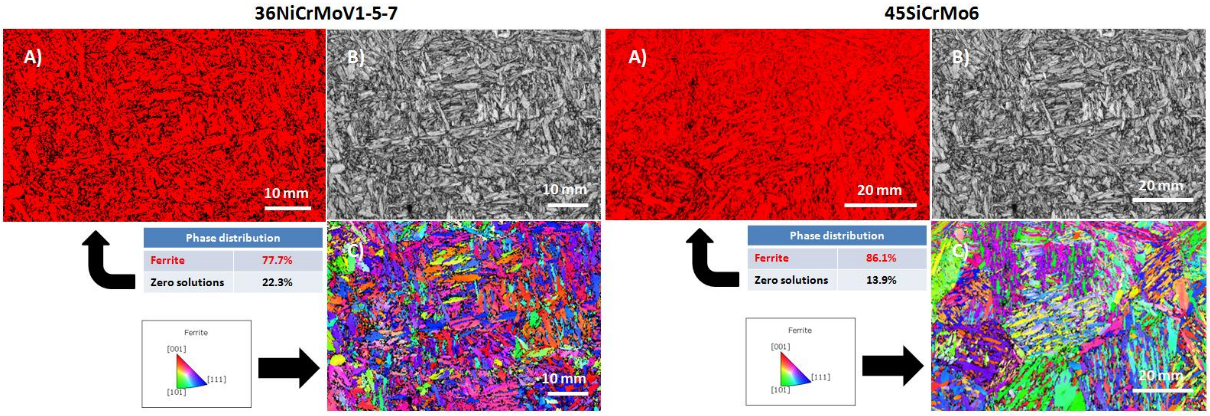

Figure 4.2: EBSD analysis of alternative alloys (36NiCrMoV1-5-7: 1.9 ± 0.3 % residual austenite, 45SiCrMo6: 1.6 ± 0.3 % residual austenite, by XRD) on the tribological surface comprised of A) Phase Map, B) Pattern Quality and C) IPFZ Map.

The images confirm the starkly martensitic character of these steels. More specifically, lath martensite is quite prominent, which is quite typical for low carbon steels, i.e. C < 0.4 wt.-% [113]. In the case of 45SiCrMo6, the enhanced silicon content (through solid solution strengthening) plays an important role in conjunction with this martensitic character. It has been reported in the literature that silicon alloying can yield benefits to tensile strength, hardenability and rolling contact fatigue life time [120]. Notably, silicon alloying can reduce the development WEAs and DEAs by preventing the formation of silica-based oxide inclusions [121]. Furthermore, it has also been reported that silicon alloying can serve as a replacement for costly chromium in bearing steels, while still maintaining high hardness [122]. As in the case of 20MnCr5, a substantial proportion of the scanned sample surface remained as unindexable “zero solutions.” This again has much to do with the martensitic distortion through heat treatment and load stresses. The result is that the scanning software cannot unequivocally identify a single lattice structure, and these areas remain black.

4.1.3 Hardness Profiles (heat-treated state)

As previously stated, all hardness depth profiles after heat treatment are given in Figure 4.3. Fairly typical hardness depth profiles are observed for the case-hardened 20MnCr5. A hardness of between 700 – 720 HV was reached directly at the sample surface. The case depth of case-hardened 20MnCr5 was determined to be approximately 2 mm. A consistent drop in hardness towards the end of the carburization zone is observed. This lower hardness outside the carburization zone is in line with the data from the manufacturer. It is noted that variations in residual austenite content did not have an identifiable influence on material hardness. This is an important consideration when selecting heat treatments to improve the quality, particularly in terms of wear performance, of low-cost materials.

The non-case-hardened high performance steels 36NiCrMoV1-5-7 and 45SiCrMo6 showed hardness profiles after their respective heat treatments that are consistent with data from the manufacturer. As neither of these steels was case-hardened, lower hardness was reasonably expected. The advantage of these steels lies with their affinity towards work hardening under high contact pressures previously mentioned with reference to studies by Scholz et al.

[113]. For 45SiCrMo6, the enriched silicon content is a contributing factor, as this has been shown in other, related studies to enhance work hardening [123]. Combined with the lack of need for energy- and time-intensive carburization processes, these steels may offer a significant economic advantage in achieving strong wear performance.

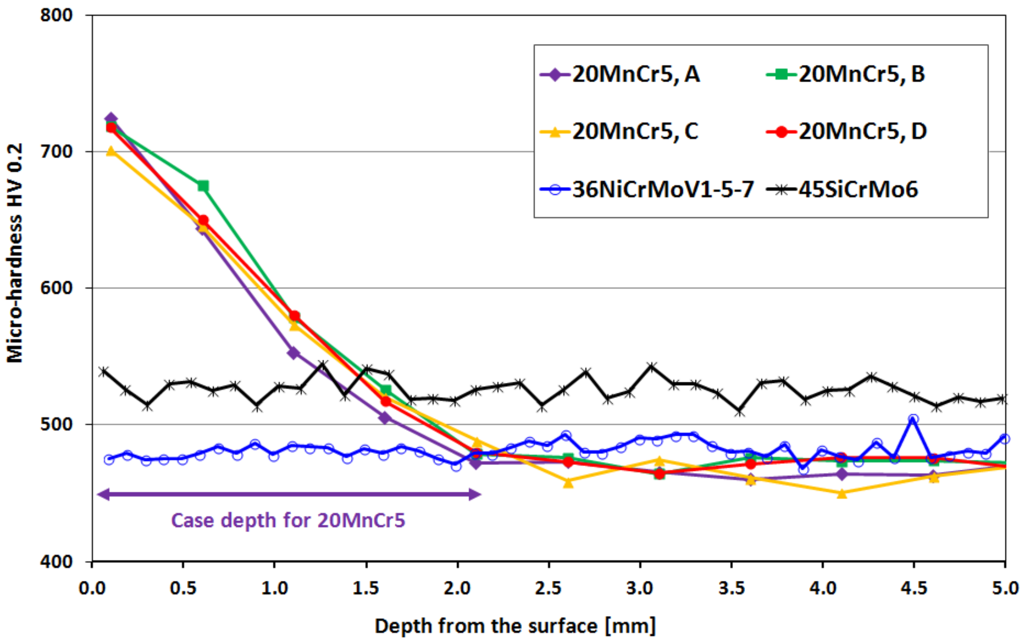

Figure 4.3: Micro-hardness depth profiles of case-hardened (case-hardened) 20MnCr5 steel, 36NiCrMoV1-5-7 (not case-hardened) and 45SiCrMo6 (not case-hardened) in the heat-treated state.

Values of influential mechanical properties of the examined steels are provided in Table 4.3. Particular focus is put on properties that have a significant impact on wear performance. The higher surface hardness of 20MnCr5 from case-hardening is most important for improvement of its wear performance. This higher hardness and the greater concentration of carbon in the carburization zone are more representative of a hardened SAE E52100, or 100Cr6/102Cr6 (useful in many bearing applications) than a non-case-hardened 20MnCr5. Consequentially, this case-hardened 20MnCr5 receives the benefits of a through hardened steel while also maintaining a relatively ductile core, i.e. reduced brittleness and, therefore, susceptibility to subsurface cracking.

Table 4.3: Mechanical properties of 20MnCr5, 36NiCrMoV1-5-7 and 45SiCrMo6.

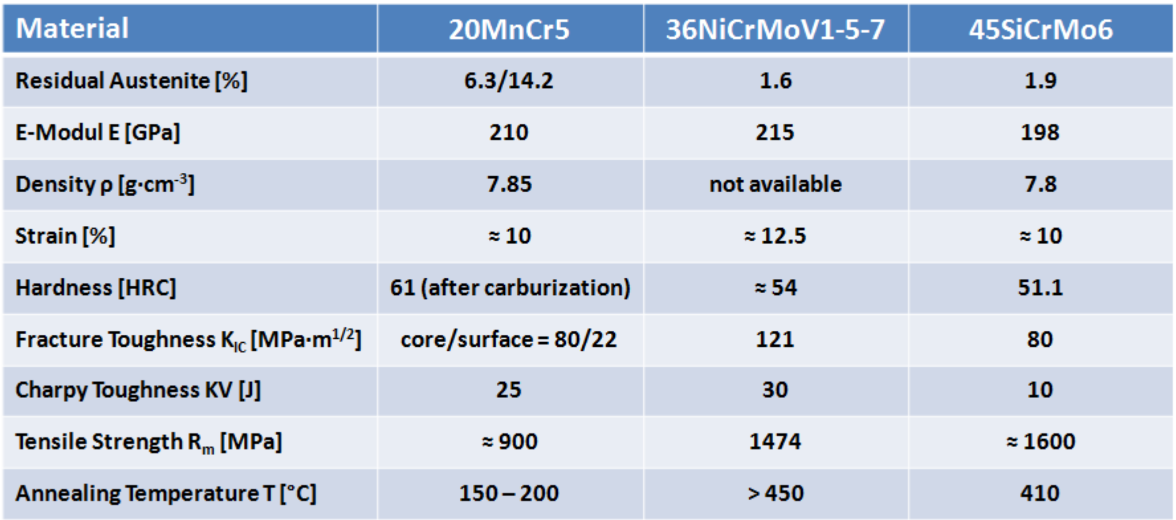

Material	20MnCr5	36NiCrMoV1-5-7	45SiCrMo6
Residual Austenite [%]	**6.3/14.2**	**1.6**	**1.9**
E-Modul E [GPa]	**210**	**215**	**198**
Density ρ [g·cm^{-3}]	**7.85**	**not available**	**7.8**
Strain [%]	**≈ 10**	**≈ 12.5**	**≈ 10**
Hardness [HRC]	**61 (after carburization)**	**≈ 54**	**51.1**
Fracture Toughness K_{IC} [MPa·m$^{1/2}$]	**core/surface = 80/22**	**121**	**80**
Charpy Toughness KV [J]	**25**	**30**	**10**
Tensile Strength R_m [MPa]	**≈ 900**	**1474**	**≈ 1600**
Annealing Temperature T [°C]	**150 – 200**	**> 450**	**410**

The high fracture toughness of the alternative steels, particularly 36NiCrMoV1-5-7, where some calcium sulfide (CaS) as well as aluminum oxide (Al_2O_3) and magnesium oxide (MgO) inclusions resulting from the calcium-argon treatment (CAB) throughout the sample bulk are present, is noted. This high fracture toughness can partially be attributed to the lath martensite found in the heat-treated alternative alloys, in contrast to the predominantly plate martensite found in 20MnCr5. This is substantiated by research conducted by Yokota and Lai [124]. By subjecting three different Fe-Ni alloys (two of predominantly lath martensite and one of predominantly plate martensite) to Charpy imact testing, they were able to determine that the plate martensitic alloy showed significantly lower impact strength and fracture toughness than the other two alloys. An essentially uniform increase in impact strength and decrease in yield strength with increase in grain size was observed for all three alloys. Lath martensite typically has a more uniform substructure than plate martensite and is absent of twins. It has also been suggested that a decrease in ductility should result in plate martensite structures containing internal twins because the potential for deformation is lower [125]. In addition, deformation twinning frequently occurs where plates martensite form at impinging angles to one another [126].

Strong resistance to crack formation, which can begin at sub-surface imperfections, and crack propagation is crucial in preventing critical material failure. The high tensile strength of both high performance steels is significant. This is particularly true for 45SiCrMo6, which is used for springs and torsion bars that are exposed to heavy workloads. Though the applied endurance testing loads may not be high enough to generate extensive work hardening, some plastic deformation can be expected.

4.1.4 Residual Stress Profiles (finished state)

The residual stress profiles for 20MnCr5 (from groups A and D, i.e. 6 and 14 % RA), 36NiCrMoV1-5-7 and 45SiCrMo6 in the finished state, i.e. after heat treatment, grinding and polishing, are given in Figure 4.4. Residual stress profiles of 20MnCr5 are very similar for both residual austenite contents. The profiles from after heat treatment and machining begin between -400 and -600 MPa. These compressive stresses are primarily a result of grinding and polishing during the mechanical finishing process, as such stresses can be introduced both by tribological manufacturing processes, as well as tribological operating processes. Alternatively, it is also possible to encounter such profile shifts when changes in component dimensions occur during mechanical finishing. The profiles then level off to approximately -200 MPa, which is a direct result of the case-hardening process. Since case-hardening was carried out to a depth of approximately 2 mm (see Figure 4.3), these stresses are well within the expected range.

Residual stress profiles of 36NiCrMoV1-5-7 and 45SiCrMo6 in the heat-treated state, both not having been case-hardened, still show some overlap with the profiles of case-hardened 20MnCr5 directly at the sample surface. This indicates that the residual stresses observed after grinding and polishing are proportionally greater in the alternative steels than in 20MnCr5. This is unsurprising as these steels were chosen for their propensity to undergo work hardening, though this is discussed later in greater detail. From directly below the surface on, the profiles of the high-performance steels level off to essentially 0 MPa, because these materials were not case-hardened.

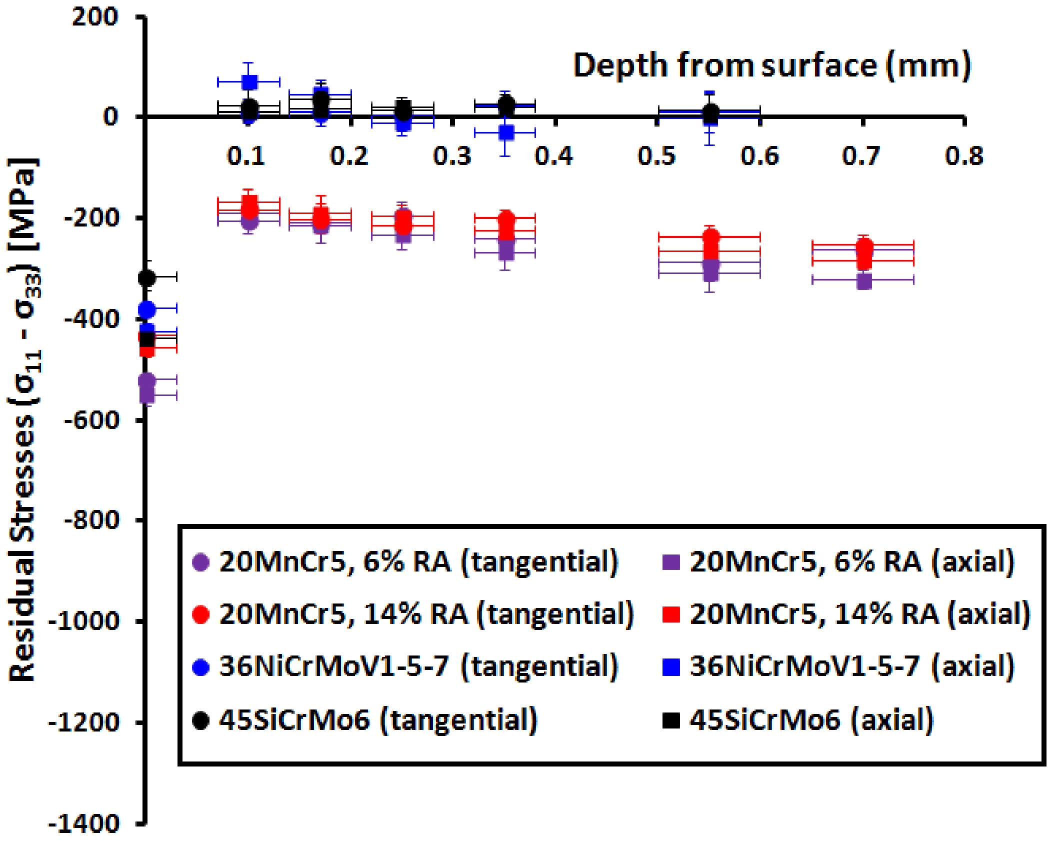

Figure 4.4: Residual stress depth profiles (calculated using the $\sin^2\psi$ method) for 20MnCr5, 36NiCrMoV1-5-7 and 45SiCrMo6 in the finished (heat treated, grinded and polished) state.

4.2 Cold Work Hardening

4.2.1 Residual Stress Profiles

Residual stress profiles for all alloys after cold work hardening are given in Figure 4.5 and Figure 4.6. The initial observation is that the residual stress profiles of 20MnCr5 are very similar for both residual austenite contents. After cold work hardening of 20MnCr5, the increase in maxima of compressive residual stresses to approximately -1200 MPa can be observed at a depth of 0.6 mm. It has been shown that such stresses in the range of 10 to 20% of the operating Hertzian contact pressure reduce the amount of equivalent stresses in the most heavily impacted areas of the material, and can help to increase the operating lifetime as well, indicating the beneficial qualities of compressive residual stresses [56]. The presence of such stresses is a strong indication of the effects of cold work hardening, primarily on the martensitic transformation of available residual austenite near the surface layer. Alternatively, grain refinement may also play a crucial role in the shifting of residual stress profiles, particularly where little residual austenite is available to be transformed into martensite. Additionally, material deformation and changes in grain size can be observed by evaluation of the full width at half maximum values (FWHM) of the XRD peaks, though these have not been provided. A decrease in diffraction peak width is indicative of increased plastic deformation, while an increase in diffraction peak width is indicative of decreased crystallite, or grain, size.

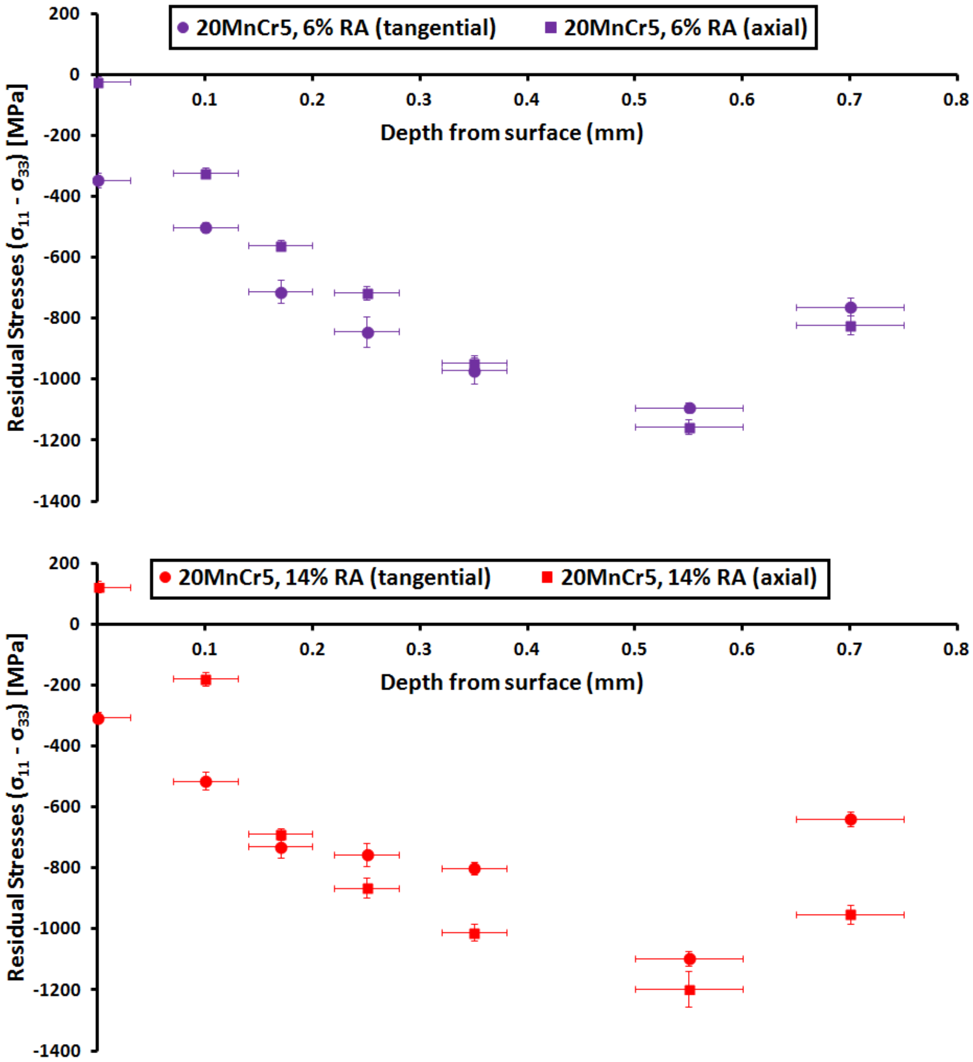

Figure 4.5: Residual stress depth profiles (calculated using the $\sin^2\psi$ *method) for 20MnCr5 after cold work hardening.*

The martensitic transformations that occur during cold work hardening are not unlike the those that occur during the quenching stage of heat treatment of the case-hardened samples, where the initial carburization leads not only to delayed transformation during direct hardening, but also to a reduction of the martensite temperature. The transformation begins directly beneath the surface layer and propagates into the core. Through the accompanying increase in volume that occur with the transformation of austenite to martensite, the still partially austenitic surface layer is plastically elongated. The delayed transformation of the surface layer materializes from the inside out, where the resulting increase in volume brings desired compressive residual stresses.

Mechanical surface treatment is able to accomplish the same transformations. Related processes through techniques such as the commonly implemented shot peening, are addressed in the literature [127].There is room to optimize the depth of the compressive stress maxima and of the treatment time (number of cycles). This is seen in the residual stress profiles for 20MnCr5 after cold work hardening by 10,000 load cycles and slip-rolling endurance testing up to 10^7 load cycles (see Figure 4.24). Notably, 10,000 slip-rolling cycles at an oil temperature of +120 °C under P_{0Mean} = 3,800 MPa were sufficient to generate microstructures typically present after slip-rolling endurance tests. This is illuminated in Figure 4.24, where compressive residual stresses from microstructural transformations achieved by pre-conditioning were stable up to 10^7 cycles in the case of 20MnCr5. A reduction of the previously introduced compressive residual stresses through unavoidable shear stresses is observed. A worthwhile goal would be to optimize pre-conditioning so that the compressive residual stress maxima lie in the same area as the expected shear stress maxima to counteract shearing effects that can lead to increased wear. Therefore the optimization of surface treatment parameters, for example by reducing the applied load to give a contact pressure of P_{0Mean} = 1.94 GPa or by running surface treatment at higher temperatures, say +140 °C as opposed to +120 °C, may still yield strong compressive stress maxima, but closer to the location of typical shear stress maxima.

Residual stress profiles of non case-hardened 36NiCrMoV1-5-7 and non case-hardened 45SiCrMo6 before cold work hardening appear relatively similar to those of case-hardened 20MnCr5, though they level off to 0 MPa since these materials were not case-hardened. Similarly, a strong increase in compressive residual stress is observable after cold work hardening. In both cases, residual stress values beyond -1000 MPa are not observed. One possible reason why fewer compressive residual stresses were introduced compared to 20MnCr5 could be the low contents of residual austenite after heat treatment and mechanical finishing, i.e. at under 2% for both alternative alloys. This would result in fewer martensitic transformations, making the alternative alloys more dependent on grain refinement for alteration of their residual stress profiles. The effects of such grain refinement can be seen in Figure 4.8, where the contact zones appear brighter than the surrounding material.

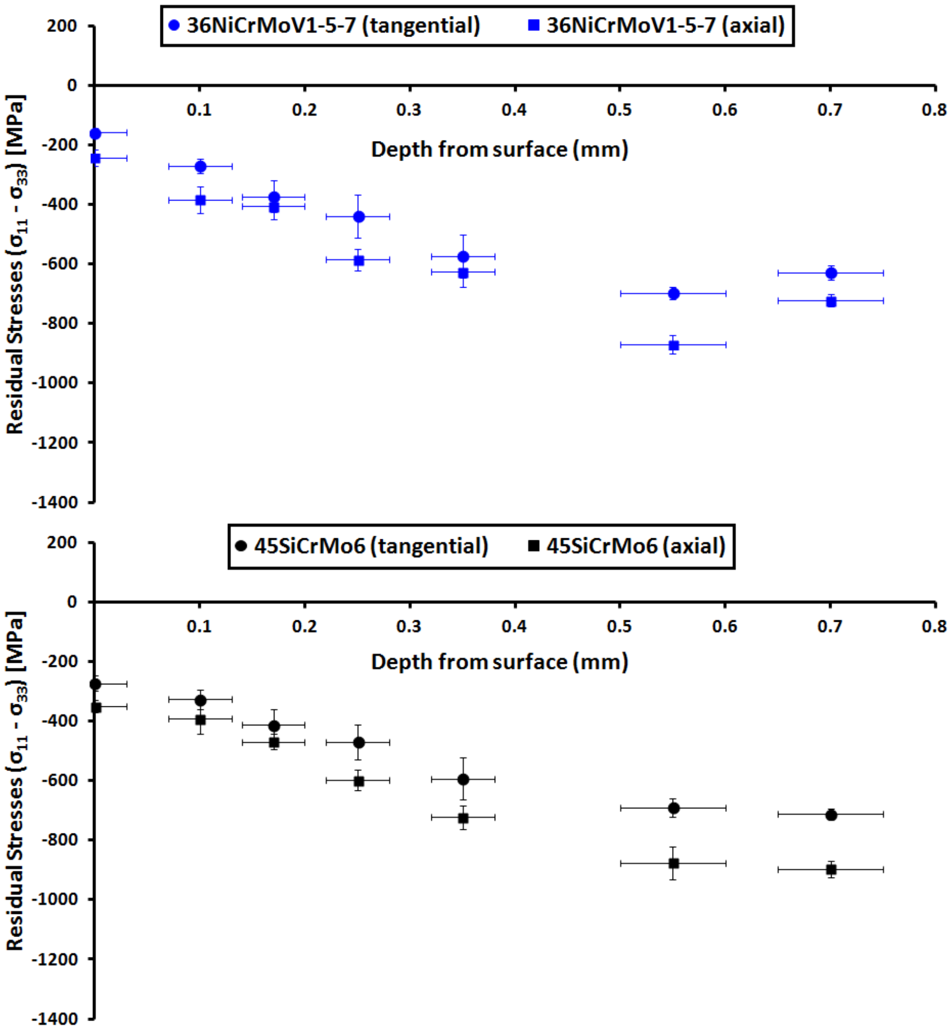

Figure 4.6: Residual stress depth profiles (calculated using the $\sin^2\psi$ method) for 36NiCrMoV1-5-7 and 45SiCrMo6 after cold work hardening.

It must be noted that with increased depth of measurement, achieved by electrolytic polishing of the surface substrate, comes less accuracy in the residual stress values obtained. Therefore measuring to depths much greater than 0.7 mm would be futile, as these depth values would begin to reside within each other's margin of error. Here, too, it is worth noting that the compressive stress maxima lie much deeper than typical sheer stress maxima from slip-rolling. Examples are available in work done by Scholz [113]. As previously mentioned, compressive stresses introduced through cold work hardening would be most beneficial were they to be found in the same areas as slip-rolling generated shear stress maxima.

4.2.2 Hardness Profiles

Changes in the surface layer hardness profiles can also be indicative of cold work hardening. The effects are especially apparent from profiles measured across the treated surface, rather than into the material. The profiles were taken from all samples after surface treatment at P_{0Mean} = 3.8 GPa up to both 1,000 and 10,000 load cycles. In the case of 20MnCr5, profiles were also taken after surface treatment up to 10,000 load cycles and slip-rolling endurance testing at P_{0Mean} = 1.5 GPa up to 10^7 load cycles. A significant increase in surface layer hardness, up to approximately 760 HV, can be observed after both 1,000 and 10,000 load cycles. 20MnCr5 with 14% residual austenite showed a stronger increase than did 20MnCr5 with 6% residual austenite. This may be an indication that residual austenite does have an influence over the work hardening behaviour of this reference steel. Significant differences in friction and wear behaviour as a result of residual austenite content are not observed later in slip-rolling testing (see section 4.4.1). Regardless, this is a strong indication that 1,000 load cycles are sufficient to generate cold work hardened 20MnCr5 surface substrates at P_{0Mean} = 3.8 GPa. Considerations can be made, on whether even a contact pressure of P_{0Mean} = 1.94 GPa is sufficient to produce similar effect after both 1,000 and 10,000 load cycles. Thus, cold work hardening can be achieved faster.

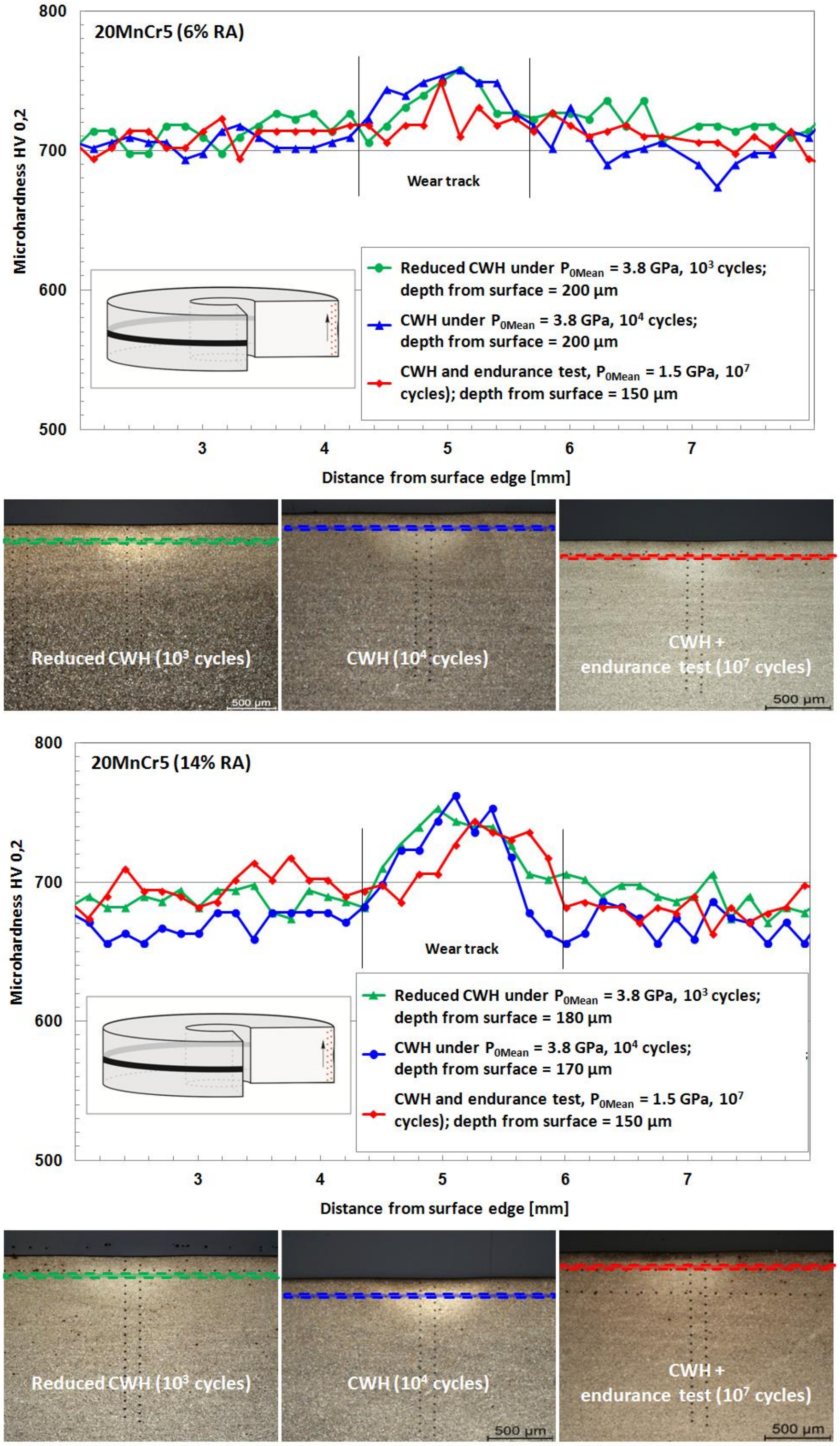

Figure 4.7: Microhardness profiles across sample surface of case-hardened 20MnCr5 after cold work hardening, and after cold work hardening and slip-rolling endurance testing.

Cold work hardened and slip-rolling endurance tested 45SiCrMo6 and 36NiCrMoV1-5-7 hardness profiles are not available, because both materials failed before reaching 10^7 load cycles. The deterioration of the alloys under this pre-conditioning regime is discussed in greater detail in section 4.4.2. As is the case with 20MnCr5, a significant increase in surface layer hardness of cold work hardened samples can be observed after both 1,000 and 10,000 load cycles for both steel substrates. The increases in hardness for 45SiCrMo6 are more pronounced, however, after 10,000 load cycles at 2.5 GPa, which may indicate that 1,000 load cycles are not sufficient to generate the desired plastically deformed surface profile.

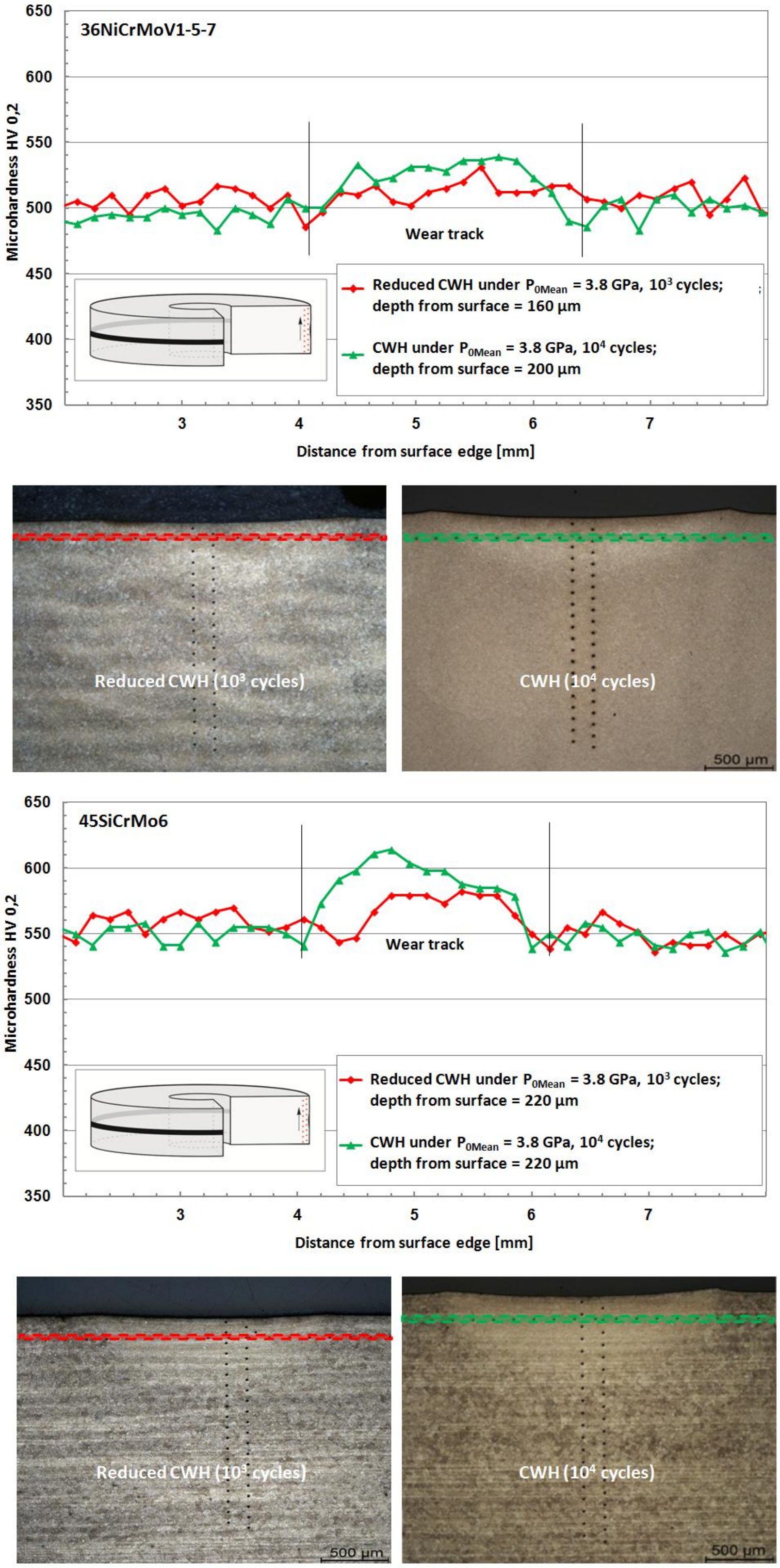

Figure 4.8: Microhardness profiles across sample surface of non-case-hardened high-performance steels, 36NiCrMoV1-5-7 and 45SiCrMo6, after cold work hardening.

As previously mentioned, the whitening of the contact areas, seen in the optical microscope images of the material cross-sections, is indicative of a combination of grain refinement and material hardening, the former of which contributes to the alteration of residual stresses. Such whitened areas are observable in both the reference alloy and the alternative alloys, meaning that the work hardening observed in all materials is influenced by grain refinement. Since the alternative alloys have extremely low residual austenite contents, i.e. under 2%, these alloys are particularly dependent on such grain refinement to achieve work hardening, while 20MnCr5, with its higher residual austenite content, can achieve work hardening through both grain refinement and the conversion of austenite to martensite. These considerations help to explain why 20MnCr5, which on paper appears to be a weaker alloy, still yields good performance in practice.

4.2.3 Residual Stress Profiles from Optimized Cold Work Hardening

It was previously mentioned that pre-conditioning through generated cold work hardening resulted in such severe deformation of the non-case-hardened steel surface substrates that these steels experienced critical surface failure well before reaching 10^7 load cycles in slip-rolling endurance testing. Therefore the optimization of pre-conditioning parameters to induce cold work hardening has been undertaken. The alterations made are summarized in Table 4.4. The most significant change made to the experimental parameters was the substitution of the initial hard-metal rollers with new rollers of the same material, but with a less severe curvature (R_{WC} = 21 mm). The new hard-metal rollers with a larger curvature that is equivalent to the regular spherical counterbodies produce surface deformation that is less extreme than previously observed, and has contributed to improvements in friction and wear performance, discussed later in section 4.4.3.

Table 4.4: Summary of optimized pre-conditioning parameters.

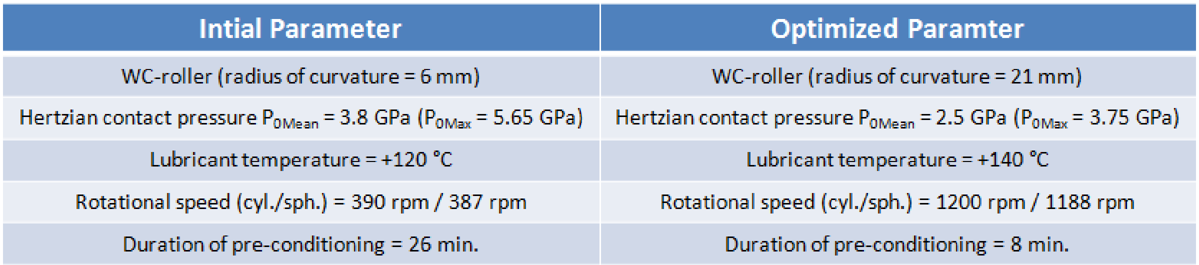

Intial Parameter	Optimized Paramter
WC-roller (radius of curvature = 6 mm)	WC-roller (radius of curvature = 21 mm)
Hertzian contact pressure P_{0Mean} = 3.8 GPa (P_{0Max} = 5.65 GPa)	Hertzian contact pressure P_{0Mean} = 2.5 GPa (P_{0Max} = 3.75 GPa)
Lubricant temperature = +120 °C	Lubricant temperature = +140 °C
Rotational speed (cyl./sph.) = 390 rpm / 387 rpm	Rotational speed (cyl./sph.) = 1200 rpm / 1188 rpm
Duration of pre-conditioning = 26 min.	Duration of pre-conditioning = 8 min.

The residual stress depth profile for 36NiCrMoV1-5-7 after optimized cold work hardening is given in Figure 4.9. In contrast to the residual stress profiles from before, i.e. non-optimized cold work hardening, greater compressive stresses are observable directly at the surface. It must be noted, however, that significant statistical deviation in the magnitude of stress is present, which likely points to effects from shearing stresses, which would be most severe at the sample surface. A second contrast to the profiles from before optimization is the increase in compressive stresses toward the sample depth of 800 µm. This is related to the third contrasting profile feature, namely, that although this increase is statistically legitimated, it is still unclear if this represents the true maximum of compressive residual stress, because measurements at greater depths would lead to significant statistical deviation in the measured magnitude of stress. Whether the optimization of testing parameters to generate cold work hardening has been truly effective will be discussed further in terms of material hardness in the next section, and furthermore, in terms of slip-rolling endurance in section 4.4.3.

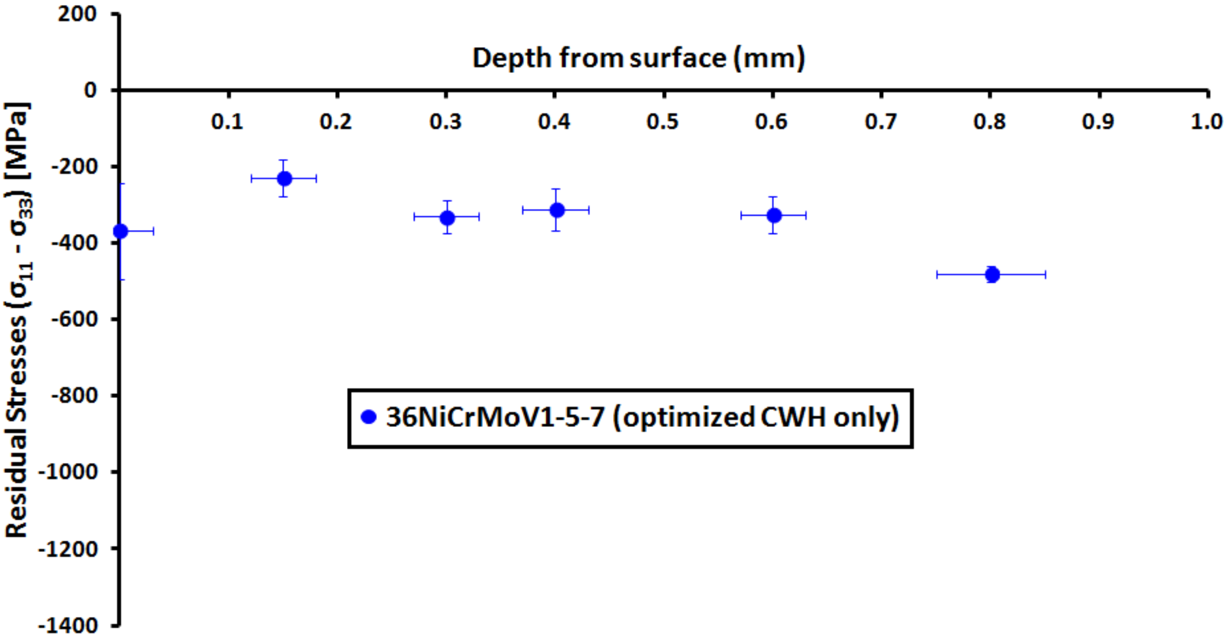

Figure 4.9: Residual stress depth profile (calculated using the sin$^2\psi$ method) for 36NiCrMoV1-5-7 after optimized cold work hardening.

4.2.4 Hardness Profiles from Optimized Cold Work Hardening

Analyses of material hardness after optimized cold work hardening (and additionally after slip-rolling endurance testing as well) were conducted in the same manner as before parameter optimization. Again, profiles from across the contact surface area have been made available (see Figure 4.10 and Figure 4.11). In Figure 4.10, the profiles of 20MnCr5, with 6% and with 14% residual austenite content, are compared. There does not appear to have been strong hardness increases generated in the case of lower austenite content, or a white etching region as seen previously in Figure 4.7. This holds true for both after pre-conditioning, as well as after pre-conditioning and 10^7 cycles of endurance testing. Some minor increases in surface hardness are likely to have occurred, however these would be below the resolution limit of the hardness testing method applied. For the case of higher austenite content, increases in hardness are more clearly observable in the contact zone, though like the lower austenite content case, these increases in hardness are more subtle than from work hardening through the non-optimized hard metal rollers.

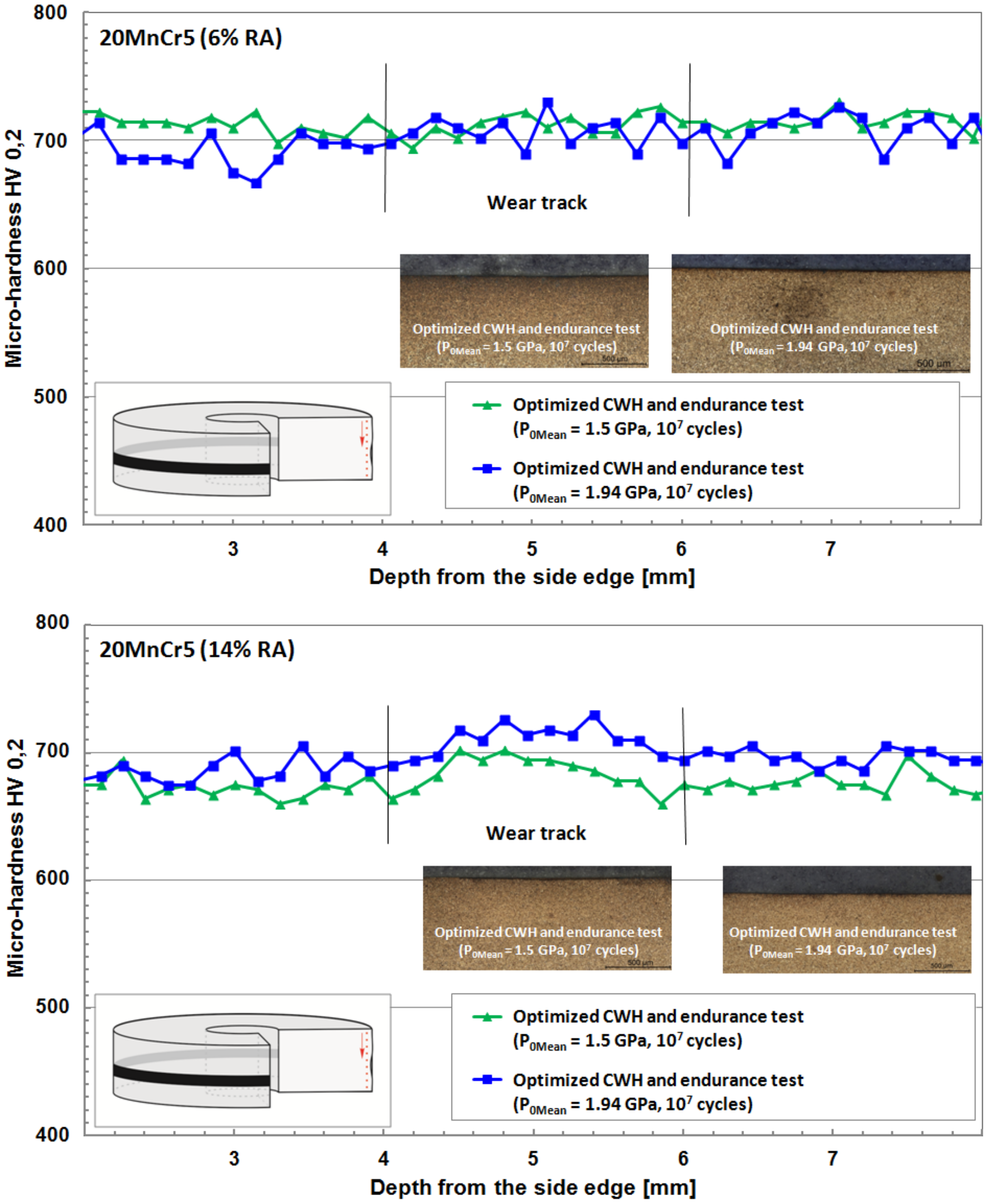

Figure 4.10: Microhardness profiles across sample surface of case-hardened 20MnCr5 after optimized cold work hardening + slip-rolling endurance testing.

In Figure 4.11 the profiles of the non-case-hardened alternative alloys are provided for comparison. As was the case with 20MnCr5 (14% RA) observable increases in surface hardness can be observed, though these increases are, again, not as strong as observed before optimization. For 36NiCrMoV1-5-7, the increases exclusively from pre-conditioning are particularly subtle, but still observable. The increases become more pronounced with increasing endurance testing load. For 45SiCrMo6, the hardness increases are more clearly defined than for 36NiCrMoV1-5-7, though again, less pronounced compared to cold work hardening without optimization. Some white etching areas are observed in the contact zones. This whitening is most visible in 36NiCrMoV1-5-7.

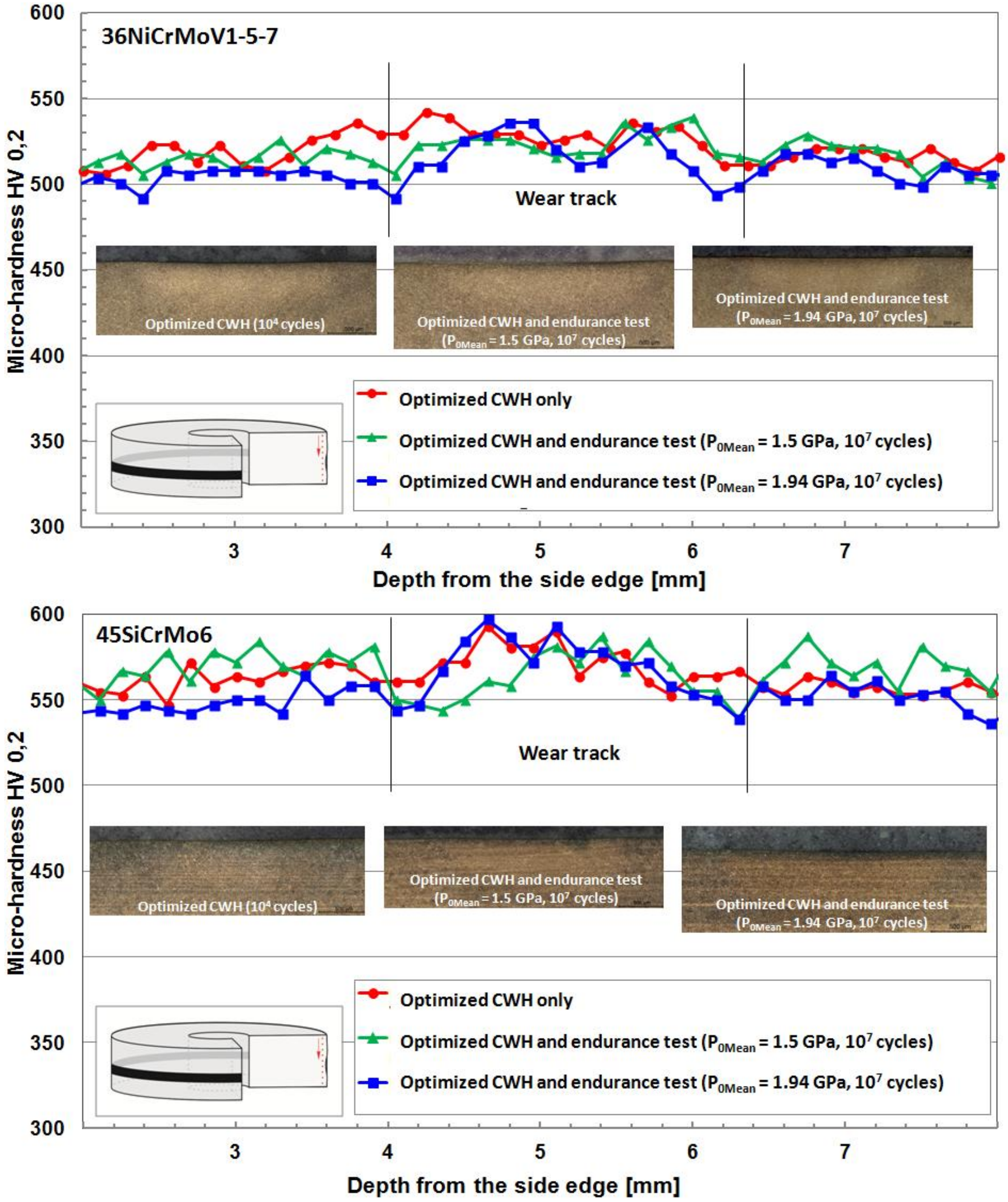

Figure 4.11: Microhardness profiles across sample surface of non-case-hardened high-performance steels, 36NiCrMoV1-5-7 and 45SiCrMo6, after optimized cold work hardening, and after optimized cold work hardening + slip-rolling endurance testing.

4.3 Tribofilm Generation

4.3.1 SEM-EDX Element Mapping

The process of transferring running-in into the final phase of mechanical finishing must also be economically viable if it is to find further industrial application. The process as a whole is time-, and therefore, cost-sensitive. The inner and outer races of bearings provide the best available surfaces for such applications. Other parameters chosen are standard for the slip-rolling resistance testing that follows. Following tribofilm generation, the samples were analyzed by SEM-EDX with Element-Mapping. The tested surface areas were compared with the untested areas of the surface substrate in order to determine a difference in concentration of particular elements. Because the staging area of the SEM has limited space, all samples had to be prepared by separating a sliver of tribofilm-treated surface from the bearing for further analysis. The same applied for XPS analysis.

It is important to pay close attention to the contact pressure applied, because some steels, such as 36NiCrMoV1-5-7, can show greater wear resistance at higher contact pressures. The same applies to the potential for work hardening, such as in 45SiCrMo6, which can influence the adhesion ability of tribofilms to the surface substrate. It was also shown in previous work by Scholz, that many tribofilms are generated more effectively at higher contact pressures [113]. Therefore it is important to fit the applied contact pressure to the particular material being tested.

Testing on 20MnCr5 in Wisura LS514, at different contact pressures was carried out in an attempt to optimize the contact pressure needed for the quick and efficient generation of reactive tribolayers. At P_{0Mean} = 1.5 GPa, Ca, C and O (see Figure 4.12) were found only in small creases in the wear track. At P_{0Mean} = 1.94 GPa, the concentration of Ca, C and O were found to be significantly stronger in the wear track alone. At P_{0Mean} = 2.5 GPa, only C was detected, though not exclusively within the wear track. These results speak to the ability of this steel substrate to allow the generation of tribofilms: a contact pressure of P_{0mean} of 1.5 GPa is too low for the generation of a tribofilm within 10,000 cycles for “squeezing” out additives and nano-sized additives as well as active film formation, but contact pressures of P_{0Mean} = 2.5 GPa or higher are too high, because even when a tribofilm is generated, it is quickly worn away through mechanical wear.

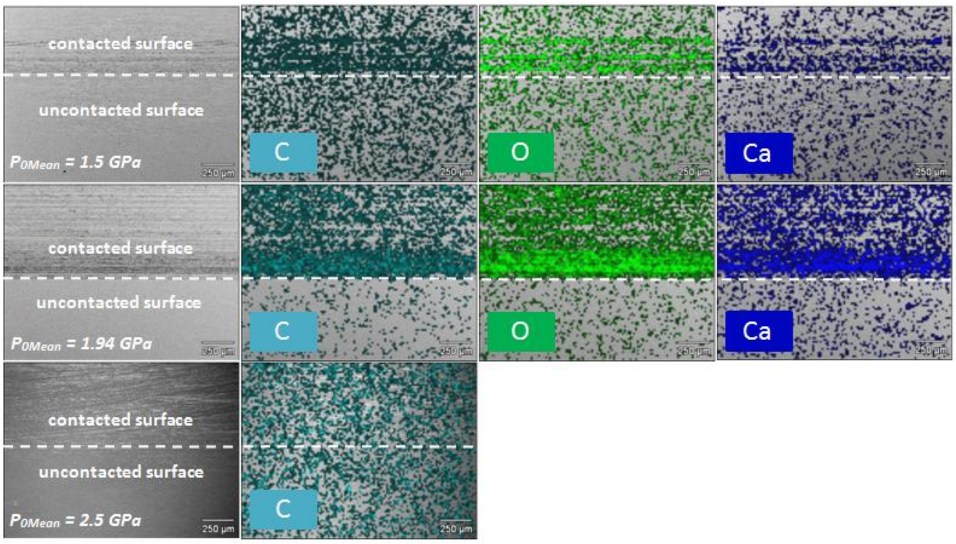

Figure 4.12: SEM-EDX Element-Mapping of 20MnCr5 from inside and outside the wear track, tested in Wisura LS514 at P_{0Mean} = 1.5 GPa, P_{0Mean} = 1.94 GPa and P_{0Mean} = 2.5 GPa.

Initial results of tests with Wisura ZO 3180 Plus (similar to LS514) at P_{0Mean} = 1.94 GPa proved to be extremely positive. On all tested steels, except for the additionally tested 102Cr6, the elements Ca, C and O were much more concentrated on the tested surface area compared to the untested area, which was also in contact with the lubricant during testing. This further supports the finding that a given contact pressure is necessary for the generation of reactive tribofilms. Furthermore, the elements Fe and Cr appeared to be much weaker in the tested areas, which indicate that they were, in fact, covered by a reactive tribolayer.

In the case of 102Cr6, the distribution of elements was not so clear. For virtually all detected elements, traces could be found both within and outside of the wear track. At closer inspection, stronger traces of Ca, C and O could be found within the wear track, though only in µm wide areas of greater wear. This is a possible indication that a certain amount of surface wear is necessary for the elements of a tribologically induced protective layer to adhere to a given surface substrate. Results from the Element-Mapping of 20MnCr5 and 102Cr6 are provided below. All other steels showed nearly identical results to 20MnCr5, and are, therefore, not depicted.

Testing in VPX + 10% Molyvan 822 (molybdenum di-n-butyl-dithiocarbamate (MoDTC) in oil) was carried out. MoDTC is not present in the VP1 used for slip-rolling endurance tests and act as a “tracer.” Strong positive results were observed at P_{0Mean} = 1.94 GPa. Significantly higher concentrations of Mo (found only in MoDTC) and O were observed in the wear track in comparison to outside the wear track. Furthermore, a reduced concentration of Fe was also observed in the wear track, a strong indication of the formation of a tribologically induced protective layer. Further testing with this additive on other material surface substrates is being considered. Most importantly, the molybdenum from the MoDTC can be easily distinguished from the Zinc (ZDDP) present in the VP1 engine oil.

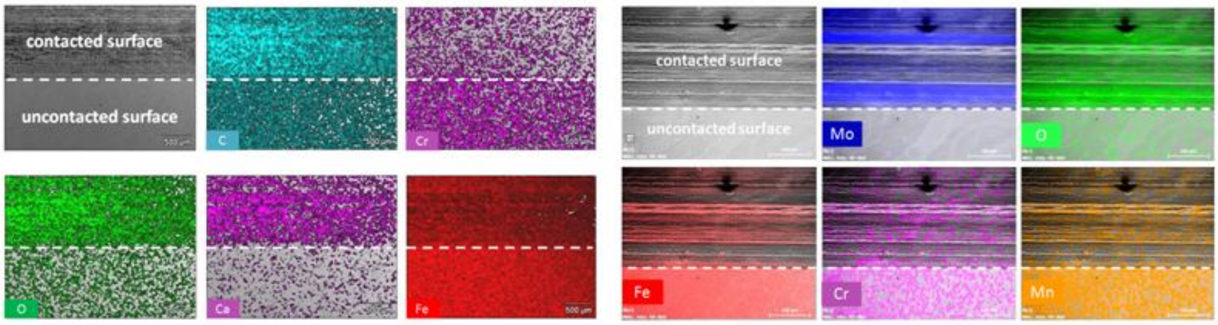

Figure 4.13: SEM-EDX Element-Mapping of 20MnCr5 from inside and outside the wear track after 10^4 load cycles under P_{0Mean} = 1.94 GPa in Wisura ZO 3180 Plus (left) and VPX + 10% Molyvan 822 (right).

Other additive testing was less successful, and therefore not incorporated further into this study, though the results are worth mentioning. Testing in Wisura LS 516 (sodium sulfate-based) at 2.5 GPa was less successful, as virtually no traces of Na and S were found at all. Furthermore, testing with VPX + 10% Molyvan A (molybdenum di-n-butyldithiocarbamate in powder form) and VPX + 10% Desilube 88 (sodium thiosulfate) has not been successful, thus far. The suspicion here is that the additive particles are not sufficiently dispersed in the lubricant, which hinders them from being in contact with the impacted surface substrate. Therefore, three different dispersants from Giovanni Bozzetto S.p.A. (Filago, Italy) were obtained: Hydrodis 253 BS (naphthalene sulfonate with low molecular weight), Hydrodis 100 Na (naphthalene sulfonate with high molecular weight) and Kelcor 1265 (oil-soluble phosphonate). Further testing has not yet yielded positive results. In the case of Desilube 88, a solvent more polar than the oil-based lubricants used thus far may be required in order to unleash the reactive potential of this additive [128]. Other possible dispersion processes for similar additives are also described in the literature, and may be applicable [129].

Two newly tested additives, Irgalube 349 [80939-62-4] from BASF, an organic compound with active amino-phosphates and in parallel dibenzyl disulfide (DBDS, [150-60-7]) from Merck, have positively contributed to the generation of new reactive tribolayers. Testing in Irgalube 349 yielded strong concentrations of P and O (i.e. phosphates) in the wear track, though nitrogen was not found above the limit of detection. This is unsurprising, as the excitation energy required for nitrogen signals is very minimal, which would make adjusting the applied acceleration voltage needed for simultaneous detections of other, heavier elements extremely difficult. Strong concentrations of S and O from DBDS were also detected in the wear track.

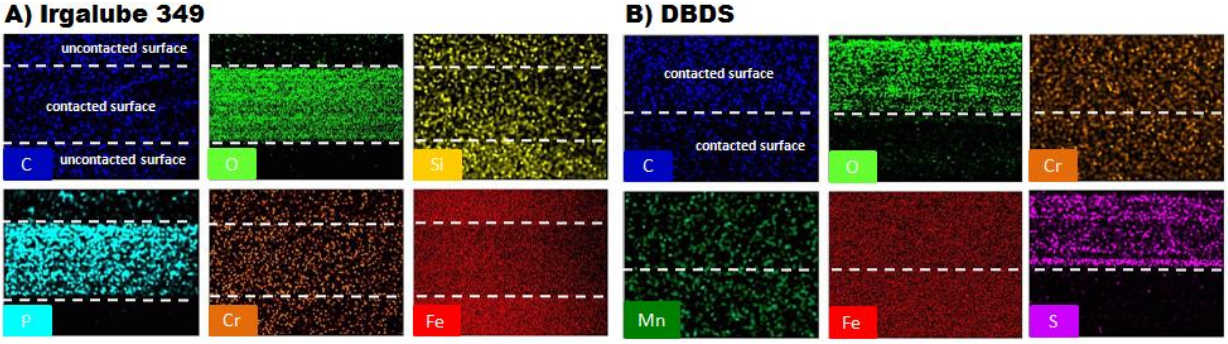

Figure 4.14: SEM-EDX Element-Mapping from inside and outside the wear track of A) 45SiCrMo6, tested in VPX + 10% Irgalube 349 and B) 20MnCr5, tested in VPX + 10% DBDS at +120 °C, P_{0Mean} = 1.94 GPa up to 10,000 cycles.

4.3.2 Raman Spectroscopy

Although SEM-EDX Element-Mapping provides clear visual images of generated tribofilms, it does not definitively prove what the molecular composition of these films is. It only shows which elements are involved. With this in mind, Raman spectroscopy was carried out on LS514 and M822 tribofilms, the spectra for which are given in Figure 4.15 and Figure 4.16, respectively. The main component of the LS514 tribofilm, $CaCO_3$, is prominently represented by the strong, sharp peak at 1085 cm^{-1} [130]. The clarity of this peak proves to be the exception, as the amorphous character of the tribofilms results in otherwise wider peaks of relatively low intensity. The possibility of the presence $Ca(OH)_2$ is also indicated. This is difficult to verify, because the normally characteristic peak at 356 cm^{-1} (unmarked) is, at most, only present as a minor shoulder that is barely visible, while the weaker peak normally found at 680 cm^{-1} is buried beneath the more prominent peak from Fe_3O_4 [131,132]. CaO is even more difficult to verify, both because of peak overlap, particularly with $CaCO_3$, and because its propensity to react with atmospheric H_2O, yielding $Ca(OH)_2$ and CO_2 [131]. The authors of the referenced study claim the reaction takes place with CO_2, rather than H_2O, though this would not yield $Ca(OH)_2$. It should also be noted that the equilibrium of this reaction is shifted markedly towards $CaCO_3$, meaning $Ca(OH)_2$ is only a very minor product. In addition to Fe_3O_4, Fe_2O_3 is verified by the peaks at 247 cm^{-1} and approximately 293 cm^{-1} [133].

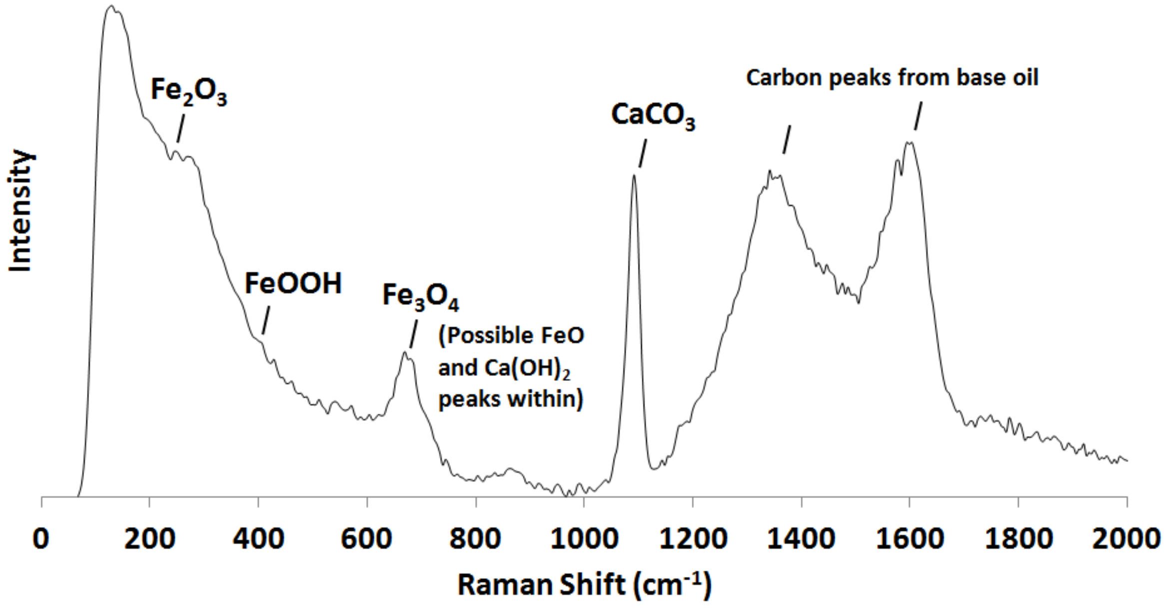

Figure 4.15: Raman spectrum of LS514 tribofilm on 20MnCr5 surface.

As indicated by the Element-Mapping images of the M822 tribofilm, molybdenum oxides are the most significant contributors to the protective chemical tribofilm, though there are some minor peaks indicating the presence of iron oxides (unmarked). Several peaks that are attributable to either MoO_2 or MoO_3 are marked and compared with results that are available in the literature [134,135,136,137]. Though no significant sulfur signals were detected with SEM-EDX, the peak pattern seen between 380 cm^{-1} – 410 cm^{-1} can very readily be attributed to MoS_2 [138]. Analysis of both the LS514 and M822 tribofilms by X-ray photoelectron spectroscopy (XPS) is currently underway to provide further verification of the proposed tribofilm components.

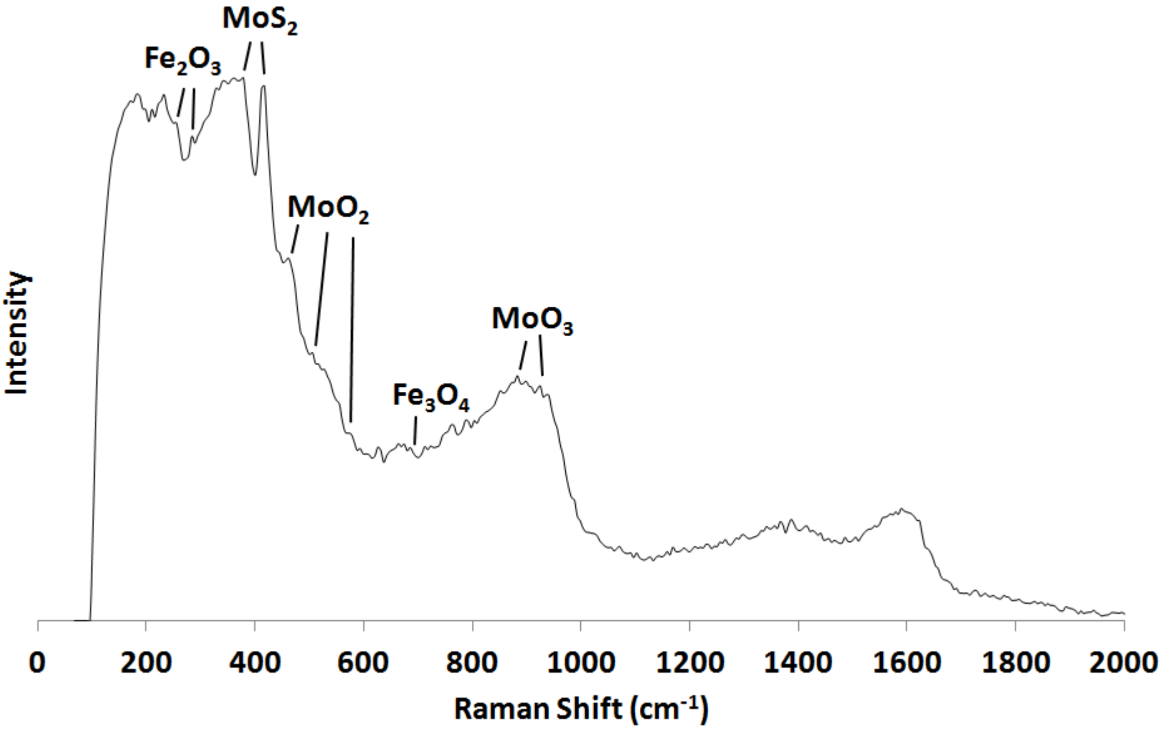

Figure 4.16: Raman spectrum of M822 tribofilm on 20MnCr5 surface.

4.3.3 XPS

With more concrete information on both the elemental and molecular composition of the chemically reactive tribofilms from SEM-EDX and Raman spectroscopy, XPS analysis allows for more definitive conclusions to be drawn in combination with the results previously obtained. XPS is also an extremely useful method for the characterization of such films because of its ability to be limited to very low penetration depths, i.e. to the order of approximately 1 – 10 nm. XPS spectra of pre-conditioned tribofilms from both LS514 and M822 are given in Figure 4.17.

The spectrum of the LS514 tribofilm unequivocally indicates the presence of $CaCO_3$, seen in the characteristic pattern of the peaks for Ca 2s, Ca 2p, C 1s and O 1s orbital electrons [139]. Furthermore, these peaks are far more prominent than those for the other species, notably iron. This is indicative of significant participation of $CaCO_3$ in the analyzed tribofilm, because unlike in Raman spectroscopy, the size of the peaks is, ultimately, representative of the quantity of elements present in the irradiated sample area. Therefore it can also be concluded that the abovementioned iron species are not present in the tribofilm in great quantities, but they are, nevertheless, present in the analyzed surface area and must be reported [140].

The spectrum of the M822 tribofilm confirms that which was ascertained from Raman spectroscopy, namely the presence of MoS_2, MoO_2 and MoO_3 [141,142,143]. The characteristic molybdenum peaks are particularly strong, whereby the Mo 3d peak at 229 eV nearly covers the S 2s peak at 227 eV, though both are visible even with significant overlap. As is the case with the LS514 tribofilm, iron species show little participation in the tribofilm composition. Consequently, MoDTC is clearly very effective at covering the surfaces in the tribocontact.

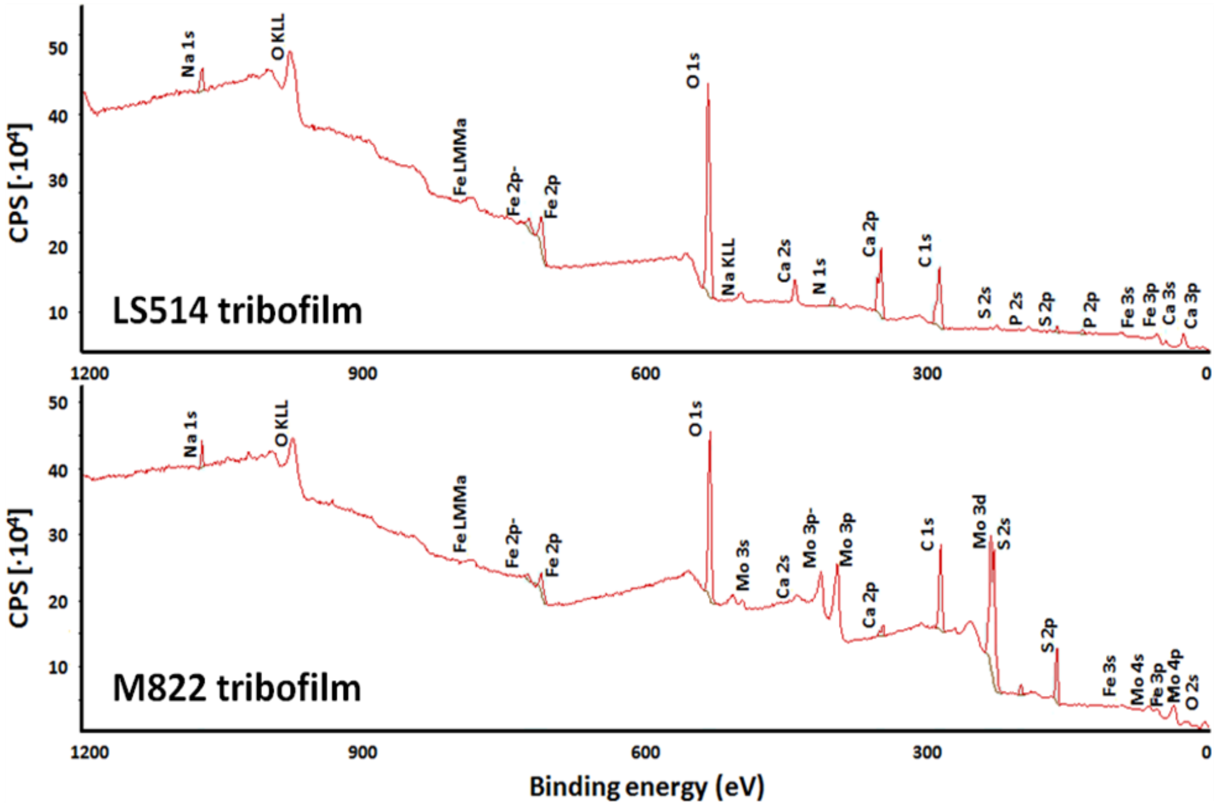

Figure 4.17: XPS spectra of pre-conditioned tribofilms on 20MnCr5 surface.

With the most important chemical species in the tribofilms identified, it is worthwhile to describe the reaction mechanisms that are most likely to yield such species. The previously mentioned reaction model, proposed by Schulz and Holweger [66], gives a clear outline of the mechanism(s) involved in forming the LS514 tribofilm. Iron oxides on the steel sample surfaces are essentially unavoidable under normal atmospheric conditions, regardless of the antioxidants that may be present in a chosen lubricant. This means that the slightly polar positive iron bonded to slightly polar negative oxygen may react with newly introduced lubricant additives, in this case $CaCO_3$. Polar negative oxygen from $CaCO_3$ interacts with polar positive iron in the steel, while polar positive calcium interacts with the polar negative oxygen present in the superficial iron oxides. The subsequent reactions have also been described by Kubo et al. in the context of steel-DLC contacts and are summarized as follows [144]:

1. The initial reaction of calcium with oxygen forms a Fe- and CaO-containing base film.
2. $CaCO_3$ accumulates on the sample surface.
3. Additional $CaCO_3$ reacts to form the increasingly thick tribofilm.

The abovementioned reaction models provide parallels to the interactions of components from M822 with steel surfaces. Description of the mechanism of formation of the M822 tribofilm is bolstered by the abundance of literature on MoDTC, the essential component of M822, due to its popularity as a lubricant additive in internal combustion engines [145]. Consequently, the decomposition mechanism of MoDTC (see Figure 2.20) that leads to reaction with steel surfaces has been thoroughly described in the literature [146,147,100]. The first step in the decomposition is a radical electron transfer that cleaves the bond between Mo and the S from the dithiocarbamate. This leaves three free radical species, two of which are from the chain ends of MoDTC and the third from the core component. This core component undergoes further decomposition into MoS_2 and MoO_2 species, the latter of which will oxidize in the presence of atmospheric oxygen, yielding MoO_3 as well.

4.4 Slip-Rolling Endurance Test Results

4.4.1 Baseline of Slip-Rolling Resistance

All untreated samples were able to run for 10^7 load cycles without critical material failure, the criteria for which have been specified in the experimental procedures. This was apparent upon visual inspection of the contact surfaces after testing, and furthermore, in the optical microscope images of these areas, provided in Figure 4.18. Optical microscope images of sample surfaces exposed to the higher testing loads, P_{0Mean} = 2.5 GPa and P_{0Mean} = 2.62 GPa, are currently being generated.

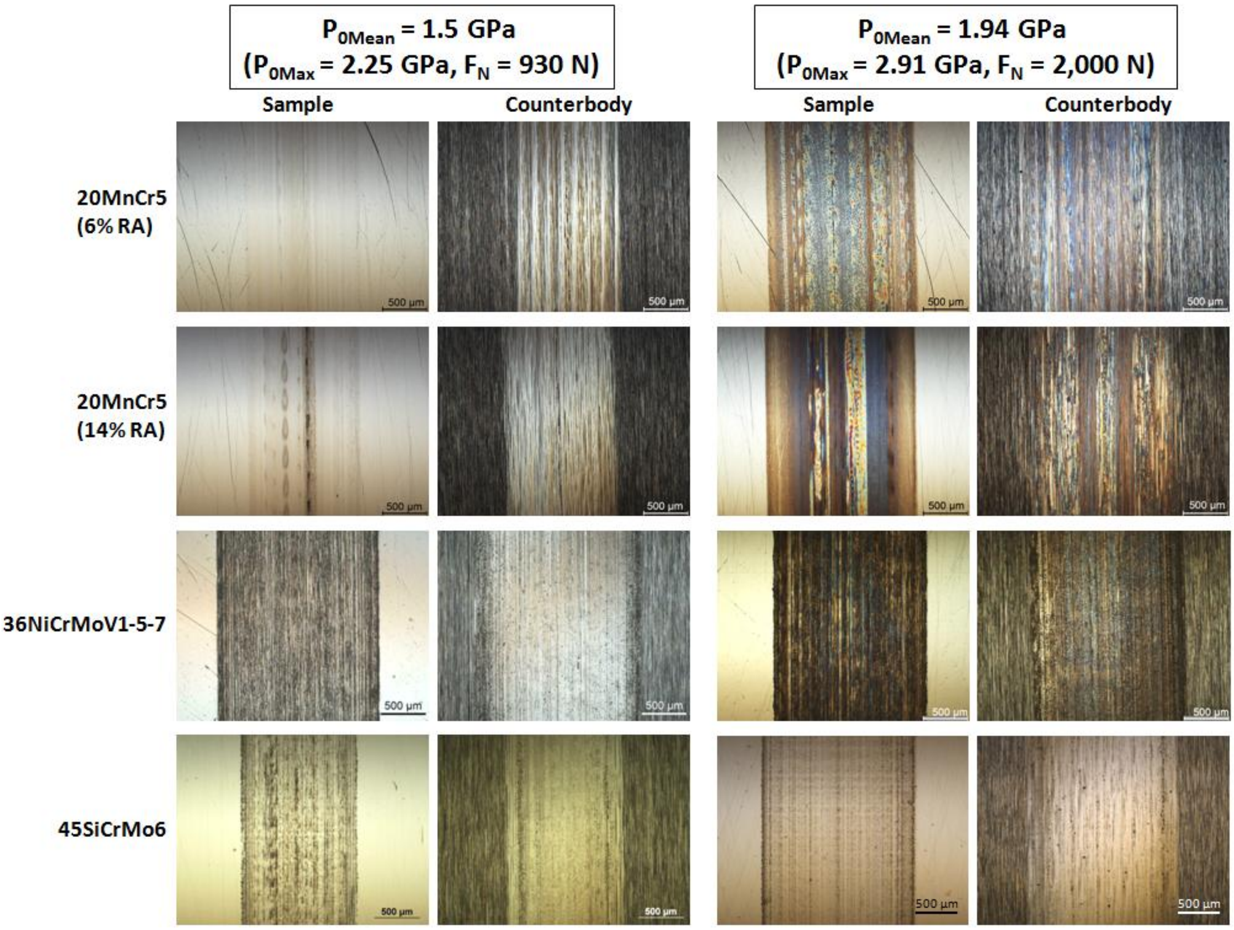

Figure 4.18: Optical microscope images of the contact surfaces of the cylindrical samples and spherical counterbodies (both untreated) after 10^7 load cycles of slip-rolling endurance testing at T = +120 °C in BMW FF SAE 0W-30 VP1, ACEA A3/B4, dynamic viscosity at +120 °C = 5.33 mPa·s.

Both the cylindrical sample bodies and spherical counterbodies remained relatively undamaged at both of the lower testing loads, whereby wear can only be observed in the wear track, created by the points of contact. Neither scuffing nor pitting phenomena can be observed from either the lower or higher applied testing load. This is in large part due to the testing lubricant, BMW FF SAE 0W-30 VP1, which is fitted with a comprehensive additive package that is designed to protect contact surfaces from such phenomena. At the lowest testing load, 20MnCr5 and 45SiCrMo6 showed comparable wear track widths, while the wear track of 36NiCrMoV1-5-7 was slightly wider. All wear tracks appeared to be of a more consistent width as contact pressure increased.

Although the testing materials did not experience critical failure, some minor surface cracking and/or flaking was observed. Such behaviour became more prevalent at higher loads, and some exemplary optical microscope images of areas that experienced this surface damage are provided in Figure 4.19. SEM investigations showed only some minor, singular, sub-surface microcracks of the order already reported and evaluated for these materials by Scholz [113]. This is unsurprising for testing at less extreme load settings, particularly for the high-performance steels, which can be expected to resist excessive crack formation in light of their high fracture toughness. Moreover, the strongly martensitic character of both of these steels, observable in and Figure 4.2, and later in Figure 4.22, is also of particular relevance.

Types of wear have been defined for dry wear testing of pearlitic steels in rolling-sliding contact by Bolton et al. as simply “mild” and “severe” [148] and later specified from least to most severe as Types I, II and III [149]. The optical microscope images from Figure 4.18 do not provide a clear indication as to which wear type is most relatable to the wear observed in this study. This is partially due to a lack of large-scale observable flaking, which would constitute critical material failure in this study. Furthermore, the generated wear particles would need to be chemically analyzed to determine their composition, i.e. if they are purely metallic or partially oxidic.

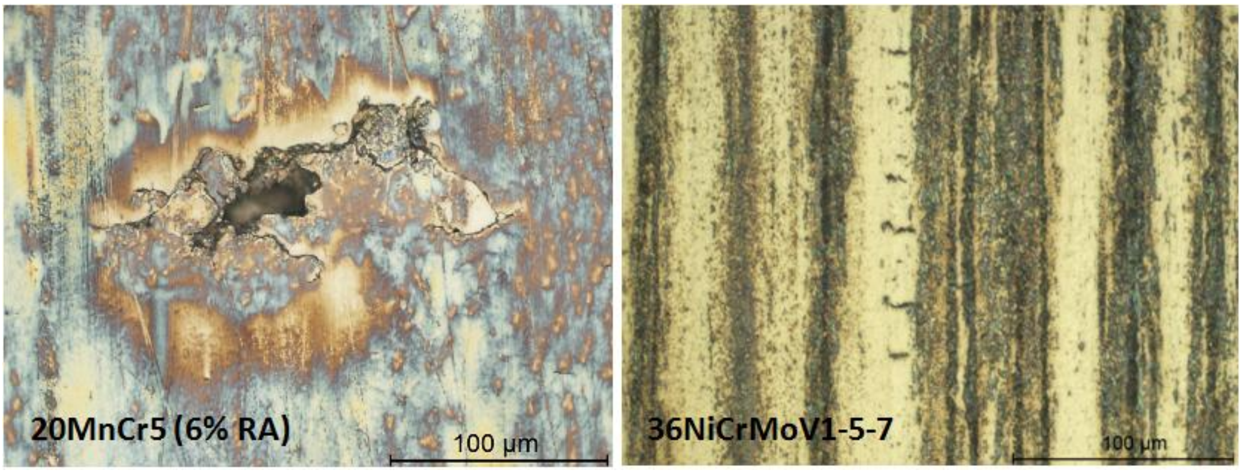

Figure 4.19: Optical microscope images of damaged surfaces of cylindrical samples after 10^7 load cycles of slip-rolling endurance testing at P_{0Mean} =1.94 GPa (P_{0Max} = 2.91 GPa, F_N = 2,000 N) and T = +120 °C in BMW FF SAE 0W-30 VP1, ACEA A3/B4, dynamic viscosity at +120 °C = 5.33 mPa·s.

Coefficients of friction from directly before the end of slip-rolling endurance testing up to P_{0Mean} = 2.62 GPa (P_{0Max} = 3.92 GPa, F_N = 5,000 N) are provided in Figure 4.20. As expected, increases in COF were observed with increasing contact pressure. At all load stages, the alternative alloys showed lower friction than 20MnCr5. This difference became less pronounced at higher testing loads, which is commonly observed in many steels, namely that the range in friction above FZG 12 decreases with increasing contact stress [12]. The alloying with molybdenum and silicon reduced the coefficients of friction under mixed/boundary lubrication.

Comparing the friction behaviour of 36NiCrMoV1-5-7 to that of 45SiCrMo6 reveals that the latter generally shows lower friction at the lower testing loads, but that the two materials show essentially equivalent friction behaviour at the higher testing loads. This may be an indication that the improvements in material performance yielded through the enhanced silicon content of 45SiCrMo6 may be limited to lower loading conditions. This is also partially reflected in the wear performance of these steels (see Figure 4.21), though as will be discussed, 45SiCrMo6 still maintains a slight advantage, even at the higher testing loads.

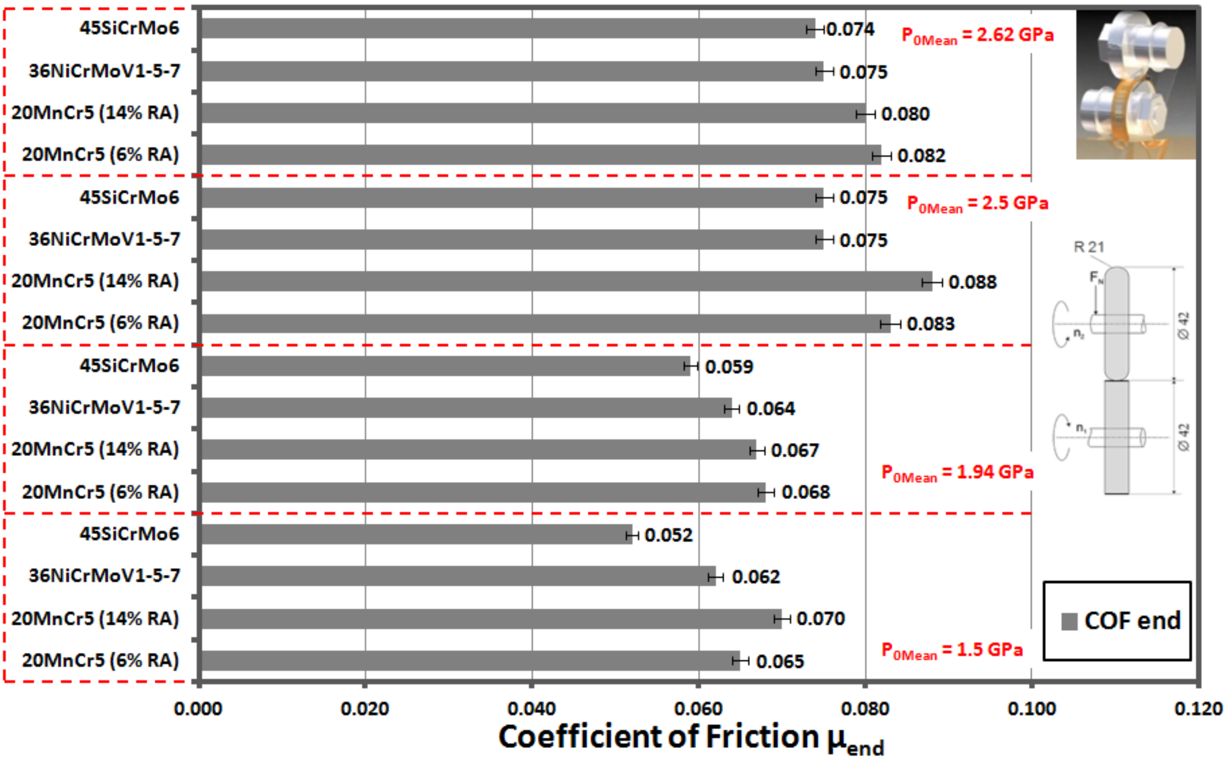

Figure 4.20: Coefficients of friction at the end of slip-rolling testing at T = +120°C in BMW FF SAE 0W-30 VP1, ACEA A3/B4, dynamic viscosity at +120 °C = 5.33 mPa·s.

Profilometric wear coefficients from all slip-rolling testing are provided in Figure 4.21. At both lower testing loads, comparable wear coefficients were determined for all materials. Due to the standard error values determined from repeat testing (a minimum of three separate endurance tests, each spanning approximately 19 days, were conducted for each material), some overlap in wear coefficient values is observed. This can be said for comparison of materials, as well as comparison of loads. It can also be observed that the spherical counterbodies showed very similar amounts of wear to the cylindrical sample bodies. This serves to indicate that no significant distortion of the counterbody geometry occurred with respect to the mechanically finished radius of curvature. Reducing material distortion is very important for improved material performance in many real-world applications. Automobile component contacts, many of which are well-simulated by this form of twin disk testing, are a prominent example.

The most significant observation from baseline testing is that the case-hardened 20MnCr5 did not appear to deliver significantly better wear performance than the alternative alloys, neither of which are case-hardened. Indeed, the k_v values of 20MnCr5 and 45SiCrMo6 are nearly identical at the lower testing loads. This held true even at P_{0Mean} = 2.5 GPa, though the case-hardened 20MnCr5 begins to look more appealing at P_{0Mean} = 2.62 GPa. 36NiCrMoV1-5-7 showed a slight tendency toward higher wear than the other two steels, though the difference is nearly negligible, particularly in the context of mixed/boundary lubrication. Metallographic considerations also provide some explanation as to the slight differences in wear performance. Most notably, 36NiCrMoV1-5-7 has slightly higher populations of non-metallic inclusions, previously described. In light of the slightly more heterogeneous microstructural arrangement of 36NiCrMoV1-5-7, less consistent wear performance can be expected. Case-hardening was likely the most influential factor in the strong wear performance of 20MnCr5, even at higher loads, while the silicon alloying of 45SiCrMo6 is thought to enhance its tendency towards work hardening, yielding competitive wear performance even at the most extreme testing load.

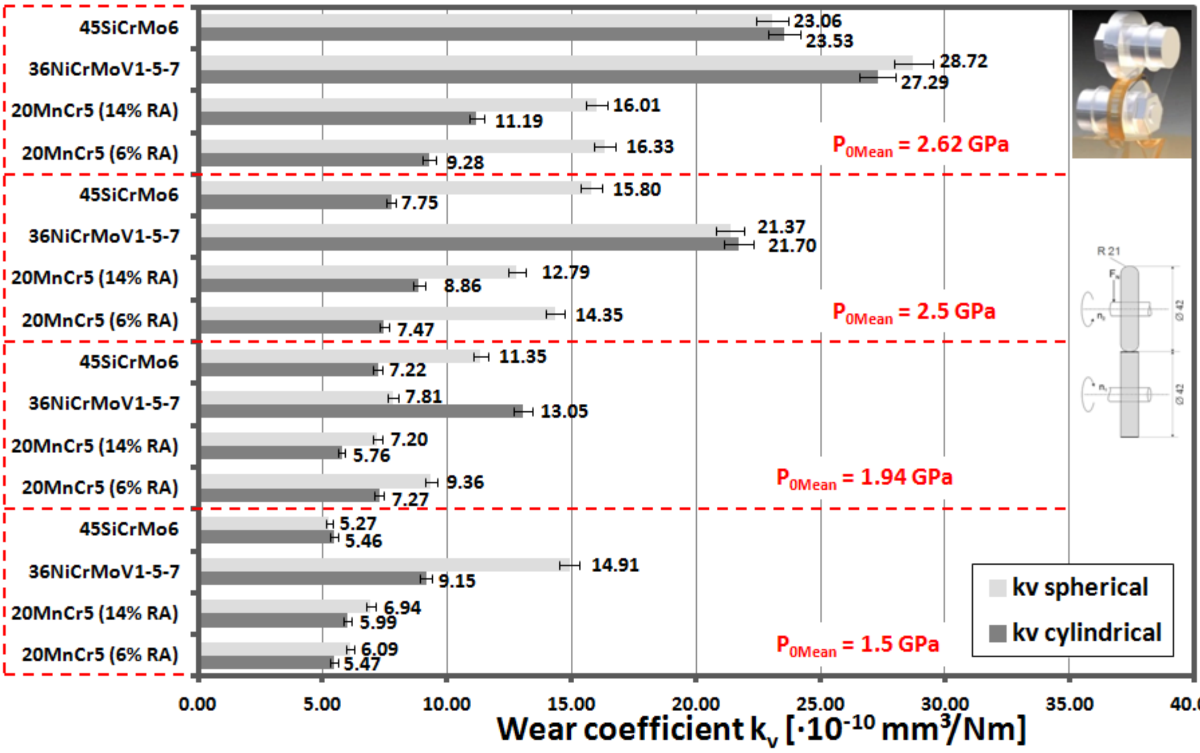

Figure 4.21 Wear coefficients of the spherical and cylindrical disks after slip-rolling testing at T = +120 °C in BMW FF SAE 0W-30 VP1, ACEA A3/B4, dynamic viscosity at +120 °C = 5.33 mPa·s.

Again, it is of great significance that the non-case-hardened steels showed comparable performance to the case-hardened 20MnCr5. Although the high performance steels have a lower initial hardness than the case-hardened 20MnCr5, they still show comparable wear rates. The most concrete explanation is that the measured surface hardness of the samples in the heat-treated state does not account for the aforementioned work hardening processes that can occur in 36NiCrMoV1-5-7 and 45SiCrMo6 and generate increased hardness in the contact zone. Work hardening can be observable through the generation of compressive residual stresses. The compressive stress behaviour of these steels has already been reported by Scholz et al. [113,115]. So-called dislocation hardening, in conjunction with plastic deformation, is of particular relevance, where the resistance to dislocation becomes more pronounced with the increase of dislocation density [70].

Changes in hardness due to loading, however, are also measureable. In Figure 4.22, hardness profiles of 45SiCrMo6 after slip-rolling endurance testing at P_{0Mean} = 1.94 GPa, both from the surface into the bulk and across the loaded contact surface, are provided. A strong increase in hardness at and directly beneath the contact zone is clearly observable, and is strongest directly in centre of contact, where the generated contact pressure is greatest. The optical image provided shows a brightening in colour of this area to an off-white. This is still relatively difficult to observe and has therefore been outlined. The SEM image was taken from 350 µm below the surface, inside the contact zone. In comparison to the previously shown image in Figure 4.2, the overall martensitic character becomes somewhat more uniform, lacking the larger ferritic plates observed in the heat-treated state. In other words, the overall structuring appears to be more refined.

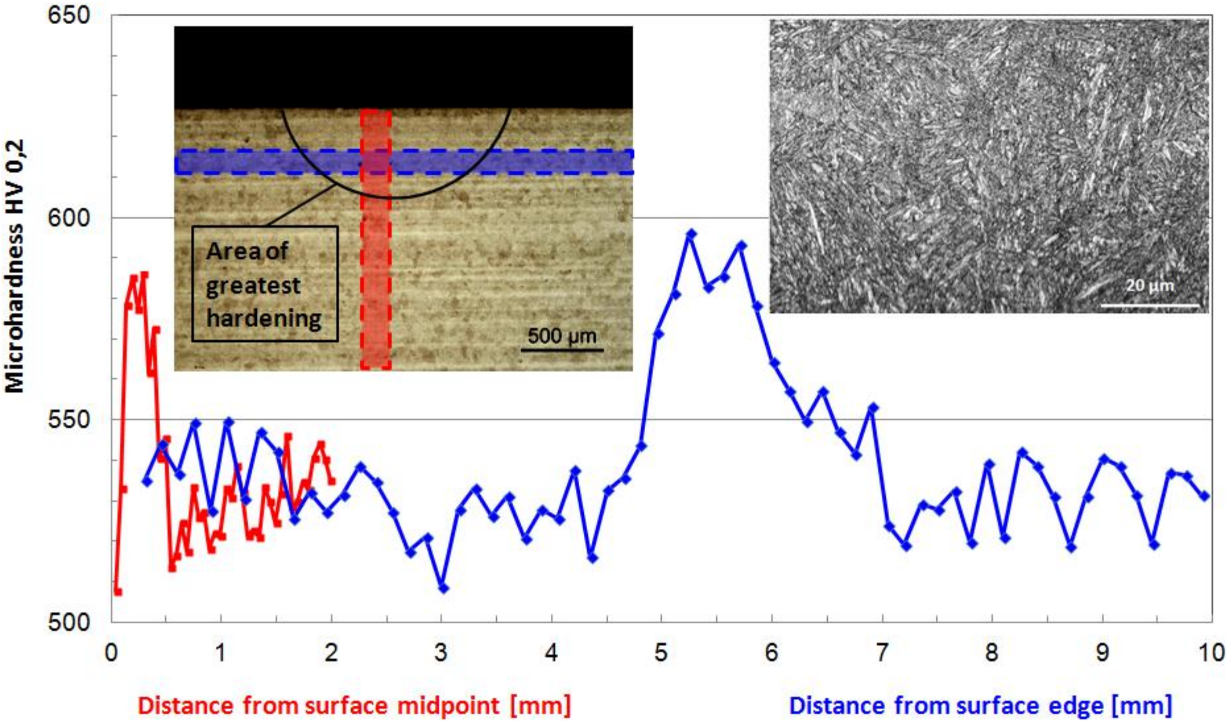

Figure 4.22: Micro-hardness profiles of untreated 45SiCrMo6 after slip-rolling testing at P_{0Mean} = 1.94 GPa (P_{0Max} = 2.91 GPa, F_N = 2,000 N) and T = +120 °C in BMW FF SAE 0W-30 VP1, ACEA A3/B4, whereby dynamic viscosity at +120 °C = 5.33 mPa·s, with corresponding optical microscope and SEM images.

4.4.2 Slip-Rolling Friction and Wear Resistance of Cold Work Hardened Surface Substrates

Slip-rolling testing was carried out on samples with cold work hardened surface substrates, all of which were generated at P_{0Mean} = 2.5 GPa within 10,000 cycles in the finishing process. Again, only the cylindrical samples were pre-conditioned, while the spherical specimen remained untreated and tested as self-mated couples alloywise. Coefficients of friction from the end of endurance testing and profilemetric wear coefficients were obtained for both cold work hardened samples, as well as for untreated baseline samples. These results for 20MnCr5 are given in Figure 4.23. Results for the non-case-hardened steels are not available, as these steels experienced premature critical surface failure during endurance testing. Cold work hardening does not to appear to have contributed to any significant improvement in the frictional behaviour of 20MnCr5. The COF values from the end of endurance testing are nearly identical for the work hardened samples compared to the untreated steel. An improvement in wear performance, however, after cold work hardening was observed in all 20MnCr5 samples, particularly with 14% residual austenite, which yielded a reduction of wear by over 80% for the cylindrical sample. Neither the pre-conditioned samples nor the counterbodies run against them in endurance testing showed any clear increases in wear. The pitting failures experienced by the non-case-hardened steels were eventually replicated in 20MnCr5 at higher contact loads. The indication is that the conditions of the cold work hardening treatment applied were too severe for these steels. It was, therefore, deemed necessary to optimize the parameters applied in this particular pre-conditioning regime. The differences in wear resistance between 20MnCr5 and the alternative alloys, after cold work hardening, is a result of the case hardening of 20MnCr5. This is discussed in greater detail later in this section.

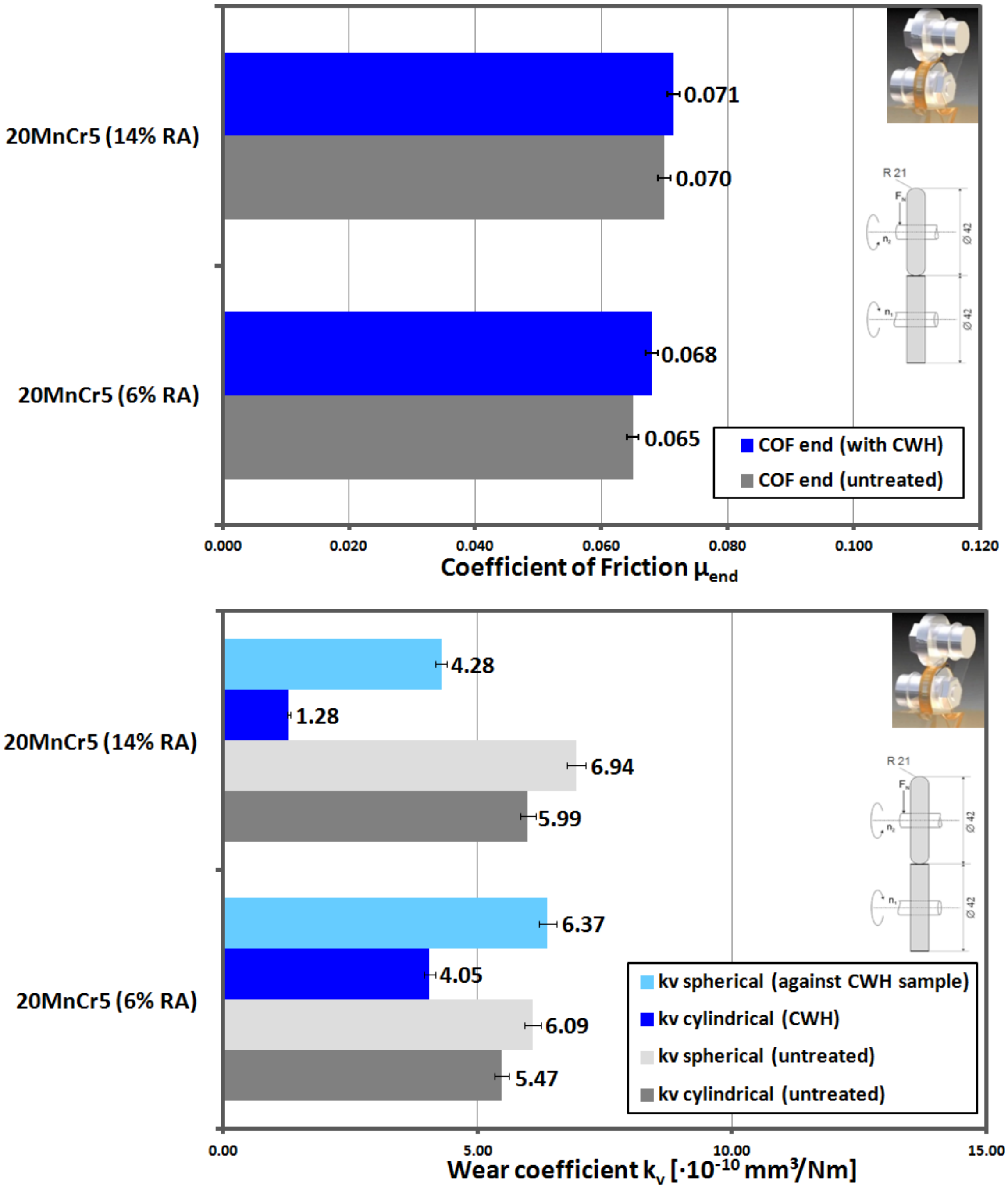

Figure 4.23: COF values at end of and k_v values after 2Disk slip-rolling testing for case-hardened and cold work hardened 20MnCr5 (1.7147) up to 10,000,000 cycles at P_{0Mean} = 1.5 GPa (P_{0Max} = 2.25 GPa, F_N = 930 N) and T = +120°C in BMW FF SAE 0W-30 VP1, ACEA A3/B4, whereby dynamic viscosity at +120 °C = 5.33 mPa·s.

Residual stress depth profiles of 20MnCr5 after cold work hardening, and additionally, cold work hardening and slip-rolling endurance testing at P_{0Mean} = 1.5 GPa are provided in Figure 4.24. Comparing these new profiles to the profiles of cold work hardened 20MnCr5 before endurance testing (also see Figure 4.5), it can be determined that the compressive residual stresses generated during pre-conditioning are, essentially, stable. A slight decrease in the depth of the maxima can be observed, as well as a decrease in the magnitude of these maxima to less than 1000 MPa, compared to the previously observed maxima of nearly 1200 MPa.

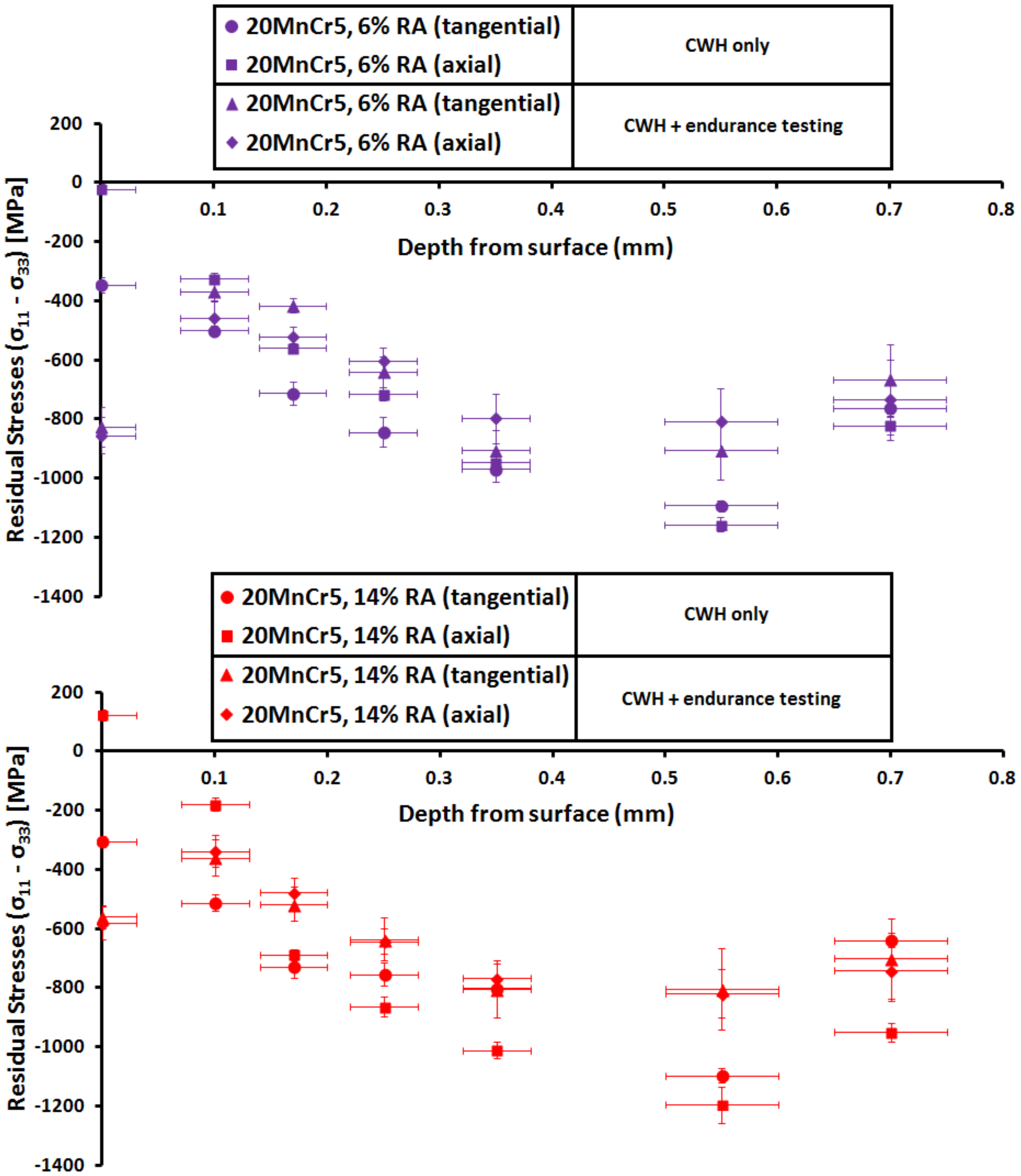

Figure 4.24: Residual stress depth profiles (calculated using the sin$^2\psi$ method) for 20MnCr5 after cold work hardening, and additionally, cold work hardening and slip-rolling endurance testing (endurance testing at P_{0Mean} = 1.5 GPa, P_{0Max} = 2.25 GPa, F_N = 930 N.

The indication is that there is still room to optimize the depth of the compressive stress maxima, as a reduction of the previously introduced compressive residual stresses through unavoidable shear stresses is observed. Ultimately, the goal is to optimize pre-conditioning so that the compressive residual stress maxima lie in the same area as the expected shear stress maxima to counteract shearing effects that can lead to increased wear.

Surface profiles of a cylindrical sample of cold work hardened 45SiCrMo6 and of an untreated spherical sample are provided in Figure 4.25, along with an optical image of the damaged surface of the spherical sample after critical failure during slip-rolling endurance testing. The surface profiles are arranged in the contact that occurred at the start of endurance testing. It immediately becomes apparent that the intensity of the work hardening procedure led to extreme deformation of the surface of the cylindrical sample. The new surface geometry results in point contacts at the edges of the work hardened area, rather than at the midpoint of the spherical sample. Consequently, contact pressure extremes arise at these points of contact, while at the same time a significant portion of the centre of the samples do not experience any contact at all. The result of such a distribution of contact between the samples is clear from the optical image, where the zones of contact pressure extremes experience premature critical material failure, while the mid-sections that experienced no contact, reasonably, experienced no wear.

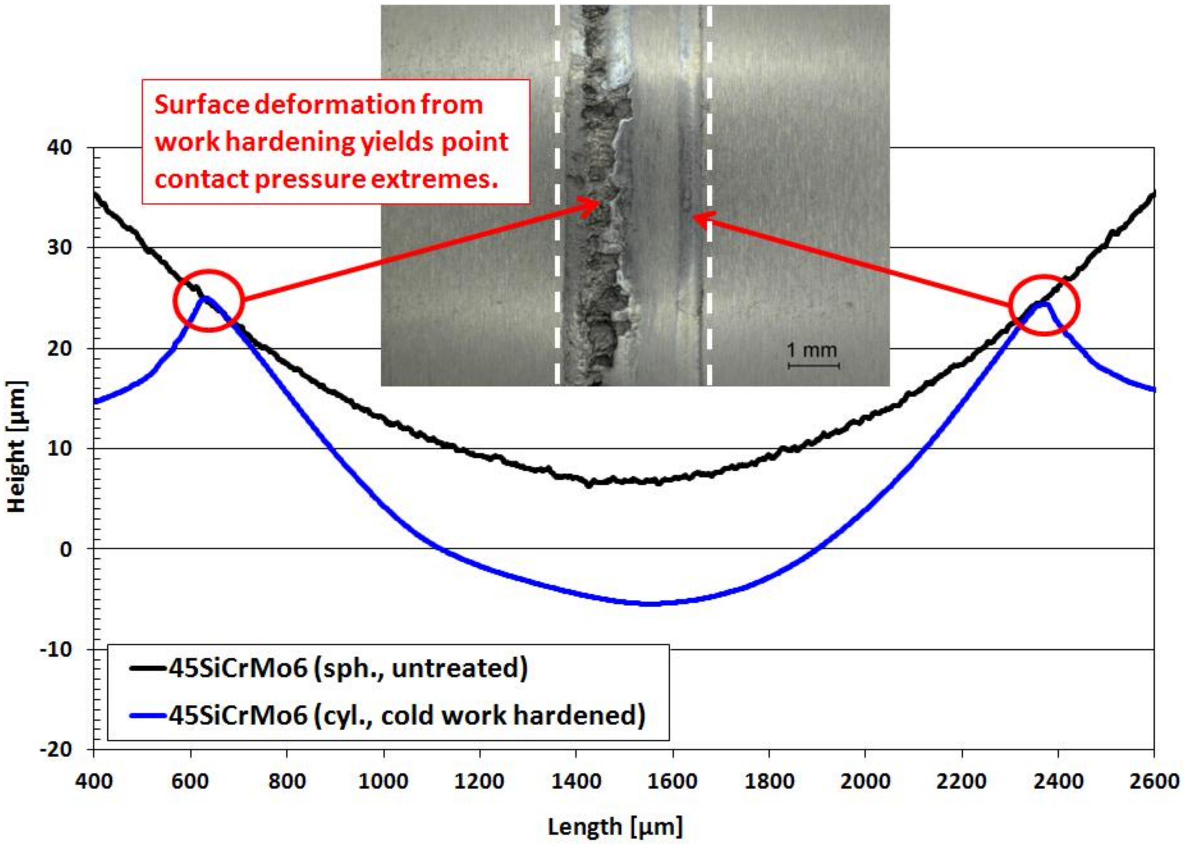

Figure 4.25: Comparison of surface profiles from cold work hardened (using WC-roller with R_{WC} = 6 mm) cylindrical sample of 45SiCrMo6 vs. untreated spherical sample, with optical image of premature critical material failure on spherical sample during slip-rolling endurance testing at (before surface deformation) P_{0Mean} = 1.5 GPa (P_{0Max} = 2.25 GPa, F_N = 930 N) and T = +120°C in BMW FF SAE 0W-30 VP1, ACEA A3/B4, dynamic viscosity at +120 °C = 5.33 mPa·s.

It is important that pre-conditioning of the steels does not result in material damage before what would be normal operation of the component. Such extreme surface deformation may be seen as material damage, particularly due to the fact that it led to premature critical failure of the non-case-hardened steels in endurance testing. Case-hardened 20MnCr5 did not experience such extreme surface deformation during work hardening due to the surface layer that is already significantly harder from case hardening alone. This is observable in previously provided hardness profiles of all tested alloys in the finished state. Even after cold work hardening of the alternative alloys, the maximum hardness values reached in the centre of the contact zone for these steels are barely greater than 600 HV, while the surface hardness of case-hardened 20MnCr5 is well over 700 HV, even before any cold work hardening is induced. Simply put, the alternative alloys are notably softer than the case-hardened 20MnCr5. Therefore it is important to consider the initial material hardness, as well as propensity towards material deformation, before applying the conditions for a pre-conditioning regime based on cold work hardening. In this respect, it is clear that the conditions for work hardening, particularly of the non-case-hardened steels, need to be optimized to avoid excessive surface deformation and losses in geometrical integrity.

4.4.3 Slip-Rolling Friction and Wear Resistance of Optimized Cold Work Hardened Surface Substrates

The parameter adjustments for optimized cold work hardening have been described at the end of section 4.2.3. These parameters include changes to the curvature of the hard metal roller used (increased WC-roller radius), lubricant temperature, rotational speed and, consequently, duration of pre-conditioning. The effect that these adjustments have had on the resulting wear and friction during endurance testing is visibly dramatic. Optical microscope images of the sample and counterbody surfaces are provided in Figure 4.26.

As the optimized cold work hardening ensured that none of the endurance tested materials experienced critical failure, no strong cracking or pitting was observed. Some minor, superficial cracks may be observed on the surface of 20MnCr5 (14% RA) after endurance testing at P_{0Mean} = 1.5 GPa. Interestingly, this same material showed very little wear at all in the area of the pre-conditioned sample surface at the higher endurance testing load. The extremely low wear coefficient (see Figure 4.30) reported comes as little surprise. Additionally, there appear to be some superficial grooves present on the cylindrical surfaces of 20MnCr5, which are particularly prominent after testing at 2,000 N. These are indicative of some light, though not critical, abrasive wear, and appear darker than the surrounding area as a result of a chemical tribofilm that remains bonded to these surfaces. This tribofilm is generated from the additives, particularly ZDDP, of VP1 when the surfaces are exposed to sufficient contact pressure [155].

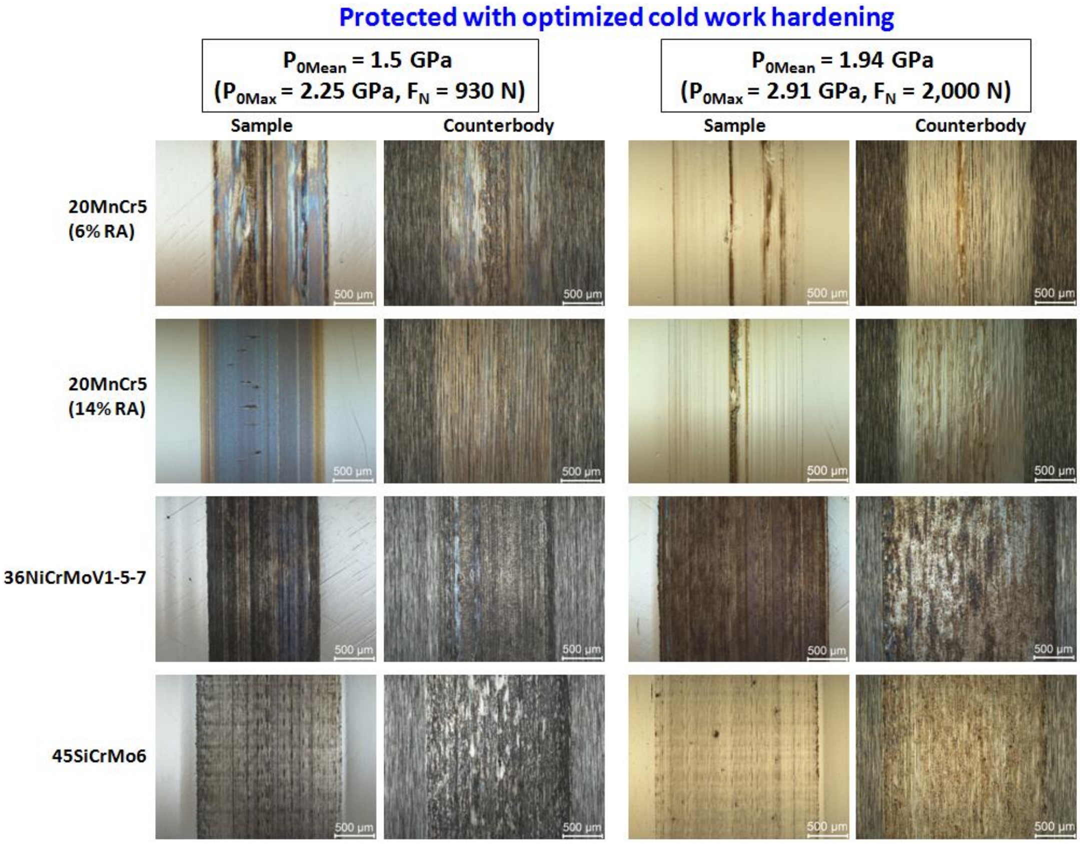

Figure 4.26: Optical microscope images of the wear tracks of the cylindrical samples (with pre-conditioned cold work hardening) and spherical counterbodies after 10^7 load cycles of slip-rolling endurance testing at T = +120 °C in BMW FF SAE 0W-30 VP1, ACEA A3/B4, whereby dynamic viscosity at +120 °C = 5.33 mPa·s.

Both of the non-case-hardened steels showed quite wide wear tracks, especially after exposure to the higher endurance testing load (2,000 N). The deformation of the sample surfaces from pre-conditioning means that a greater proportion of these surfaces come in contact with the spherical counterbodies during endurance testing, however their increased hardness provides them with significantly higher wear resistance. This results in the quite wide, but shallow, wear tracks observed, and ultimately the reduced coefficients of wear, which are calculated on the basis of both the width and the depth of the wear tracks.

SEM investigations of all materials were conducted, both before and after tribological testing. Images of 36NiCrMoV1-5-7 cross sections, i.e. inside the material, from directly below the testing surface, are exemplarily provided in Figure 4.27. It is immediately clear from the image of the material in the finished state that, although it is highly martensitic, with a previously verified residual autenite content of under 2%, it remains somewhat inhomogeneous due to the presence of non-metallic inclusions. It was revealed in a study of this material by Scholz et al. that the inclusions are composed of CaS and alumina-silicates, which are a result of a prior calcium-argon treatment (CAB) [115]. Such non-metallic inclusion populations can have severe consequences for material endurance, as they often act as crack initiators, particularly if they are locally agglomerated directly beneath the stressed surface. The stresses from cyclic tribological contact contribute to crack growth and propagation, which means that these cracks may eventually reach the contact surface and cause pitting or spalling failures. Therefore investigation of both the surface and sub-surface regions of the materials is crucial to detect signs of a tendency towards material failure.

Naturally, there are no such microcracks present in the material in the mechanically finished state. The same holds true for the material after pre-conditioning, which allays fears that the extreme conditions during pre-conditioning, namely use of hard tungsten carbide rollers at P_{0Max} = 3,750 MPa, would cause severe damage of the materials. Most importantly, no subsurface cracks of any kind are visible after endurance testing. Furthermore, non-metallic inclusions are no longer visible after endurance testing, i.e. grain refinement has occurred, which explains why the increase in hardness below the contact zone after pre-conditioning is maintained. Possible grain refinement was already indicated by the whitening of the contact zones presented in Figure 4.11.

Again, white etchings are of particular concern when non-metallic inclusions, such as those observed in 36NiCrMoV1-5-7, are present. The description of the development of white etchings, offered by Schlicht et al., is applicable here [150]. Elastic energy becomes concentrated within non-metallic inclusions when they are exposed to cyclic stressing. As cyclic stressing of the inclusions continues, this concentrated energy is exerted by the inclusions on the material surrounding the inclusions in the form of shear and tensile stresses. These stresses can lead to the initiation of cracks, which may then propagate in the direction of the main shear stress.

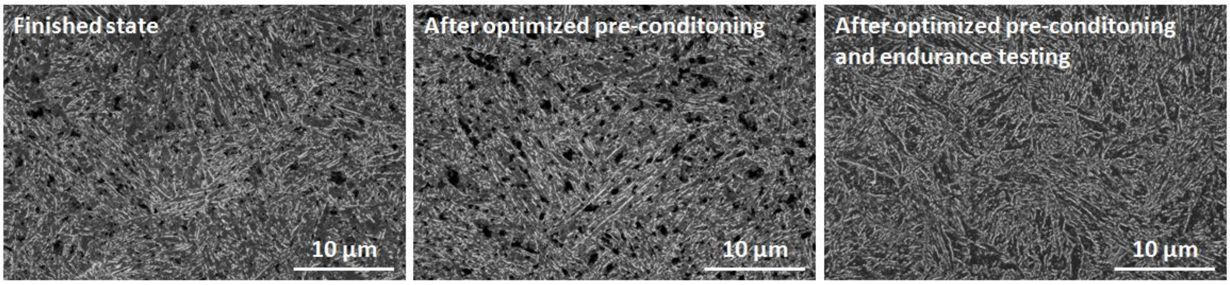

Figure 4.27: SEM images of cross sections of 36NiCrMoV1-5-7 contact zones.

The residual stress depth profiles for 20MnCr5 (14% RA) and 36NiCrMoV1-5-7 after optimized cold work hardening, and additionally, cold work hardening and slip-rolling endurance testing are given in Figure 4.28. Generally, an increase in compressive residual stresses with increasing contact pressure was observed at the sample surfaces. This indicates that the materials are still able to undergo some additional work hardening during endurance testing. For 20MnCr5, the compressive stress maximum is located between 400 µm and 550 µm after preconditioning. A slight decrease in this maximum is observed after endurance testing, though the maximum appears to remain relatively stable even after 10^7 cycles. For 36NiCrMoV1-5-7, the profiles for the endurance tested samples decrease to roughly the same level as the profile from optimized cold work hardening only. As previously mentioned, there may be an observable increase in compressive stresses toward a sample depth of 800 µm, but again, measurements to greater sample depths, which are subject to greater statistical error, would be needed to confirm this.

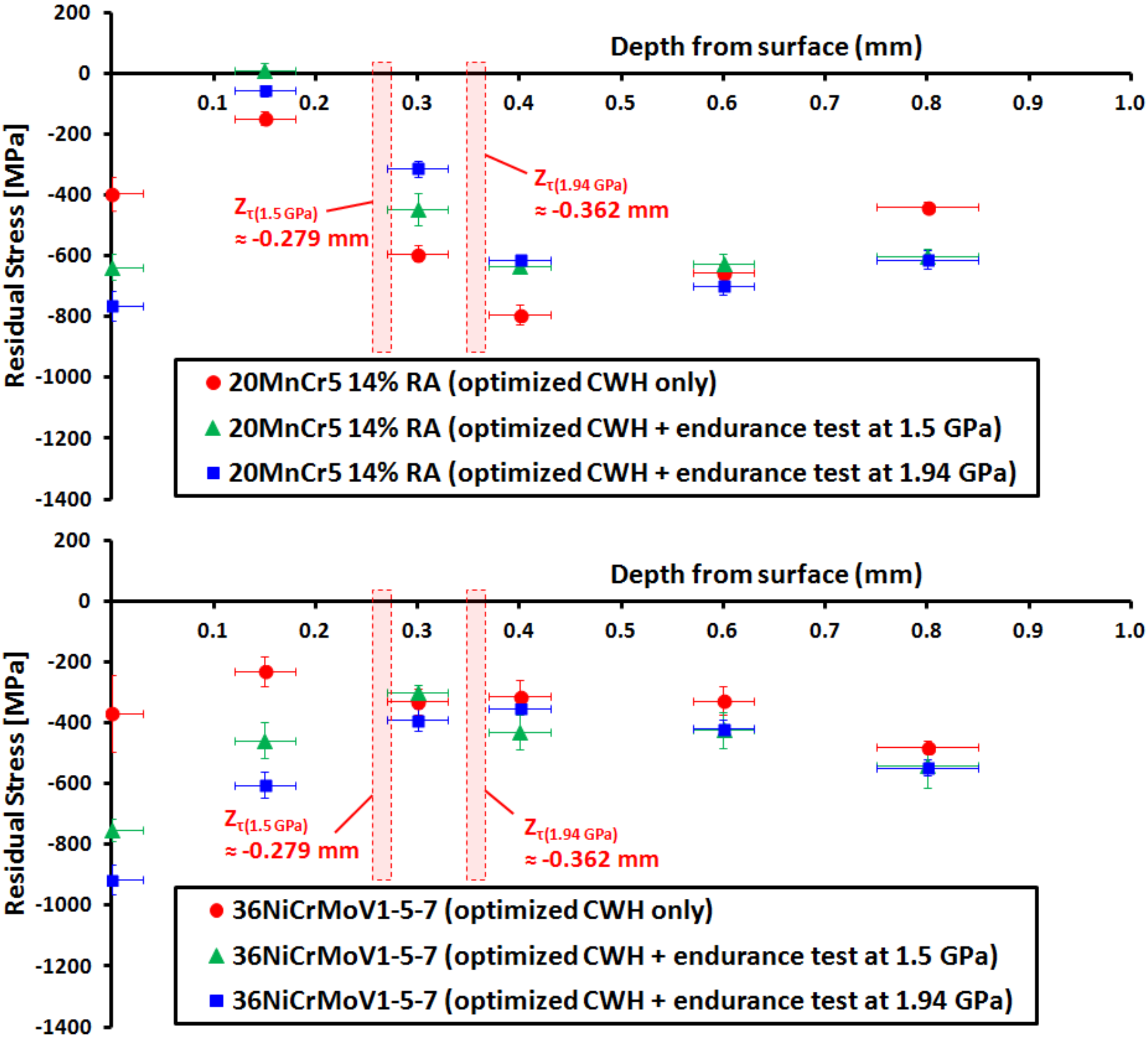

Figure 4.28: Residual stress depth profiles (calculated using the $\sin^2\psi$ method) for 20MnCr5 (14% RA) and 36NiCrMoV1-5-7 after optimized cold work hardening, and additionally, optimized CWH and slip-rolling endurance testing at both P_{0Mean} = 1.5 GPa (P_{0Max} = 2.25 GPa, F_N = 930 N) and P_{0Mean} = 1.94 GPa (P_{0Max} = 2.91 GPa, F_N = 2,000 N); approximated shear stress maxima are marked Z_τ.

It was previously stated that a worthwhile goal would be to optimize pre-conditioning so that the compressive residual stress maxima lie in the same area as the expected shear stress maxima. The purpose of this is to counteract shearing effects, particularly in the case of repeated cyclic stressing that occurs during rolling contact, which can lead to increased wear or even pitting failures. The depth of the shear stress maximum is dependent on the applied contact pressure and can be approximated according to the shear stress hypothesis, developed by Henri Tresca in 1864 [113]. The approximated depths of shear stress maxima for endurance testing at both P_{0Mean} = 1.5 GPa ($Z_{\tau(1.5GPa)}$) and P_{0Mean} = 1.94 GPa ($Z_{\tau(1.94GPa)}$) are also given in Figure 4.28. It is observed that the depths of the compressive residual stress maxima correspond more closely to the depths of the shear stress maxima compared to before optimization of pre-conditioning. However, there is still room for further optimization of the compressive residual stresses to align these maxima more closely with the shear stress maxima. Notably, the optimal depth of the compressive stress maximum is dependent on what contact pressure is eventually implemented during endurance testing, i.e. endurance testing at higher loads would call for compressive residual stress maxima at greater depths to counteract the shear stress maxima.

Figure 4.29 shows that sweeping reductions in friction were achieved. The results for the non-case-hardened steels are most impressive, whereby cold work hardened 45SiCrMo6 was able to achieve the lowest COF value at 0.039 at the testing load 930 N. Furthermore, increasing the testing load to 2,000 N did not result in a significant increase in COF. The particular significance of these strong COF reductions is that these appear to be in the same range as even DLC coated slip-rolling alloys, i.e. DLC vs. DLC contact [113]. Case-hardened 20MnCr5 also showed verifiable reductions in COF after cold work hardening, though it was not able to reach the same reduced level as the alternative alloys.

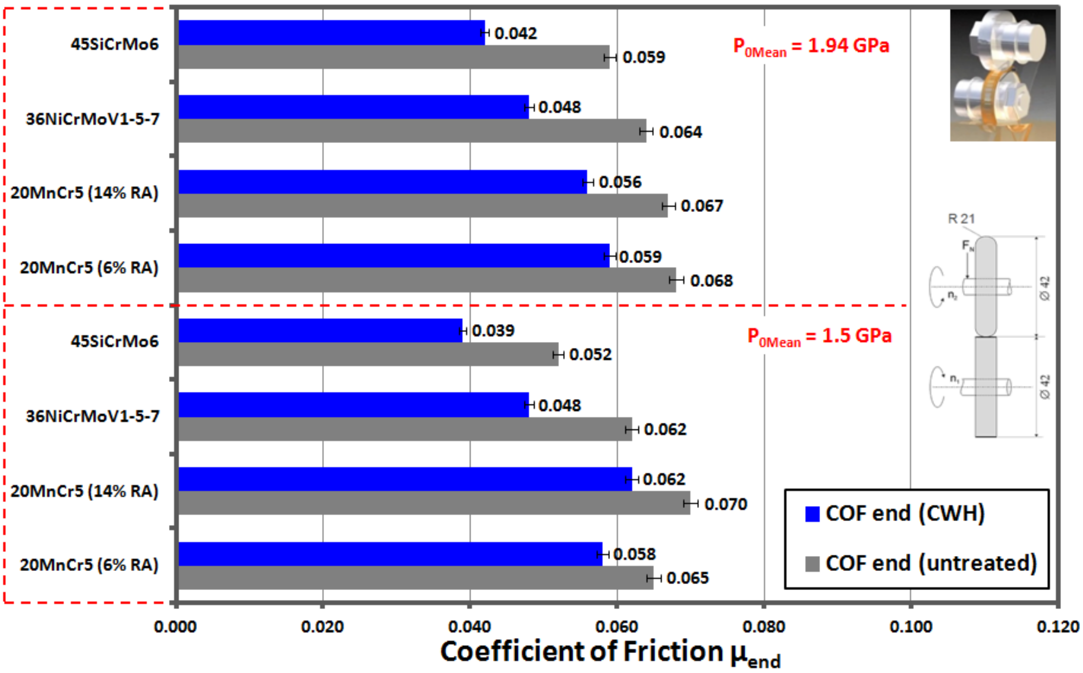

Figure 4.29: Coefficients of friction at the end of slip-rolling testing of samples, cold work hardened under optimized conditions, up to 10,000,000 cycles at T = +120°C in BMW FF SAE 0W-30 VP1, ACEA A3/B4, dynamic viscosity at 120 °C = 5.33 mPa·s.

Previous attempts, such as by Mikhin and Lyapin, to define the dependence of these properties on each other appear to be insufficient for a modern understanding of the material processes involved in friction reductions from work hardening [151]. Their explanation of the friction of solid contacts, in the case of mixed/boundary lubrication, is that friction governed primarily by the processes which occur at the points that are actually in contact. Due to this contact at discreet points, the forces with which the bodies of the contact pair interact consist of elementary forces acting at these individual points. The elementary force depends on the nature and degree of deformation of the material at the contact point. Therefore the coefficient of friction, which is ultimately a function of the ratio of the friction force to the normal load, will also depend on these parameters, i.e. deformation. At the same time, some parts of one of the contacting bodies usually penetrate into the other body. This penetration results from the inhomogeneity of the mechanical properties of the contact zones and from the different profiles of the contacting bodies in the case in which both bodies are of the same material. Even when materials having the same mechanical properties but different geometric profiles are in contact, some parts of one element penetrate into the other. Therefore the adhesive component of the friction force depends on the mechanical properties of the materials in contact.

Friction reductions in lubricated systems result from increases in the elastic modulus of the contacting materials, i.e. the alloys, or as a result of reduced operational surface roughness from the “wearing away” of asperities (or, as the case may be, both). Whether work hardening occurs from martensitic transformations of available residual austenite or from grain refinement, the microstructural composition of the material will change, generating increased hardness that hinders the flow of material under shearing, leading to the decrease in elasticity. Consequently, this helps to counteract changes to the smoothened surface topography, thereby keeping friction minimal. Investigations by Kim and Johnson concluded that martensitic transformations induced by induction hardening results in a lowering of shear, Young, and bulk moduli, and a raising of the Poisson ratio [152]. Furthermore, they stated that since martensite has a greater concentration of interstitial carbon, the interstitially-induced increase in lattice volume again contributes to the reduction in moduli. Additionally, much higher concentrations of dislocations in martensite also may cause a significant reduction in moduli through reversible dislocation bowing. In light of this, the following factors may be considered as having contributed to reductions in friction after pre-conditioned work hardening:

1. Increases in static strength of the material in the contact zone near the contact surface.
2. Amorphization of the uppermost surface layers.
3. Grain refinement, as previously discussed.

The possibility of amorphization of the uppermost surface layers, likely to a depth of no more than two or three atomic layers, is particularly interesting. Investigations by Bull and Page, for example, involved the evaluation of the friction behaviour of ion-implanted sapphire in contact with diamond cones and spheres of a range of materials [153]. They showed that the enhanced amorphization of surface layers led to reductions in the coefficient of friction during single-pass scratch testing. More recent literature evaluations showed how analogous work hardening techniques, eg. high-energy shot peening (HESP), can be applied to yield concrete friction reductions through the generation of nanocrystalline surface layers [154]. It is also possible to yield friction reductions through the generation of chemically reactive tribofilms, which has been evaluated in previously published work and will be discussed in section 4.4.4 [155].

Significant improvements in wear performance were also achieved through optimized, pre-conditioned cold work hardening. The profilometric wear coefficient comparisons between untreated and cold work hardened sample pairs, given in Figure 4.30, exemplify the benefits of mechanical pre-conditioning. Strong reductions in wear were observed in all cases. In some instances, wear reductions to below 1/10 of the original value from the untreated steel were observed. At the lower testing load of 930 N, 20MnCr5 with 14% residual austenite appeared to show the strongest relative wear reduction from cold work hardening, though 36NiCrMoV1-5-7 also showed a strong relative reduction. This resulted in 36NiCrMoV1-5-7 achieving a wear rate essentially equal to 45SiCrMo6. At the higher testing load of 2,000 N, 36NiCrMoV1-5-7 again achieved a strong wear reduction from cold work hardening, though still showed a higher wear rate than either 45SiCrMo6 or 20MnCr5. Variations in wear rate due to residual austenite in 20MnCr5 were only apparent in the untreated counterbodies. It is, however, noteworthy that reductions in wear were achieved, not just for the cold work hardened samples, but also the untreated counterbodies. The simultaneous increase in both hardness and toughness from the work hardening offers a clear explanation of the observed wear rates. Most importantly, comparison of the case-hardened reference steels to the non-case-hardened high performance steels shows equivalent or, as the case may be, better friction and wear performance through pre-conditioning for the latter materials, in spite of having forgone carburization. Therefore the conclusion is drawn that, with careful selection of proper metallurgies, technically simple pre-conditioning methods used to induce work hardening may be able to replace classical strategies, particularly case-hardening, which is expensive, time-consuming and energy-inefficient.

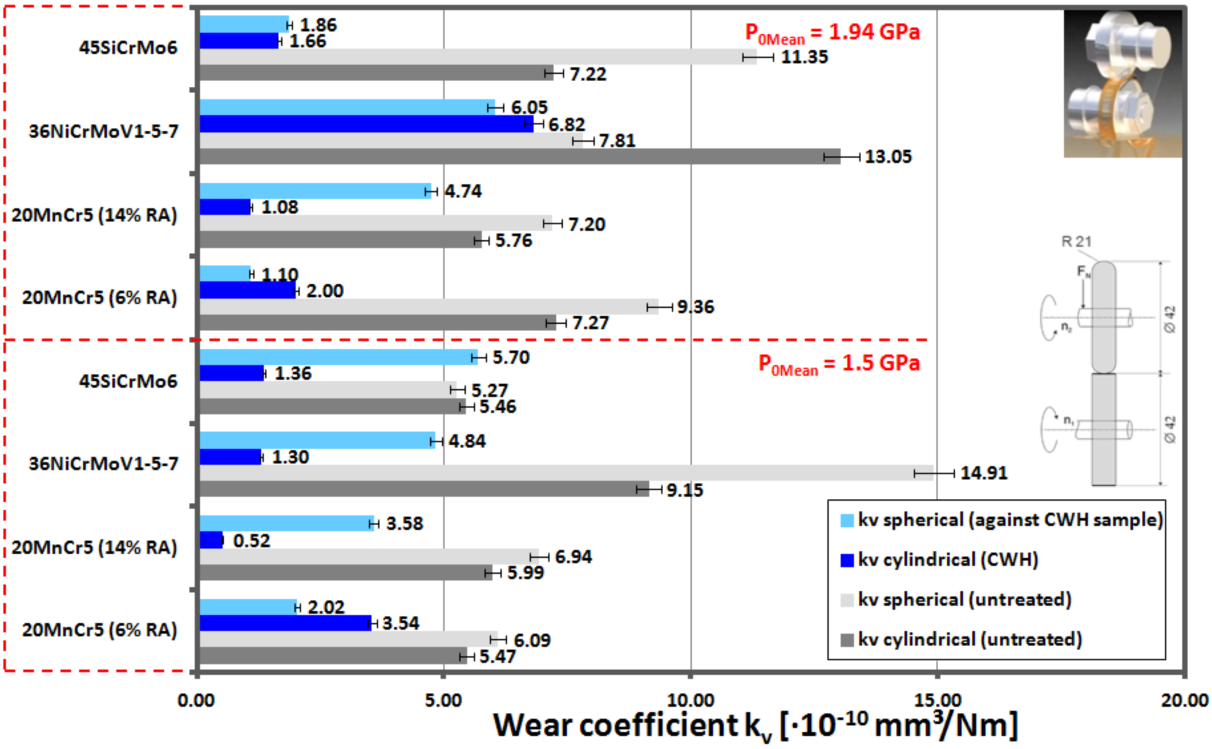

Figure 4.30: Wear rates of the spherical and cylindrical disks, cold work hardened under optimized conditions, after slip-rolling endurance testing at T = +120 °C in BMW FF SAE 0W-30 VP1, ACEA A3/B4, whereby dynamic viscosity at 120 °C = 5.33 mPa·s.

4.4.4 Slip-Rolling Friction and Wear Resistance of Tribofilm-Protected Surface Substrates

All materials subjected to slip-rolling endurance testing, both with and without reactive tribofilms were able to reach 10^7 cycles without experiencing critical surface material failure. Optical microscope images of tribofilm-protected sample and counterbody surfaces after endurance testing are provided in Figure 4.31.

As observed in the images of the disks after endurance testing, wear can only be observed in the wear track, which was created by the points of contact. It is noted that the scuffing pictured on 20MnCr5 (6% RA) to the right of the wear track in the first image is not from endurance testing, but rather a sample processing error that occurred after testing. Neither scuffing nor pitting phenomena can be observed from either the lower or higher applied testing load, though a slight increase in the width of the wear tracks is observed at the higher testing load. Furthermore, no superficial cracking can be observed in the optical images. Generally, all materials showed comparable wear track widths, however these widths tend to increase with testing load.

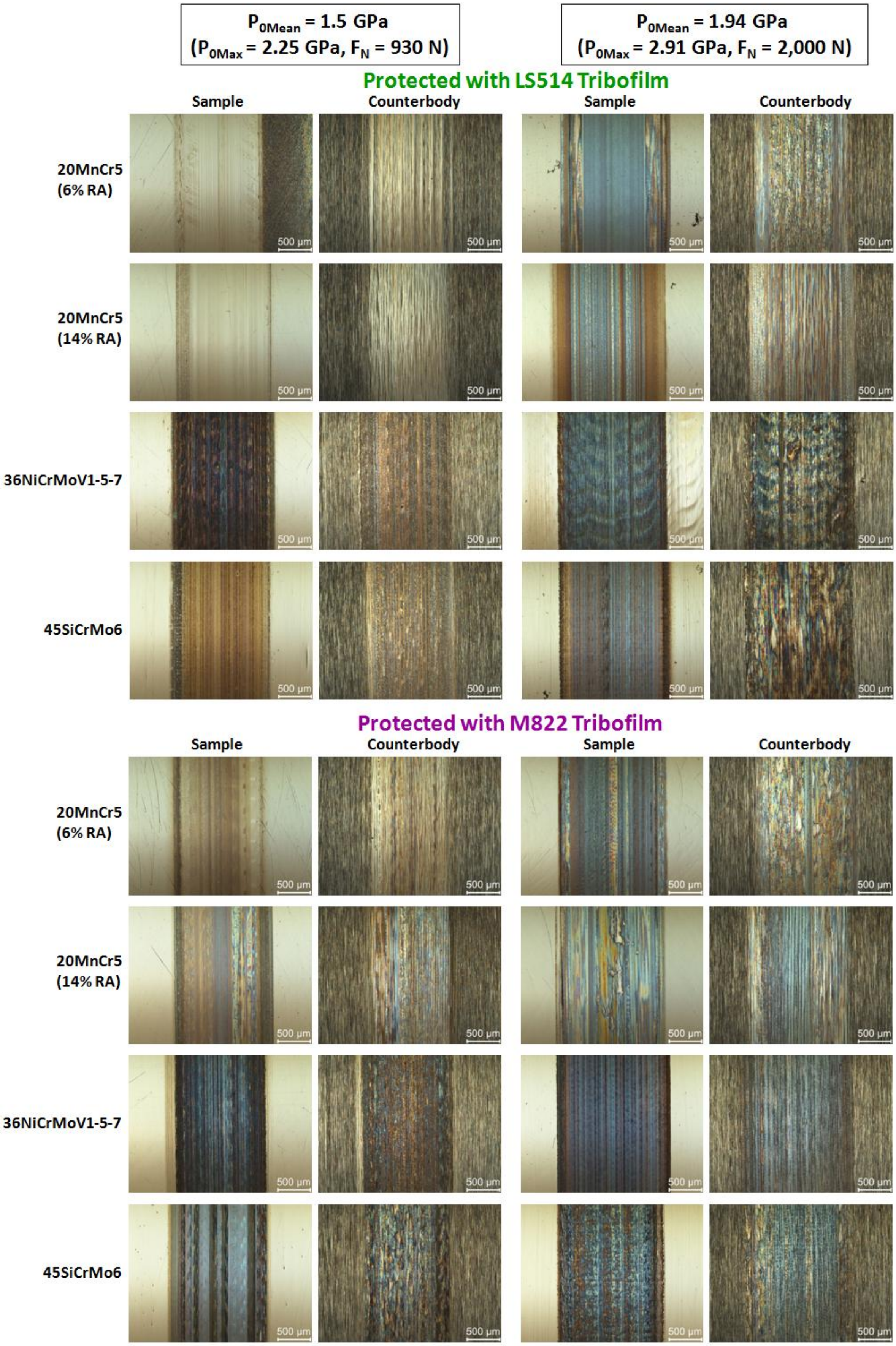

Figure 4.31: Optical microscope images of the contact surfaces of the cylindrical samples (with pre-conditioned tribofilm) and spherical counterbodies after 10^7 load cycles of slip-rolling endurance testing at T = +120 °C in BMW FF SAE 0W-30 VP1, ACEA A3/B4, dynamic viscosity at +120 °C = 5.33 mPa·s.

Ultimately, the optical images show wear tracks that are very similar to those from the untreated alloys. The wear protection offered by the pre-conditioned tribofilms is naturally greatest at the beginning of endurance testing. As mechanical wear of the pre-conditioned tribofilms begins to set in, other processes begin to take place, which are discussed in greater detail later in this section. SEM investigations were indeed carried out on tribofilm-protected samples after slip-rolling endurance testing, though these investigations focused primarily on the effects of tribological contact on tribofilm stability and composition, rather than subsurface microstructures, which have already been discussed in some detail.

Coefficients of friction from the end of endurance testing are provided in Figure 4.32. Comparison of COF values from tribofilm protected samples to untreated baseline samples shows several singular friction reductions. Particularly tribofilm-protected 36NiCrMoV1-5-7 showed unambiguous friction reductions at both endurance testing loads. The lowest coefficient of friction at the end of endurance testing appears to have been yielded with 45SiCrMo6, whereby a value of 0.036 at P_{0Mean} = 1.5 GPa is well within the range DLC-coated equivalent materials [113]. It is also important to note that no significant increases in friction as a result of tribofilm generation during pre-conditioning were observed. On the other hand, the reductions in coefficients of friction through a tribofilm formation are more linked to alloys with low residual austenite content, which can be seen for the results for 20MnCr5 with 14% RA.

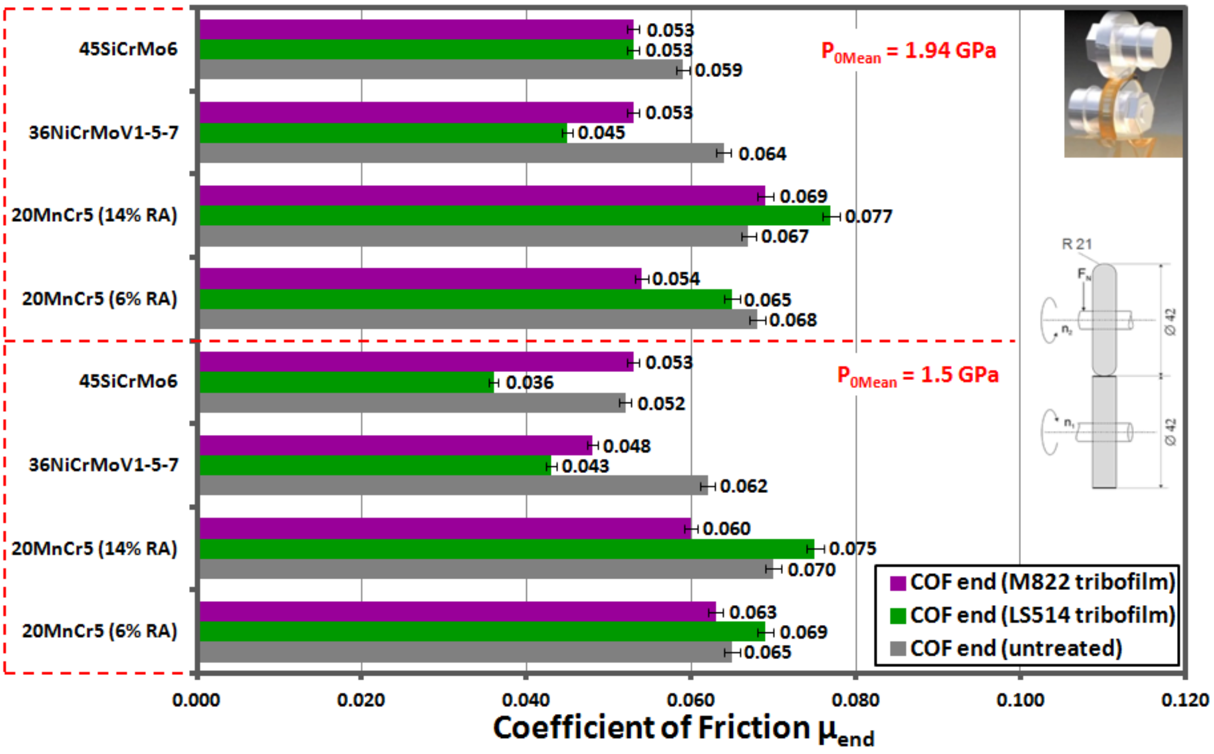

Figure 4.32: Coefficients of friction at the end of slip-rolling testing up to 10,000,000 cycles at T = +120°C in BMW FF SAE 0W-30 VP1, ACEA A3/B4, dynamic viscosity at 120 °C = 5.33 mPa·s.

In the case of LS514, the mechanism of friction reduction through tribofilm formation involves the establishment of a base film containing Fe and CaO, followed by the accumulation of $CaCO_3$ in increasingly thick sheets, i.e. boundary layers. For M822, essentially MoDTC, most literature attributes its friction modification abilities to the formation of sheets of MoS_2 between tribocouple components. The mechanism of the decomposition of MoDTC, proposed by Grossiord et al., has previously been discussed. As was noted by Morina et al., further experimental verification of the mechanism is needed, as the basis of friction modification claims is simply the presence of MoS_2 in tribofilms where friction happens to be reduced [100]. This study focused on the interactions between MoDTC and ZDDP, and what effect these interactions have on the formation and evolution of chemically reactive tribofilms. As the reference testing lubricant VP1 contains ZDDP, these interactions need to be considered carefully, particularly when evaluating results from endurance testing on M822-tribofilm protected alloys.

Important considerations of the interactions between MoDTC and ZDDP regarding tribofilm formation and friction reduction have been made, whereby several literature studies reported that MoDTC on its own is less effective in reducing friction than when used in conjunction with ZDDP [156,157,158]. This may not always be the case however, as seen in Figure 4.33 from the abovementioned study by Morina et al. Testing with only MoDTC additive yielded the lowest coefficient of friction profile, though the addition of ZDDP appeared to add stability. Furthermore, the increase in friction observed with the addition of ZDDP appeared to be rather minor. This may be acceptable for certain applications given the wear reductions that ZDDP can achieve.

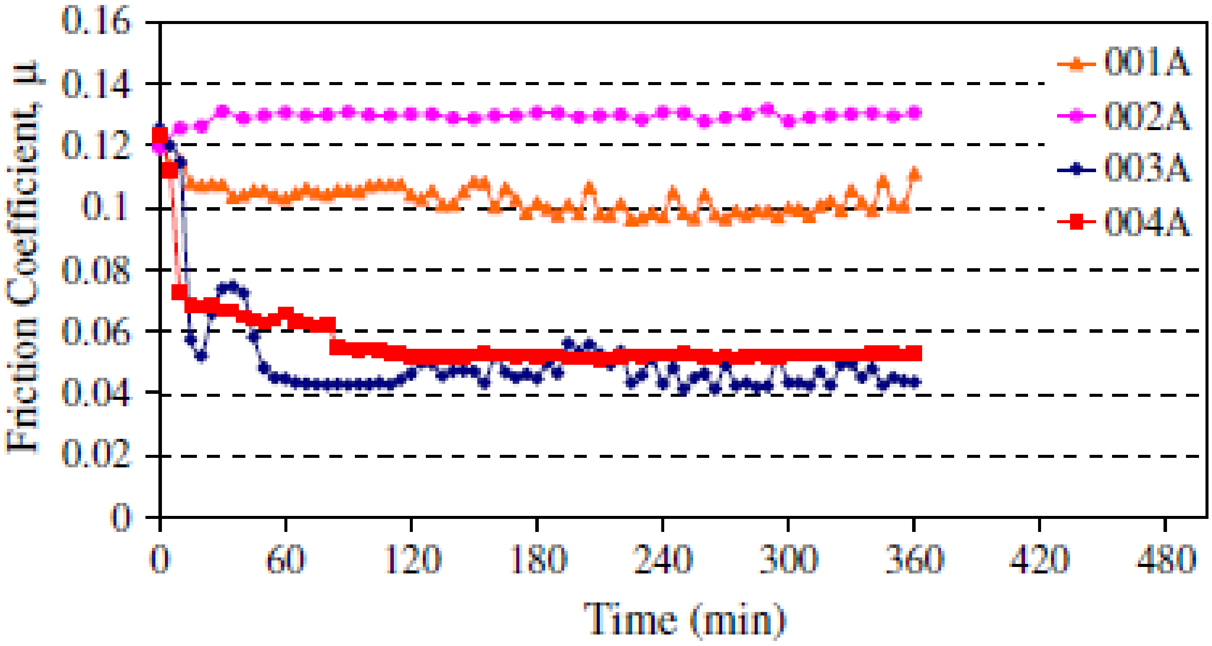

Figure 4.33: LITERATURE: Friction traces from pin on plate tests using lubricants 001A (base oil, no additives), 002A (with ZDDP), 003A (with MoDTC) and 004A (with ZDDP + MoDTC) [100].

Profilometric wear coefficients of all samples and counterbodies, untreated and with protective tribofilms, are provided in Figure 4.34 to allow for comparison between untreated and tribofilm-protected sample pairs. As previously mentioned, untreated sample pairs show, for the most part, comparable wear coefficients at both testing loads. Tribofilm protected pairs, however, show very strong reductions in wear, in some cases with coefficients reduced to below 1/10 (over 90% reduction) of the original value from the untreated steel. These strong reductions are consistent for all materials at both endurance testing loads.

At the lower testing load of 930 N, tribofilm protection of 45SiCrMo6 led to the strongest wear reductions. LS514 and M822 appeared to provide equal enhancement of wear performance in this case. Several interesting comparisons can be made between 36NiCrMoV1-5-7 and 20MnCr5 at this testing load. Firstly, 20MnCr5 still showed better overall wear performance with LS514 tribofilms, but the actual relative reduction in wear from protection with this tribofilm was greater for 36NiCrMoV1-5-7. Secondly, residual austenite does not appear to have been an influential factor in wear performance with the LS514 tribofilm, recalling that 36NiCrMoV1-5-7 has less than 2%. Finally, wear performance improvements, particularly for 36NiCrMoV1-5-7, were strongest with the M822 tribofilm, whereby both non-case-hardened steels were able to show better wear performance than the case-hardened 20MnCr5.

At the higher testing load of 2,000 N, overall wear reductions from tribofilm protection appear to have been even more substantial than at the lower testing load. This is particularly visible in the comparison of the wear coefficients for 20MnCr5. Both tribofilms appear to have provided more or less equal enhancement of wear performance, though M822 may show a slightly more positive effect. The same appears to be true for the non-case-hardened alternative alloys. The tribofilm-protected alternative and non-case-hardened alloys show nearly equal wear performance compared to tribofilm-protected and case-hardened 20MnCr5. More importantly, the relative wear reductions from tribofilm protection were greater for the non-case-hardened alloys than for case-hardened 20MnCr5.

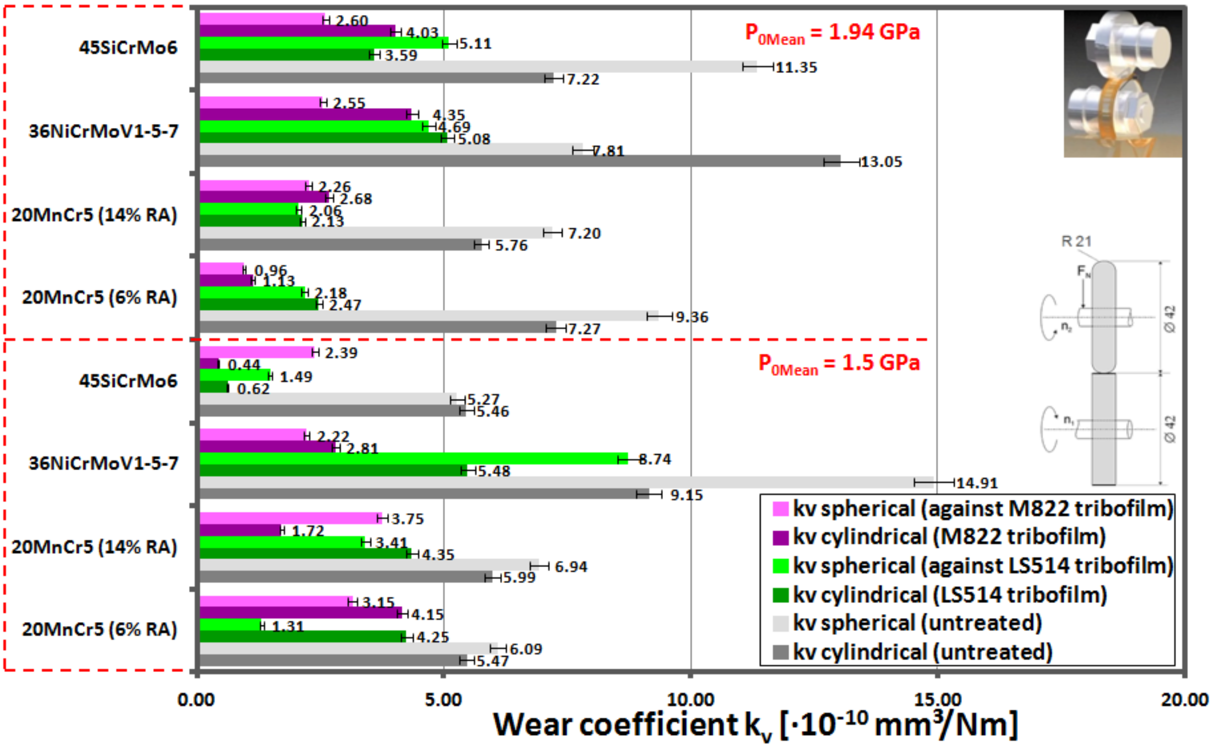

Figure 4.34: Wear rates of the spherical and cylindrical disks, with and without tribofilms after slip-rolling endurance testing at T = +120 °C in BMW FF SAE 0W-30 VP1, ACEA A3/B4, whereby dynamic viscosity at 120 °C = 5.33 mPa·s.

Overall, it is difficult to say definitively which tribofilm was most effective in reducing wear, as all tribofilm-protected pairs show fairly consistent wear coefficients, though M822 appears to yield slightly better wear performance. Particularly any interactions with ZDDP, found in VP1, must be considered. It has been stated in the literature that the efficacy of ZDDPs is retarded through a competition of detergents and dispersants either absorbing on the surface or limiting the interaction between ZDDPs and the metal [159,160,161], both routes resulting in antagonistic behaviour with respect to antiwear performance [162]. Such detergents are predominantly composed of calcium derivatives, such as $CaCO_3$. Therefore such antagonisms between $CaCO_3$ in the LS514 tribofilm and ZDDP would not be unthinkable. This is further substantiated by a study on the interaction of overbased metallic detergents with ZDDP on the formation of tribofilms under boundary lubrication by Wan et al [163]. In this study, calcium phenate and salicylate detergents, in high and low overbased forms, were used in combination with ZDDP. It was found that Ca^{2+} ions are replaced for Zn^{2+} in the polyphosphate structure of tribofilms, forming short chain polyphosphates, ultimately affecting tribological performance.

An important consideration in comparing the observed wear coefficients is whether these wear reductions are exclusively the result of tribofilm protection, or simply the result of the removal of asperities and consequential surface smoothening that would have occurred during normal running-in. For example, Henein et al. studied the wear of cylinder liners and showed that significant smoothening may occur during an engine break-in period of several hours [164]. Furthermore, they showed that the surface roughness, R_a, was reduced from approximately 0.82 µm to 0.60 µm during their chosen three hour break-in period. Referring to Table 3.1, it can be observed that the grinded counterbodies in this study are several times smoother than the samples in the previously referenced study, and the grinded and polished cylindrical samples, on which the tribofilms are generated, are even several orders of magnitude smoother. Furthermore the pre-conditioning step used to generate the tribofilms was carried out to no more than 10^4 cycles, which lasts approximately 25 minutes. The initial smoothness of the machined disks and the short duration of pre-conditioning resulted in less extreme wear during such running-in than might otherwise be observed during a longer running-in period. Wear tracks measured after pre-conditioning showed depths to the order of 0.1 – 0.3 µm, while wear tracks measured after slip-rolling endurance testing showed depths of approximately 1 – 10 µm. This indicates that while some minor wear may occur during the initial pre-conditioning, this does not account for the dramatic reductions in wear seen across the entire spectrum of tested materials and applied testing loads.

Other processes, notably work hardening, also occur during the pre-conditioning period and have been observed in previous study of these materials [155]. Particularly the alternative alloys have shown a strong tendency towards work hardening, further increasing their already high fracture toughness. This increased fracture toughness is crucial in preventing the initiation and spread of microcracks, which can cause critical material failure. Work hardening provides tougher and harder surface substrates with increased wear resistance, even while the surface substrates are coated with chemical tribofilm. Therefore the reduced wear coefficients are a consequence of a combination of processes, where the chemical tribofilms provide the initial wear protection during the simultaneous generation of work hardening, and the work hardened surfaces resist further wear, even with the wearing away of the chemical tribofilms.

Significant implications arise from comparison of the case-hardened reference steels to the non-case-hardened high performance steels. Even without tribofilm protection, the non-case-hardened steels show comparable wear performance to the case-hardened gear steels. This is due to shrewd metallurgical customization of the non-case-hardened steels, which gives them not only high fracture toughness, but also a tendency to undergo work hardening. Tribofilm protection significantly reduces wear in what would normally be the running-in phase. Therefore the tribofilms protect against wear during what was the running-in phase, in which work hardening occurs, and even if the tribofilms are worn off before completion of testing, the now work hardened surfaces are more wear-resistant than in the heat-treated state.

When evaluating improvements to wear performance with tribofilm protection from M822, it is once again crucial to consider MoDTC interactions with ZDDP because of the ZDDP content in the chosen endurance lubricant VP1. Figure 4.35 shows a comparison of wear factors from the same pin on plate testing in the literature study by Morina et al. The same lubricant formulations as before are evaluated, i.e. base oil, ZDDP only, MoDTC only and ZDDP + MoDTC.

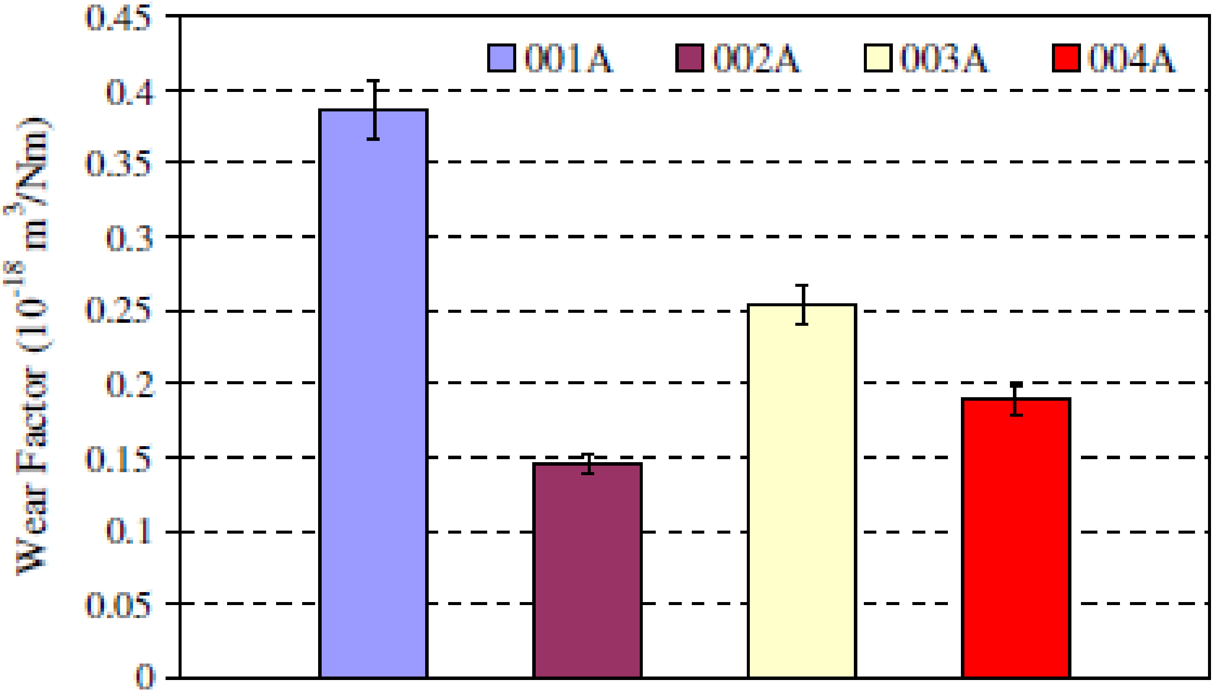

Figure 4.35: LITERATURE: Wear coefficients from pin on plate tests (wear on pin measured) using lubricants 001A (base oil, no additives), 002A (with ZDDP), 003A (with MoDTC) and 004A (with ZDDP + MoDTC) [100].

Naturally, the highest wear was experienced with base oil lubrication, while the lowest wear was experienced with ZDDP-enhanced lubrication. What is particularly interesting is the significant reduction in wear from the addition of MoDTC, which is purposed primarily as a friction modifier. The implication of this is that MoDTC has, in addition to friction modification properties, potential for anti-wear contribution, which helps to partially explain wear reductions observed in M822-protected steels. Naturally the additional anti-wear potential of MoDTC is not as impressive as its current use as a friction modifier, which is why lubricant formulations containing both ZDDP and MoDTC receive so much attention. The slight antagonism that may occur between the two additives is observable in the comparison of formulation 002A to 004A in Figure 4.35. It therefore becomes clear that one must carefully consider which property, ie. anti-wear or friction modification, is more important for the desired lubricant application in determining what proportions of ZDDP and MoDTC to enhance a lubricant with.

The operational endurance of chemical tribofilms themselves, however, is still of importance in this study, because the additives used to generate these tribofilms during pre-conditioning are not supposed to be present in the endurance testing lubricant, and cannot, therefore, aid in the replenishing of the tribofilms. VP1 does contain some $CaCO_3$, which is used as a corrosion inhibitor, meaning tribofilms containing $CaCO_3$ can continue to form and be replenished during endurance testing. Further evaluation of the endurance of the M822 tribofilm, however, is indeed possible as VP1 does not contain MoDTC, the essential additive used to generate the M822 tribofilm. Figure 4.36 provides a visual comparison of a 20MnCr5 sample surface after M822 tribofilm generation vs. after slip-rolling endurance testing. The tribofilms generated in pre-conditioning do not yet appear to be stable enough to withstand wear effects for the entire duration of endurance testing. There are some indications that $CaCO_3$ may be present in a tribofilm even after endurance testing, however this $CaCO_3$ would be from the corrosion inhibitor in VP1, and not be related to the original M822 tribofilm. Zn, S and P signals are far more prominent, indicating that ZDDP tribofilm is generated and stabilized during endurance testing. Mo was not detected after endurance testing, which shows definitively that the pre-conditioned tribofilm was worn away, because Mo is found in neither 20MnCr5 nor the VP1 lubricant and, therefore, acts as a “tracer” element. Improved wear resistance of the pre-conditioned tribofilms will be essential for the applicability and sustainability of this pre-conditioning technique, and will be sought in future work. Particularly the application of $Na_2S_2O_3$ or serpentines such as $Mg_3Si_2O_5(OH)_4$ to improve tribofilm durability will be considered. This will require additional testing for verification.

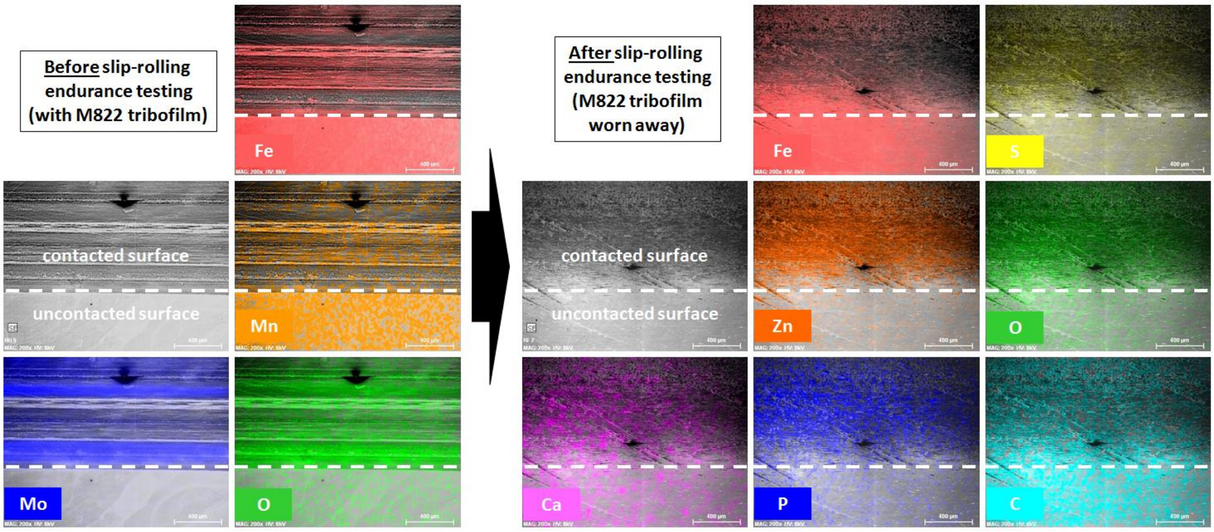

Figure 4.36: Wearing away of M822 tribofilm: SEM-EDX Element-Mapping images of sample surfaces taken before (left) and after (right) slip-rolling endurance testing at P_{0Mean} = 1.5 GPa (P_{0Max} = 2.25 GPa, F_N = 930 N) and T = +120 °C in BMW FF SAE 0W-30 VP1, ACEA A3/B4.

5 Further Discussion

5.1 The Drive for New Alloy Strategies

Case-hardened 20MnCr5 has demonstrated respectable wear resistance under even very high slip-rolling loads. The increase in carbon concentration in the surface, and consequently surface hardness, of 20MnCr5 through carburization is a significant factor in the improvement of this wear resistance, because it allows the material to maintain a tough core. This is evident in a core fracture toughness value comparable to the high performance alternative alloys. Although residual austenite in 20MnCr5 did not appear to have a clear influence on the wear resistance of the steel in this study, lower residual austenite appeared to lead to reduced COFs and to enhance the tribofilm formation. 20MnCr5 itself is a relatively inexpensive steel that is easy to acquire, as it is produced in large quantities due to its universality as a standard gear steel all over the world. The case-hardening applied to it, however, adds significant costs, is energy-intensive and can be a lengthy process. With the peak of its performance likely reached, the future of this steel among more advanced materials is questionable.

The alternative alloys chosen for this study may initially appear to be rather expensive in terms of the cost of raw material, but appear to be far more economical than 20MnCr5 when no case-hardening needs to be applied. This economic viability is predicated on their providing equivalent or better friction and wear performance than the current standard, i.e. 20MnCr5. These alternative steels alloyed with molybdenum and/or silicon have demonstrated better friction behaviour in all slip-rolling endurance testing, both untreated and with pre-conditioning. In many instances, this improved friction behaviour is significantly better. The same applies to the wear performance of the alternative alloys. Even before any pre-conditioning was applied, they were able to show wear performance equivalent to case-hardened 20MnCr5. The application of pre-conditioning to all steels showed that the alternative alloys were able to maintain this equivalent wear performance, and in some cases even exceed that of the case-hardened 20MnCr5. These results are grounded in the material properties that arise from the novel metallurgies, but pre-conditioning offers an additional route to friction and wear reductions.

Though it was difficult to discern the influence of residual austenite in 20MnCr5 on friction and wear performance in slip-rolling contacts, it is well documented (and described in 2.1.2) that reduction of residual austenite is crucial for the improvement of the wear resistance. Both 36NiCrMoV1-5-7 and 45SiCrMo6 have residual austenite contents of under 2% and appear to be quite promising. Since both alternative alloys have annealing temperatures of over 400 °C, they can be used in high temperature applications where 20MnCr5, with an annealing temperature of under 200 °C, cannot, eg. deposition of DLC coatings. The lower initial hardness values of the alternative alloys are not problematic due to their propensity for work hardening, particularly at higher contact pressures. This, in combination with their high toughness and strength values, results in very good slip-rolling wear resistance. Good fracture toughness is crucial to prevent the spread of sub-surface microcracks. This is particularly important for the 36NiCrMoV1-5-7 batch in this work, which has been found to contain non-metallic inclusions that are known to promote the initiation of microcracks. In this context, the cleanliness of materials with respect to a desired application must be considered. Some of the advantages offered by the alternative alloys over classical steels like 20MnCr5 are summarized:

- high level of hardenability and strong wear resistance, even without case hardening
- high yield strength together with high fracture toughness
- good high temperature strength and high annealing temperature
- low residual austenite content yielded after simple heat treatment
- low COFs and high wear resistance even under very high slip-rolling loads

5.2 Extreme Friction Reductions: Pre-Conditioned Alternative Alloys

It has been stated that one of the central goals of this research is, ultimately, to develop greater efficiencies in tribological systems in order to reduce friction-related energy waste. Therefore the pre-conditioning strategies developed were applied with the intention of reducing mechanical running-in as much as possible, ideally eliminating it altogether. Even before any pre-conditioning was applied, the alternative alloys, 36NiCrMoV1-5-7 and 45SiCrMo6, showed clearly lower frictional profiles than 20MnCr5. However, observation of profiles of the evolution of the coefficients of friction for the untreated alternative alloys reveals that these, too, require a certain period of running-in before their lowest COF values are reached.

In the same manner that thin film coatings such as DLC are applied to components before regular operation to reduce their frictional profiles, so to were the alloys chosen in this study pre-conditioned. In Figure 5.1, profiles of the evolution of COF values for the alternative alloys during slip rolling endurance testing at P_{0Mean} = 1.5 GPa (F_N = 930 N, P_{0Max} = 2.25 GPa) are presented to compare the untreated alloys to the cold work hardened ones. Ultimately, 45SiCrMo6 yielded the lowest COF, both untreated and with cold work hardening, though 36NiCrMoV1-5-7 remains competitive. What is most important, though, are the strong reductions in frictional profiles of the alternative alloys from cold work hardening, particularly towards the end of endurance testing, to the point that the pre-conditioned alloys can be grouped together in a discrete and separate domain compared to the untreated alloys.

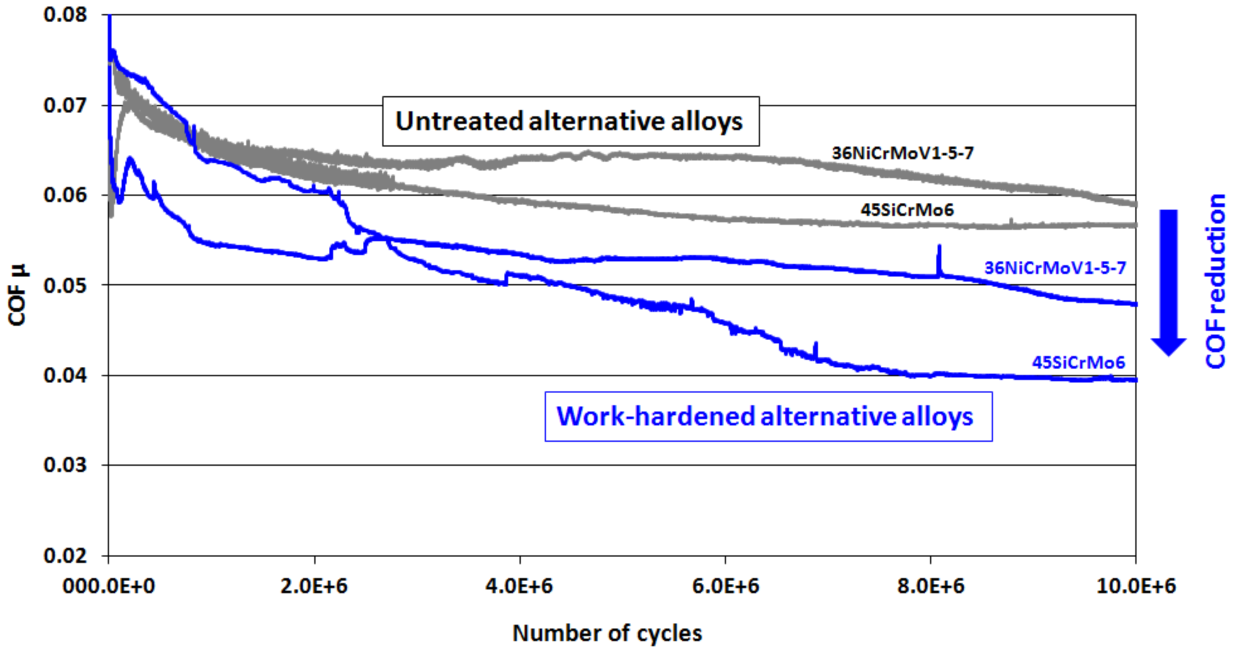

Figure 5.1: Evolution of coefficients of friction during slip-rolling testing at P_{0Mean} = 1.5 GPa (F_N = 930 N, P_{0Max} = 2.25 GPa) and T = +120°C in BMW FF SAE 0W-30 VP1, ACEA A3/B4, dynamic viscosity at +120 °C = 5.33 mPa·s.

In Figure 5.2, profiles of the evolution of COF values for the alternative alloys during slip rolling endurance testing at P_{0Mean} = 1.5 GPa (F_N = 930 N, P_{0Max} = 2.25 GPa) are presented to compare the untreated alloys to those protected with pre-conditioned LS514 tribofilms. As was the case from cold work hardening, strong overall frictional profile reductions are clearly observable. Again, the profiles of the pre-conditioned alloys are within a discreetly lower range of friction coefficients compared to the untreated materials.

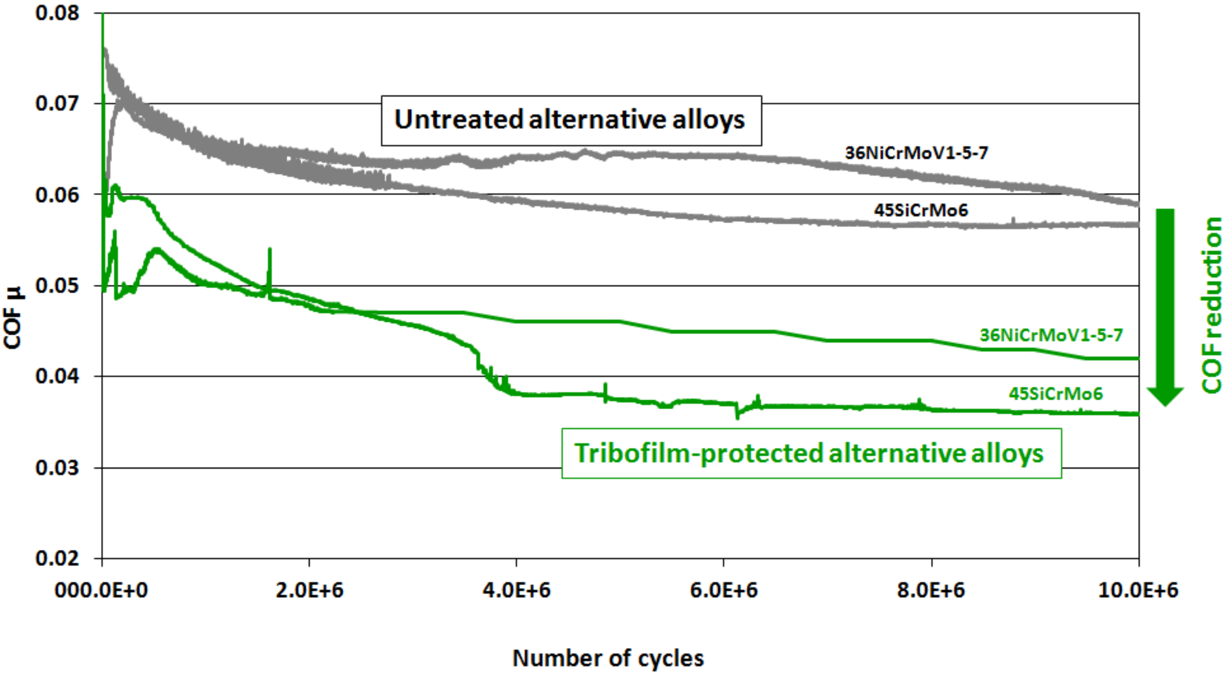

Figure 5.2: Evolution of coefficients of friction during slip-rolling testing at P_{0Mean} = 1.5 GPa (F_N = 930 N, P_{0Max} = 2.25 GPa) and T = +120°C in BMW FF SAE 0W-30 VP1, ACEA A3/B4, dynamic viscosity at +120 °C = 5.33 mPa·s.

The strong reductions of the frictional profiles of the alternative alloys from pre-conditioning are particularly impressive, because these alloys already produce very low coefficients of friction in the untreated state, i.e. without any pre-conditioning. The reduced frictional profiles of the pre-conditioned alternative alloys, either with cold work hardening or tribofilm protection, offer clear competition to many of the popular thin film coating systems. Recalling the work done by Scholz, the pre-conditioned alloys in this study are able to offer friction reductions equivalent to DLC vs. DLC contacts. It is less clear, however, if the goal of eliminating running-in during normal operation, i.e. endurance testing, was achieved. The low COF values observed in the DLC vs. DLC profiles presented by Scholz are achieved very early on in endurance testing, whereas the low COFs from the pre-conditioning undertaken in this work really only appear to be stable after several million load cycles, indicating that there may still be running-in processes occurring.

5.3 An Alternative Additive for Tribofilm Generation

The ability to generate stable chemical tribofilms under slip-rolling conditions from the additive Molyvann 822, in essence MoDTC, has been verified through the thorough surface analysis presented in section 4.3. The positive effect that these tribofilms have on friction and wear during slip-rolling endurance testing has also been verified. These positive results are in addition to the already abundant literature studies on the effectiveness of MoDTC as a friction modifier. Unfortunately, the negative toxicological properties of MoDTC remain prominent, and cannot be avoided in the search for ecologically responsible lubricant formulations.

Bismuth dialkyl-dithiocarbamate (BiDTC, [CAS: 21260-46-8]) is less well known in the literature compared to MoDTC. Bismuth itself is essentially benign, hence why it is found in so many consumer products, eg. lipstick. Originally, bismuth dithiocarbamates were manufactured by reacting bismuth halides, such as bismuth trichloride, with a dithiocarbamate species, resulting in hydrogen chloride by-product. Chloride residues from partially reacted by-products, unreacted bismuth halides or other metal halides are undesirable, even in trace amounts. Improvements to this process have been developed, such as through the implementation of an exchange reaction between a bismuth carboxylate and a metal dithiocarbamate [165]. The product from this process is indeed free of chloride residue, but still remains contaminated with metal carboxylate. Further developments would reveal a process to produce bismuth dithiocarbamate or dithiophosphorate by the reaction of bismuth hydroxide, bismuth oxide or bismuth oxynitrate, either with a dithiocarbamate or dithiophosphoric acid, respectively [166]. The only by-product from this process is water, which can be easily removed. None of the organometallic dithio-contaminants, observed in earlier methods, appear. Particularly the bismuth dithiocarbamate, described in the same patent, proves to be a very good extreme pressure agent, and displays very good anti-wear properties. This, in conjunction with its mild toxicological properties, makes it a worthwhile subject for further investigation. For the purposes of this investigation, bismuth dodecylbenzenesulfonate (Bi-ddbsa) was chosen for in chemical tribofilm generation and subsequent slip-rolling endurance testing. This choice was based on the industrial applicability of this additive. Similar additives show great promise, such as Bismuth octanoate [CAS: 85736-59-0] in the automotive/industrial grease Shell Gadus S3 Wirerope T Aerosol [167].

A Bi-ddbsa tribofilm was generated for initial surface analysis on a 20MnCr5 substrate under the same conditions as previously described, and subsequently subjected to analysis by Raman spectroscopy. The Raman spectrum of this tribofilm is given in Figure 5.3. The thermal decomposition of tris(N,N-disubstituted dithiocarbamate) complexes of Bi(III) has been described in the literature [168]. The presence of bismuth as the complexing metal, rather than previous cases involving molybdenum, will result in a different tribofilm composition than from MoDTC. This tribofilm appears to be dominated by Bi_2S_3 and Bi_2O_3, the Raman peaks of which are verified by previous literature investigation [169,170]. Other components of the tribofilm have not yet been evaluated extensively, and the corresponding peaks are, therefore, unmarked.

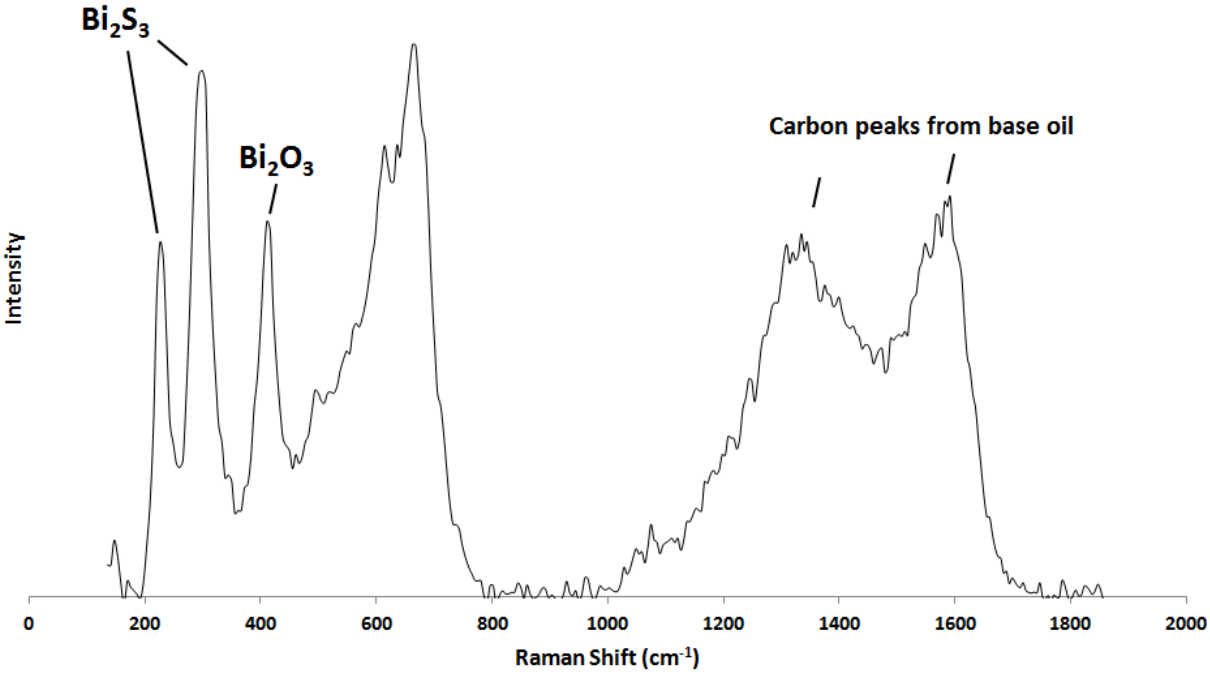

Figure 5.3: Raman spectrum of Bi-ddbsa tribofilm on 20MnCr5 surface.

Slip-rolling endurance testing, under the same testing regime used on steels with LS514 and M822 tribofilms, was begun on all alloys with Bi-ddbsa tribofilms. Thus far, results are only available for testing at P_{0Mean} = 1.5 GPa (F_N = 930 N, P_{0Max} = 2.25 GPa). Coefficients of friction from the end of endurance testing are given in Figure 5.4. Overall, very clear COF reductions resulted from the pre-conditioning of Bi-ddbsa tribofilms for all alloys compared to the untreated state.

Strong COF reductions were observed for 20MnCr5, whereby 20MnCr5 with 14% residual austenite was able to achieve a reduction with Bi-ddbsa tribofilm to 3/5 the original value for the untreated pairing. While the ability of the LS514 and M822 tribofilms to reduce friction in slip-rolling contacts has been evaluated and verified, initial results for the alternative alloys with Bi-ddbsa tribofilms are mixed. Bi-ddbsa tribofilm-protected 36NiCrMoV1-5-7 showed a COF reduction to 0.049, a reduction roughly equivalent to the M822 tribofilm. The lowest coefficient of friction at the end of testing was achieved by Bi-ddbsa tribofilm-protected 45SiCrMo6 at a value of 0.037. This is in line with similar results with the LS514 tribofilm.

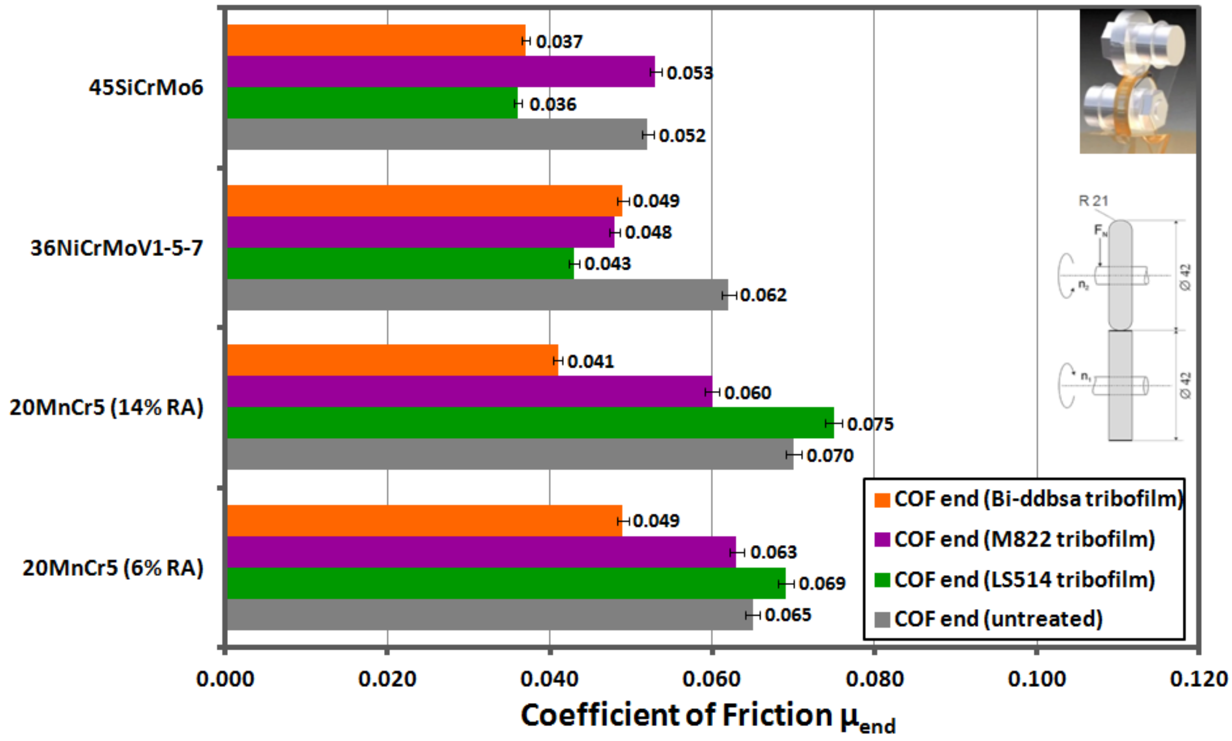

Figure 5.4: Coefficients of friction from directly before the end of slip-rolling testing up to 10,000,000 cycles at P_{0Mean} = 1.5 GPa (F_N = 930 N, P_{0Max} = 2.25 GPa) and T = +120°C in BMW FF SAE 0W-30 VP1, ACEA A3/B4, dynamic viscosity at 120 °C = 5.33 mPa·s.

Not only is it apparent that strong friction reductions could be achieved with pre-conditioned Bi-ddbsa tribofilms compared to the untreated state, but that the bismuth-based films yielded much better friction behaviour than the molybdenum-based ones. This statement is presented visually in Figure 5.5. The evolution of coefficients of friction for both the reference alloy 20MnCr5 and the alternative alloy 45SiCrMo6 are given to compare the untreated, M822-treated (Mo-DTC) and Bi-ddbsa-treated states.

It is quite significant that the bismuth-based tribofilm was able to yield notably stronger friction reductions than the molybdenum-based film, because MoDTC is such a conventional friction modifier in automobile applications, in spite of concerns about its harmful environmental impact. These concerns may prove to be a driving force in the search for environmentally friendly alternative, such as those based on bismuth. Though the EP properties of such bismuth-based additives are better known to industry insiders, there is very little literature dealing with possible corresponding FM properties. The results presented here, however, show that bismuth can indeed contribute to friction modification at an equivalent if not higher level than molybdenum. Further research will be needed to determine influences on AW properties, though as in previous testing in this study, wear coefficients were determined for all tested alloys.

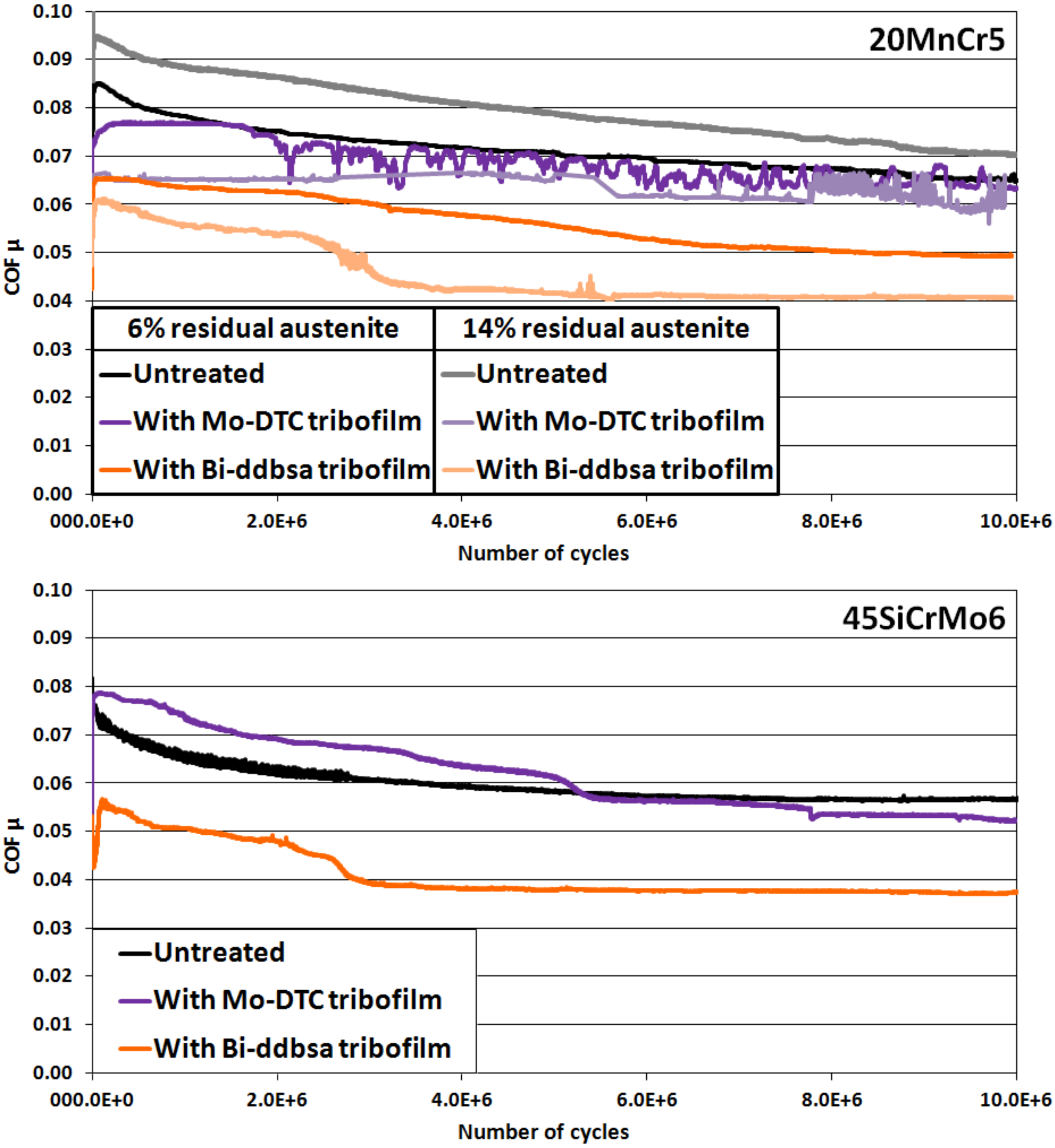

Figure 5.5: Evolution of coefficients of friction in slip-rolling tests up to 10,000,000 cycles at T = 120°C and P_{0Mean} = 1.5 GPa (P_{0Max} = 2.25 GPa, F_N = 930 N) in BMW FF SAE 0W-30 VP1, ACEA A3/B4, dynamic viscosity at 120 °C = 5.33 mPa·s.

Bi-ddbsa tribofilm-protected 20MnCr5 shows reductions in profilometric wear coefficients that are essentially on par with those observed with application of the LS514 and M822 tribofilms. The wear coefficients of the Bi-ddbsa tribofilm-protected alternative alloys, on the other hand, show far stronger reductions in wear compared to the untreated alloys. A reduction of k_v for the cylindrical sample disks of the alternative alloys to under an astonishing 1/20 (less than 5%) of the original value for the untreated alloy was observed. It must be noted that these values are at the limit of resolution for calculation of the wear coefficient, and must be treated with caution. It is clear, however, that a strong wear reduction occurred, which must also be verified through further repeat testing. It remains to be seen if such strong wear performance can be achieved at higher testing loads. This applies to both the bismuth-based, as well as the molybdenum-based tribofilms.

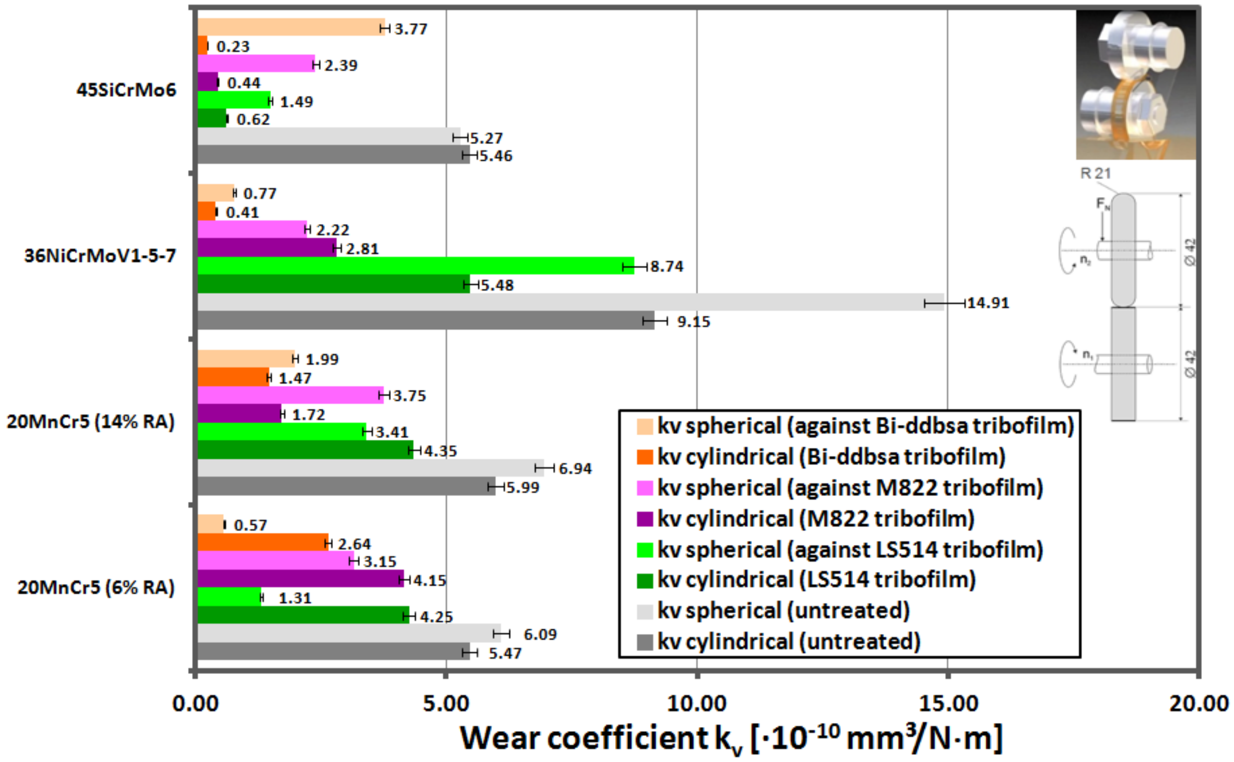

Figure 5.6: Wear rates of the spherical and cylindrical disks, with and without tribofilms after slip-rolling endurance testing at P_{0Mean} = 1.5 GPa (F_N = 930 N, P_{0Max} = 2.25 GPa) and T = +120 °C in BMW FF SAE 0W-30 VP1, ACEA A3/B4, with dynamic viscosity at 120 °C = 5.33 mPa·s.

5.4 The Influence of Pre-Conditioning on Global Trends in Friction and Wear

The greatest strength of the pre-conditioning techniques developed in this study lies in their brutal effectiveness despite their overall simplicity and low energy input. The observed improvements to friction behaviour and wear performance are indicative of this. In this regard, Figure 5.7 and Figure 5.8 provide a complete overview of the global reductions in friction and wear achieved with the implementation of pre-conditioning. Friction and wear results from both cold work hardening and tribofilm generation are grouped together as part of a single pre-conditioning strategy. The greater aim of continued research in this area will be the physical combination of pre-conditioning techniques for more friction and wear reductions, discussed later in Summary and Outlook. The coloured areas contain the complete spread of k_v and COF values from slip-rolling endurance testing, ranging from P_{0Mean} = 1.5 GPa to P_{0Mean} = 2.62 GPa. The arrows in the coloured areas indicate the movement trends in these values with increasing contact pressure. The wear rates (y-axis) are scaled logarithmically so as to provide good visualization over the lower range, where the spread of values is small, as well as the higher range, where the spread of values is quite large.

Figure 5.7 represents the wear rates from the cylindrical samples vs. COF values from the end of endurance testing. Looking at the untreated steels, both friction and wear increase with contact pressure, as expected. The nature of this increase varies between the materials. The reference steel 20MnCr5, and the alternative alloy 45SiCrMo6, show proportionally larger increases in friction than wear as contact pressure rises. For 20MnCr5, this wear resistance comes from case hardening, while for 45SiCrMo6, wear resistance is gained from work hardening, particularly at the beginning of testing. This work hardening is also more intense under higher contact pressures, which is why this steel is able to withstand high loads even without case hardening. Untreated 36NiCrMoV1-5-7 shows a more proportional increase in wear vs. friction with rising contact pressure. While the material also shows positive work hardening tendencies, its material cleanliness and microstructural inhomogeneities become more problematic when subjected to higher slip-rolling loads.

Looking at the pre-conditioned alloys, unambiguous reductions in friction and wear are observed throughout. Due to the logarithmic scaling of wear rates, the value spread for the pre-conditioned samples may appear to be greater than for the untreated alloys, though the opposite is the case. Moreover the reductions in friction and wear were so great that the value spreads are completely separated for the respective materials. For 20MnCr5, strong wear reductions are observed, while the range of COFs appears to have remained fairly consistent, though this range begins and ends at lower COF values. For the alternative alloys, similar reductions in the range of wear rates were observed. Additionally, even greater reductions in the range of COFs could be achieved, contrasting with 20MnCr5. Though a trend towards higher COFs with increasing contact pressure can be observed in the alternative alloys as well, this trend is very subtle, and may be almost non-existent for 36NiCrMoV1-5-7. It is of great significance that the alternative alloys are able to maintain such a stable frictional profile, even with increases in slip-rolling loads. By limiting this increase in friction over a range slip-rolling loads, net energy savings can be achieved, which is one of the central focuses of this work.

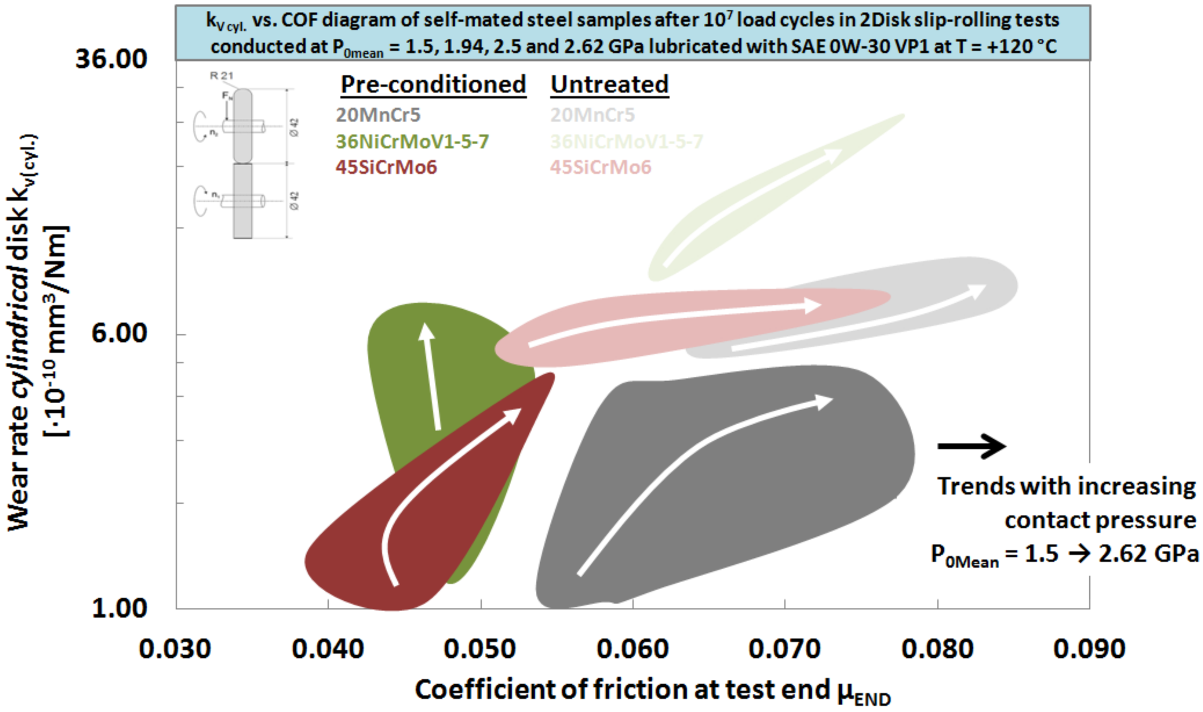

Figure 5.7: Global reductions in friction and wear of the cylindrical sample from pre-conditioning.

Similar trends can be observed in Figure 5.8, which compares wear rates from the spherical counterbodies to the same COF values from the end of endurance testing. In general, more wear can be observed for the spherical disks than for the cylindrical ones. There also appears to be a slightly larger range of the wear rates yielded. This larger variation in wear rates may be reasonably expected, because only the cylindrical samples were pre-conditioned, not the spherical counterbodies. For work hardening, the spherical counterbodies run against a cylindrical surface that is harder than for the untreated steel, naturally leading to greater wear on the surface that has, in relative terms, lower hardness than before. For tribofilm generation, the protection offered to the cylindrical sample is likely greater than to the spherical counterbody. While the tribofilm acts as a boundary layer between both contact bodies, it is only chemically bonded to the cylindrical sample on which is was generated, leaving the contact surface of the spherical counterbody relatively more greatly exposed than the cylindrical sample. In spite of this, strong reductions in both wear and friction from pre-conditioning were achieved for the spherical disks as well. Several trends resulting from pre-conditioning remain prominent for the spherical counterbodies, such as the nearly complete separation of value spreads per material and the tendency of the alternative alloys, particularly 36NiCrMoV1-5-7, to maintain a stable frictional profile with increasing contact pressure.

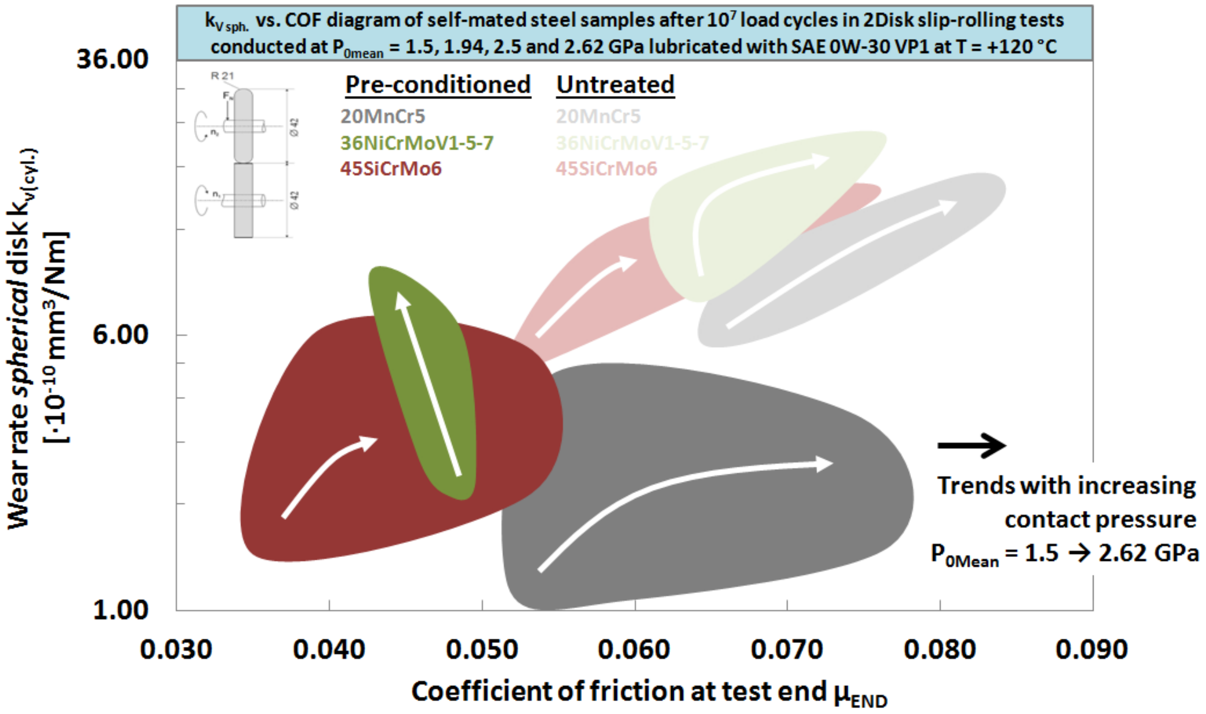

Figure 5.8: Global reductions in friction and wear of the spherical counterbody from pre-conditioning.

The observed trends in friction and wear reinforce the advantages of the alternative alloys and the applied pre-conditioning techniques. The metallurgical strategy of alloying with molybdenum and silicon appears to be very effective, as these alloys can show equal wear performance and better friction behaviour than a standard case-hardened steel. This holds true even under high slip-rolling loads. The generation of cold work hardening and reactive tribofilms in pre-conditioning of these alloys further emphasizes their advantages. The tendency of these alloys towards work hardening under high loads and the receptiveness of their contact surfaces to chemical bonds with targeted lubricant additives are already observable during normal operation, i.e. endurance testing, without pre-conditioning. Achieving these improvements before normal operation leads to a net reduction of the energy losses that occur during running-in. The strong reductions in wear, and particularly friction, show the potential to challenge current standard thermochemical treatments such as DLC, achieving equal performance more efficiently that rivals thin film coatings.

6 Summary and Outlook

The main goal of this work was to transfer the running-in phase into the final step of the mechanical finishing process through the targeted pre-conditioning of novel, high toughness steel bearings without thermo-chemical treatments and compare these to conventional, case-hardened steels. This was achieved by inducing cold work hardening and chemically reactive tribofilms, ultimately leading to significant reductions in friction and wear in slip-rolling endurance tests (T = +120 °C, 10^7 cycles, approximately 19 days in a factory fill engine oil. Ultimately, the non-case-hardened alternative steels showed competitive wear performance and better friction behaviour compared to the case-hardened 20MnCr5. Pre-conditioning led to COF reductions to under 70% and wear coefficient reductions to an astonishing 1/10 (90% reduction) of the original values for the untreated steels. The observed improvements to friction behaviour and wear performance are indicative of a technically simple, cost- and energy-efficient pre-conditioning strategy that may prove to replace existing thermochemical treatments for steel alloys. It is clear from Figure 6.1 that such improvements in material efficiency are crucial if further reductions in fuel consumption, particularly in the global automobile industry, are to continue.

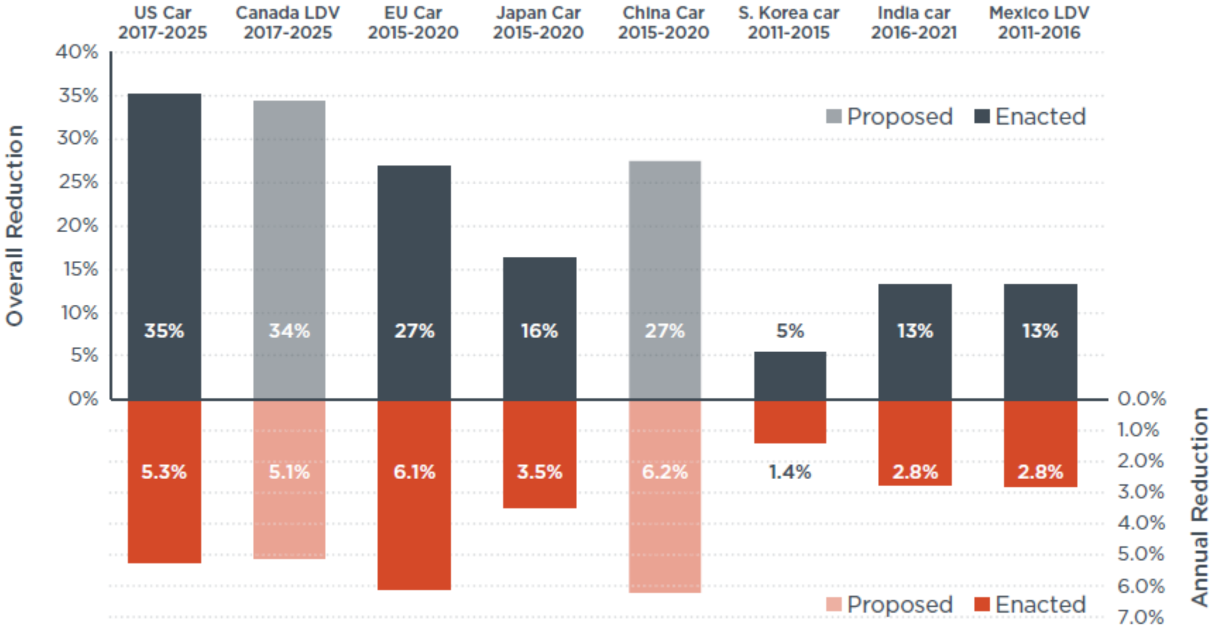

Figure 6.1: LITERATURE: Comparison of overall and annual average fleet fuel consumption rates under proposed or enacted standards across regions [4].

The technical simplicity of the developed pre-conditioning techniques makes them interesting for expanded applications. Testing using twin-disk rigs is one of many possibilities. The work hardening tendencies of the alternative alloys indicate that they could be used in gear applications with the aim of strengthening the tooth root during mechanical finishing without excess material damage. Figure 6.2 provides a schematic for such a pre-conditioning operation on appropriate gear materials. The tool gears would be of the same material as the WC rollers used in testing up to this point. Niobium carbide could be used as an alternative for the hard metal tool gears, as current market trends may be leading key industries away from tungsten carbide.

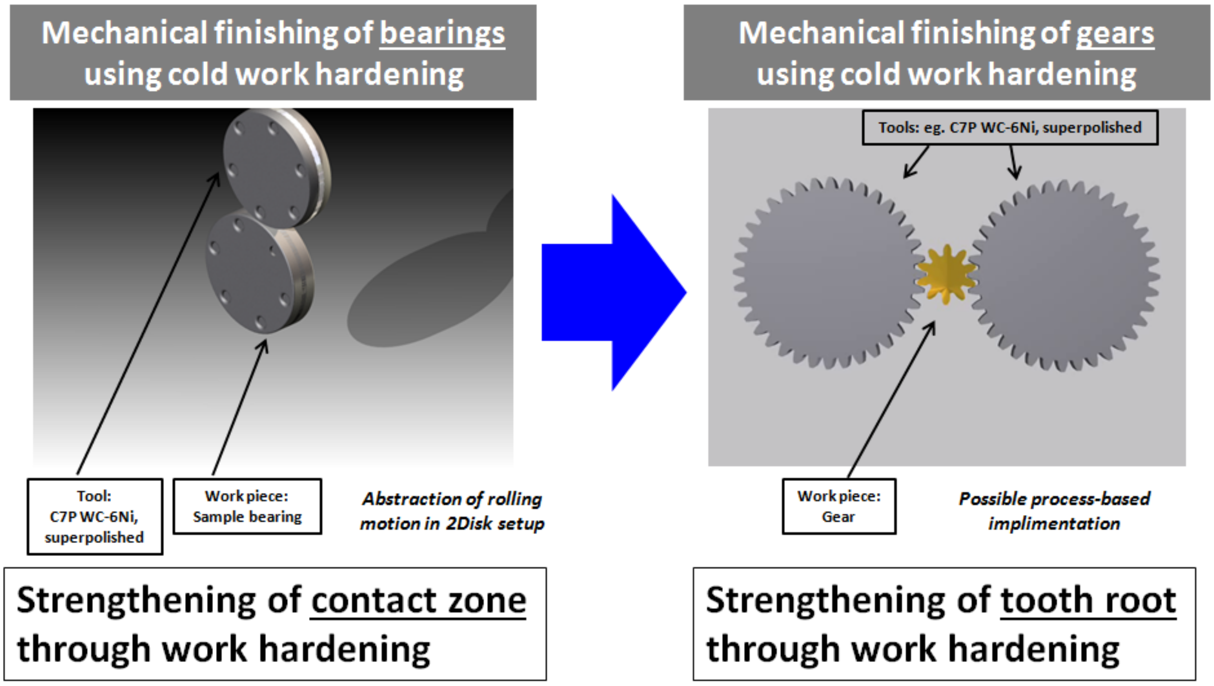

Figure 6.2: Abstraction of slip-rolling motion and "technology transfer" of the cold work hardening pre-conditioning procedure to gear applications.

Integration of both pre-conditioning techniques is a particularly important consideration for future development of new pre-conditioning strategies. The simultaneous generation of cold work hardening and protective tribofilms offers the potential for significant reductions in required energy input, as well as reduced energy expenditure during operation. Particular emphasis for future experimentation is placed on the reduction of running-in time, i.e. reducing energy consumption, and the implementation of more environmentally friendly additive regimes, such as bismuth-based additives.

The goal of combined pre-conditioning can only be achieved when uniform conditioning parameters for generation of both cold work hardening and chemical tribofilms are developed, particularly regarding the applied rolling load. This load must be high enough to generate contact pressures (using hard metal rollers) that can induce work hardening in the chosen alloys, while at the same time low enough so as not to degrade the chemical tribofilms also being generated in the process. Further study will also need to be done on the effectiveness of polished contacts and the potential to generate chemical tribofilm reactions on steel surfaces. Ultimately, though, these difficulties can be overcome with the selection of appropriate metallurgies and lubrication strategies. The combination of such optimal metallurgies and proper lubrication can allow the pre-conditioning techniques, developed in this work, to be combined for the eventual application in the series production of steel components across an increasingly diverse spectrum of tribological applications.

7 References

[1] Regulation (EC) No 443/2009 of the European Parliament and the Council: setting emission performance standards for new passenger cars as part of the Community's integrated approach to reduce CO2 emissions from light-duty vehicles, Official Journal of the European Union, L 140/1 – 140/15, 05.06.2009.

[2] Office of the Press Secretary, Obama Administration National Fuel Efficiency Policy: Good For Consumers, Good For The Economy And Good For The Country, The White House, 19.05.2009.

[3] R. Leonhard, Reducing CO2 emissions with optimized internal-combustion engines, 60th Automotive Press Briefing, Boxberg, 06.2011.

[4] J.D. Miller, C. Façanha, The State of Transport Policy: A 2014 Synthesis of Vehicle and Fuel Policy Developments, International Council on Clean Transportation, Policy Update, 03.2014, retrieved on 27.05.2015 from http://www.theicct.org.

[5] C. Scholz, D. Spaltmann, M. Woydt, Slip-rolling resistance of thin films and high toughness steel substrates under high Hertzian contact pressures, Wear 270 (2011) 506-514.

[6] M. Woydt, C. Scholz, Slip-rolling resistance of alternative steels under high contact pressures in engine oil, Bearing Steel Technology, In: Bearing Steel Technology, 10th volume, ASTM STP 1580, Ed.: J. M. Beswick, American Society for Testing and Materials International, West Conshohocken, PA, 2014, pp. 210-238, ISBN 978-0-8031-7605-8.

[7] DIN EN ISO 2639: Stahl - Bestimmung und Prüfung der Einsatzhärtungstiefe (Steels - Determination and verification of the depth of carburized and hardened cases), 2003-04, Deutsches Institut für Normung (German Institute for Standardization), Berlin, Germany.

[8] ISO 6336-5:2003(E): Calculation of load capacity of spurs and helical gears – Part 5: Strength and Quality of Materials, 2003-07-01, International Organization for Standardization, Geneva, Switzerland.

[9] E.V. Zaretsky, Rolling Bearing Steels - A Technical and Historical Perspective, Technical Memorandum NASA/TM—2012-217445, 2012-04, Glenn Research Center, Cleveland, U.S.A.

[10] ISO 683-11: Heat-treatable steels, alloy steels and free-cutting steels – Part 11: Wrought case-hardening steels, 1987-04-01, International Organization for Standardization, Geneva, Switzerland.

[11] DIN ISO 3990-5:1987-12: Calculation of load capacity of cylindrical gears; endurance limits and material qualities, 1987-12, German Institute for Standardization, Berlin, Germany.

[12] ISO 14635-1:2000: Gears -- FZG test procedures, 2000-06-01, International Organization for Standardization, Geneva, Switzerland.

[13] R.P. Carlisle, Scientific American Inventions and Discoveries: All the Milestones in Ingenuity, John Wiley & Sons, 2004. ISBN 0-471-24410-4.

[14] R. Stribeck, Kugellager für beliebige Belastungen (Ball bearings for any loads), Zeitschrift des Vereins Deutscher Ingenieure 45 (1901) 3, 73-79.

[15] N.N. (R. Stribeck), Kugellager (ball bearings), Glasers Annalen für Gewerbe und Bauwesen (Glaser's Annals for Industry and Construction) 577 (1901) 2-9.

[16] D.F. Wilcock, E.R. Booser, Bearing Design and Application, McGraw-Hill Book Co., New York, 1957.

[17] E.V. Zaretsky, Bearing and Gear Steels for Aerospace Applications, Technical Memorandum, NASA TM-102529, Lewis Research Center, Cleveland, Ohio, 1990.

[18] E.N. Bamberger, B.L. Averbach, P.K. Pearson, Improved Fracture Toughness Bearings, AFWAL TR–84–2103, (Avail. NTIS, AD–B094304L.), 1985.

[19] W.J. Anderson, E.N. Bamberger, W.E. Poole, R.L. Thom, R.L., E.V. Zaretsky, Materials and Processing, STLE Life Factors for Rolling Bearings, E.V. Zaretsky, ed., Society of Tribologists and Lubrication Engineers, 1992, Park Ridge, IL, USA, 71-128.

[20] E.N. Bamberger, Status of Understanding for Bearing Materials, Tribology in the ’80’s, Vol. 2, NASA CP–2300–VOL–2, W.F. Loomis, ed., National Aeronautics and Space Administration, 1983, Washington, D.C., pp. 773–794.

[21] T.V. Philip, New Bearing Steel Beats Speed and Heat, Power Transmission Design 28 (1986) 6, 43-46.

[22] J.L. Maloney, C.M. Tomasello, Case carburized stainless steel alloy for high temperature applications, United States Patent, 13.06.1995, Patent Number 5424028.

[23] D.P. Townsend, E.N. Bamberger, Surface Fatigue Life of Carburized and Hardened M50NiL and AISI 9310 Spur Gears and Rolling-Contact Test Bars, AIAA Paper 89-2819, NASA TM-101979, 1989.

[24] D.P. Townsend, E.V. Zaretsky, Effect of Shot Peening on Surface Fatigue Life of Carburized and Hardened AISI 9310 Spur Gears, NASA TP-2047, 1982.

[25] J.C. Straub, Shot Peening in Gear Design 1964, AGMA Paper 109.13, American Gear Manufacturers Association, 1964.

[26] H. Kanisawa, T. Ochi, Y. Koyasu, Development of High-Strength Carburized Steels for Automobile Gears, Nippon Steel Technical Report No. 64, 1995.

[27] F.B. Abudaia, Microstructure and Fatigue Strength of High Performance Gear Steels, Doctoral Thesis, University of Newcastle, 2003.

[28] R. Rentsch, Material flow analysis for hot-forming of 20MnCr5 gear wheel blanks, 40 (2009) 5-6, 374–379.

[29] I. Eisbrecher, B. Clausen, M. Hunkel, R. Rentsch, Anisotropies and inhomogeneities in the microstructure of the case hardening steel SAE 5120. Mat.-wiss. u. Werkstofftech. 43 (2012) 1-2, 78-83, DOI: 0.1002/mawe.201100892.

[30] L. Cheng, C.M. Brakman, B.M. Korevaar, E.J. Mittemeijer, The Tempering of Iron-Carbon Martensite; Dilatometric and Calorimetric Analysis, Metallurgical Transactions, 19A (1988) 2415 – 2426.

[31] P.G. Winchell, M. Cohen, Strength of Martensite, Trans. A.S.M. 55 (1962) 347-361.

[32] C.S. Roberts, Effect Of Carbon On The Volume Fractions And Lattice Parameters Of Retained Austenite And Martensite Trans. AIME 197 (1953) 203-204.

[33] G. Lucas, H. Nützel, Untersuchungen über die Umwandlung des Restaustenits in niedrig legierten Stählen mit rd. 1% C (Investigations of the transformation of residual austenite in low-alloy steels with approx. 1% C), Sonderdruck aus Archiv für das Eisenhüttenwesen, 12 (1966) 981-987.

[34] G. Lucas, H. Nützel, Gefüge- und Maßänderungen von Wälzlagerteilen bei erhöhten Betriebstemperaturen (Structural and dimensional changes in rolling bearing components at elevated temperatures), SKF Kugellagerfabriken, Dd 5379, 1,·69 (1969), Re g. 417 15.

[35] V. Läpple, Wärmebehandlung des Stahls (Heat treatment of steel), 9th edition, Verlag Europa-Lehrmittel, Haan-Gruiten, 2006, pp. 169, ISBN: 9783808513095.

[36] S.C. Wang, Y.W. Wu, Y. Hua, Z.C. Li, H. Zhang, Microstructure and crystallography of 20MnCr5 steel tempered at different conditions, J. Mater. Sci. 45 (2010) 5892–5901.

[37] A. Irretier, Stoffwertbestimmung: Schlussbericht (Final Report) Januar 2008 – Dezember 2009, Universität Bremen, Sonderforschungsbereich 570 Distortion Engineering, Projekt C1.

[38] M. Hunkel, Modelling of phase transformations and transformation plasticity of a continuous casted steel 20MnCr5 incorporating segregations, Mat.-wiss. u. Werkstofftech. 43 (2012) 1-2, 150-157, DOI: 10.1002/mawe.201100903.

[39] E. Brinksmeier, T. Lübben, U. Fritsching, C. Cui, R, Rentsch, J. Sölter, Distortion Minimization of Disks for Gear Manufacture, International Journal of Machine Tools & Manufacture, 51 (2011) 4, 331-338.

[40] M. Hunkel, Anisotropic transformation strain and transformation plasticity: two corresponding effects, Mat.-wiss. u. Werkstofftech. 40 (2009) 5-6, 466-472.

[41] M. Hunkel, F. Hoffmann, H.-W. Zoch, Simulation of the Distortion of Cylindrical Shafts during Heat Treatment due to Segregations, IJMMP 3 (2008) 1, 162-177.

[42] M. Hunkel, M. Dalgic, F. Hoffmann, Plasticity of the low alloy steel SAE 5120 during heating and austenitizing, BHM 155 (2010) 125-128.

[43] C.H. Surberg P.F. Stratton, K. Lingenhöle, Einfluss der Wärmebehandlungsparameter auf die Maßhaltigkeit von Stählen (Influence of heat treatment parameters on the dimensional tolerance of steels), BHM Berg- und Hüttenmännische Monatshefte, Springer-Verlag GmbH, 2010, DOI: 10.1007/s00501-010-0593-4.

[44] Harichand, S. Chaturvedi, S. Sharma, Optimization of Heat Treatment Processes for 16MnCr5, International Journal of Engineering Science and Technology (IJEST) 4 (2012) 3, 998-1004.

[45] P. Stratton, The effect of cold treatments on the lubricated wear of case-hardened components, European Conference on Heat Treatment for Industrial Competitiveness, Verona, Italy, 07.05.2012 – 09.05.2012, La Metallurgia Italiana 1 (2010) 1-6.

[46] Y.M. Rhyim, S.H. Han, Y.S. Na, J.H. Lee, Effect of Deep Cryogenic Treatment on Carbide Precipitation and Mechanical Properties of Tool Steel, Solid State Phenomena, 118 (2006) 9-14, DOI: 10.4028/www.scientific.net/SSP.118.9.

[47] R.H. Richman, R.W. Landgraf, Some effects of retained austenite on the fatigue resistance of carburized steel, Metallurgical Transactions A 6 (1975) 5, 955-964..

[48] R. Wagar, J. Speer, D. Matlock, P. Mendez, Examination of Pitting Fatigue in Carburized Steels with Controlled Retained Austenite Fractions, SAE Technical Paper 2006-01-0896, 2006, DOI: 10.4271/2006-01-0896.

[49] G.E. Totten, Steel Heat Treatment: Metallurgy and Technologies, CRC Press, 2006, pp. 387, ISBN 9780849384554.

[50] S. Binkowski, M. Woydt, E. Dietrich, Ungewöhnliche Aufhärtung des 100Cr6 in einem ausgefallenen Keramik-Hybrid-Wälzlager (Irregular hardness increase of 100Cr6 in a failed ceramic-hybrid-roller bearing), Sonderbände der Praktischen Metallographie 37 (2005) 247-252, ISBN 3-88355-343-3.

[51] W. Ramberg, W.R. Osgood, Description of stress-strain curves by three parameters, National Advisory Committee For Aeronautics, Washington, DC, USA, Technical Note No. 902, 1943.

[52] T. Lund, Structural alterations in fatigue tested ball bearing steel, Jernkontorets Annaler 153 (1969) 337-343.

[53] O. Vingsbo, R. Österlund, Phase changes in fatigued ball bearings, Metallurgical Transactions A 11A (1980) 701-707.

[54] O. Zwirlein, H. Schlicht, R. Eberhard, Werkstoffanstrengung bei Wälzbeanspruchung (Material stressing under rolling loading), HTM 30 (1975) 338-345.

[55] O. Zwirlein, H. Schlicht, Rolling Contact Fatigue Mechanisms-Accelerated Testing Versus Field Performance, Rolling Contact Fatigue Testing of Bearing Steels, ASTM 771, J.J.C. Hoo, Ed., American Society for Testing and Materials, 1982, pp. 358-379.

[56] H.-J. Böhmer, Wälzverschleiß und -ermüdung von Bauteilen und Maßnahmen zu ihrer Einschränkung (Rolling contact wear and fatigue of component parts and measures to reduce these), in: M. Woydt, Reibung und Verschleiß von Werkstoffen und Dünnschichten, Bauteilen und Konstruktionen, Ursachen – Analyse – Optimierung (Friction and wear of materials and thin films, components and structures: causes – analysis – optimization), expert verlag, Renningen, 2010, ISBN 978-3816927938.

[57] J.-H. Kang, B. Hosseinkhani, P.E.J. Rivera-Díaz-del-Castillo, Rolling contact fatigue in bearings: multiscale overview, Materials Science and Technology 28 (2012) 1, 44-49.

[58] H. Schlicht, Über die Entstehung von White Etching Aeras (WEA) in Wälzelementen (On the emergence of white etching areas (WEA) in rolling elements), HTM 28 (1973) 2, 112-123.

[59] H. Swahn, P.C. Becker, O. Vingsbo, Martensite decay during rolling contact fatigue in ball bearings, Metallurgical Transactions A 7 (1976) 8, 1099-1110.

[60] O. Zwirlein, H. Schlicht, Werkstoffanstrengung bei Wälzbeanspruchung - Einfluß von Reibung und Eigenspannungen (Material stressing under rolling loading – Influence of frction and residual stresses), Z. Werkstofftechnik 11 (1980) 1-14.

[61] G. Lundberg, A. Palmgren, Dynamic Capacity of Rolling Bearings., The Royal Swedish Academy of Engineering Sciences, Acta Polytechnica, Mechanical Engineering Series 1 (1947) 3.

[62] D. Nélias, M.L. Dumont, F. Champiot, D. Girodin, R. Fougères, L. Flamand, Role of Inclusions, Surface Roughness and Operating Conditions on Rolling Contact Fatigue, Journal of Tribology 121 (1999) 2, 240-251, DOI: 10.1115/1.2833927.

[63] C.-A. Manier, Slip-rolling resistance of novel Zr(C,N) thin film coatings under high Hertzian contact pressures, Doctoral Thesis, Technische Universität Berlin, 2010, BAM-Dissertationsreihe (BAM dissertation series), Band 60, ISBN 978-3-9813550-3-1.

[64] H. Hertz, Über die Berührung fester elastischer Körper (On the contact of solid elastoc bodies), Journal für die reine und angewandte Mathematik 92 (1881) 156-171.

[65] J. Shigley, C.R. Mischke, R.G. Budynas, Mechanical Engineering Design 7th edition, McGraw-Hill Science, New York, USA, 2003.

[66] J. Schulz, W. Holweger, Wechselwirkung von Additiven mit Metalloberflächen (Interaction of additives with metal surfaces), expert Verlag, Renningen, Germany, 2010.

[67] C. Wink, Predicted Scuffing Risk to Spur and Helical Gears in Commercial Vehicle Transmissions, AGMA925–A03, Gear Technology November/December (2012) 82-86.

[68] L. Feher, B. Jurconi, G. Vlase, T. Vlase, N. Doca, Decomposition Kinetic of a Synthetic Oil Absorbed on Different Silico-Alumina, Journal of Thermal Analysis and Calorimetry 88 (2007) 3, 621–624.

[69] H. Czichos, K.-H. Habig, Tribologie-Handbuch, 2nd edition, Vieweg Verlag, Wiesbaden, Germany, 2003.

[70] W.D. Callister, Materials Science and Engineering: An Introduction, 7th ed., John Wiley & Sons, Inc., New York, USA, 2007.

[71] D. Tabor, The hardness and strength of metals, J. Inst. Metals 79 (1951) 1-18.

[72] J.R. Cahoon, An improved equation relating hardness to ultimate strength, Metallurgical Transactions 3 (1972) 11, 3040.

[73] H. O'Neill, The Hardness of Metals and Its Measurement, Chapman and Hall, Ltd., London, UK, 1934.

[74] F. Hirano, N. Kuwano, K. Ichimaru, Effect of Work Hardening during Rolling Contact on Pitting of Gear Materials, Proceedings of the Institution of Mechanical Engineers, Conference Proceedings 181 (1966) 15, 85-93, DOI:10.1243/PIME_CONF_1966_181_302_02.

[75] N. Kino, N. Uchiyama, T. Yamaguchi, K. Otani, Rolling element for a continuously variable transmission (CVT), a CVT using the rolling element and a method for producing the rolling element, United States Patent, 22.02.2005, Patent Number 6858096.

[76] P.S. Pervey III, Method and apparatus for providing a residual stress distribution in the surface of a part, United States Patent, 09.07.2002, Patent Number 6415486.

[77] W. Jandeska, G. Hoffman, R. Slattery, F. Hanejko, A. Rawlings, T. Murphy, Rolling Contact Fatigue of Surface Densified Material: Microstructural Aspects, Advances in Powder Metallurgy and Particulate Materials 10 (2004) 35-52.

[78] L. Quanshun, Tribofilms in solid lubricants, in: Q.J. Wang, Y.-W. Chung (Eds.), Encyclopedia of Tribology, Springer, USA, 2013.

[79] G. Nehme, R. Mourhatch, P.B. Aswath, Effect of contact load and lubricant volume on the properties of tribofilms formed under boundary lubrication in a fully formulated oil under extreme load conditions, Wear 268 (2010) 1129 – 1147.

[80] D. Uy, S.J. Simko, R.O. Carter III, R.K. Jensen, A.K. Gangopadhyay, Characterization of anti-wear films from fresh and aged engine oil, Wear 263 (2007) 1165-1174.

[81] H. Spikes, The history and mechanisms of ZDDP, Tribology Letters 17 (2004) 3.

[82] K. Ito, J. M. Martin, C. Minfray & K. Kato, Formation Mechanism of a Low Friction ZDDP Tribofilm on Iron Oxide, Tribology Transactions 50 (2007) 2, DOI:10.1080/10402000701271010.

[83] J. Schulz, P. Feinle, A. Hirdt, J. Rigo, G. Pfeiffer, C. Seyfert, Möglichkeiten der Entwicklung von Umformprodukten auf Basis von Prüfmaschinenwerten (Possibilities of the development of custom products on the basis of test machine values), GfT-Tagung 2011, Göttingen, ISBN 978-3-00-035439-7.

[84] S. Giasson, D. Espinat, T. Palermo, Study of Microstructural Transformation of overbased Calcium Sulphonates during Friction, Lubrication Science 5 (1993) 2, 91-111.

[85] K. Wagner, H. Kloss, R. Langenstrassen, K. Meyer, Untersuchungen zur Wirkung von Schmierstoffadditiven auf Schichtbildung, Reibung und Verschleiß (Investigations of effects of lubricant additives on film formation), Schmierungstechnik 11 (1980), 330 - 336.

[86] A. Endou, T. Onodera, S. Nara, A. Suzuki, M. Koyama, H. Tsuboi, N. Hatakeyama, H. Takaba, C.A. Del Carpio, M. Kubo, A. Miyamoto, A Theoretical Study of Dynamic Behavior of Diphenyldisulphide Molecule on Fe Surface: Novel Ultra-Accelerated Quantum Chemical Molecular Dynamics Approach, Tribology Online 3 (2008) 280-284, http://doi.org/10.2474/trol.3.280.

[87] S. Płaza, R. Grusińsky, Homogeneous and heterogeneous thermal decomposition of diphenyl disulphide, Wear, (1996) 212-218, DOI: 10.1016/0043-1648(95)06859-7.

[88] O.N. Anand, V. Kumar, V.P. Malik, R.P.S. Bist, Load-carrying characteristic of reaction films of alkyl aryl sulphides, Wear 154 (1992) 349-359, DOI: 10.1016/0043-1648(92)90164-4.

[89] S. Płaza, Some chemical reactions of organic disulfides in boundary lubrication, ASLE Trans. 30 (1987) 493-500, DOI: 10.1080/05698198708981784.

[90] T. Murakami, T. Sakai, Y. Yamamoto, H. Hirano, Lubricating Performance of Organic Sulfides Under Repeated Rubbing Conditions, ASLE Trans. 28 (1985) 3, 363-373, DOI: 10.1080/05698198508981632.

[91] T. Sakai, T. Murakami, Y. Yamamoto, Lubricating Performance of Organic Sulfides Under Repeated Rubbing Conditions. Part II: Effect of Additive Concentration, Tribol. Trans. 34 (1991) 2, 215-222, DOI: 10.1080/10402009108982029.

[92] T. Sakai, T. Murakami, Y. Yamamoto Effect of dissolved oxygen concentration on the lubricating performance of an oil containing an organic sulphide, Wear, 156 (1992) 175-187, DOI: 10.1016/0043-1648(92)90152-X.

[93] T. Onodera, Y. Morita, A. Suzuki, R. Sahnoun, M. Koyama, H Tsuboi, N Hatakeyama, A. Endou, H. Takaba, C.A. Del Carpio, R.C. Deka, M. Kubo, A. Miyamoto, Tribochemical reaction dynamics of molybdenum dithiocarbamate on nascent iron surface: a hybrid quantum chemical/classical molecular dynamics study, J. Nanosci. Nanotechnol. 10 (2010) 4, 2495-2502.

[94] R.M. Mortier, S.T. Orszulik, Chemistry and Technology of Lubricants, Blackie, Glasgow and VCH, New York, 1992.

[95] B.A. Khorramian, G.R. Iyer, S. Kodali, P. Natarajan, R. Tupil, Review of antiwear additives for crankcase oils, Wear 169 (1993) 87-95, DOI: 10.1016/0043-1648(93)90394-2.

[96] D.K. Tuli, A.S. Verma, M. Rai, A.K. Bhatnagar, Additive-additive interactions: Search for synergistic FM-EP-AW composition, Wear, 174 (1994) 93-102, DOI: 10.1016/0043-1648(94)90090-6.

[97] D. Wei, H. Song, R. Wang, An investigation of the effects of some motor oil additives on the friction and wear behaviour of oil-soluble organomolybdenum compounds, Lubr. Sci. 4 (1991) 51-72, DOI: 10.1002/ls.3010040106.

[98] V.K. Lashki, Lowering fuel consumption by the addition of special motor oil additives, Khim. Tekhnol. Topliv Masel, 19 (1983) 33.

[99] R. Sarin, A.K. Gupta, A.V. Sureshbabu, V. Martin, A.K. Misra, A.K. Bhatnagar, Soluble molybdenum compound and sulphur ep additive combinations: Synergistic and adverse effects on antifriction and antiwear characteristics, Lubr. Sci. 5 (1993) 3, 213-239, DOI: 10.1002/ls.3010050305.

[100] A. Morina, A. Neville, M. Priest, J.H. Green, ZDDP and MoDTC interactions and their effect on tribological performance – tribofilm characteristics and its evolution, Tribology Letters, 24, (2006) 3, 243-256.

[101] Y. Yamamoto, S. Gondo, T. Kamakura, N. Tanaka, Frictional characteristics of molybdenum dithiophosphates, Wear 112 (1986) 79-87, DOI: 10.1016/0043-1648(86)90202-4.

[102] H. Isoyama, T. Sakurai, The lubricating mechanism of di-thio-dithio-bis(die-ethyldithiocarbamate)dimolybdenum during EP lubrication, Tribol. Int. 7 (1974) 151.

[103] C. Kajdas, Review of AW and EP working mechanisms of sulphur compounds and selected metallo-organic additives, in: Proceedings of the 5th International Colloquium on Additives for Lubricants and Operational Fluids, Ostfildern, Germany, Paper 4.6, vol. I, 1986.

[104] R. Hein, Evaluation of Bismuth Naphthenate as an EP Additive, Journal of the Society of Tribologists and Lubrication Engineers, November, 2000

[105] M.R.V. Raghavan, Structure and Mechanical Properties of Fe-Ni-Co Alloys with and Without Carbon, D. Eng. Thesis, 1972, Lawrence Berkeley Laboratory Report, LBL-477, Berkeley, California, USA.

[106] G.Y. Lai, W.E. Wood, R.A. Clark, V.F. Zackay, E.R. Parker, The effect of austenitizing temperature on the microstructure and mechanical properties of as-quenched 4340 steel, Met. Trans. 5 (1974) 1663-1670.

[107] A. Stenico, Werkstoffmechanische Untersuchungen zur Zahnfußtragfähigkeit einsatzgehärteter Zahnräder (Material-mechanical investigations of the tooth root load carrying capacity of case-hardened gear wheels), Dr.-Ing. Dissertation, TU München, 2007.

[108] DIN EN 10084: Einsatzstähle - Technische Lieferbedingungen (Case-hardening steels – Technical delivery conditions), 2008-06, German Institute for Standardization, Berlin, Germany.

[109] ASTM Standard E975: Standard Practice for X-Ray Determination of Retained Austenite in Steel with Near Random Crystallographic Orientation, ASTM International, West Conshohocken, PA, 2003, DOI: 10.1520/E0975-13.

[110] L. Spieß, G. Teichert, R. Schwarzer, H. Behnken, C. Genzel, Moderne Röntgenbeugung (Modern X-Ray diffraction), 2. Auflage (2nd edition), Vieweg + Teubner Verlag, 2009, ISBN 978-3-8349-9434-9.

[111] L. Lutterotti, S. Matthies, H.-R Wenk, MAUD: a friendly Java program for material analysis using diffraction, IUCr: Newsletter of the CPD, 21:14--15, 1999.

[112] ISO 15472:2010: Surface chemical analysis - X-ray photoelectron spectrometers - Calibration of energy scales, 2010-04-19, International Organization for Standardization, Geneva, Switzerland.

[113] C. Scholz, Low friction slip-rolling contacts – Influences of alternative steels, high performance thin film coatings and lubricants, Doctoral Thesis, Technische Universität Berlin, 2012, BAM-Dissertationsreihe (BAM dissertation series) – Band 96, ISBN 978-3-9815360-2-7.

[114] J. Burbank, M. Woydt, Comparison of slip-rolling behaviour between 20MnCr5 gear steel, 36NiCrMoV1-5-7 hot working tool steel and 45SiCrMo6 spring steel, Wear, 328-329 (2015) 28–38.

[115] C. Scholz, M. Woydt, H. Mohrbacher, The potential of 36NiCrMoV1-5-7 steel in applications demanding high slip-rolling resistance and high load carrying capacity, Proc. 2nd Int. Symp. on Nb and Mo Alloying in High Performance Steels, 24.-26. April 2013, Jeju Island, South Korea, TMS, ISBN 978-0-692-34620-4.

[116] Buderus Hot Work Tool Steel 9966 Super C; Buderus Edelstahl GmbH: Wetzlar, Germany, 07/2010, Material data sheet retrieved 15.05.2012.

[117] A&D V 300 Steel (45SiCrMo6); Aubert & Duval: Gennevilliers, France. Material data sheet retrieved 29.05.2012.

[118] N. Coniglio, C.E. Corss, W. Österle, Phase formation in 6060/4043 aluminum weld solidification, Materials Science and Engineering, A 517 (2009) 321–327.

[119] S.C. Wang, Y.W. Wu, Y. Hua, Z.C. Li, H. Zhang, Microstructure and crystallography of 20MnCr5 steel tempered at different conditions, Journal of Materials Science, 45 (2010) 5892 – 5901.

[120] K.-H. Kim, L. Jae-Seung, L. Duk-Lak, Effect of Silicon on the Spheroidization of Cementite in Hypereutectoid High Carbon Chromium Bearing Steels, Metals and Materials International, 16 (2010) 6, 871-876.

[121] A.G. Glebov, A.B. Arabey, A.N. Lutsenko, M.V. Pikunov, A.A. Nemtinov, Role of Silicon in the Macro- and Microstructure of High-Strength Steel, Steel in Translation, 40 (2010) 5, 398-406.

[122] H.K.D.H. Bhadeshia, Steels for bearings, Progress in Materials Science, 57 (2012) 2, 268-435.

[123] J.C. Imlau, Zusammenhang zwischen Mikrostruktur, Schädigungsverlauf und mechanischen Eigenschaften bei TRIP-Stählen (Relationship between microstructure, development of damage and mechanical properties in TRIP-steels), Berichte aus dem Institut für Eisenhüttenkunde, Band 1, Aachen, 2009, ISBN 978-3-8322-7952-3.

[124] M.J. Yokota, G.Y. Lai, Toughness of Lath vs Plate Martensites, Metallurgical Transactions, 6A (1975) 1832-1835.

[125] P.M. Kelly, J. Nutting, The Morphology of Martensite, Journal of the Iron and Steel Institute, 197 (1961) 199-211.

[126] A.R. Marder, A.O. Benscoter, Microcracking in Fe-C Acicular Martensite, Trans. ASM, 61 (1968) 293-299.

[127] R. Schreiber, P. Starker, H. Wohlfahrt, H. Macherauch, Werkstoffzustand und Biegewechselfestigkeit von kugelgestrahltem 16MnCr5 (Material condition and bending fatigue strength of shot-peened 16MnCr5), Conf. Proc.: ICSP-1 (1981) 695-702.

[128] J. King, A novel solid extreme pressure/antiwear lubricant additive, Presented by Dr. James P. King, Desilube Technology Inc., 1998 ELGI Annual General Meeting, Dublin, Ireland.

[129] Y. Hwang, J.-K Lee, J.-K. Lee, Y.-M. Jeong, S.-i. Cheong, Y.-C. Ahn, S.H. Kim, Production and dispersion stability of nanoparticles in nanofluids, Powder Technology 186 (2008) 145-153.

[130] G.P.S. Smith, K.C. Gordon, S.E. Holroyd, Raman spectroscopic quantification of calcium carbonate in spiked milk powder samples, Vibrational Spectroscopy, 67 (2013) 87– 91.

[131] T. Schmid, P. Dariz, Shedding light onto the spectrum of lime: Raman and luminescence bands of CaO, Ca(OH)2 and CaCO3, J. Raman Spectrosc., 46 (2015) 141–146.

[132] Y.S. Li, J.S. Church, A.L.Woodhead, Infrared and Raman spectroscopic studies on iron oxide magnetic nano-particles and their surface modifications, Journal of Magnetism and Magnetic Materials 324 (2012) 1543–1550.

[133] D.L.A. de Faria, S. Venâncio Silva, M.T. de Oliveira, Raman Microspectroscopy of Some Iron Oxides and Oxyhydroxides, J. Raman Spectrosc., 28 (1997) 873–878.

[134] M.A. Py, Ph.E. Schmid, J.T. Vallin, Raman Scattering and Structural Properties of MoO3, Il Nuovo Cimento B Series 11, 38 (1977) 271-279.

[135] P.A. Spevack, N.S. McIntyre, Thermal Reduction of MoO3, J. Phys. Chem., 96 (1992) 9029-9035.

[136] M. Dieterle, G. Mestl, Raman spectroscopy of molybdenum oxides Part II.: Resonance Raman spectroscopic characterization of the molybdenum oxides Mo_4O_{11} and MoO_2, Phys. Chem. Chem. Phys., 4 (2002) 822–826.

[137] I. Navas et al., Growth and characterization of molybdenum oxide nanorods by RF magnetron sputtering and subsequent annealing, J. Phys. D: Appl. Phys., 42 (2009) DOI:10.1088/0022-3727/42/17/175305.

[138] H. Li et al., From Bulk to Monolayer MoS 2 : Evolution of Raman Scattering, Adv. Funct. Mater., 22 (2012) 1385–1390.

[139] M. Ni, B.D. Ratnera, Differentiating calcium carbonate polymorphs by surface analysis techniques – an XPS and TOF-SIMS study, Surf. Interface Anal., 40 (2008) 1356–1361.

[140] A.P. Grosvenor, B.A. Kobe, M.C. Biesinger, N.S. McIntyre, Investigation of multiplet splitting of Fe 2p XPS spectra and bonding in iron compounds, Surf. Interface Anal., 36 (2004) 1564–1574.

[141] J.-G. Choi, L.T. Thompson, XPS study of as-prepared and reduced molybdenum oxides, Applied Surface Science 93 (1996) 143-149.

[142] J. Baltrusaitisa, B. Mendoza-Sanchez, V. Fernandez, R. Veenstrab, N. Dukstienee, A.Roberts, N. Fairley, Generalized molybdenum oxide surface chemical state XPSdetermination via informed amorphous sample model, Applied Surface Science 326 (2015) 151–161.

[143] N.M.D. Brown, N. Cui, A. McKinley, An XPS study of the surface modification of natural MoS_2 following treatment in an RF-oxygen plasma, Applied Surface Science 134 (1998) 11–21.

[144] T. Kubo, S. Fujiwara, H. Nanao, I. Minami, S. Mori, Boundary film formation from overbased calcium sulfonate additives during running-in process of steel–DLC contact, Wear 265 (2007) 3-4, 461-467.

[145] Y. Yamamoto, S. Gondo, Friction and Wear Characteristics of Molybdenum Dithiocarbamate and Molybdenum Dithiophosphate, Tribol. Trans. 32 (1989) 251–257.

[146] C. Grossiord, K. Varlot, J.M. Martin, T. Le-Mogne, C. Esnouf, K. Inoue, MoS_2 single sheet lubrication by molybdenum dithiocarbamate, Tribol. Int. 31 (1998) 737–743.

[147] M.I. de Barros'Bouchet, J.M. Martin, T. Le-Mogne, B. Vacher, Boundary lubrication mechanisms of carbon coatings by MoDTC and ZDDP additives, Tribology International 38 (2005) 257–264.

[148] P.J. Bolton, P. Clayton, I.J. McEwen, Wear of Rail and Tire Steels Under Rolling/Sliding Conditions, ASME/ASLE Lubrication Conference, 18-21 August, 1980, San Francisco, U.S.A.

[149] P.J. Bolton, P. Clayton, Rolling-Sliding Wear Damage in Rail and Tyre Steels, Wear, 93 (1984) 145-165.

[150] H. Schlicht, E. Schreiber, O. Zwirlein, Effects of Material Properties on Bearing Steel Fatigue Strength, in: J.J.C. Hoo, Effect of Steel Manufacturing Processes on the Quality of Bearing steels, STP 987, ASTM International, 1988, Philadelphia, USA.

[151] N.M. Mikhin, K.S. Lyapin, Hardness dependence of the coefficient of friction, Soviet Physics Journal, 13 (1970) 3, 317-321.

[152] S.A. Kim, W.L. Johnson, Elastic constants and internal friction of martensitic steel, ferritic-pearlitic steel, and α-iron, Materials Science and Engineering A 452–453 (2007) 633-639.

[153] S.J. Bull, T.F. Page, The effects of ion implantation on the friction behaviour of sapphire, Journal of Materials Science 30 (1995) 5356-5370.

[154] G. Li, J. Chen, D. Guan, Friction and wear behaviors of nanocrystalline surface layer of medium carbon steel, Tribology International, 43 (2010) 11, 2216-2221.

[155] J. Burbank, M. Woydt, Friction and wear reductions under slip-rolling contact through chemically reactive tribofilm generation during pre-conditioning of steel alloys, Wear 338-339 (2015) 133-143.

[156] M. Kasrai, J.N. Cutler, K. Gore, G. Canning and G.M. Bancroft, The chemistry of antiwear films generated by the combination of ZDDP and MoDTC examined by X-ray absorption spectroscopy Tribol. Trans. 41 (1998) 69–77.

[157] M. Muraki, Y. Yanagi and K. Sakaguchi, Synergistic effect on frictional characteristics under rolling-sliding conditions due to a combination of molybdenum dialkyldithiocarbamate and zinc dialkyldithiophosphate, Tribol. Int. 30 (1997) 69–75.

[158] R. Unnikrishnan, M.C. Jain, A.K. Harinarayan, A.K. Mehta, Additive–additive interaction: an XPS study of the effect of ZDDP on the AW/EP characteristics of molybdenum based additives, Wear 252 (2002) 240–249.

[159] K. Inoue, H. Watanabe, Interactions of Engine Oil Additives, ASLE Trans. 26 (1982) 189-199.

[160] F.T. Barcroft, D. Park, Interactions on heated metal surfaces between zinc dialkyldithiophosphates and other lubricating oil additives, Wear 108 (1986) 213-234.

[161] M. Suominen-Fuller, M. Kasrai, G. M. Bancroft, Advanced series in physical chemistry: part 2, (ed. T. K. Sham), Vol. 12B, World Scientific Publishing Co., 2002, Singapore.

[162] G. Pereira, A. Lachenwitzer, M. Kasrai, G.M. Bancroft, P.R. Norton, M. Abrecht, P.U.P.A. Gilbert, T. Regier, R.I.R. Blyth, J. Thompson, Chemical and mechanical analysis of tribofilms from fully formulated oils Part 1 – Films on 52100 steel, Tribology 1 (2007) 1, 48-61.

[163] Y. Wan, M.L. Suominen Fuller, M. Kasrai, G.M. Bancroft, K. Fyfe, J.R. Torkelson, Y.F. Hu, K.H. Tan, Effects of detergent on the chemistry of tribofilms from ZDDP: studied by X-ray absorption spectroscopy and XPS, Tibology Series 40 (2002) 155–166.

[164] N. Henein, Z. Ma, S. Huang, W. Bryzik, J. Glidewell, In Situ Wear Measuring Technique in Engine Cylinders, Tribology Transactions, 41 (1998) 4, 579-585, DOI: 10.1080/10402009808983785.

[165] T.J. Karol, S.G. Donnelly, Preparation of bismuth dithiocarbamates, United States Patent, 20.05.1997, Patent Number: 5631214.

[166] R. Cisler, S.-Y. Hsu, A. Phillips, B. Pastore, R. Krinker, H. Faci, C. Lege, Process for producing bismuth dithiocarbamates and dithiophosphorates, International Patent, 10.05.2001, Patent Number: CA2389296 A1.

[167] Shell Gadus S3 Wirerope T Aerosol, MSDS No. D8501, Regulation 1907/2006/EC, Jungent AS, Latvia, Effective Date 21.01.2011.

[168] M. Lalia-Kantouri, G.E. Manoussakis, Thermal decomposition of tris(N,N-disubstituted dithiocarbamate) complexes of As(III), Sb(III) and Bi(III), Journal of Thermal Analysis, 29 (1984) 1151-1169

[169] F.D. Hardcastle, I.E. Wachs, The Molecular Structure of Bismuth Oxide by Raman Spectroscopy, Journal of Solid State Chemistry 97 (1992) 319 - 331.

[170] K. Trentelman, A note on the characterization of bismuth black by Raman microspectroscopy, J. Raman Spectrosc., 40 (2009) 585 – 589.